ORNL/Sub/86-55936/01

Solid Particle Erosion in Turbulent Flows Past Tube Banks

Report Prepared by

Joseph A.C. Humphrey
Department of Mechanical Engineering
University of California at Berkeley
Berkeley, CA 94720

February 1990

under

Subcontract No. 19X-55936C
WBS Element UCB-3

for

OAK RIDGE NATIONAL LABORATORY
Oak Ridge, Tennessee 37831
operated by
MARTIN MARIETTA ENERGY SYSTEMS, INC.
for the
U.S. DEPARTMENT OF ENERGY
under Contract No. DE-AC05-84OR21400

ORNL/Sub/86-55936/01

Solid Particle Erosion in Turbulent Flows Past Tube Banks

Research sponsored by the U.S. Department of Energy,
Fossil Energy
Advanced Research and Technology Development Materials Program

Report Prepared by

Joseph A.C. Humphrey
Department of Mechanical Engineering
University of California at Berkeley
Berkeley, CA 94720

February 1990

under

Subcontract No. 19X-55936C
WBS Element UCB-3

for

OAK RIDGE NATIONAL LABORATORY
Oak Ridge, Tennessee 37831
operated by
MARTIN MARIETTA ENERGY SYSTEMS, INC.
for the
U.S. DEPARTMENT OF ENERGY
under Contract No. DE-AC05-84OR21400

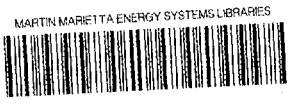

TABLE OF CONTENTS

Abstract

Executive Summary

1. Introduction

2. Theoretical Analysis and Computation

    2.1 Fluid Mechanics

    2.2 Particle Tracking and Erosion

    2.3 Heat Transfer

3. Experiments

4. Conclusions and Recommendations

Appendices

    A-1 "Fundamentals of Fluid Motion in Erosion by Solid Particle Impact"

    A-2 "Numerical Calculation of Particle-Laden Gas Flows Past Tubes"

    A-3 "Fluid Mechanics Effects on Particle Erosion in Non-Isothermal Turbulent Flows Past Tubes"

    A-4 "Note on the Experimental Measurement of Particles Embedded in One and Two In-Line Tubes in a High Speed Gas Stream"

Research sponsored by the U.S. Department of Energy, Fossil Energy AR&TD Materials Program, DOE/FE AA 15 10 10 0, Work Breakdown Structure Element UCB-3.

ABSTRACT

A review is presented for research performed on the influence of fluid mechanics on erosion by solid particle impact. The main findings are presented in summary form, with the necessary supporting technical details relegated to substantial self-contained appendices. The investigation has shown that fluid motion, especially turbulent fluid motion, can have a significant effect on particle speeds and trajectories, thus altering particle erosion potential. The investigation also shows that all major particle transport and wear phenomena can be rendered predictable for engineering purposes using appropriate physico-mathematical models. However, uncertainties in the empirical inputs to the models result in corresponding uncertainties in the predictions that are difficult to quantify. The calculation procedures developed in the course of this work provide a carefully tested basis for advancing the mathematical modeling and numerical prediction of erosive particle-laden gas flows.

EXECUTIVE SUMMARY

The erosion of material surfaces by solid particle impact is a problem of considerable importance to industry. It is highly desirable for engineering purposes to render predictable fluid and particle motions, and the attendant erosion of material surfaces. The existing methodologies that currently do this neglect the influence of turbulence and are limited to rather simple geometrical configurations. During the period of research for this project, the PI and his students have developed a body-fitted coordinate numerical procedure for calculating isothermal and non-isothermal particle-laden turbulent gas flows past tubes. In addition, measurements of particle deposition on one and two in-line tubes, performed for this work, provided experimental data for comparison with the calculations, and the agreement is good between the two. These and other careful checks of the numerical procedures give confidence in relation to their use for predictive purposes. During the course of the investigation, a substantial amount of useful information was uncovered which has been documented in the form of a major review on the subject. The review is included in this report.

1. INTRODUCTION

The problem of erosion by solid particle impact is of considerable importance to industry. Safety, material resources and energy cost considerations contribute to the forces spurring research on the subject.

Material scientists have long been involved in erosion research. However, the interpretations of their findings have been strongly conditioned by the "materials" viewpoint, which draws heavily upon what is known about material properties and the mechanisms by means of which materials interact under applied forces. Although all useful material wear models recognize the importance of relative speed and incidence angle between interacting pieces of matter, they pay virtually no attention to the displacement history of these pieces of matter relative to their respective origins. For example, it is common in air/sand jet-blast experiments to correlate wear with the jet air speed at the nozzle origin (this is the step that recognizes that particle kinetic energy matters to erosion and is somehow connected to the air jet speed). However, detailed analysis will show that the flow conditions near the impacted surface, and the particle speeds and trajectories at the instant of impact, differ considerable from the air flow conditions at the nozzle origin. To be generally applicable, models of erosion must distinguish among such basic differences and bring to the forefront the major effects of fluid mechanics in erosion.

The purpose of this study has been to redress the above state of affairs by first establishing what is the "state-of -the-art" of fluid mechanics effects in erosion, and then working on a few specific issues of engineering importance amenable to theoretical analysis and experimentation.

The results of the first step are provided in Appendix A-1: "Fundamentals of Fluid Motion in Erosion by Solid Particle Impact." This substantial review will appear as the feature article in the September 1990 issue of the International Journal of Heat and Fluid Flow. It represents an important component of the present report through which it will be disseminated quickly and effectively among the readers most likely to benefit immediately from its contents. The main conclusions of the review are given on pages 68 to 71 of Appendix A-1 and are summarized here:

1. Numerous important erosion findings have been attributed to materials-related causes that, in fact, admit purely fluid mechanics interpretations.

2. Most experimental work in erosion fails to adequately control, let alone quantify to within bounded uncertainties, the fluid mechanics variables that affect solid particle motion and surface impaction.

3. In spite of the fact that appropriate measurement techniques exist, no fundamental experimental study of erosion by solid particle impact has yet been performed where the characteristics of the turbulence are varied in a controlled and systematic manner over a meaningful range of relevant parameters.

4. Direct numerical simulations of particle-laden turbulent fluid flows are unlikely to benefit the industry in the immediate future. Phenomenological modeling approaches will continue to be the workhorse for the complex configurations of interest. In this regard, lagrangian formulations of particle motion are more useful than eulerian for predicting erosion.

5. There are many important aspects of the erosion process that are, at present, too complex to model and too difficult to measure. These relate to particle-particle collisions, and particle-surface interactions such as rebounding, fragmentation and spin. Here, innovative experimental and theoretical approaches are sorely needed.

6. Significant research advances have been made in the materials area that explain wear phenomena and show promise for the development of more generally applicable theory. However, it is important to note that such advances cannot be successfully concluded without a consideration of the relevant fluid mechanics aspects of the erosion problem. In this regard, the effective communication between material scientists and fluid mechanicians is indispensable, should be encouraged and must be appropriately supported.

The review in Appendix A-1 identifies the need to measure and model the effects of turbulence on particle motion in order to render erosion by particle impact more accurately and generally predictable. The bulk of the present investigation has been directed to the physico-mathematical modeling aspects of the problem, with limited measurements performed to provide

fundamental guidance and verify some of the computed results. Section 2 of this report summarizes the theoretical approach for calculating particle-laden gas flows past tubes. Appendices A-2 and A-3 provide the details relating to the fluid mechanics, particle tracking and heat transfer (for non-isothermal flows). Section 3 summarizes the results of an experiment specifically conducted to measure particle deposition on tube surfaces. Section 4 presents the major conclusions and recommendations for future work resulting from this study.

2. THEORETICAL ANALYSIS AND COMPUTATION

The numerical modeling of dilute particle-laden gases flowing past solid tube surfaces and producing erosion was identified as the main objective of this work. This has required the accomplishment of two major tasks: calculating the isothermal and non-isothermal fluid flow fields around tubes; calculating the associated particle velocities and the attendant wear.

2.1 Fluid Mechanics

Throughout the course of this investigation, attention has centered on dilute particle-laden gases wherein particle-particle collisions are infrequent and the particle density to gas density ratio corresponds roughly to that of sand in air. Non-interacting particle systems are referred to as being "one-way coupled," meaning that particle motion is dictated solely by surface forces due to the fluid and body forces such as that induced by gravity. The diluteness and high density ratio restrictions considerably simplify the computation of particle velocities and hence erosion. However, the matter of determining the flow that drives the particles past a tube in a bank of tubes is very complex and has presented the single most difficult undertaking in this study.

The first problem to address was the calculation of turbulent flow conditions. The equations of motion for turbulent flow past tubes are well known but, because of the large range of scales of motion involved, cannot be solved directly for the flow field. They must be Reynolds-decomposed and time averaged, which leads to the appearance of new turbulent stresses. The ensuing closure problem is overcome by employing an appropriate mathematical model for the extra stresses. Because the isotropic eddy viscosity model represents the simplest level of clo-

sure that accounts for field variations of turbulent viscosity, it has been explored in this work. Thus, the two-equation model developed by Dosanjh and Humphrey to calculate particle-laden jets was adapted to the tube flow problem (see Appendix A-2).

With a model available to compute turbulent flows past tubes, the next level of difficulty to overcome was the formulation of a coordinate system and equation transformation appropriate for the calculations. The approach described in Appendix A-2 is based on the use of non-orthogonal body-fitted coordinate systems wherein coordinate line spacings and shapes can be controlled.

Boundary conditions must be specified for the calculations. In the case of a tube in a tube bank, it was assumed that the flow is developed and periodic in the streamwise direction. The no-slip condition for velocity was applied at the tube wall through a law-of-the-wall relation. For non-isothermal flows it was necessary to reformulate the heat transfer problem in terms of appropriate variables so that it also could be considered "developed."

The numerical algorithm employed is well-documented in the literature and works along the lines of the SIMPLE procedure described in Appendix A-2. Details concerning the calculation sequence and algorithm performance are also provided in that appendix together with a discussion of the test results for both laminar and turbulent flows. The results of these tests were quite favorable and lend confidence to the additional exploratory calculations performed for different tube configurations and flow conditions.

2.2 Particle Tracking and Erosion

The velocity (speed and trajectory) of each particle was computed using a fourth-order adaptive step size Runge-Kutta scheme, using a lagrangian equation of motion for that particle. The particle momentum equation results from a force balance involving fluid drag and gravitational forces. For simplicity, the particles were assumed to be spherical in shape, for which the drag relations are well known. A detailed discussion of the particle momentum equation and of the drag relations used is given in Appendix A-2, together with an explanation of the interpola-

tion procedure developed to evaluate fluid velocity at each particle location on the calculation grid.

The deterministic trajectories of particles released at different arbitrary initial locations were computed to predict their incidence speeds and angles with respect to a tube surface. Erosion was calculated from these values using a cutting wear model. In the case of the stochastic calculations, a random perturbation was added to the mean velocity field in order to simulate more accurately the direct effects of the turbulent fluctuations on particle velocities, and hence erosion. As shown and discussed in Appendix A-2, the two approaches yielded quite distinct results depending on the characteristic response time of the particles.

2.3 Heat Transfer

The first stage of the theoretical component of the project (summarized above) addressed isothermal conditions in flows past tubes; see Appendix A-2. The numerical calculation procedure was subsequently extended to predict the behavior of non-isothermal flows. Specifically, we were interested in the flows of hot particle-laden gases past tube surfaces at lower temperature.

Because of the high Reynolds numbers of interest, the fluid momentum and energy equations are decoupled, constant fluid properties are assumed and the fluid flow field can be evaluated independently from its temperature field. A subsequent solution of the energy equation yields the field distribution of temperature from which the field variation of viscosity can be determined. While the variation of viscosity is of no consequence to the fluid mechanics problem (because of the constant properties assumption) it is significant for the calculation of particle trajectories. Thus, in non-isothermal flows, the field variation of viscosity is accounted for in the calculation of the drag term in the force balance upon a particle, to obtain its correct speed and trajectory.

The extension and testing of the calculation procedure described in Appendix A-2 to calculate non-isothermal flows past tubes is described in detail in Appendix A-3. Briefly, the fluid

phase energy equation and pertinent boundary conditions were programmed into the code and all calculations of temperature were performed using the same body-fitted coordinate technique described in Appendix A-2. However, the non-isothermal calculation procedure described in Appendix A-3 differs in two significant ways from the isothermal procedure described in Appendix A-2:

1. It dispenses with the law-of-the-wall assumption, by postulating a Prandtl mixing length model to calculate the turbulent components of momentum and heat transfer near solid walls.
2. It incorporates a generalization of the idea of fully developed flow and heat transfer to calculate non-isothermal flow past in-line tubes in periodic arrays.
3. It interpolates an equation of state for values of viscosity (in addition to velocity) at the various particle locations from values of temperature stored at the four nearest grid points on the calculation mesh.

3. EXPERIMENTS

The original study called for an experimental investigation of the flow of particle-laden gases past tubes. However, many of the issues that were originally considered important for the model, requiring experimental or theoretical support, were subsequently resolved by reference to the measurements and theory of others. As a result, a more modest experimental effort was focused on a point of special interest to this work, for which no data were available: the effect of a tube on the deposition of particles upon a second tube lying in the wake of the first.

For this, a high speed, isothermal air flow apparatus was assembled to measure the deposition of 40 and 97 micron glass beads at mass loading ratios less than 0.007. A technique was developed to determine the circumferential distribution of particle deposition around a tube. This consisted in placing Crisco shortening in small triangular grooves machined along the length of the tubes and weighing the mass of particles as a function of time caught in the circumferentially distributed grooves.

The apparatus, the measurement conditions and procedure, and the results are discussed in detail in Appendix A-4. The main observations are summarized here:

a) Single Tube

i) For both particle sizes, the particle deposition curves show maximum deposition in the forward stagnation region of the tube. A cosine fall-off in deposition, from the front of the tube to the 90 degree location on either side, was displayed only by the larger, more inertial particles.

ii) The deposition curves show that particles can be trapped in the recirculating flow regions behind a tube and impact the downstream surface of the tube.

iii) Because the ratio of large to small particle momentum equilibration numbers was 5.88, the large particles impacted the front of the tube in larger numbers than the smaller particles.

b) Two In-Line Tubes

i) The upstream tube of two in-line tubes drastically alters the amount and pattern of particle deposition upon the downstream tube.

ii) This protective effect is very significant, even for tubes spaced 5 diameters apart.

4. CONCLUSIONS AND RECOMMENDATIONS

4.1 Conclusions

The major conclusions of this investigation are as follows:

1. The numerical calculation of the flow and heat transfer of particle-laden gases in tube arrays can be performed with sufficient accuracy for engineering purposes. For this, however, it has been necessary to postulate statistically stationary, constant property flow conditions. Two numerical algorithms, for isothermal and non-isothermal flows respectively, have been developed and tested for this purpose.

2. The accuracy of the calculations depends on the curvilinear grids used and the turbulence model embodied in the calculation algorithm. The first inaccuracy can be controlled, by refining and redistributing the grid empirically, according to problem needs. The second inaccuracy can be diminished by employing more sophisticated levels of turbulence model closure, but this was beyond the scope of the present investigation.
3. Erosion can be calculated from particle speeds and trajectories evaluated at the instant of surface impact, using appropriate wear models. The calculations of this work reveal a strong dependence of erosion on configuration geometry and turbulent flow conditions which, traditionally, have not preoccupied the material scientist.
4. While the local effect of temperature on particle speeds and trajectories in the tube bank configuration is small, the cumulative effect may not be negligible since small changes in initial conditions are significantly amplified in passage through the tube bank as a result of particle rebounding and fragmentation.

4.2 Recommendations

As a result of this investigation, the following recommendations are offered for continuing work:

1. There is a need to emphasize the accurate control of fluid mechanics conditions, and the exploration of appropriate parameter ranges, in future experimental work on erosion by solid particle impact.
2. The assumption of non-interacting particles (dilute flows) should be relieved, to deal with the more concentrated particle flow configurations of interest to industry.
3. Closer attention must be paid to modeling the direct effects of turbulence on particle motion especially near solid surfaces. The stochastic approach of this work is a first attempt to achieve this, and points to the importance of the problem by revealing how different the results can be between deterministic and stochastic calculations of particle velocities and attendant erosion.

4. There are various phenomena very difficult to measure and/or model that bear significantly on particle motion and erosion. Examples are: evolving surface topography, particle fragmentation, particle rebounding, the influence of transverse forces (Magnus and Saffman) on particle motion, turbulent effects near surfaces. The review in Appendix A-1 discusses many of these phenomena and emphasizes the need to address them in future investigations.

APPENDICES

A-1 "Fundamentals of Fluid Motion in Erosion by Solid Particle Impact"

A-2 "Numerical Calculation of Particle-Laden Gas Flows Past Tubes"

A-3 "Fluid Mechanics Effects on Particle Erosion in Non-Isothermal Turbulent Flows Past Tubes"

A-4 "Note on the Experimental Measurement of Particles Embedded in One and Two In-Line Tubes in a High Speed Gas Stream"

FUNDAMENTALS OF FLUID MOTION IN EROSION BY SOLID PARTICLE IMPACT

by

Joseph A.C. Humphrey
Department of Mechanical Engineering
University of California at Berkeley
Berkeley, California 94720

Report No. FM-89-2

October 1989

Accepted for Publication in International Journal of Heat and Fluid Flow, 1990

ABSTRACT

Judging from the extensive literature on the subject, the phenomenon of material erosion by solid particle impact continues to challenge both practitioners and theoreticians with very complex problems. Although the importance of fluid motion to this form of wear was recognised in early works, many researchers continue to interpret and attempt to understand particle impact erosion almost exclusively in terms of the material properties involved. Little attention has been given to clarifying the influence of fluid motion, especially in the turbulent flow regime. A review of some relevant issues is presented here. It starts with an exposition of the general problem and the need for better understanding. The discussion of experimental techniques is followed by various fundamental considerations relating to the motion of solid particles conditioned by the presence of a carrier fluid, neighboring particles and a constraining solid surface. Of the experimental techniques used in erosion studies, non-intrusive optical methodologies are the most promising for measuring particle and fluid phase velocities simultanteously near a surface. Numerical models for calculating particle-laden flows and their application to predict erosion in practical engineering flow configurations are briefly discussed. Emphasis is placed throughout on uncovering areas of inadequate fundamental understanding of fluid mechanics phenomena that significantly affect erosion by solid particle impact.

TABLE OF CONTENTS

Abstract

Table of Contents

1. Introduction

    1.1 The Problem of Interest

    1.2 Material versus Fluid Mechanics Aspects of Erosion

    1.3 Scope of this Review

2. Experimental Techniques

    2.1 Characterization of Surface Damage and Erosion

    2.2 Measurement of Particle and Fluid Motion

3. Fundamental Considerations

    3.1 Fluid Motion

    3.2 Particle Motion

        3.2.1 Non-Interacting Particles

        3.2.2 Interacting Particles

        3.2.3 The Effects of Turbulence

        3.2.4 Lagrangian versus Eulerian Descriptions of Particle Motion

        3.2.5 Numerical Modeling and Applications

    3.3 Particle-Surface Interactions and Related Phenomena

        3.3.1 Determination of Restitution Coefficients

        3.3.2 Particle Fragmentation and Multiple Impacts

        3.3.3 Magnus and Saffman Forces

        3.3.4 Particle-Particle Interactions Near Surfaces

        3.3.5 Surface Topography

    3.4 Temperature Effects

4. Conclusions

Acknowledgements

References

Tables

Figures

1. INTRODUCTION

1.1 The Problem of Interest

The erosion of material surfaces by solid particle impact is a problem in nature and many multiphase flow industrial devices. It is the latter situation that concerns this review, especially in the context of particle-laden gases. Figure 1 shows four flow configurations frequently arising in engineering practice which serve to illustrate some of the main issues that will concern this review. The impinging jet geometry shown in Fig. 1-a spans a variety of applications ranging from research into material resistance to wear to metal cutting; the boundary layer drawn in Fig. 1-b characterizes the flow over blades in turbomachinery equipment; the confined flow illustrated in Fig. 1-c arises in the pneumatic transport of solids; and the obstructed flow sketched for laminar and turbulent regimes in Fig. 1-d is typical of many heat exchangers.

The anticipated dynamic behavior of large and small particles of the same material has been loosely interpreted in the figures. The ability of a particle to respond to changes in fluid velocity and so alter its trajectory is characterized by its momentum equilibration number, λ. This is algebraically defined by Eq. 6b further below and is the ratio of two time scales that characterize the dynamics of the solid and fluid phases respectively. Here it suffices to note that particles with $\lambda \gg 1$ are highly inertial and very slow to respond to changes in fluid velocity. In contrast, particles with $\lambda \ll 1$ faithfully follow the flow and, in principle, could be used to visualize fluid motion.

If the detailed velocity history were known for a particle ultimately impacting a surface, one could compute the impact velocity from which the corresponding incidence angle and incidence speed would follow. Accurate measurements of impact velocity are difficult and a numerical computation is

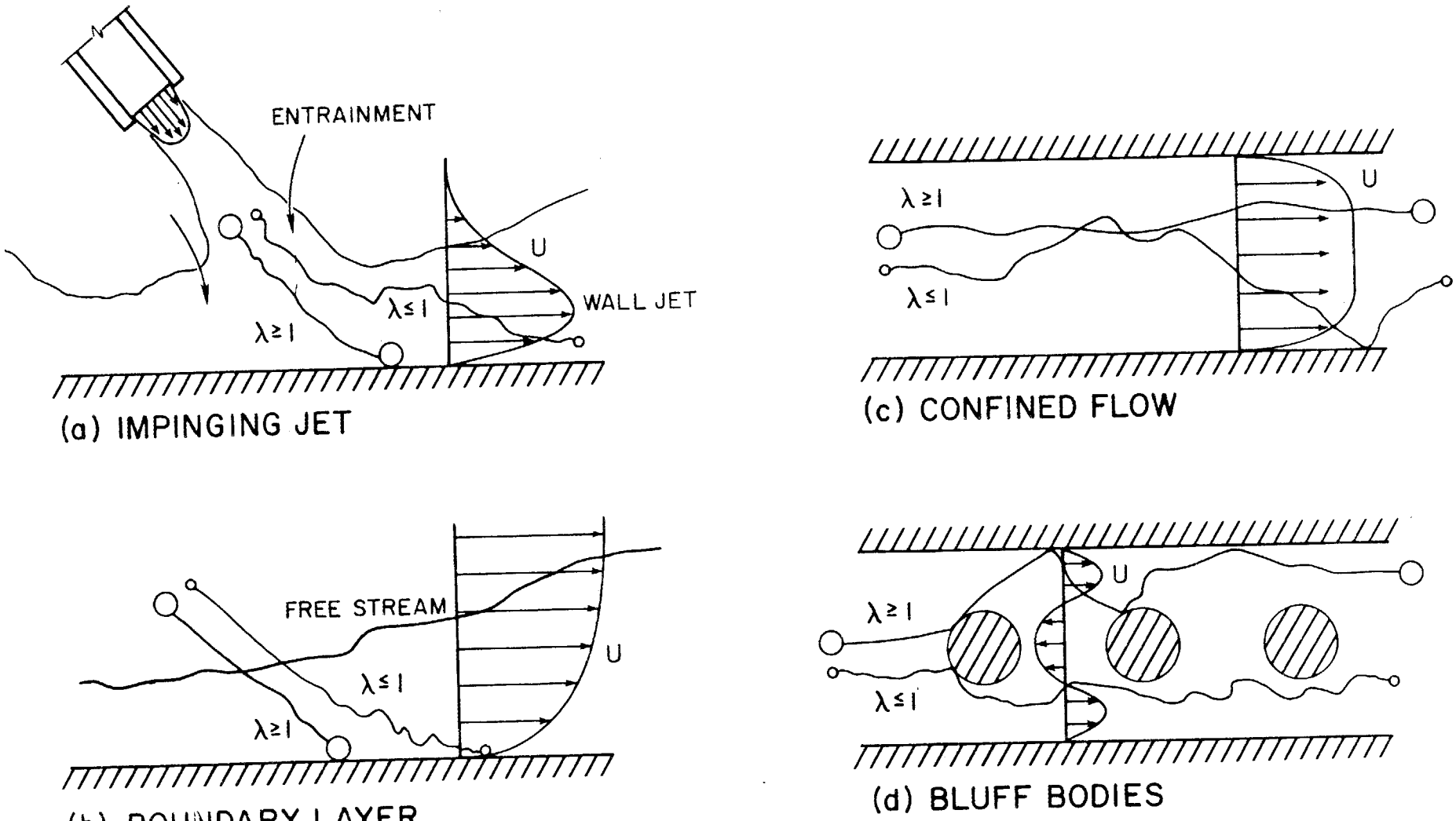

Figure 1. Examples of flow configurations prone to erosion by solid particle impact.

rendered highly uncertain by many of the assumptions underpinning the calculations. Notwithstanding, as will be shown, the theories developed by the material scientists require a knowledge of particle incidence speed and angle in order to predict surface erosion. In many past jet-blast experiments, erosive wear correlations have been based on the angle formed between the jet and the impacted surface. This has led to the incorrect interpretation of this angle, by many, as the particle incidence angle and has contributed to confusion in the literature.

It should be clear that the value of a particle's incidence velocity depends critically on particle-fluid, particle-particle and particle-surface interactions as a particle approaches a surface. The characteristics of particle-fluid interactions depend on the nature of the fluid phase flow regime (laminar vs. turbulent), as well as the size, shape, relative density and motion of the particles comprising the solid phase. Particle-particle interactions are a strong function of particle concentration and the relative motions arising from particle-surface interactions. Particle-surface interactions in turn depend on surface rebounding, surface topography, particle fragmentation and localized thermal effects resulting from particle impacts.

There are essentially two ways for reducing undesirable erosion of material surfaces exposed to impacting particles:

1. Selection of appropriate materials for maximizing resistance to wear.
2. Alteration of the conditions affecting fluid-suspended particle behavior such as particle size, concentration, impact speed, impact angle and impact location.

Much work has been done to improve the mechanical impact-wear characteristics of material surfaces. This has led to the production of exotic,

highly resistant, super alloys and ceramic materials. Unfortunately, the chemical constituents and/or the methods of production of these materials can be costly, so that their use is often restricted to only the most specialized or critical applications. The use of protective coatings and sacrificial surfaces has also been found to prolong the lifetime of system components prone to erosion [1-3] but problems arise in relation to obtaining good adhesion between coatings and substrates, and the approach is restricted to situations where erosion-induced changes in surface shapes and their effects on the particle-laden flows can be tolerated. This method requires periodic system shutdowns and component replacements. As a result it can be expensive and/or inconvenient to implement.

The elimination of potentially erosive particles from flows wherein their presence is undesirable is the most obvious, but not the most simple, solution to the problem of erosion. Cyclones, particle separators and filter units are examples of devices used for this purpose. Unfortunately, this approach can also be expensive and inconvenient to implement due to the periodic equipment shutdowns required for the replacement of parts. In any event, the complete elimination of all particle sizes is impossible, and those which cannot be deflected or trapped may still be damaging in some systems; for example, 1-10 μm diameter coal-ash particles in large utility gas turbines. Of course, such an approach does not apply to situations where the transport of particles is essential to the application.

Measurements of erosion, with "erosion" defined as

$$E = \frac{\text{mass removed from a surface}}{\text{total mass of particles impinging on a surface}}$$

show that this quantity depends markedly on the incident particle speed, V_1, and the incident angle, β_1, (the angle between a plane tangent to the surface at

the impact location and the direction of motion of the incident particle). The form of the relation established empirically [4] is given by

$$E = k V_1^n f(\beta_1) \qquad (1)$$

In this equation, k and n are constants that are assumed to depend on the physical characteristics of the materials involved, while $f(\beta_1)$ describes the dependence of erosion on the particle incidence (or impact) angle. Two commonly observed forms of this empirically determined function are shown in Fig. 2 for ductile and brittle materials respectively. Values of n for ductile materials range between 2.3 and 2.7, while values for brittle materials range between 2 and 4. These ranges are approximate.

It is clear from Eq. (1) that by altering the conditions affecting particle motion it should be possible, in principle, to project the particles along less damaging trajectories. Thus, the control of particle trajectories and impact speeds offers a means for controlling erosion. However, such control can only be achieved if the mechanisms governing particle motion are understood and can be predicted. The mechanisms encompass a rich variety of complex physical phenomena arising from particle-surface, particle-fluid and particle-particle interactions.

1.2 Material versus Fluid Mechanics Aspects of Erosion

To date, much effort has been expended researching the material-related aspects of particle impact erosion. By contrast, only relatively recently (since the mid-sixties) has there been a sustained effort aimed at learning how to control particle erosion by controlling particle motion. Some of the earliest studies can be traced back to erosion problems in turbomachinery components. In these studies the main objective has been to correlate predictions of particle

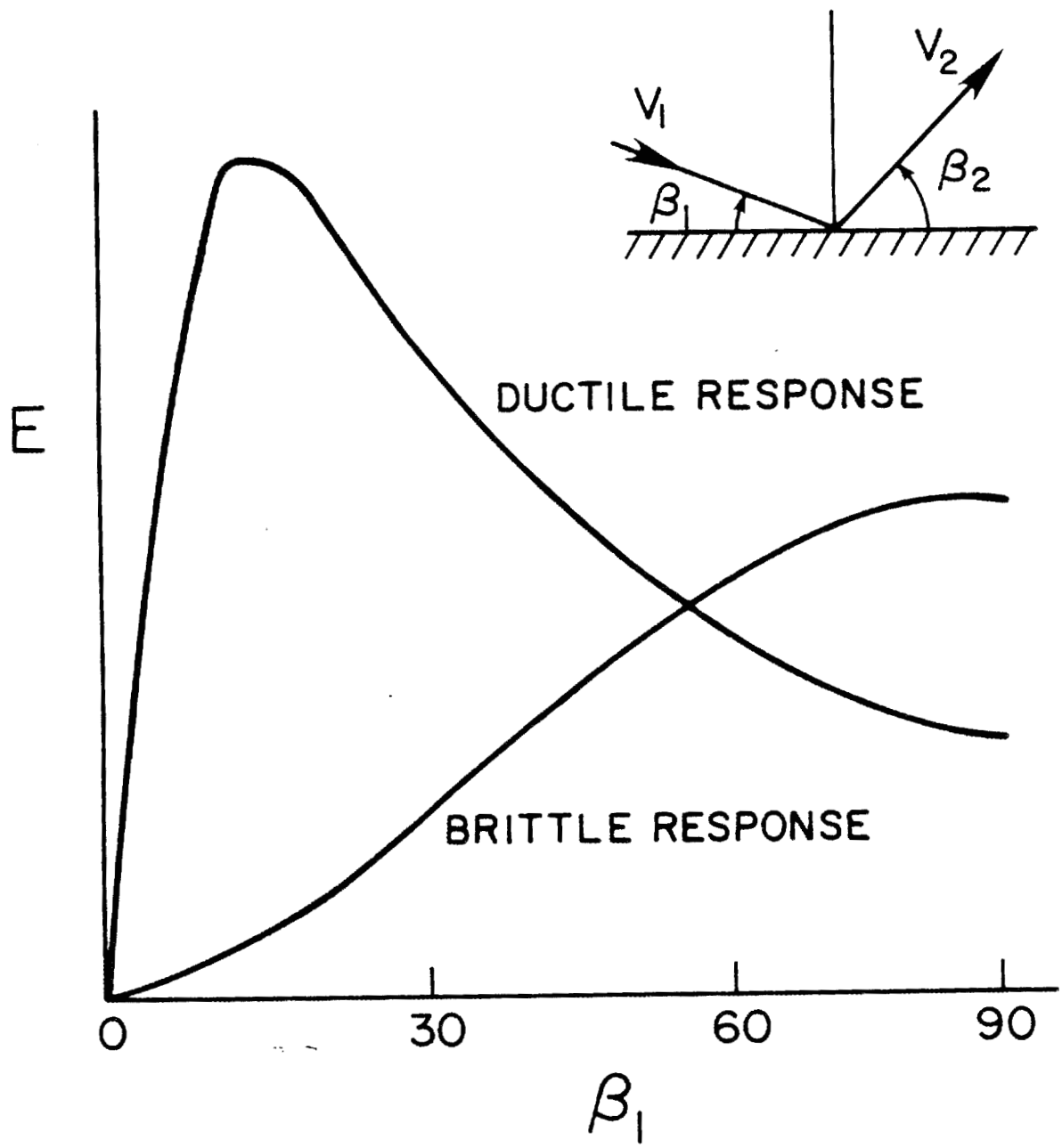

Figure 2. Typical erosion curves for ductile and brittle materials as a function of particle incidence angle, β_1, in degrees. E and β_1 are defined in the text.

incidence speeds, incidence angles and impact locations with surface erosion measurements for a practical range of conditions. While various idealizations permit the detailed analysis of two-phase flows through some turbomachinery components, in many systems such an analysis is curtailed by the complexities of the flows. Notwithstanding, practical solutions to real erosion problems often arise as a result of the improved qualitative understanding of particle-fluid motion in idealized systems.

There are numerous studies on the subject of material erosion by impacting solid particles. Examples of these are the works in [4-33] which include some fairly comprehensive reviews of the subject. Without exception, all of these works have emphasized the material-related aspects and physical properties dependence of wear in attempting to formulate physical models and mechanisms for erosion. Erosion rate differences for various substrates under similar test conditions have led to the broad classification of materials as "ductile" or "brittle" [4,6,24]. Depending on the mechanism involved, the erosion of ductile materials is further classified as "cutting" erosion or "deformation" erosion. This latter classification appears to be due to Bitter [13,14] and has received renewed attention [25,28,34]. While early studies focused on the analysis of single particles impacting a surface, the importance of multiple overlapping impacts is now recognized and currently receives considerable attention [11,24,25,28].

The objective of most erosion studies has been to provide information for establishing the form of Eq. (1) so that, for systems with known k and n, the erosion, E, may be found given V_1 and β_1. Early studies focused on obtaining wear data in systems or equipment of practical interest for which fairly specific erosion relations were derived. Presently, assisted by the availability of more advanced measurement technology and a somewhat improved theoretical

understanding of the basic mechanisms involved in erosion, the focus is on establishing more universal forms of Eq. (1) based on the interpretation of results obtained from carefully controlled experiments designed to yield fundamental and more generally applicable information. Results of studies along these lines have been summarized in [8,20,29,31]. Table 1 lists various important factors affecting erosion that have been investigated to greater or lesser extent.

Although not all of the factors listed in Table 1 are readily controlled or measured, and although most are interrelated in a rather complex manner, distinct and sometimes quantifiable trends have emerged from their investigation. Consider, for example, the very different angular dependencies of erosion displayed by brittle and ductile materials, respectively, mentioned earlier in relation to Fig. 2. Other trends revealed by experimentation, however, are inconclusive or conflicting. A case in point, discussed in some detail in [20], is the assessment of the influence of particle concentration. Fortunately, the conflicting evidence discussed by the authors is explained by the relatively narrow and rather disparate ranges in particle con-centration investigated in the past, which have led to very different observations and attendant interpretations. More difficult to answer with the data available are such questions as: How do particle concentration effects on erosion vary with flow conditions near a surface?; Are interpretations of these effects, based on measurements made in vacua, relevant to systems where particle-surface and particle-particle interactions are potentially affected by the flow conditions near a surface?

The point to emphasize is that the behavior of a particle colliding with a surface is dependent on its environment. For example, a particle which responds to part or all of the spectrum of the surrounding flow fluctuations will react differently from a particle moving in a vacuum. Similarly, the

Table 1

Factors investigated that affect the erosion of material surfaces by solid particle impact

For particles

1. Impact and rebound angles
2. Impact and rebound speeds
3. Rotation before and after impact
4. Shape and size
5. Volume concentration and surface flux
6. Physical properties (hardness, strength, density)
7. Fragmentation
8. Interactions (with surfaces, fluid or other particles)
9. Temperature
10. Presence of additives
11. Electrical charge

For surfaces

1. Physical properties
2. Change in shape due to erosion
3. Stress level
4. Temperature
5. Presence of oxide (or other) coatings
6 Simultaneous occurrence of corrosion

For the carrier fluid

1. State of motion (laminar vs. turbulent)
2. Velocity
3. Temperature
4. Chemical composition and physical properties

motion of a single particle will be different from that of one which collides with its neighbors. Except for the case of large inertial particles, flow conditions will affect particle concentrations and trajectories and, therefore, the surface fluxes, speeds and angles of attack that determine erosion.

From Adler's [4] extensive review it is clear that the early recognition given to particle speed and angle of attack, as critical parameters affecting erosion, was strictly within the context of material response to particle impact. Subsequent studies, and especially attitudes towards the interpretation of observations, have been fixed in this mold. Thus, consider a particle entrained in a fluid which approaches a surface of arbitrary shape. As the particle approaches the surface, the fluid around the particle starts deviating from the particle's trajectory in order to flow along the surface. This, in turn, induces a drag on the particle which, depending on the particle's momentum equilibration (or inertia) number, λ, will alter its original trajectory. The component of motion of the particle towards the surface is decelerated while the component of motion parallel to the surface is accelerated. As a result, the particle kinetic energy varies along the particle trajectory and will differ from the initial value (far from the surface) at the instant of impact.

The above situation differs totally from that arising in a vacuum. In systems containing fluids it is incorrect to assume that the particle velocity at the instant of impact is equal to the surrounding fluid velocity. This mismatch in velocities is frequently ignored (or overlooked) when establishing the specific form of Eq. (1). The problem has been studied by Laitone [35] and is illustrated in Fig. 3. Laitone's analysis shows that particles with $\lambda = 0.5$ approaching along the normal to any blunt surface always impinge with angles less than 90° (except for the few particles impacting directly upon the stagnation point) so that there is always a difference between the true incidence

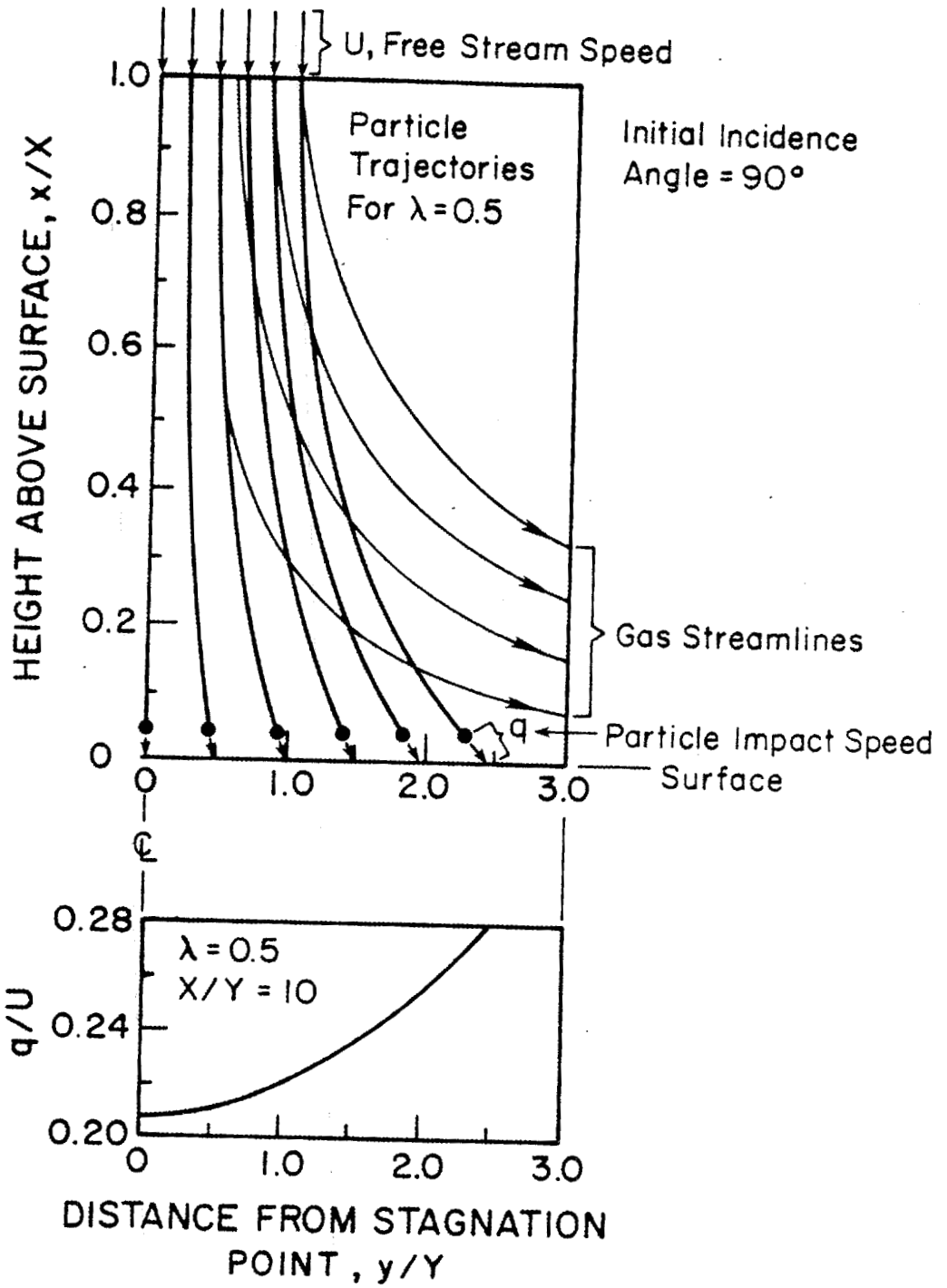

Figure 3. Gas streamlines, particle trajectories and impact speeds for particles with a momentum equilibration number $\lambda = 0.5$ in a 2-D stagnation point flow. The particles have initial positions $0 < y/Y < 1$ and $x/X = 1$ and initially travel with the gas velocity. X and Y are characteristic lengths. Based on calculations by Laitone [35].

angle and the initial angle of a particle approaching a surface. A second outcome of Laitone's analysis is the finding that the particle incidence speed is given by an expression of the form

$$V_1 \propto U_f^m \tag{2}$$

where the exponent m is a function of the average fluid speed, U_f, and varies between the limits of 1 and 2.13. At very high fluid velocities m = 1, regardless of the value of the inertia number, λ. As the fluid velocity is decreased, for each particle size there exists a critical fluid velocity below which m = 2.13. This is an important result since it affords a non-materials-related explanation for the fluid velocity exponents greater than two observed in many ductile erosion experiments. To show this, substitute Eq. (2) into Eq. (1) and, following Finnie [8], take n = 2. The result is

$$E \propto U_f^{2m} \qquad 2 < 2m < 4.26 \tag{3}$$

where, according to the analysis, the particular value of 2m depends only on U_f.

Laitone's analysis is based on the assumption of negligible interactions among particles in a streamlined flow. However, most particle-laden flows of engineering interest are turbulent and it is known [20,36] that the erosion of ductile materials decreases with increasing particle concentration due to particle-particle interactions. The complex dependence on fluid mechanic conditions of the net particle surface flux in systems with significant particle-particle interactions is compounded into the experimentally determined velocity exponent 2m.

Besides Laitone [35,37,38], other authors have drawn specific attention to the importance of "aerodynamic effects" in erosion. For example, the work in

[7,31] distinguishes between fluid flow conditions determining the number, direction and speed of particles striking a surface and the mechanisms by which surface material is actually removed. Finnie [7] recognized the importance of fluid turbulence in erosion, but Dosanjh and Humphrey [39] appear to have been the first to conduct an explicit analysis. In [7] it was suggested that local turbulence along a roughened surface might increase erosion, although no arguments were provided to support this conjecture. Interestingly, for the impinging jet configuration investigated numerically in [39], increasing turbulence was found to reduce erosion, due to the enhanced radial diffusion of particles.

1.3 Scope of this Review

The above fluid mechanics interpretation for the range of values observed in the exponent for velocity in the equation for erosion contrasts sharply with earlier interpretations based exclusively on wear mechanisms for explaining particle-surface interactions and material removal. For example, Tilly and Sage [19] have suggested that velocity exponents greater than two are a manifestation of secondary erosion due to particle fragmentation upon impact. Finnie and McFadden [10] reexamined the cutting analysis of [8] and reconsidered the assumptions concerning the location of forces during particle-surface interactions. This resulted in a theory that yielded better agreement between measurements and predictions of the velocity exponent. However, both interpretations are based on considerations which exclude potentially influential fluid mechanics effects.

The main purpose of this review is to identify and assess fluid mechanics phenomena that can significantly influence the erosion of material surfaces by impacting particles. Little will be said here concerning the actual mecha-

nisms of erosion; excellent references addressing this topic have been given in Section 1.2. Instead, attention is focused on flow-related factors which significantly modify, or control, the wear process. These factors either change the dynamic conditions of particles approaching a surface (such as speed, impact angle and surface flux) or change the conditions at the surface at the time of impact (temperature, roughness, deposition, rebounding and fragmentation).

Although attention is restricted to solid particles, much of what is said here concerning their motion applies to liquid particles also. This is true prior to surface impaction, provided the liquid particles are small and interactions among them are negligible. Large liquid particles are deformed in shearing flows. Shearing can induce circulating motions inside the liquid particles and, if the motions are intense, can also alter their size distribution and concentration. To explain these effects surface tension forces must be considered. A review including such interesting but complicated phenomena is beyond the scope of this work. Schmitt [32] has documented much of the information available on erosion by liquid particle impact.

Currently, there is an inadequate experimental data base for furthering the fundamental understanding of the influence of fluid mechanics, particularly turbulence, on erosion. Notwithstanding, the practical use of fluid mechanics to control particle erosion dates back to the forties when in 1946, Wahl and Hartstein, see [6], described various German patents for the protection of bends in pipes carrying abrasive materials. The erosion of turbomachinery components also stimulated early interest in aerodynamically-induced particle erosion, both in relation to commercial and military applications. The study of erosion in highly concentrated particle-liquid flows, such as in coal slurry pipelines, has revealed additional fundamental aspects of the problem which are very poorly understood, due to the more complicated particle-particle and particle-fluid interactions that arise in these non-Newtonian flows.

The problem of erosion by particle impact is ubiquitous and has attracted considerable attention. The abundant literature on the subject, much of which is devoid of adequate discussions of experimental and/or numerical uncertainties, attests to its fundamental and practical importance. Even when restricting attention to flow-related aspects of the problem in gas-solid systems, one discovers a vast amount of information, not all of which can be incorporated or even appropriately referenced in a review of reasonable length. From the sources of information available an attempt has been made to isolate for consideration a few of the major fundamental issues. Some readers may disagree with the choice of topics or may find that important contributions known to them are missing in this review. For these limitations I apologize in advance hoping, nevertheless, that what is offered here will stimulate further thought and technical advances in this most challenging subject area.

2. EXPERIMENTAL TECHNIQUES

The rate of erosion of a material surface is determined by measuring the mass removed from the surface as a function of time. In the laboratory this can often be done sufficiently accurately by weighing test specimens before and after their exposure to impacting particles. In the field it is preferable to employ in situ techniques that allow remote sensing of the rate of wear. An example of the latter is the ultrasonic pulse-echo technique for monitoring wall thickness [40].

It is of special interest to separately monitor erosion and particle motion under carefully controlled, usually accelerated erosion, laboratory conditions. Both the time and spacial development characteristics of the wear process are important. Various erosion testers have been devised to investigate these characteristics among which the jet-blast rig, the whirling-arm rig and the

centrifugal particle accelerator are used most often. The testers and their relative advantages and limitations are described in, for example, [27,28,41].

While the main practical objective is to quantify and correlate cumulative wear due to numerous particle impacts, it is necessary to inquire into the fundamental characteristics of single particle impact erosion. Of special interest are the relation of single particle erosion to cumulative erosion and the particle-fluid dynamic conditions affecting the trajectories and speed of the particles causing erosion. We consider briefly several techniques that have proved particularly useful for investigating these effects.

2.1 Characterization of Surface Damage and Erosion

The total amount of mass eroded from a test specimen over a period of time may be determined by simple weighing or by stylus profilometry, if sufficient mass is removed to allow precise measurement. By contrast, Andrews [42] describes a gravity-insensitive technique, based on the detection of changes in vibration frequencies, for measuring *in situ* changes of mass as small as 20 μg of specimens with total masses in the range of 0 - 5 g. Although more laborious, profilometry provides the spatial distribution of wear. Optical microscopy at low and high magnification and conventional metallographic techniques to examine sections through eroded specimens, used in conjunction with photography, complement the profilometry technique [41]. When very small amounts of mass removal are involved, for example when accelerated erosion conditions are undesirable, it may be possible to use optical interferometry to quantify spacial variations in surface topography [43].

The above techniques are suitable for measuring the cumulative wear and/or wear patterns induced by large numbers of particles eroding an extended portion of a surface. Other techniques are better suited for investigating the result of

single particle impacts. Among these, scanning electron microscopy (SEM), microanalysis by X-ray spectrometry (combined with SEM), transmission electron microscopy (TEM) and selected-area electron channeling patterns (SACP) have emerged as especially powerful methods [41,44-47]. SEM micrographs reveal topographic details while TEM micrographs display subsurface lattice defect structures such as dislocations, stacking faults and twins. The SACP technique allows the determination of plastic strain in and around particle impact sites [44].

2.2 Measurement of Particle and Fluid Motion

The techniques available for quantifying the spatial and temporal characteristics of the concentration, size-distribution and motion of a particle-laden flow can be broadly divided into mechanical and optical. The latter are non-intrusive while the former must be rugged and should influence the flow minimally. Leaving aside the non-trivial problem of monitoring bulk two-phase flow conditions that guarantee statistically reproducible conditions in an experimental apparatus, of special interest to erosion is an understanding of the characteristics of the particle-laden flow in the vicinity of the surface undergoing erosion, particularly of the complex particle impact/rebound process.

Mechanical and non-intrusive optical techniques have been used with varying degrees of success to advance this understanding. The accuracy of mechanical methods for determining particle velocity and impact/rebound angles generally decreases with decreasing particle size and increasing particle concentration. As an example, consider the rotating disk method of [48] to determine the speed of particles in particle-laden erosive jet flows. Using a pair of parallel and concentric disks a fixed distance apart, rotating at a known constant angular velocity, these authors have obtained measurements of the time of flight of par-

ticles passing through a radial notch in the first disk and impinging upon the second. However, details are not provided concerning the particle characteristics (size, concentration and density) in the flows tested. The authors recognize, but do not quantify, the disturbing effect which the rotating solid disks can induce in the jet flow pattern. Therefore, it must be surmised that the technique is restricted to the measurement of speeds of fairly inertial particles ($\lambda >> 1$) or of particles projected in a vacuum.

Among the non-intrusive optical techniques, photography has been used extensively to measure the speeds and angles of particles approaching surfaces [49]. Photographic methods include: multiple flash photography [50,51], high speed cameras [52], and streaking cameras [53]. While photography can provide an impression of the phenomena occurring within a relatively large field of view, it is expensive, labor intensive and restricted to the plane of illumination. In addition, limitations arise relating to the minimum particle size and maximum concentrations that can be adequately resolved. For example, particles smaller than 25 μm and moving at high speeds are difficult to detect with accuracy. Some of these limitations can be relieved by using laser light sheets to illuminate the field of view as in, for example, the laser-speckle photography technique [54,55], or by employing the laser-Doppler velocimetry (LDV) technique.

In contrast to photography, which is a field-of-view technique, LDV allows pointwise determinations of particle velocity. The LDV technique has been described in considerable detail [56,57]. In this approach if some particles are small enough that $\lambda << 1$ they closely follow the instantaneous fluid motion [58]. Thus, by seeding a particle-laden flow with much smaller particles having good light-scattering characteristics it is possible, in principle, to measure both the fluid and particle phase velocities. For this, however, it is

necessary to be able to distinguish between signals emitted by small and large particles respectively, something that can be accomplished using Doppler signal amplitude and/or frequency discriminating techniques [59-66]. Discussions concerning the accuracy of particle-flow velocity measurements, particle sizing and concentration distributions using LDV and related techniques are given in [67-72].

Specific applications of LDV to flows involving erosion by solid particles are reported in [73]. These authors obtained statistical distributions of the tangential and normal velocity components of 0.5 - 60 μm ash particles impacting a metal surface (unspecified) at speeds ranging between 72 and 96 m/s. Although their velocimeter system could not resolve the corresponding velocity components of rebounding particles, absolute values ranged between 6 and 60 m/s. Substantial differences have been observed between particle velocities determined using the LDV and rotating disk methods, respectively [49]. The uncertainty of the particle phase mean velocity was estimated to be ± 2.5% using LDV and ± 18% using the rotating disk method.

The potential usefulness of LDV in erosion experiments, is limited by difficulties peculiar to the erosion environment. First, use of the LDV technique is restricted to fairly dilute particle-laden gas flows. Second, even in dilute systems measurements of particle velocities near a surface are subject to serious uncertainties. These arise as a result of the finite size of the measurement volume and the need to correlate the incident characteristics of a given particle with the rebound characteristics of the same particle. When a single particle crosses the measurement volume, it is necessary to resolve the directional ambiguity of the motion (i.e., distinguish between the incident and rebound components of velocity). In principle, this can be done using frequency shifting techniques that bias the velocity measurements. However, when particles

collide (or shatter) within the measurement volume it may not be possible to distinguish between their respective velocity components (or those of the fragments). Third, in most erosion experiments particle size is a controlled variable. Consequently, in monodisperse particle flows with eroding particle diameters larger than 10-20 μm it should still be possible to distinguish between the motions of the fluid and particle phases on the basis of Doppler signal amplitude and/or frequency discriminating techniques. However, the distinction becomes increasingly difficult to make as the size of the eroding particles becomes smaller, approaching that of the particles following the motion of the fluid phase, and this may be an important source of uncertainty in highly turbulent flows.

3. FUNDAMENTAL CONSIDERATIONS

Various basic issues are considered in this section of the review that help explain some of the difficulties facing experimental and theoretical investigations of erosive particle-laden gases while identifying and bounding the relevant problem parameters.

3.1 Fluid Motion

The bulk of particle-laden gas flows occur in the turbulent flow regime and are characterized by irregularity, diffusivity, and three-dimensionality; all of which are guaranteed above a critical value of a characteristic Reynolds number. Although fluid turbulence is a continuum phenomenon appropriately described by the conservation equations of fluid mechanics [74] direct numerical solutions of these equations are, for the moment, impossible to obtain for the complex configurations of engineering interest. This is due to non-linear terms which are responsible for the very large range of scales of motion requiring extensive computer storage and calculation times to achieve accurate numerical solutions.

An alternative is to employ Reynolds decomposition of the field variables in the instantaneous equations, and to time (or ensemble) average these to obtain the mean flow equations. However, this procedure generates the Reynolds stresses which must be approximated since, after averaging, there are more unknowns than there are equations to solve them. Several authors have reviewed various closure schemes that have proven especially useful to the engineering community [75-80]. Of these, the k-ε model [39,81-83] is of special interest since it combines a degree of accuracy for turbulent fluid flow simulation commensurate with the approximations necessary to render particle motion and erosion predictable.

3.2 Particle Motion

Flows wherein suspended particles interact are not limited to situations involving the direct physical contact of the particles. Situations arise where even though the particles do not collide (or do so infrequently) they are sufficiently large in number or size that they affect one another through their collective influence on the fluid. For example, a particle passing through the wake of a larger particle, or through a cloud of particles, falls into this category. The question of averaging arises in relation to continuum (or "eulerian") formulations of two-phase flow transport equations. This leads quite naturally to a comparative evaluation between continuum and discrete (or "lagrangian") theoretical descriptions of particle-laden flows. In this section we consider these issues but attention should be called to more comprehensive sources of information on the general subject of two-phase flow [84-100]. However, the reader should note that none of these references deals specifically with the role of fluid mechanics in erosion by particle impact.

3.2.1 Non-interacting Particles

Non-interacting particle motions arise when the dynamics of any one particle are uninfluenced by the presence of neighboring particles (either directly, through collisions, or indirectly, through the perturbed fluid field). The conditions for this correspond to fairly dilute systems characterized by volume fractions α (volume of solids/total volume) less than 10^{-3} and mass loading ratios γ (mass of solids/total mass) less than 1 for particle-fluid systems with pure phase density ratios $\rho_p/\rho_f \simeq 10^3$. Typically, then, interparticle distances are of the order of 20 x d_p or greater [98], where d_p is the effective (spherical equivalent) diameter of a particle.

The general lagrangian equation of motion for a single particle in arbitrary accelerated motion is given in [97] who discuss its derivation and solution. For the condition that $\rho_p/\rho_f >> 1$ the equation is:

$$\frac{du_{pi}}{dt} = \left(\frac{3\ \rho_f\ C_D}{4\ d_p\ \rho_p}\right)\ (u_{fi} - u_{pi})\ |\ \vec{u}_f - \vec{u}_p\ |\ +\ g_i \qquad (4)$$

where i = 1, 2, 3 are the three cartesian coordinate directions, and instantaneous velocity components for the particle, u_{pi}, and the fluid, u_{fi}, are implied. In this equation, $|\ \vec{u}_f - \vec{u}_p\ | = |\ \vec{u}_r\ |$ is the modulus of the instantaneous relative velocity of the particle and g_i is the i-component of gravity. For the particle drag coefficient, C_D, empirical relations covering a wide range of particle Reynolds number are frequently used. Thus, for example, [98] suggests

$$C_D = \frac{24}{Re_p}\ \left(1 + \frac{1}{6}\ Re_p^{2/3}\right) \qquad 0 \le Re_p \le 500 \qquad (5)$$

where $Re_p = |\ \vec{u}_r\ |\ d_p\ /\nu$ is the particle translational Reynolds number based on the modulus of the instantaneous relative velocity, the particle diameter and the fluid kinematic viscosity, ν .

The drag coefficient given by Eq. (5) has been obtained experimentally, using smooth spheres in streams of uniform flow with low turbulence intensity. However, in many systems the relative flow past a particle is turbulent due to pre-existing time and length scales of motion. Where these scales are commensurate with those of the particle, the effect of the turbulence is to modify the instantaneous flow field around the particle and, hence, the net drag, which will differ from that predicted by Eq. (5). Experimental relations are available that explicitly acccount for the effect of turbulence structure on the drag coefficients for spheres. Turbulence-dependent coefficients for subcritical, critical and supercritical flow conditions as a function of the free stream relative turbulence intensity are tabulated in [97]. In principle, these correlations could be used in Eq. (4) to calculate $\vec{u}_p$.

It is rarely the case however, that the instantaneous fluid velocity, $\vec{u}_f$, in Eq. (4) is known for turbulent flow configurations of practical interest. More likely, the mean velocity, $\vec{U}_f$, will have been determined experimentally, or via numerical computation employing a turbulence model. Ensemble averaging the terms in Eq. (4), subject to the assumption that the instantaneous velocities $\vec{u}_f$ and $\vec{u}_p$ can be Reynolds-decomposed into means ($\vec{U}_f$, $\vec{U}_p$) plus fluctuations ($\vec{u}_f'$, $\vec{u}_p'$), yields an equation for the mean particle velocity, $\vec{U}_p$, which depends on $\vec{U}_f$ and on a separate, rather complicated term that accounts explicitly for the correlations among the velocity fluctuations. The correlations account for the so-called "turbulence drift velocity" [101] due to turbulent diffusion, which is frequently calculated using a flux or gradient model approximation. An alternative to modeling the drift velocity is to calculate $\vec{u}_p$ directly from Eq. (4) using $\vec{u}_f = \vec{U}_f + \vec{u}_f'$ for the instantaneous fluid velocity, where the fluctuation is determined and added to the mean velocity according to some rule. Then, the mean particle velocity, $\vec{U}_p$, if required, must be found by averaging over several

realizations of the computed flow. Direct determinations of $\vec{u}_p$, subject to rules for $\vec{u}_f$ that preserve the basic character of the turbulent motion, have been performed [83,102-104].

The assumptions embodied in Eq. (4) are: a) quasi-steady motion of non-interacting spherical particles; b) negligible virtual mass, pressure gradient, Basset, Magnus and Saffman forces; c) the only body force is that due to gravity. The accuracy of assumptions (a) and (b) are discussed by in [98] who concludes that, except for the neglect of the Basset history term, the assumptions are justified in particle-laden gas flows. For density ratios $\rho_p/\rho_f > 10^3$, [98] shows that the Basset force becomes smaller than 10% of the Stokes drag for times larger than $1/2\ \tau_p$, where τ_p is the characteristic particle relaxation or response time given by

$$\tau_p = \frac{\rho_p\ d_p^2}{18\ \mu\ f_D} \tag{6a}$$

in which μ is the fluid viscosity and $f_D = Re_p C_D/24$. If τ_p is nondimensionalized by a characteristic flow time scale, such as $\tau_f = L_c/|\vec{U}_{fc}|$ where L_c and $|\vec{U}_{fc}|$ are a characteristic length and a mean fluid velocity scale respectively, the "momentum equilibration" number, λ, is defined

$$\lambda = \tau_p f_D / \tau_f \quad . \tag{6b}$$

For $f_D = 1$, corresponding to creeping flow, λ becomes identical to the "inertia" or Stokes number, $St = \tau_p/\tau_f$. In this review the two names for λ will be used interchangeably, its precise value being determined by Eq. (6b).

While the neglect of Magnus and Saffman forces may be reasonable in the bulk of a flow, at solid surfaces where particles can rebound with large angular velocities and near which regions of strong fluid shear are induced, the magni-

tudes of these terms may be significant relative to the drag term. Even in the bulk of the flow, if the turbulence fluctuations are intense, Saffman forces can alter particle trajectories and induce corresponding large scale flow inhomogeneities [93].

For a prescribed variation of the fluid velocity components, u_{fi}, the numerical solution of Eq. (4) is readily achieved using a Runge-Kutta integration technique. The trajectory of a particle can be found from it velocity components according to:

$$\frac{dx_i}{dt} = u_{pi} \quad . \tag{7}$$

With a knowledge of particle speeds and trajectories it is possible to extrapolate for the incidence speeds and angles at the impact locations [35,37-39,83]. From the incidence values erosion may be determined with an appropriate wear model [39,83].

3.2.2 Interacting Particles

The dynamics of interacting particle flows have been the subject of in-depth research [87-89]. Calculations based on the theories of [105,106] suggest that for mass loading ratios $\gamma < 1$ ($\alpha < 10^{-3}$) of particle-gas systems with $\rho_p/\rho_f \approx 10^3$, particle-particle collisions are infrequent. However, for these conditions the average interparticle distance is less than 20 x d_p and in turbulent flow this may not be sufficient to rule out indirect interactions among particles, especially in regions where large slip velocities arise between the two phases. For conditions where the motion of the particle phase affects the motion of the fluid phase (two-way coupling) the two motions must be calculated simultaneously [107,108].

Indirect particle interactions have been considered by Hinze [93] who distinguishes among: a) effects due to the increased effective shear rates in the fluid; b) effects due to the wakes of the particles with large relative velocities; c) effects on the turbulence intensity, the integral scale, the eddy diffusivity and viscous dissipation of the fluid due to the fact that the fluid occupies less space; d) clustering of particles, which on the scale of the clusters may modify the fluid flow pattern. Associated with (a) and (b) are modifications to the energy spectrum of the fluid in the wave number ranges corresponding to the average inter-particle distance and the particle diameter respectively. This implies increasing fluid phase dissipation rates with increasing particle concentrations, in agreement with experimental measurements and theoretical analyses performed for dilute systems.

In principle, it should be possible to extend the form of Eq. (4) to include acceleration terms arising from direct and indirect particle interactions, respectively. For example, numerical simulations of the air flow of 10 μm and 210 μm alumina-silica particles through a venturi meter show that the inclusion of direct particle-particle interactions significantly alters the predicted characteristics for $\gamma > 2$, as a result of the momentum exchanges between the two phases [109]. The model used for direct interactions assumes elastic collisions among particles and neglects multiple scattering [90]. The form of the interaction term is complex and, while there is no direct evidence of its validity, its inclusion in the numerical formulation improved the agreement between measurements and calculations of pressure drop and pressure recovery through a venturi meter for mass loading ratios $\gamma > 2$.

In flows where strong particle interactions arise, it is inappropriate to use standard (single sphere) drag coefficient relations and modified drag coefficients are required [98]. Because of the complexities involved, one must rely

on experimental measurements of the coefficients for specific configurations and flow conditions of interest. Unfortunately, the associated experimental uncertainties are rather large.

3.2.3 The Effects of Turbulence

There is considerable literature pertaining to the influence of turbulence on particle motion, particularly in relation to particle dispersion in the bulk of a fluid. By contrast, there is very little information regarding how the presence of a surface: a) alters the dispersion mehanism(s); b) changes the particle flux to the surface; c) influences the evolution of the wear patterns observed as a result of evolving surface topography. Among others, Owen [92] and Hinze [93] have considered some fundamental aspects of turbulent fluid-particle interactions. A brief summary of the most relevant findings in these and some related investigations is offered here.

Hinze [93] has investigated the response time of a discrete spherical particle relative to the various characteristic times of the turbulent carrier fluid. Among his major conclusions are that particles with $d_p/\eta \leq 1$, where η is the Kolmogoroff (dissipative) micro-scale of turbulence, will respond to the motion of the smallest eddies. The approximate condition for this is given by:

$$\frac{d_p}{\eta} < \left(\frac{10}{\rho_p/\rho_f + \beta}\right)^{1/2} \tag{8}$$

where β is a coefficient of order 1 related to the virtual mass contribution to the particle momentum balance. For sand in air ($\rho_p/\rho_f \sim 2000$) this condition gives $d_p/\eta \simeq 0.1$. In a typical turbulent flow at high Reynolds number $\eta \simeq 10 - 100$ μm, implying that particles with $d_p < 1 - 10$ μm will respond to this scale of motion. By contrast, the condition for particles of the same den-

sity ratio to adapt to the motions of the large energy-containing eddies, say of size ℓ, is given by:

$$\frac{d_p}{\ell} < \left(\frac{\nu/\tilde{u}_f \ell}{\rho_p/\rho_f + \beta}\right)^{1/2} \tag{9}$$

where the tilde in $\tilde{u}_f$ denotes the r.m.s. component (or some related characteristic measure) of the turbulent fluid velocity. For the case of sand in air flowing through a 20 inch (0.5 m) diameter pipe, noting that typically $\nu/\tilde{u}_f \ell < 100$, Eq. (9) yields $d_p < 10^{-3}$ m. Thus, heavy particles larger than 1 mm will be relatively insensitive to all scales of turbulent motion in air.

From the above results it is clear that in many industrial particle-laden flows there can exist a range of particle sizes and flow conditions capable of satisfying Eq. (9) while not satisfying Eq. (8). These particles do not experience the full spectrum of turbulence and one anticipates considerable difficulty in attempting to model the influence of turbulence on their motion [93,110].

For particle suspensions with $\rho_p/\rho_f >> 1$ the Magnus force induced by particle rotation is generally small. By contrast, particles with $d_p/\eta \leq 1$ immersed in the thin shear layers that can develop between eddies may experience large lateral forces that drive them through the shear layers during the lifetime of the eddies. This force is referred to as the Saffman force. It can induce clustering of particles within eddies, where the shear rates are lower, and promote large scale concentration fluctuations that affect the turbulence characteristics of the suspension. The Magnus and Saffman forces are discussed in more detail in Section 3.3.3 for particles rebounding from surfaces.

For long diffusion times, analyses of particle motion must allow for the possibility that the particle will escape from the fluid surrounding it originally. Most theoretical analyses yield $\nu_p/\nu_f < 1$ for the ratio of particle phase to fluid phase eddy diffusion coefficients, but this is at variance with experimental evidence [111,112] and numerical calculations [110,113,114], which show that for large dense particles it is possible to find $\nu_p/\nu_f > 1$. Theory predicts that ν_p/ν_f increases markedly when the particle size becomes of the order of, or larger than, the Taylor microscale, λ_T [111]. Because $\eta << \lambda_T << \ell$, this suggests a filtered response of the particles to the spectrum of fluid turbulence.

The effects of particles on the turbulence of a gas phase have also been investigated by Owen [92] in relation to the pneumatic transport of particles through horizontal pipes. For dilute systems of small particles in Stokes flow regime, he shows that the dissipation of turbulent kinetic energy by the fluid phase in a pipe flow at fixed Reynolds number increases with increasing particle concentration. A related result is that the ratio of characteristic gas-phase velocity fluctuations with and without small particles present should vary according to:

$$\frac{\tilde{u}_{f,p}}{\tilde{u}_f} \simeq (1 + \alpha\, \rho_p/\rho_f)^{-1/2} \qquad (10)$$

Assuming that the turbulent length scale ℓ is not affected by the presence of the particles, the ratio of eddy diffusion coefficients for fluid with and without particles, $\nu_{f,p}/\nu_f$, should also vary according to Eq. (10). The result is a reduced eddy diffusion coefficient of fluid with particles relative to fluid without particles.

The extension of Eq. (10) to apply to larger particles prone to turbulence-spectrum filtering effects yields:

$$\frac{\tilde{u}_{f,p}}{\tilde{u}_f} \simeq \left(1 + (\alpha\, \rho_p/\rho_f)\, (\tau_e/\tau_p)\right)^{-1/2} \qquad (11)$$

where τ_p is given by Eq. (6) and τ_e ($\equiv \ell/\tilde{u}_f$) is the characteristic time of an energy-containing eddy.

In considering how particles in pipe flow are projected towards a wall, Owen proposes that the particles are convected from regions of intense turbulence outside the viscous sublayer by occasional eddies that penetrate the sublayer. From the particle dynamics point of view, Owen divides the wall flow region into two layers. Away from the wall particles are dispersed (in a direction normal to the wall) by the action of turbulent diffusion, leading to the "diffusion regime" layer. Near the wall the particles are convected instead, hence the terminology "convection regime" layer. Within the diffusion layer $\tau_p/\tau_e < 1$, while within the convective layer $\tau_p/\tau_e \geq 1$. (Near the wall a more appropriate estimate for τ_e is given by ν/u_τ^2 where $u_\tau = (\tau_w/\rho_f)^{1/2}$ is the friction velocity at the pipe wall, τ_w being the wall shear stress.)

Rizk and Elgobashi [115] have analyzed the influence of a plane wall on the motion of spherical particles suspended in a turbulent fluid. The study is an extension of earlier work [116] wherein the lagrangian equation of particle motion is treated as a linear, stochastic integro-differential equation to which the Fourier transform is applied. The authors extended the formulation in [116] to account for the additional wall-induced drag on a particle and the Saffman lift force due to shear. Expressions were obtained that relate the turbulence intensity, energy spectrum and double velocity correlation coefficient of the

two phases. Their results apply to particles smaller than the dissipative scale of motion for which both $Re_p << 1$ and $Re_s << 1$. (Re_p is the particle translational Reynolds number as defined above while $Re_s = d_p^2 \Omega_f / \nu$ is the particle shear Reynolds number based on the modulus of the fluid vorticity vector, $\vec{\Omega}_f$. Their main conclusions are that in the vicinity of a wall: i) turbulent fluid fluctuations are more strongly damped than turbulent particle fluctuations; ii) the r.m.s. velocity of a particle near a wall is greater than that of a particle removed from the wall, particularly in the direction normal to the wall to which the shear lift force contributes strongly; iii) the relative influence of the lift force on particle motion extends further from the wall than the additional viscous drag; iv) a particle's response to turbulent fluid fluctuations decreases with increasing particle size and density. The authors provide closed form expressions for the wall-distance dependence of the above observations. The Fourier transform methodology developed in [116] allows them to find expressions of the form,

$$(\tilde{u}_{pi} / \tilde{u}_{fi})^2 = \int_0^\infty \Omega \, F(\omega) \, d\omega \qquad (12)$$

which relate the turbulence intensity of the particle motion to that of the surrounding fluid through the latter's energy spectrum and the ratio of two polynomials, Ω, which depends on the flow fluctuation frequency, the particle fluid density ratio and the distance from the wall.

Figure 4 from these authors' work shows normalised particle and fluid r.m.s. velocities parallel and normal to a wall as a function of the dimensionless wall distance $y^+ = y u_\tau / \nu$. The calculations are for $\rho_p / \rho_f \simeq 1500$, roughly corresponding to coal particles in air at 25°C. As for y, the particle sizes have been normalised by ν / u_τ. The dots in the figure correspond to measurements [117] of pure fluid phase fluctuations with which the authors obtain agreement

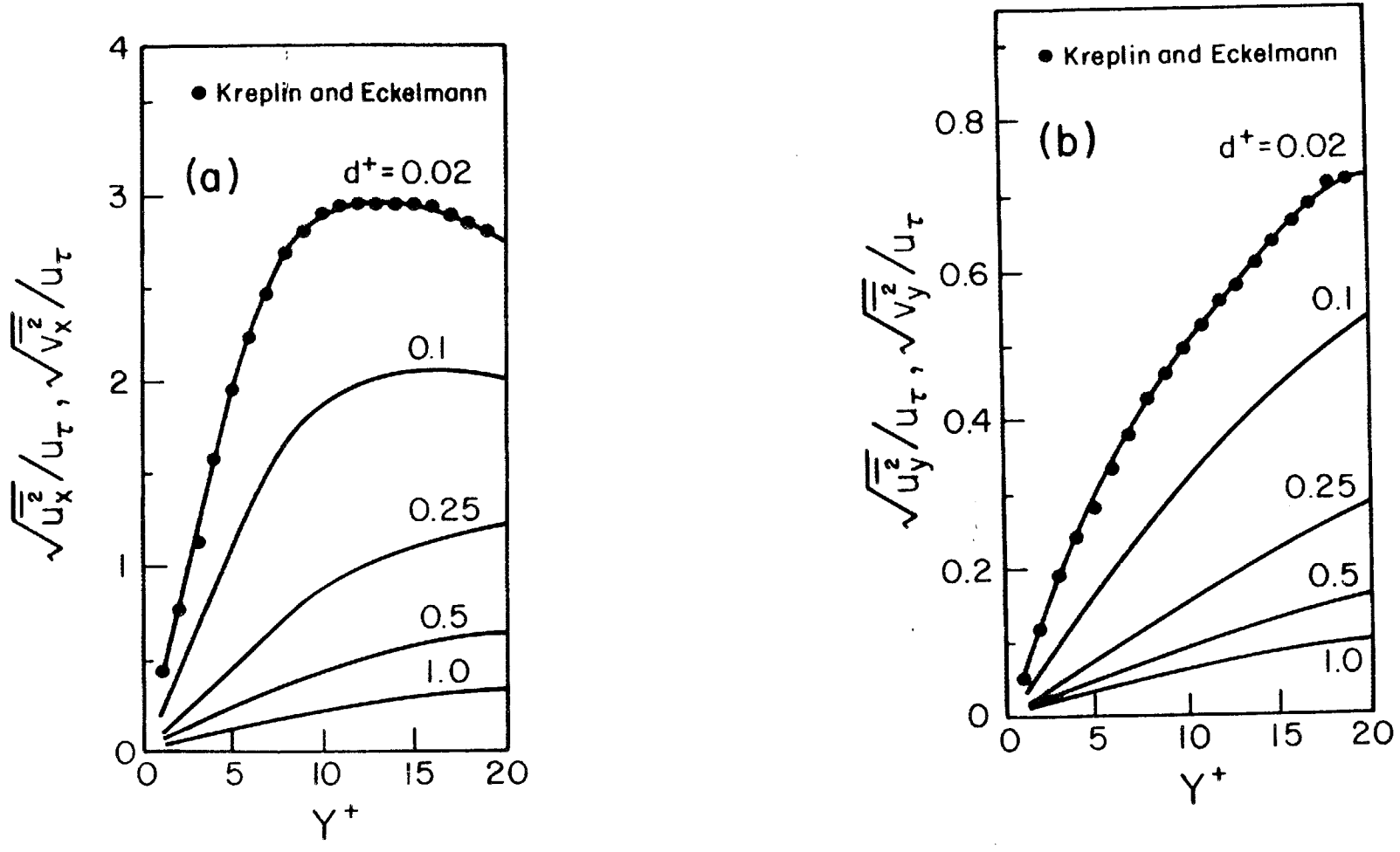

Figure 4. Fluid (u, dots) and particle (v, lines) rms velocities parallel (x-component) and normal (y-component) to a wall for a particle/fluid density ratio ρ_p/ρ_f = 1500 and different dimensionless particle sizes, d^+. Conditions correspond to a dilute suspension of spherical particles in a fully developed turbulent channel flow with Re = 7,700. Based on calculations by Rizk and Elgobashi [115] and measurements by Kreplin and Eckelmann [117].

provided $d_\rho^+ \leq 0.02$.

Qualitative confirmations of many of the findings presented in this section are to be found in numerous experiments performed in particle-laden jets and pipe flows [66,82,104,118-121]. In [120], the fluid turbulence and its mean velocity gradient were markedly reduced by particles near a wall in pipe flow. Impacting particles accounted for a large fraction of the wall shear stress and the attendant observed reduction in the friction factor. In [66,121], laser-Doppler measurements provide a clear impression of the response of the mean and fluctuating flow components to particle size and concentration. The authors of [66] investigated the flow of particle-laden air through a vertical pipe. Flows with particles ranging in size from 200 μm to 3 mm were investigated at pipe Reynolds numbers of approximately 2.2×10^4. In general, over a pipe cross-section, large particles were found to increase the air turbulence while small particles reduced it. Both of these effects were observed to vary in direct proportion to particle concentration. Increases in turbulence were most noticeable in the core of the flow, while the decreases were marked near the pipe wall. Intermediate particle sizes (500 μm) showed both effects simultaneously.

In summary, in spite of considerable work of which a small sample has been discussed here, a wide gap persists between the qualitative and quantitative understanding of the effects of turbulence on particle motion in two-phase flow. Most of the trustworthy quantitative information available for particle-laden gases pertains almost exclusively to dilute systems of small particles away from walls. The important constraints imposed by the presence of solid surfaces in the flow, and the implications for erosion, remain undocumented and very poorly understood. Theoretical attempts to model turbulence effects on particle motion

rely either on experimentally determined drag correlations that are prone to serious uncertainties, or on ad hoc extensions of formulations premised on considerations relating to single particles. Even for gas-solid systems, where the condition $\rho_p/\rho_f >> 1$ simplifies the particle equation of motion considerably, analytical solutions are few and one must rely instead on numerical methods to calculate particle speeds and trajectories.

3.2.4 Lagrangian versus Eulerian Descriptions of Particle Motion

A lagrangian description of particle motion implies a particle phase which is discrete in nature. The eulerian description treats the particle phase as a continuum that admits appropriate definitions of averaged field quantities. Both approaches have been used extensively in the literature.

The lagrangian approach predicts the speeds and trajectories of individual particles as a result of a force balance taken on each particle; see Eq. (4). By assuming different initial locations and sizes, and using statistical techniques, the motion of the particle phase and its interactions with the fluid can be calculated. In the eulerian approach conservation equations embodying postulated constitutive relations are solved to predict the field distributions of momentum and volume fraction of each phase. The form of the eulerian particle momentum equation is closely connected to its lagrangian equivalent since the former can be derived from the latter by averaging over the particle phase. In both the lagrangian and eulerian approaches, the particle-fluid momentum equations are coupled through the drag source/sink terms and through the volume fraction of the particle phase. If the volume fraction of particles is very small, two-way coupling between the phases is reduced to the drag interactions mutually induced. A one-way coupling condition exists when the influence of particle drag on the momentum balance of the fluid phase is negligible.

The relative advantages and disadvantages of lagrangian and eulerian descriptions of particle motion have been discussed [122-125]. Because the lagrangian approach yields a more detailed physical description of the particle phase, such as individual particle speeds, trajectories and residence times, it is more germane to the problem of predicting erosion. The lagrangian approach appears to be less prone to numerical diffusion errors, is more stable in flows with large particle velocity gradients and is readily applied to polydispersed particle systems. On the negative side are the facts that in concentrated systems with significant particle-fluid and particle-particle interactions: a) model formulations are inadequate due to a lack of fundamental understanding concerning the interactions; b) limitations related to computer storage, calculation times and convergence arise.

In principle, the eulerian discription is favored by high concentrations of the particle phase. Through rigorous definitions of averaging procedures it offers a formal methodology for developing numerical models dealing with direct and indirect particle interactions and fluid turbulence [100,126-129]. In spite of its formal framework, however, in practice the continuum modeling of interactions leading to constitutive relations for particle-particle and particle-fluid stresses is in its infancy. The reason for this is the same as for the lagrangian approach; an insufficient understanding of the complex particle-particle and particle-fluid interactions that arise in turbulent flow, and the mathematical complexities of representating these phenomena, even in an averaged sense. However, one cannot deny the usefulness of formal eulerian formulations and the potential of hybrid lagrangian-eulerian formulations has yet to be explored. In a hybrid approach to predict erosion, for example, the particle phase could be described via a lagrangian formulation near surfaces and via an eulerian formulation away from surfaces.

For the eulerian description of particle-fluid motion the question arises: under what conditions can the dispersed particle phase be viewed as a continuum? The question is important since, in principle, the continuum framework greatly facilitates the derivation of formal theoretical relations describing the influence of particle-fluid and particle-particle interactions in the mixture flow, and this can be of great computational advantage. In formulating a set of averaged field equations appropriate to fluid-particle flows, it may be preferable to postulate macroscopic equations without reference to the microscopic details [130,131]. But, for guidance, one should consider the averaging methods of Drew [100,126,127] and others and look to the discrepancies between measurements and predictions of relevant flow variables to assist in the convergence of this approach.

The continuum equations proposed by Hinze [93,130] have been the basis for eulerian calculations of particle-laden turbulent flows. The equations are obtained by applying the Reynolds decomposition procedure followed by averaging of the instantaneous transport equations. Extended forms of these equations and the constitutive relations have been used for calculating erosive wear in curved channels [82], to calculate particle dispersion in a mixing layer flow [118], and to predict solid-liquid suspensions in stirred vessels [132]. The main issue is that, even if the particle phase is dilute ($\alpha << 1$), there must be sufficient particles in the smallest turbulent eddy to appropriately define statistical averages of particle-related variables such as density and velocity. This point is addressed by Hinze [93] who suggests that $s/\eta \leq 0.1$, where s is the average separation-distance between particles, for the concept of a continuum to apply. Notwithstanding, Hinze gives examples of continuum formulations that proved applicable in situations that did not meet this criterion.

3.2.5 Numerical Modeling and Applications

Among the major contributions to the subject of predicting particle motions in systems of engineering interest is the classical analysis performed by Taylor [133] relating to raindrop impingement and icing on aircraft wings. In this study a lagrangian formulation was pursued in which the force acting on a particle was attributed solely to mean flow drag. Both Stokes' and Newton's resistance laws for specifiying the particle drag coefficient were considered, but the analysis focused on solutions for the former condition only, for the cases of inviscid stagnation point flows on a flat surface and on a large cylinder respectively. Taylor found that for values of the particle inertia number $\lambda < 1/4$, if at any time a particle is travelling with the fluid velocity, at no subsequent time will it strike the surface. For $\lambda > 1/4$ a particle always strikes the surface provided that at some time in its trajectory it moves with the fluid velocity.

From his analysis Taylor drew various important qualitative conclusions pertaining to the density distribution of surface particle impacts. In later studies of the same problem, using Taylor's analytical approach, Laitone [35,37] quantified the surface particle flux distribution as well as the particle impact angles and speeds, as a function of initial location, initial velocity and inertia number. Erosion was calculated using these results in conjunction with an empirically adjusted cutting wear model [8]. The relative rate of erosion predicted in [37] is shown in Fig. 5 as a function of particle inertia number, λ. The rate of erosion is seen to increase by more than one order of magnitude when λ is increased from 0.4 to 2. The minimum shown in the erosion curve, between $\lambda = 0.25$ and 0.4, is due to the reduced particle impact velocity in this range of λ. From the analytical model, Laitone established a range for the variation of the exponent in the velocity dependence of erosion; see Eq. (3). As

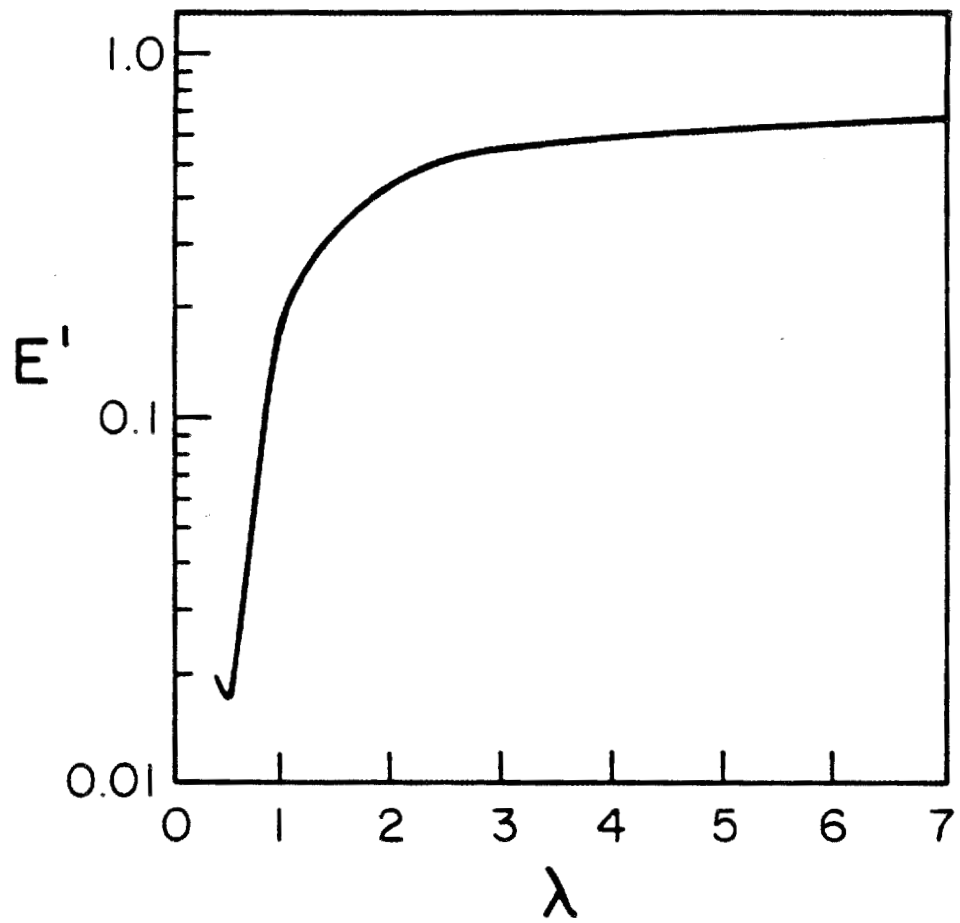

Figure 5. Effect of particle momentum equilibration number, λ, on the relative erosion of a wall in a region of 2-D stagnation point flow. In the figure, $E' = E \times$ total mass of particles impacting the surface. $E' \propto V_1^3$ for $n = 2$ in Eq. (1). The steep rise in erosion is due to the strong dependence of V_1 on λ. Based on calculations by Laitone [37].

discussed in the Introduction, the range predicted for the exponent is in agreement with experimental findings and, more importantly, the analysis affords a purely fluid mechanical interpretation of the exponent variation in velocity, as opposed to a materials-related interpretation.

The studies by Taylor and Laitone, respectively, assumed inviscid flows in so far as a prescription of the fluid velocity was concerned. (Viscosity entered the formulations only to determine the drag force acting on a particle via a resistance law.) Such an approach yields no information on possible boundary layer effects on particle motion and erosion. Near a solid surface the no-slip condition imposes a surface-normal gradient in the fluid velocity component tangential to the surface. This, in turn, can affect the drag exchanges between fluid and particles traversing the boundary layer. The problem has been investigated analytically for turbulent flow, by prescribing a 1/7 power law distribution for the mean tangential velocity component of the fluid phase [134]. This velocity distribution was used as the driving force in the tangential component of the lagrangian particle equation of motion to calculate the effects of a boundary layer on the impact speeds and incidence angles of particles entering the boundary layer with specified initial velocity components.

The above studies illustrate the value of analytical approaches for investigating particle motion and erosion in relatively simple flow configurations with one-way (fluid to particle) coupling. Other examples are given in [90,135,136]. However, most flows of engineering interest are three-dimensional, turbulent and often constrained by highly complex boundary conditions. For such systems theoretical analysis must be performed numerically, using high-speed large-storage computers.

Numerical calculation approaches for particle-laden flows can be divided into two groups, according to whether the particle phase is considered discrete

or continuous in nature. Further subclassification follows according to whether the particle phase is dilute or concentrated and one-way or two-way coupling considerations apply, and whether the flow is laminar or turbulent. For turbulent flows a final classification rests upon the type of closure scheme (turbulence model) used. Examples of numerical procedures developed and applied to predict erosive turbulent flows include lagrangian (discrete particle phase) formulations [38,39,83,137] and eulerian (continuum particle flow) formulations [82]. The present author and his colleagues in Berkeley have used a deterministic two-equation k-ε model of turbulence to simulate the turbulence of the fluid phase. Even though limited by the assumption of an isotropic turbulent viscosity, this model illustrates the importance of turbulence in particle dispersion and erosion. In principle, more accurate simulations of the anisotropic erosive flows typical of the industry should be possible with more advanced closure schemes [79,80,138,139] but these approaches can be computationally intensive, especially in three-dimensional configurations. Most studies simply take the mean motion of the fluid field to act as the driving force in the particle equation of motion. However, studies where velocity fluctuations are directly superimposed on the mean flow [83,103,107,113,114] show that the resulting "turbulence drift velocity" of the particle phase can be significant.

In the remainder of this section we briefly review a few examples of lagrangian model formulations used to predict particle motion and erosion in some complex flows of engineering interest.

Turbomachinery Flows. Two-phase flows through turbomachinery equipment and related system components are of considerable importance to the power and transportation industries. Gas turbines in ground vehicles, aircraft and naval installations are frequently operated in highly erosive particle-laden environ-

ments containing sand, dust or salt [21]. Many of the advanced power plants being considered for utilization of coal-derived fuels will have to contend with the presence of particles in the expansion gases flowing through the combustion turbines and it becomes imperative to determine the level of gas cleanup which will allow an acceptable, safe and reliable turbine performance [140]. Erosion in steam turbines can arise from the presence of water droplets or of scale displaced from the inner surfaces of steam generator tubes. Units which frequently undergo start-up and shut-down favor scale displacement and it is estimated that blade replacements are necessary after about 40,000 hours to avoid secondary damage to the turbine [141]. Numerous studies and references on problems due to liquid-impact turbine erosion are available in the various proceedings of the International Conferences on Erosion by Liquid and Solid Impact held periodically in Cambridge, England [142,143]. Although erosion by liquid-droplet impact is not discussed here, much of what is said about the calculation of solid particle trajectories in turbomachinery flows applies.

Early theoretical studies on the degradation of turbine performance due to particles lagging behind the gas phase both in velocity and temperature suggested the importance of erosion since this can change blade shape, which degrades turbine performance, and ultimately leads to blade failure [144-146]. As a result, numerical methods were developed for calculating solid particle trajectories in axial flow compressors and turbine stages that model the particle impacts with the blades and their subsequent rebounds [147-149]. The blade airfoil shape and the blade-to-blade flow field at the mean radius were included in the three-dimensional particle trajectory calculations [147,148]. The only force considered in the particle equation of motion was that due to fluid drag. Fits to experimental data were used to predict the magnitude and direction of particles rebounding from the blade surfaces.

The heterogeneous nature of particle flows through turbomachinery was subsequently modeled using a Monte Carlo method to simulate particle ingestion and subsequent erosion [149]. Specific conditions for individual particles were chosen at random from prescribed statistical distributions of particle size, particle location, rotor location and the restitution ratio. The motion of the particle was calculated using deterministic equations. By considering a large number of particles the statistical solution to the heterogeneous particle flow and erosion problem was obtained.

Applications of the above numerical procedures have been restricted to inviscid flows in two-dimensional blade-to-blade channels, assuming zero radial gradients in either the flow configuration or its properties. Therefore, the calculation procedures are not suited for particle trajectory calculations of inlet flow fields which are characterized by significant hub and tip contouring and they cannot represent the variation of the flow field and vane shape in the radial direction. These limitations were removed in [150] by using the three-dimensional, inviscid, numerical calculation procedure of [151]. In this procedure the flow field solution is obtained on a mid channel hub-tip stream surface using a finite difference stream function formulation for subsonic flow and a blade-to-blade velocity gradient method for transonic flow. Improved applications of this approach for predicting erosion patterns produced by particles rebounding from twisted blades have been reported [152,153].

Other calculations of particle trajectories and erosion based on inviscid, three-dimensional solutions of the fluid flow field have been performed along the lines of the studies discussed previously [137,154-156]. Figure 6 illustrates the kind of particle trajectory predictions from which [137] were able to make specific recommendations for the cleaning up of a turbine expansion gas. This work is a detailed parametric investigation of the

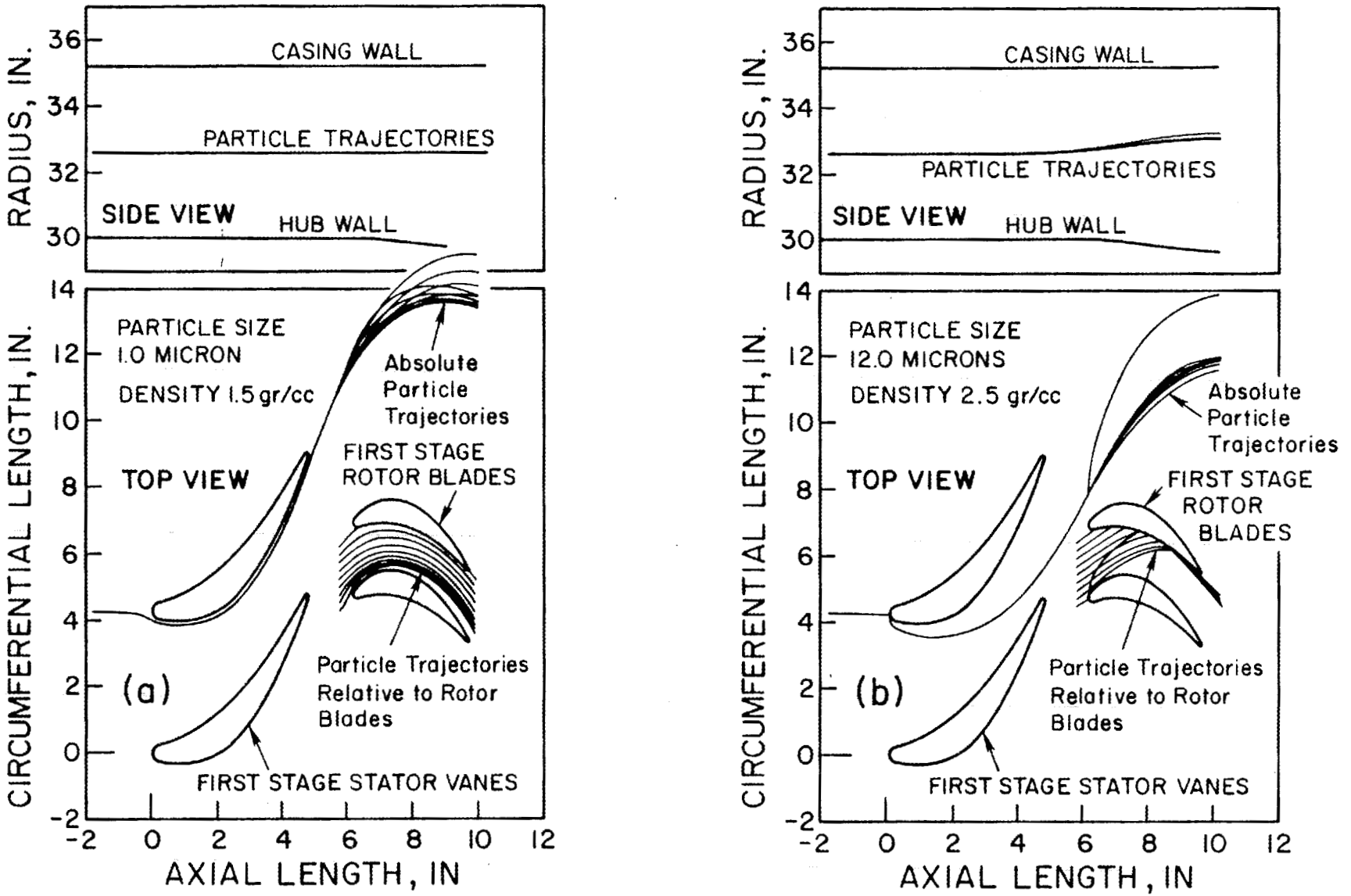

Figure 6. Trajectories of 1 μm ash particles (a) and 12 μm dolomite particles (b) passing through the stator and rotor passages of a turbine. In the figures, the top portion shows the trajectories in the flow channel. The bottom portion is the top view of the axisymmetric blade-to-blade stream surface. Due to their inertia, the large particles collide several times with the first stage rotor blade. Based on calculations by Menguturk and Sverdrup [137].

flow and erosion by coal-gas ash particles in the first stage of a large electric utility gas turbine, based on projected particle distributions in the gas leaving the cleaning system of a pressurized fluidized-bed gasifier system. Some of the problems related to scaling experiments in cascades and small turbines in order to simulate particle flows and erosion through large utility turbines in advanced coal-fired power plants are discussed in [154]. The experiments are essential for determining gas cleanup requirements for successful turbine operation. To this end, the relative effects of physical scale, rotation speed and pressure differences on erosion were evaluated numerically using the erosion damage model of [137]. Using a simplified version of the same procedure, a numerical exploration of the erosion potential throughout the expansion section of a multistage turbomachine has been performed in [155]. In [156] the authors show the importance of accurately resolving the flow field near the blade leading edge in order not to invalidate subsequent particle trajectory calculations in gas turbine blade passages.

These and similar inviscid flow numerical investigations complement what have always been very difficult experiments to perform. In general, broad qualitative agreement has been found between predicted patterns and rates of erosion of exposed turbomachinery surfaces and the limited experimental data available. This has further encouraged the advancement of numerical work for predictive purposes, and is resulting in a wealth of information for which, often, there is no experimental counterpart. For example, the trajectories of the large particles shown in Fig. 6 are dominated by impact-rebound phenomena, the large relaxation times being responsible for the reduced influence of the flow field on their trajectory. Small particles with $\lambda < 1$ rapidly acquire the local gas velocity after each impact, with the possibility of subsequent impacts increasing erosion damage. Near swirling vanes, large particles impacting a hub

can reenter the engine core flow field after impacting the tip. This results in reduced separator effectiveness and increased erosion of later stages. The maximum erosion for large particles occurs at the blade hub near the trailing edge. As particle size decreases, the location of maximum erosion on the blade moves both radially and axially away from the hub trailing edge corner.

Cascade and small turbine experiments do not yield erosion rates and erosion tolerances typical of large utility turbines, and measurements of erosion rates in simulation tests can differ from utility erosion rates by up to an order of magnitude. The effects of physical scale, rotation speed and pressure differences must be considered carefully when attempting to apply experimental and numerical results obtained in simulation devices to large utility turbines. Velocity triangle variations and progressive gas expansion are major factors contributing to the differences in erosion between stages in multistage turbomachines. Gas expansion results in reduced particle concentration and hence reduced flux to blade surfaces. This tends to decrease erosion in progressing through the turbine stages. However, the effect is somewhat offset by reduced drag forces acting on the particles which, in deviating from the fluid streamlines, can strike the blade surfaces with more adverse impact angles.

Boundary Layers and Secondary Flows. While inviscid flow schemes have been in widespread use in turbomachinery applications, more generally applicable viscous flow procedures are gaining popularity in these and other complex configurations [79,157-162]. Boundary layers and secondary cross stream flows are characterized by strong viscous effects that can alter the relative velocities, and hence the potential for erosion, of particles moving near or towards surfaces. For example, a high-speed particle penetrating a lower-speed boundary layer will be decelerated and, depending on the new incidence angle, the potential for erosion may be reduced.

A major factor determining the magnitude and extent of boundary layer-reduced erosion is the particle inertia number λ. If in the definition of λ (see Section 3.2.1) we substitute for the characteristic length the boundary layer thickness, δ, and for the mean velocity of the fluid phase the component of particle velocity normal to the surface, V_N, evaluated at $y = \delta$, we can define

$$\beta \equiv \frac{\delta}{s} = \frac{\delta}{V_N \, d_p^2 \rho_p / 18\mu} \tag{13}$$

In Eq. (13), the quantity s is referred to as the particle "stopping distance." It is a conservative estimate of the maximum distance a particle is expected to travel at constant mean speed V_N in the direction normal to the surface, starting at the edge of the boundary layer along that surface, before it adjusts to the local mean velocity which, within the boundary layer, is primarily aligned parallel to the surface [134]. Only for values of $\beta < 1$ will particles penetrate a boundary layer sufficiently deeply to impact and possibly erode a surface.

The effects of a boundary layer on particle deposition and erosion for conditions typical of turbine flows have been modeled numerically by matching an inviscid outer-flow solution to a two-dimensional compressible boundary layer flow calculation [163,164]. The lack of experimental information forced these authors to assume a unit particle deposition ("sticking") probability. Erosion rates were predicted using the model of [137]. Based on these numerical results it is possible to distinguish among three main regimes for particle transport within a boundary layer: 1) A Brownian or molecular diffusion regime ($d_p \leq 0.1$ μm), characterized by very small particles transported mainly by molecular diffusion; 2) A turbulent diffusion regime (0.1 μm $\leq d_p \leq$ 1 μm), charac-

terized by the transport of particles which diffuse under the influence of turbulent fluctuations; 3) An inertial regime (1 μm < d_p), characterized by particles moving under the influence of their own inertia.

The numerical studies of [163,164] were conducted for specific turbine stages and the results do not lend themselves readily to general interpretations. However, calculations in the inertial regime are in good agreement with the more general analysis in [134]. While the numerical results strongly suggest that boundary-layer induced particle deposition can seriously degrade the performance of a turbine stage, the calculations are subject to serious uncertainties due to the lack of accurate information concerning particle deposition probability.

In relation to erosion, viscous flow analysis [134] shows that: 1) The presence of a boundary layer always decreases particle impact speed and increases particle impact angle (relative to the normal to the surface); 2) These two effects are only significant for boundary layers containing particles with $\beta > 0.4$ but can substantially reduce erosion; 3) Due to the characteristic erosion incidence angle dependence of ductile-type materials, the erosion of ductile surfaces impacted by particles with $\beta < 0.4$ can also be markedly reduced over a narrow range of particle boundary layer entry angles; 4) In an application of the theory to rotor trailing edge erosion, for flow conditions typical of large turbines, significant boundary layer-reduced erosion occurred only for particles less than about 4 μm in diameter.

Secondary motions arising from lateral curvature of the main flow can significantly affect the velocity and erosion potential of small particles. This has been clearly demonstrated in various curved flow configurations by Mason and Smith [165] who performed experiments in curved duct sections made from transparent plexiglass in order to visualize the time dependent effects of primary and secondary motions on erosion. Turbulent air flows of dilute

($\alpha \simeq 10^{-3}$) suspensions of alumina particles ranging from 50 to 60 μm in diameter were passed through two 90° bends of square cross-section of bend curvature to radius ratios 2 Rc/D = 20 and 12 respectively. The duct flow Reynolds number was varied between Re_D = 88,000 and 152,000, approximately, and the mass loading ranged from γ = 0.5 to 3.8 kg alumina/kg air. Erosion was first observed at a bend angle of 21° on the concave surface where a wear "pocket" was gradually formed. After the pocket attained a critical depth, erosion became noticeable on the convex surface of the bend, approximately between 30° and 60°, the extent and amount of wear depending on the flow speed and particle concentration. The change in surface shape at the convex wall produced further changes in the secondary flow patterns through the bend, leading to the formation of secondary and tertiary wear locations on the concave wall, at 70° and 87° bend angles approximately.

These experiments show very clearly that secondary motions can significantly influence erosion and that the secondary motions themselves are subject to change as surface topography is reshaped by the erosion process. Notwithstanding, numerical simulations of these flows, based on a continuum formulation for the particle phase and neglecting the secondary motion (i.e., assuming a curved channel), have yielded erosion results along the concave wall in broad qualitative agreement with the measurements [82]. This comparison is shown in Fig. 7 where it is seen that the discrepancies increase with increasing Reynolds number, due to the more pronounced effect of the secondary flow on particle motion. Other numerical evaluations of the effect of secondary motion on erosion in curved passages are given in [166-169].

Impinging Jets and Cylinders in Cross-Flow. Particle-laden jets impinging on surfaces are used extensively in erosion experiments to investigate material resistance to wear, usually under accelerated erosion conditions [6,170-172].

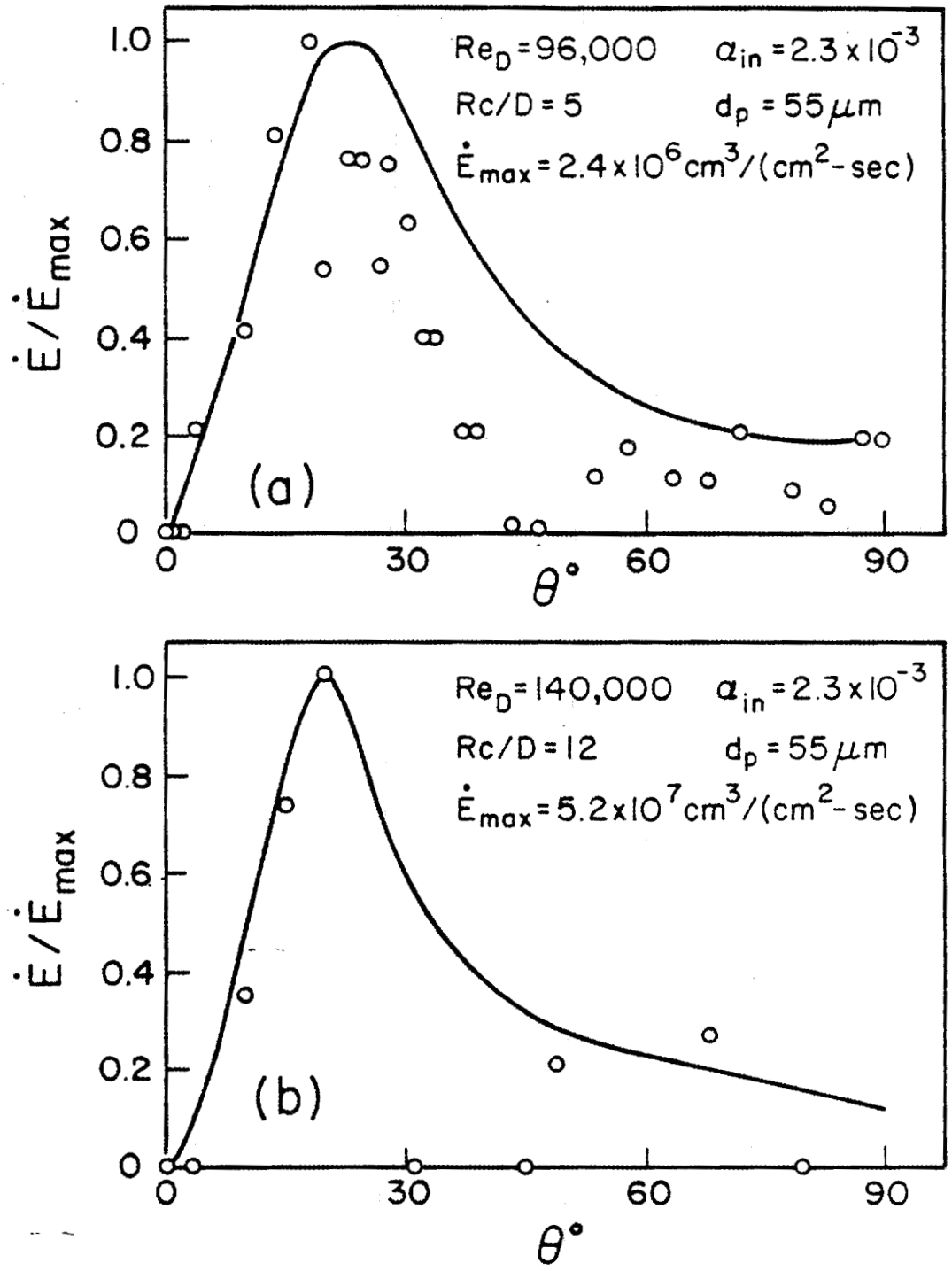

Figure 7. Two-dimensional prediction of the rate of erosion at the concave wall of a three-dimensional curved duct flow. In the figure, θ is the bend angle along the channel. Strong curvature (a) and mild curvature (b) cases shown. Based on measurements (dots) by Mason and Smith [165] and calculations (lines) by Pourahmadi and Humphrey [82].

High-pressure water jets containing abrasive particles are used to cut advanced materials in a wide variety of industries [173]. Cases of cylinders in cross-flows with eroding particles arise in heat exchange equipment including the convective zone (freeboard) of a fluidized bed combustor, and in the primary superheaters, reheaters and economizers of coal-fired boilers [174].

Taylor [133] performed the first detailed analysis of particle-laden impinging jet flows. Subsequently, Laitone [35,37,38] investigated this configuration as well as the case of particle-laden flows past cylinders. These seminal studies have already been discussed in Section 3.2.5. The main point to emphasize here is the complete absence of turbulent flow considerations in these and similar erosion analyses. The present author and his coworkers in Berkeley have tried to redress this deficiency. Two of their contributions are briefly reviewed.

The influence of turbulence on erosion by spherical sand-like particles suspended in an air jet impinging normal to a flat solid surface was first investigated by Dosanjh and Humphrey [39]. The mean motion of the fluid was calculated using a two-equation (k-ε) turbulence model and this was used as the driving force in the deterministic lagrangian equation of motion applied to each particle. Thus, the effect of the turbulence on the particles was evaluated indirectly, through its effect on the mean motion of the fluid. Impacting particle speeds, incidence angles and particle surface densities were predicted from the particle equation of motion. Erosion was subsequently calculated from this data, using a cutting wear model for ductile metals [6]. This work represents a numerical attempt to establish the qualitative dependence of surface erosion on fluid jet turbulence intensity since this kind of experimental data is unavailable. The particular metal surface-particle pair chosen for investigation in [39] is immaterial since the erosion predictions can be presented in

non-dimensional form. Figure 8, from [39] shows the influence on erosion due to altering the level of turbulence imposed in the air jet. Erosion is seen to decrease with increasing turbulence intensity. Although perhaps counterintuitive, this finding is partly explained by the fact that both particle impact speed and particle flux to the surface decrease with increasing turbulence. Both of these effects are related to the increased radial dispersion of particles, and lead to diminished erosion as predicted by the cutting wear model.

The results in Fig. 8 also show that the position of maximum erosion is significantly displaced towards the jet symmetry axis with increasing turbulence intensity. This is due to the fact that, according to the cutting wear model, maximum wear occurs for particle incidence angles of about 25 degrees with respect to the surface, and the effect of increasing the turbulence intensity is to alter (in the way shown by the figure) the position on the surface where this angle is attained.

Although limited by the simplifications made in the analysis, the findings in [39] serve to show that fluid turbulence can significantly alter erosion by particle impact and that computational fluid dynamic procedures can be usefully applied to flow configurations of engineering interest. The mathematical detail with which the fluid and particle equations of motion must be formulated in such a procedure to accurately represent the flows, and the extent to which the two phases must be coupled in a formulation, are very problem specific. For many practical configurations involving erosion by dilute particle-laden gases, one-way coupling, within the context of a phenomenological closure scheme such as the k-ε model referred to above, may suffice to correctly establish significant effects. This is further illustrated by reference to the erosion of cylinders in cross-flow, discussed next.

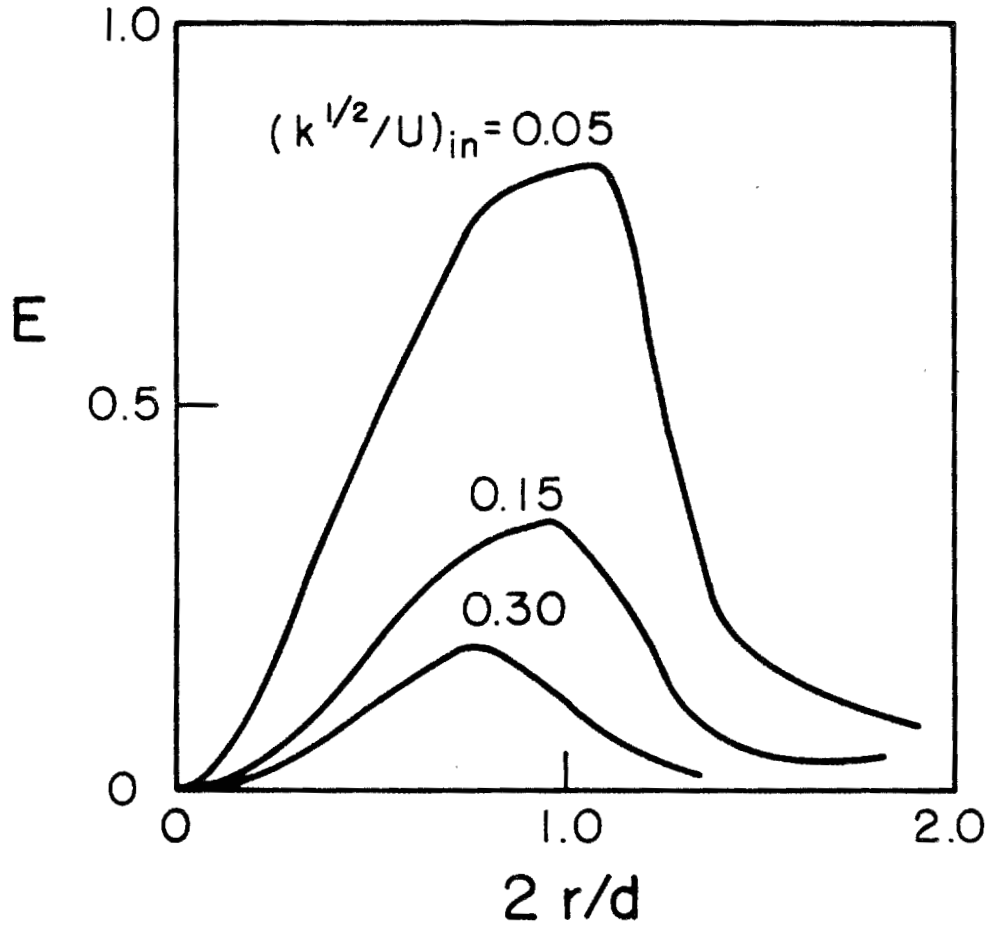

Figure 8. Erosion by a dilute particle-laden gas jet impacting a flat surface perpendicularly. In the figure, r is the radial coordinate along the surface from the stagnation point, d is the jet nozzle diameter, k is the turbulent kinetic energy of the gas flow and U is the mean jet velocity. The values of k and U are specified at the jet origin. Based on calculations by Dosanjh and Humphrey [39].

The ideas embodied in [39] were subsequently extended by Schuh et al [83] for the case of an intially turbulent particle-laden air stream flowing past one or two in-line tubes, or past a tube in an in-line tube bank. A non-orthogonal body-fitted calculation approach was used to represent the tube configurations investigated. As in the jet case, one-way coupling was assumed and the fluid turbulence was described by means of the two-equation k-ε model, with a logarithmic relation to describe the velocity on either side of the boundary layer separation point on a tube. The effect of the turbulence on particle motion was modeled two different ways: either deterministically, as in [39] or stochastically, as in [103], by superposing a random distribution of turbulent fluctuations upon the calculated mean fluid flow and using this as the forcing function in the particle equation of motion. In the latter case, tracking a statistically significant number of particles released at different locations in the calculation domain allowed average particle quantities and erosion to be obtained. Figures 9-a and b show calculated deterministic and stochastic particle trajectories for the case of two in-line tubes using identical problem conditions [83]. It is especially noteworthy that, unlike the stochastic calculations, the deterministic results for the particles with low inertia number ($\lambda < 0.1$) do not show these particles impacting the second downstream cylinder. However, the associated erosion was negligible.

Among other things, the results in [83] illustrate the importance of accounting more realistically for the influence of fluid turbulence on particle motion in erosive flows. With the availability of greater computing power, more accurate finite differencing schemes and more sophisticated numerical algorithms, one increasingly expects to see phenomenological modeling approaches being complemented by direct numerical simulation techniques capable of more accurate (model free) representations of particle-laden turbulent flows [175,176].

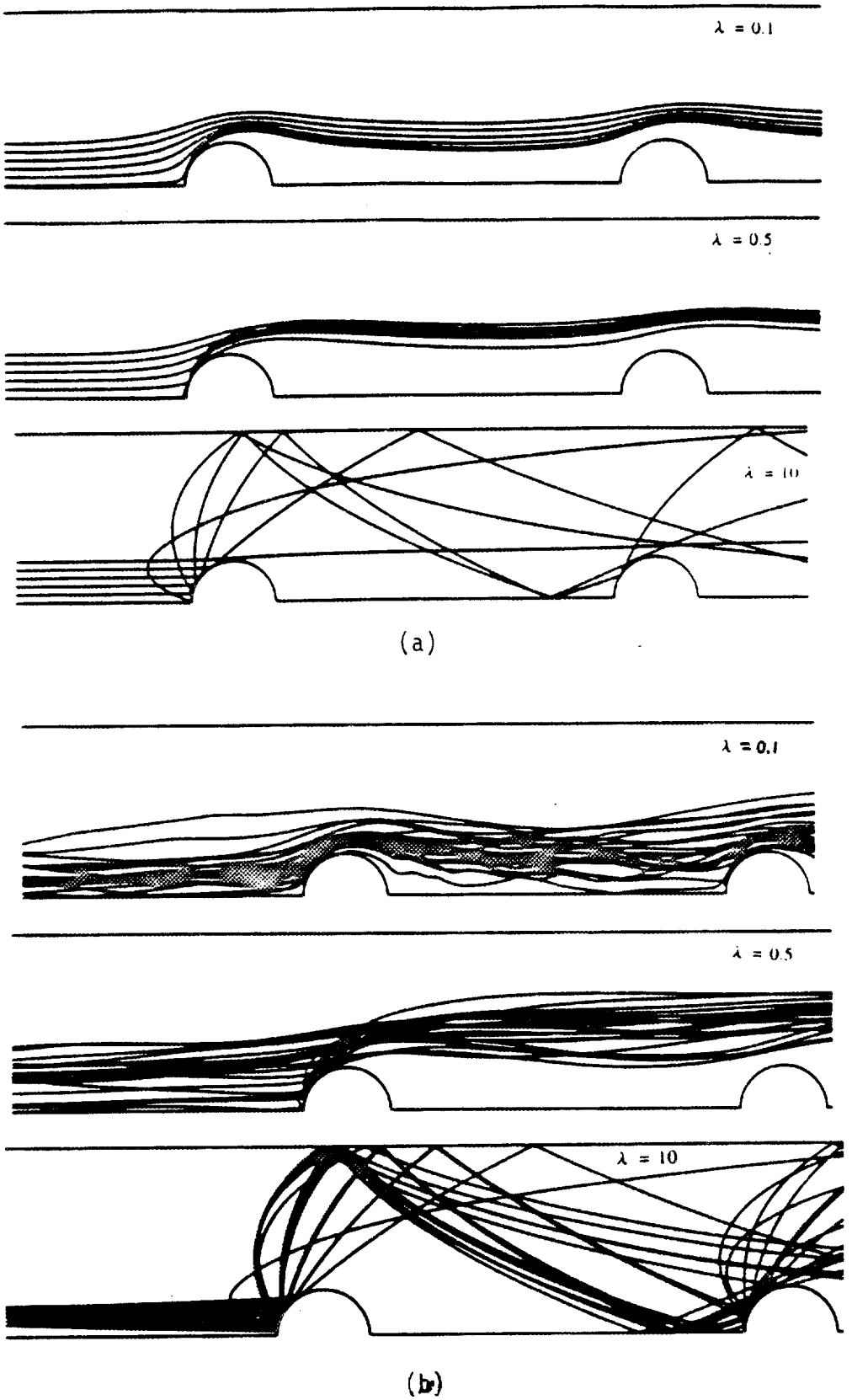

Figure 9. Deterministic (a) and stochastic (b) predictions of particle trajectories for the flow past two in-line tubes. Three momentum equilibration numbers considered for a flow with Reynolds number (based on tube diameter) $Re_D = 2.94\ 10^4$. Based on calculations by Schuh et al. [83].

3.3 Particle-Surface Interactions and Related Phenomena

3.3.1. Determination of Restitution Coefficients

The experimental measurement of particle restitution coefficients is difficult [73,148,149,177-179], but the information is necessary for solving the equations governing the trajectories of particles rebounding from surfaces and subsequently impacting the surface again. The data is generally provided in the form of least square fits to polynomial functions of the form:

$$V_2/V_1 = a + b\ \beta_1 + c\ \beta_1^2 + \ldots$$
$$\beta_2/\beta_1 = a' + b'\ \beta_1 + c'\ \beta_1^2 + \ldots \qquad (14)$$

Where V_1 and β_1 are the particle incidence speed and angle, and V_2 and β_2 the corresponding rebound values, with β_1 and β_2 measured relative to the tangent to the surface, at the impact location, in the V_1-V_2 plane. The numerical values of the coefficients a, b, c, etc. in Eq. (14) depend on the material properties of the specific particle-surface pair. Similar data for the rotation velocities of particles rebounding from surfaces appear to be unavailable.

Armstrong et al [179] designed an apparatus in which the fluid medium was essentially stagnant around the target surface material at which high speed particles were aimed. This allowed them to separate particle impingement phenomena from fluid flow effects and permitted an investigation of the influence of the Magnus force on particle trajectories. While more realistic conditions involve large spatial and temporal variations of the fluid flow conditions in the vicinity of the target [73,148,149], such conditions are considerably more difficult to control and measure since they require the use of non-intrusive techniques, especially close to the impacted surface.

The restitution characteristics of particles rebounding from surfaces require a statistical description. For fixed incidence values β_1 and V_1, the rebound values β_2 and V_2 have statistical distributions resulting from: variations in particle shape, size and rotational velocity at the time of impact; variations in the topography of the test surface; uncontrollable phenomena such as particle and/or surface fragmentation, particle-particle collisions, changes in material properties due to sudden highly localized temperature increases; and variations in near-surface fluid flow conditions which will significantly affect particle trajectories if $\lambda < 1$. Added to this are the measurement uncertainties associated with the experimental techniques, which must remain small if meaningful results are to be obtained.

Figure (10) is a histogram showing a typical statistical distribution of the velocity restitution ratio for the case of relatively hard particles striking a ductile surface. Measurements like these show that the shapes of the distributions for V_2/V_1 and β_2/β_1, as well as the mean values of these ratios, vary strongly with β_1. Notwithstanding, all attempts to date to use restitution coefficient information at boundaries for predicting particle trajectories and erosion have been limited to the use of the mean values of the distributions, the information contained in the shape of the distribution being ignored. This practice raises serious questions concerning the correspondence with reality of predictions of particle trajectories and surface wear locations when the particles are subjected to sequential impacts, such as in turbomachinery.

It should be noted that the distributions of V_2/V_1 and β_2/β_1, as well as their variations with the incidence angle, β_1, are highly dependent on the physical properties of the impacting particle/impacted material surface pair. For example, all the polymeric materials tested by in [177], using 6 mm diameter steel spheres in free fall, gave rebound angles larger than incidence angles for

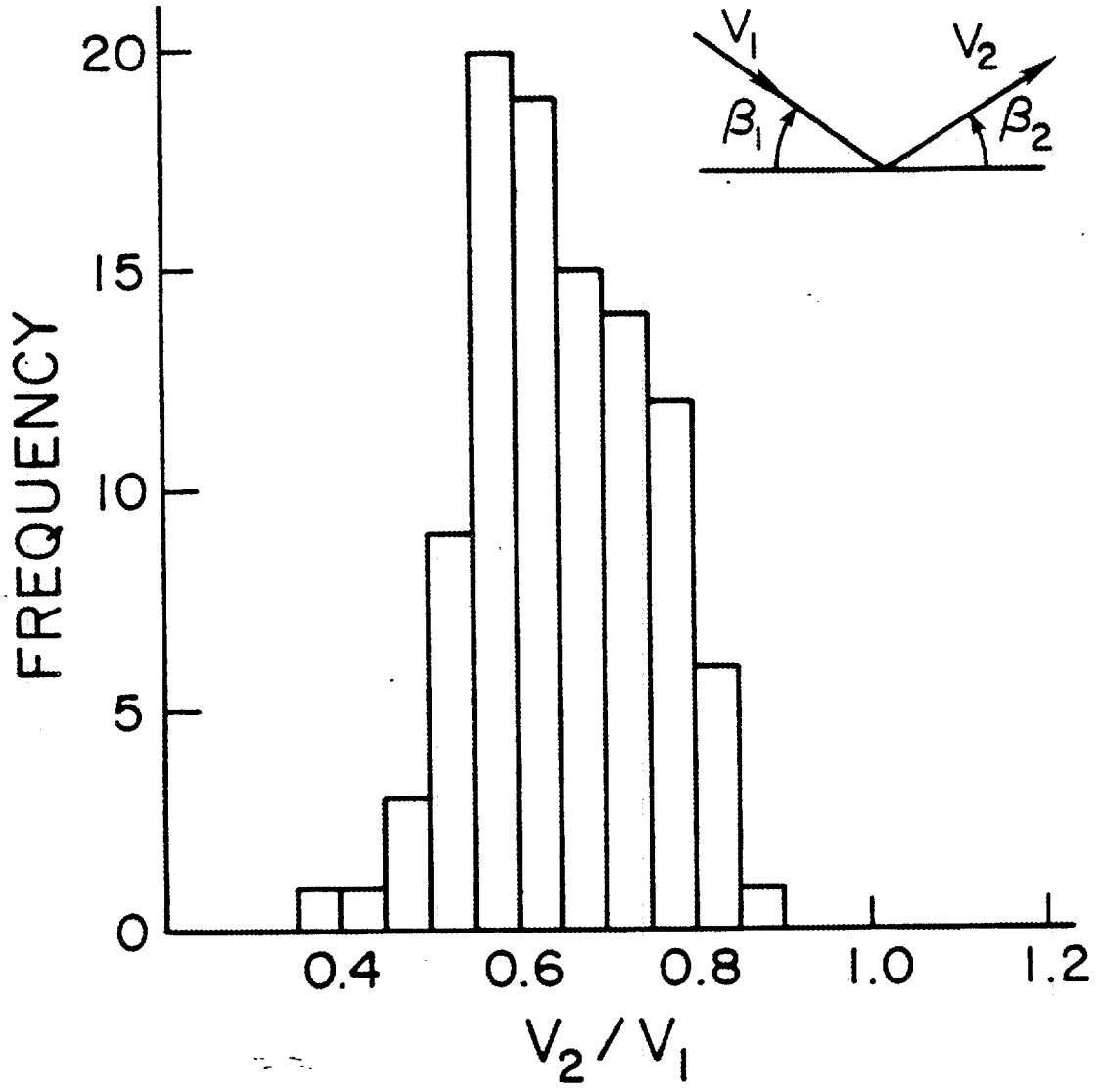

Figure 10. Histogram for the velocity restitution ratio V_2/V_1 corresponding to 200 μm quartz particles impacting 410 stainless steel at V_1 = 76.2 m/s with angle β_1 = 15 degrees. Histogram based on 101 observations. Based on measurements by Tabakoff and Sugiyama [73].

all values of the incidence angle tested. By contrast, most of the metals gave rebound angles smaller than the incidence angles. The data obtained in [73], for much smaller particles in much faster flows, show that for small incidence angles, β_1, the ratio $\beta_2/\beta_1 > 1$, and that as β_1 increases β_2/β_1 becomes substantially less than unity. The highly specific dependence of the restitution coefficients on the materials involved, and the unknown influence of transverse Magnus and Saffman forces, make it very difficult to derive general theoretical relations or postulate generally applicable empirical correlations for these from the experimental measurements.

3.3.2 Particle Fragmentation and Multiple Impacts

Particle fragmentation and secondary erosion have been discussed in [17,18,46,180,181]. Experiments show that under certain conditions particles shatter into smaller fragments upon impacting a surface. The fragments move radially outwards, their circumferential distribution depending on the impact angle, causing what has been called by Tilly and Sage [19] "secondary erosion." These authors concluded from their observations that the fragmentation process, especially the resulting fragment sizes and speeds, depends on the physical properties of the pair of particle and surface materials involved, and on the initial particle size and speed. It appears that for each pair of materials there is a threshold size below which fragmentation does not occur. For some materials a saturation level is also observed, beyond which fragmentation becomes independent of particle size.

The effect of particle fragmentation on erosion has been analyzed in [20] where the authors point out that the velocity exponent, n, in the expression for erosion given by Eq. (1) can either increase or decrease as of a critical impact velocity, depends on the pair of materials involved. Cases where n increases

involve the erosion of soft and ductile materials by abrasives which are damaged only slightly upon impact. Cases where n decreases, at a definite critical velocity, are generally observed when hard and brittle abrasives strike even harder surfaces. The critical velocity threshold marks the beginning of particle disintegration. While the resulting fragments acquire high speeds and are capable of significant secondary erosion, their formation is at the expense of the parent particle kinetic energy. It is estimated in [20] that a 1% loss of initial particle mass, in the form of radially ejected fragments, can reduce the normal component of kinetic energy of the impacting parent particle by 16%. If secondary erosion is less than the erosion which would be caused by the unfragmented particle, the velocity exponent n should decrease.

In principle, particle fragmentation should help to reduce the total amount of erosion, but the overall picture is complicated by the poorly understood influence of turbulent fluctuations and particle-particle interactions on particle motion. As a result, the smaller fragments may well be the cause for additional, often critical, erosion at previously unworn locations through repeated or multiple impacts.

Although he did not address particle fragmentation, in a study on the effects of multiple impacts Laitone [38] has predicted the trajectories of non-spinning particles rebounding from cylindrically shaped material surfaces for flow conditions typical of jet turbines. He restricted attention to dilute systems composed of sand-like particles in air, for which the dominant force acting on the particles was due to the fluid-induced viscous drag. The vortex scheme of [182] was adapted to predict the high speed unsteady recirculating viscous flow past a cylinder. The scheme is entirely lagrangian and simultaneously tracks both fluid vorticity (as discrete vortex "blobs") and particles (as coagulated packets). Experimentally determined average restitution parame-

ters were used to specify normal and tangential particle component velocities after impaction with the cylinder. Typical results for repeated particle impacts are shown in Fig. 11. These calculations reveal that particles with $\lambda = 1$ in a flow with $Re = 10^5$ can experience substantial acceleration between the first rebound and the second impact with a cylinder. The observation is significant to erosion since it means that a large fraction of the original kinetic energy may be restored to a particle accelerating around a blunt object between a primary and a secondary impact. Although subject to large uncertainties, and highly specific to the case of 200 μm quartz particles impacting on 2024 aluminum alloy, the rebound correlations allowed Laitone to conduct a qualitative assessment of the frequency of multiple particle impacts and the attendant "secondary" erosion.

Laitone's calculations also show that near the stagnation point on the cylinder potential flow theory and viscous calculation methods yield esentially identical particle trajectories. Overall, however, the inviscid approach tends to overpredict wear due to the absence of a boundary layer which slows down and helps to deflect particles around blunt objects. The effect of viscosity becomes pronounced beyond a cylinder angle (measured from the stagnation point) of 10 degrees and the trajectories of particles with inertia numbers $\lambda < 1$ were strongly affected by eddy shedding from the cylinder, resulting in particle entrainment and crossing trajectories in the wake flow region. Experimental evidence supporting these findings is given in [183].

3.3.3 Magnus and Saffman Forces.

In addition to the viscous drag force, $\vec{F}_D$, experienced by a particle that is in relative motion with respect to the fluid around it, two forces can arise that act orthogonally to the particle's direction of motion and can signifi-

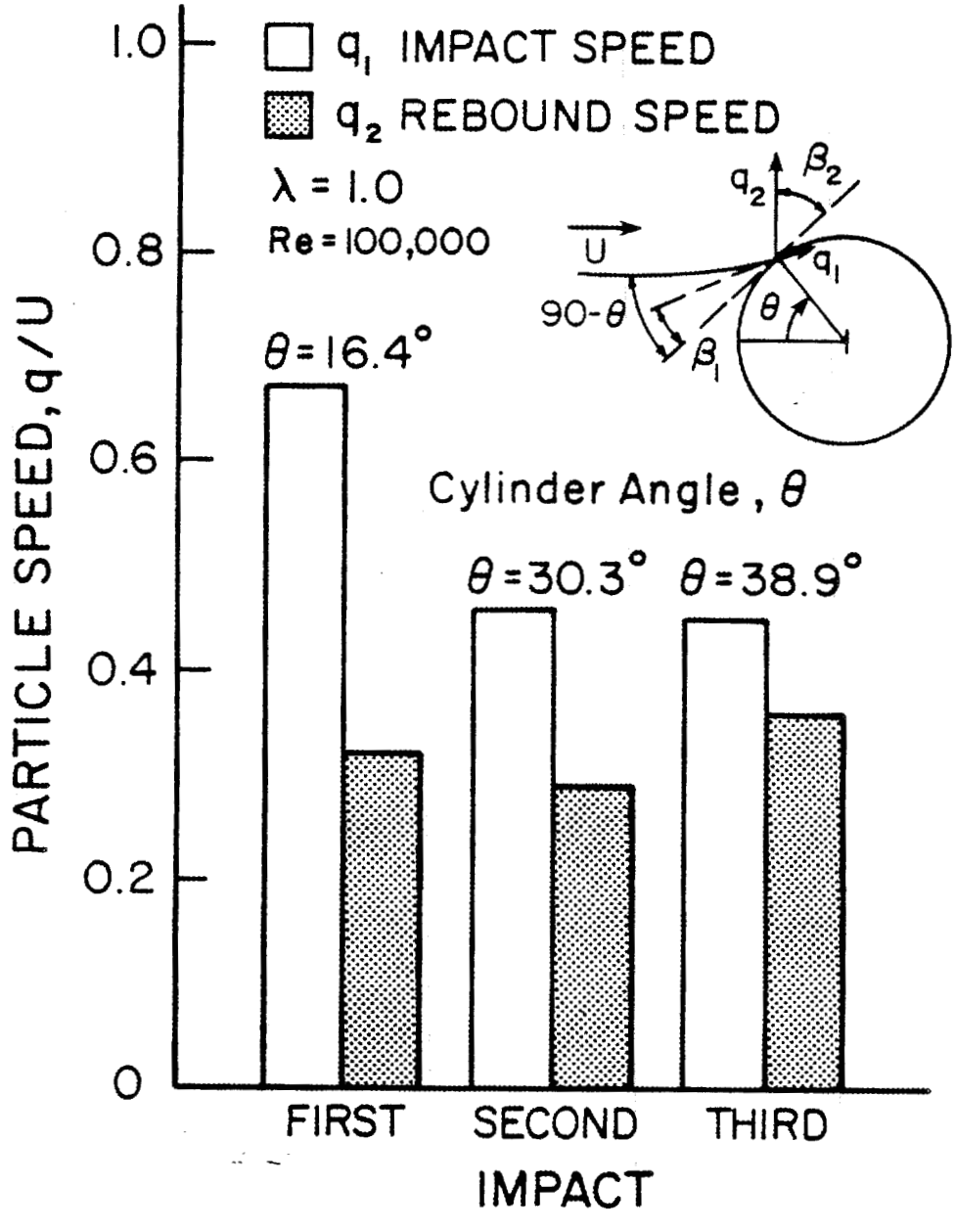

Figure 11. Variation of particle velocity with impact location θ for a triple impact and rebound with a cylinder surface. The difference in impact and rebound speeds is proportional to the momentum lost by the particle in performing erosive work on the surface. Secondary erosion due to subsequent impacts is nearly 50% of primary erosion due to first impact. Based on calculations by Laitone [38].

cantly affect its erosion potential. One, due to particle rotation, is referred to as the Magnus force [184]. The other, due to fluid shear is the Saffman force [185]. Both are due to inertia effects in the flow field around the particle and have been studied extensively for the case of spheres, to which we limit the discussion here.

A theoretical derivation of the Magnus force for the case of $Re_p << 1$ was performed by Rubinow and Keller [184] who found

$$\vec{F}_M = \pi \rho_f \left(\frac{d_p}{2}\right)^3 \vec{\Omega}_p \times \vec{U}_p \quad . \tag{15}$$

This expression states that a spherical particle with angular velocity $\vec{\Omega}_p$ moving at mean velocity $\vec{U}_p$ in a viscous fluid at rest experiences a force $\vec{F}_M$, transverse to the particle's direction of motion and with the sense indicated by the vector product. This result is independent of the fluid viscosity.

If the motion of the particle takes place relative to an unbounded fluid in uniform viscous shear, Saffman [185] shows that a transverse force will act on the particle given by

$$\vec{F}_S = k_s \rho_f \left(\frac{d_p}{2}\right)^2 \left[\frac{\nu}{|\vec{\Omega}_f|}\right]^{1/2} [\vec{\Omega}_f \times (\vec{U}_p - \vec{U}_f)] \tag{16}$$

where $k_s = 6.46$ is a constant and $\vec{\Omega}_f$ is the fluid vorticity. To order $O(\nu^{-1/2})$ this result is independent of the particle rotation, and is strictly valid only when the particle's translational, shear and rotational Reynolds numbers are: $Re_p << 1$, $Re_s << 1$, $Re_r << 1$ with $Re_p{}^2/Re_s << 1$. These restrictions limit the applicability of Eq. (16) to small particles which are almost neutrally dense with respect to a low speed fluid that transports them. In the

above, the particle translational and shear Reynolds numbers are as defined earlier, the rotational Reynolds number is defined as $Re_r = d_p^2 \Omega_p/\nu$, where Ω_p is the modulus of the particle's angular velocity, $\vec{\Omega}_p$.

Equations (15) and (16) have provided the basis for successful numerical simulations of various qualitative features concerning the radial migration of particles in liquids in pipe flow [186]. However, in many engineering devices involving solid particulates suspended in high speed gas streams, the Reynolds number constraints (particularly $Re_p << 1$) are not met. For example, it has been shown that for $Re_s > 0.6$, a sphere in shear flow rotates and the wake is oscillatory [187]. Similarly, the flow in the wake of a spinning sphere is unsteady and asymmetric, rendering extremely difficult the theoretical analysis or numerical simulation of the problem. Investigations of shear-generated lift beyond the near-Stokesian range are lacking, and evaluations of the Magnus lift force must be performed experimentally [97].

In principle, the extension of Eqns. (15) and (16) to high speed flows can be accomplished by rewriting them in terms of experimentally determined lift coefficients. For in-plane particle translational motion relative to a simply sheared fluid, with particle rotation and fluid vorticity aligned normal to this plane, the equations for the moduli of the forces are:

$$F_M = C_{LM} \frac{1}{2} \rho_f U_r^2 \pi \left(\frac{d_p}{2}\right)^2 \tag{17}$$

$$F_S = C_{LS} \frac{1}{2} \rho_f U_r^2 \pi \left(\frac{d_p}{2}\right)^2 \tag{18}$$

Where U_r is the modulus of the particle average relative velocity. For the respective analyses of [184] and [185] one finds:

$$C_{LM} = Re_r/Re_p \tag{19}$$

$$C_{LS} = 4.113\ Re_s^{1/2}/Re_p \ . \tag{20}$$

At high Reynolds number, however, $C_{LM} = f\ (Re_r/Re_p,\ Re_p)$ and a summary of the experimental data available is provided in [97,188]. Corresponding measurements for C_{LS} at high Reynolds numbers appear to be unavailable.

Data for the drag coefficient C_D, in the expression for the modulus of the drag force

$$F_D = C_D\ \frac{1}{2}\ \rho_f U_r^2\ \pi\ (\frac{d_p}{2})^2 \tag{21}$$

for the case of spinning particles is also given in [97,188]. The data reveal an insensitivity of C_D to particle rotation. Ratios of C_{LM}/C_D obtained from this data show that the Magnus force is significant for all particles with $Re_r/Re_p > 1$, regardless of the value of Re_p.

Of special interest here are the effects of the Magnus and Saffman forces on the trajectories of particles impacting and rebounding from solid surfaces at high speeds. For illustration, consider the flow of a particle-laden gas through a duct. In regions where $Re_p << 1$ the ratio of the transverse forces is given by:

$$\frac{F_M}{F_S} \alpha \frac{d_p\ \Omega_p}{(\Omega_f \nu)^{1/2}} \tag{22}$$

This can be written as

$$\frac{F_M}{F_S} \alpha \frac{d_p \Omega_p}{u_\tau} \tag{23}$$

where the relation $\Omega_f \nu \simeq \tau_w/\rho = u_\tau^2$ has been used. In turbulent duct flow we expect

$$u_\tau \quad \alpha \quad \frac{U_D^{7/8} \nu^{1/8}}{D^{1/8}} \tag{24}$$

where U_D is the mean velocity of the flow in the duct and D is the duct hydraulic diameter [189]. Substitution of (24) into (23) and rearranging yields:

$$\frac{F_M}{F_S} \quad \alpha \quad \frac{d_p \Omega_p}{U_D} \quad (Re_D)^{1/8} \tag{25}$$

where $Re_D = U_D D/\nu$ is the duct flow Reynolds number. Since $(Re_D)^{1/8} = O(1)$ for most duct flows of interest, we find

$$\frac{F_M}{F_S} \quad \alpha \quad \frac{d_p \Omega_p}{U_D} \quad . \tag{26}$$

If Ω_p is small, such as might be the case near but prior to impacting a surface, F_S is the dominant transverse force as a result of the shear acting on a particle. Upon rebounding the particle may spin up but, because of viscous dissipation, $d_p \Omega_p < U_D$ and, therefore, $F_M < F_S$ again.

While these findings pertain to $Re_p \ll 1$, they provide general guidance and suggest that in regions of strong shear, such as walls, the Saffman force may be large relative to the Magnus force. Whether or not it will significantly affect particle motion depends on the shear layer thickness. When this is thin, the trajectory of a rebounding particle that continues spinning after it emerges from the wall shear layer may be more strongly influenced by the <u>cumulative</u> action of the Magnus force. To show this, consider that according to

[184] the characteristic time for a e^{-1} decrease in Ω_p due to viscous dissipation is

$$t_M \simeq d_p^2/\nu \quad . \tag{27}$$

For a shear layer of thickness δ the characteristic time for the Saffman force is

$$t_S \simeq \delta/U_{pn} \tag{28}$$

where U_{pn} is the component of particle velocity normal to the shear layer. The ratio of these two time scales is

$$\frac{t_M}{t_S} \simeq \frac{d_p^2 \, U_{pn}}{\delta \, \nu} = \left(\frac{d_p}{D}\right)^2 \left(\frac{D}{\delta}\right)\left(\frac{U_{pn}}{U_D}\right) \, Re_D \tag{29}$$

In a duct flow with $Re_D = 10^5$ we find $\delta/D \simeq 0.1$ [190]. If we assume that $U_{pn}/U_D \simeq 0.1$, then $t_M/t_S > 1$ provided $d_p/D > 10^{-3}$. For a practical interpretation, consider that this finding would require that $d_p > 200$ μm in a duct with $D = 0.2$m, and this is a common case in many particle-laden industrial flows.

The inclusion of $\vec{F}_M$ in the force balance for a particle makes it necessary to know how $\vec{\Omega}_p$ varies with time. For a spinning sphere the conservation of angular momentum requires

$$I \, \frac{d\vec{\Omega}_p}{dt} = - \vec{T} \tag{30}$$

where I is the moment of inertia of the sphere about any diameter and $\vec{T}$ is the torque on the sphere due to viscous effects. The appropriate expression for $\vec{T}$ depends on Re_p and Re_r. For $Re_p \ll 1$ and all Re_r/Re_p, analysis in [184] gives

$$\vec{T} = - C_T \, \mu \, \left(\frac{d_p}{2}\right)^3 \vec{\Omega}_p \tag{31}$$

with $C_T = 8\pi$. For $250 < Re_p < 550$ and $Re_r/Re_p \simeq 1$, Armstrong, et al. [179] find $C_T = O(100)$ for angular coal particles. For $550 < Re_p < 1600$ when $0.2 < Re_r/Re_p < 20$, Tsuji, et al. [188] recommend the C_T correlation proposed in [191]. The solution of Eq.(30) requires an initial value for the particle angular velocity which is generally unknown. This, combined with the uncertainty in C_T, renders the calculation of $\vec{\Omega}_p$, and hence of $\vec{F}_M$, rather inexact [188].

The importance of the Magnus force to erosion has been demonstrated in [179] using a particle capture technique. These authors mapped the curved trajectories of angular coal particles of approximately 150 μm diameter rebounding from flat stainless steel and aluminum surfaces. Care was taken to ensure stagnant fluid conditions in the vicinity of the target surfaces in order to minimize the effects of air motion on the particle trajectories. The particle incidence speed ranged from 60 to 100 m/s corresponding to $250 < Re_p < 500$. Using a simplified analytical model, the authors considered the behavior of the smaller particles for conditions typical of the gas turbine environment. From results such as those shown in Fig. 12, the authors concluded that Magnus forces could affect the motions of 10 μm particles over rebound distances of about 20 mm. However, in estimating the initial particle angular velocity, the authors assumed $U_p \simeq \Omega_p\, d_p/2$, implying that the translational energy of the particle is completely converted into rotational energy. This assumption results in unrealistically large values of Ω_p.

Particle-wall collision phenomena in horizontal tubes at low volumetric concentrations of particles in a gas stream have been considered in [177]. Individual particle behavior was examined under the assumption of two-dimensional particle motion. Analysis of particle collisions with the tube wall led to the conclusion that the dependence of particle trajectories on the Magnus force is more pronounced for conditions of adhesive friction than sliding fric-

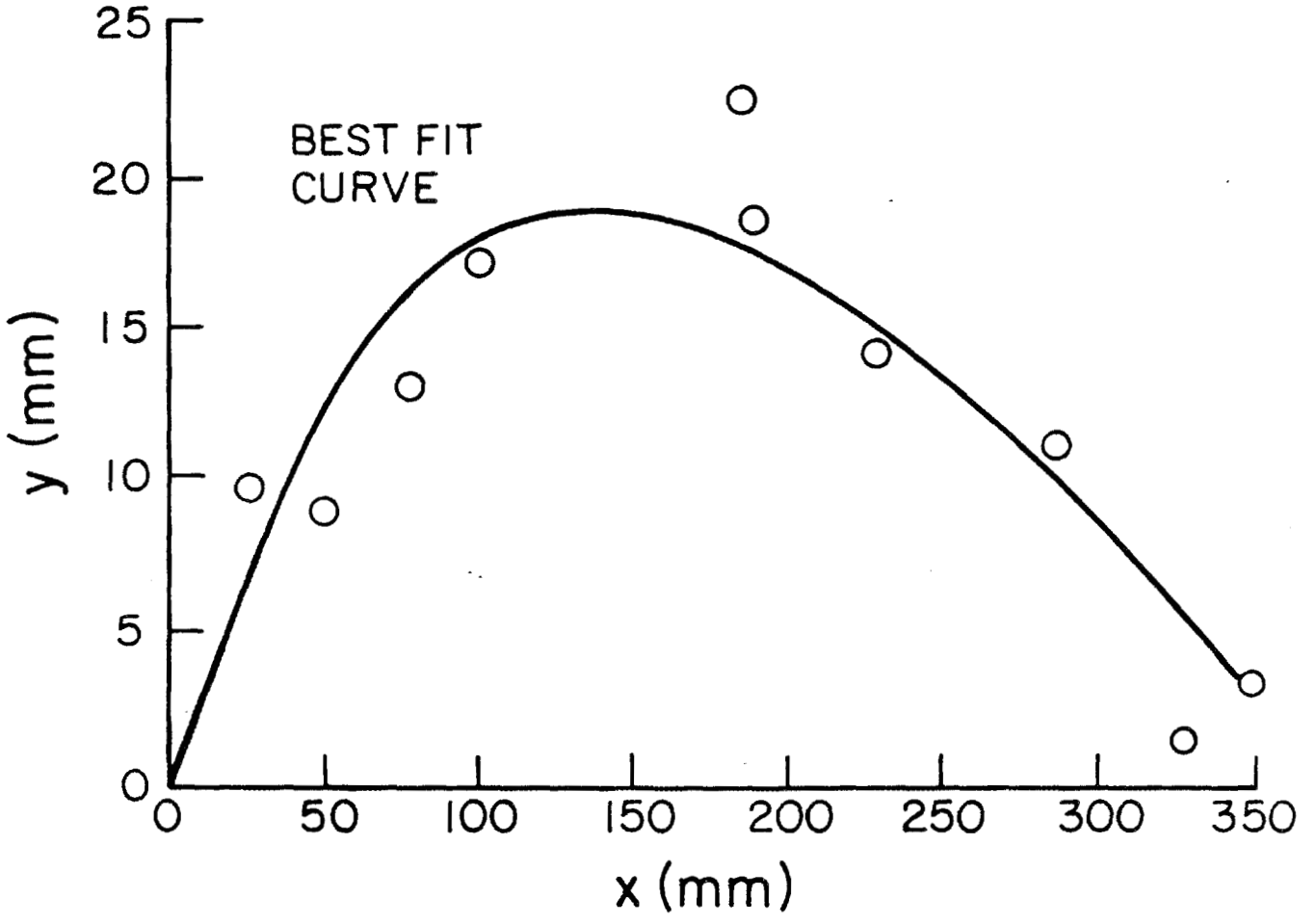

Figure 12. Best fit (line) to experimental data (crosses) for the average trajectory of an angular coal particle rebounding with spin from an aluminum surface in a quiescent air environment. In the figure the x- and y-coordinates are parallel and perpendicular to the surface respectively. The incidence particle velocity and angle were V_1 = 140 m/s and β_1 = 30 degrees respectively. Based on measurements by Armstrong et al. [179].

tion. This is because in the case of the former the sign of the Magnus force changes sign with alternate wall impacts, due to the change in sign of a rebounding particle's spin. As a consequence, the mean distance travelled by a particle between successive wall collisions is shorter, and the energy lost by the particle to the wall is higher, for conditions of adhesive friction.

3.3.4 Particle-Particle Interactions Near Surfaces

The presence of a solid surface substantially alters the nature of particle-particle interactions through the boundary constraint and it has been observed that the rate of surface erosion can actually decrease with increasing particle concentration[19,20]. Uuemois and Kleis [20] suggested that collisions between particles respectively approaching and departing from the surface work to impede the net advancement of particles moving towards the surface. According to them, the collisions create a protective barrier that reduces erosion. A similar argument has been proposed to explain concentration-dependent erosion results for high temperature hypersonic flows [192]. While it seems reasonable to suppose that the frequency of such inter-particle collisions is favored at high levels of flux, little seems to be known about the collision process itself. This is not surprising, in view of the difficulty of measuring or modeling the random, three-dimensional interactions among particles advancing towards, and rebounding from, a surface undergoing erosion in a turbulent flow.

Under idealized conditions, however, it is possible to derive useful analytical results. This has been done by, for example, Andrews and Horsfield [36] for conditions corresponding to a monodisperse stream of spherical particles travelling along initially parallel trajectories towards a flat surface. The authors' analysis is limited to low particle concentrations (low flux) and, because it ignores fluid friction effects, is limited to relatively inertial

particles ($\lambda >> 1$). The authors further assume that, in the absence of collisions among particles approaching the surface and particles departing from the surface, all particles approach the surface at velocity V_1 and angle β_1 and, upon rebounding, depart from the surface at velocity V_2 and angle β_2. For these conditions the authors derive an expression for the mean free path, λ_m, of a particle approaching the surface before colliding with a particle departing from the surface:

$$\lambda_m \simeq \frac{2\, V_1 V_2}{\pi\, d_p \Omega_1 \Omega_2} \cos^2 (\alpha/2) \quad . \tag{32}$$

In this expression $\alpha = \pi - \beta_1 - \beta_2$, and the Ω's are the frequencies of spheres moving along an approaching trajectory (Ω_1) or departing trajectory (Ω_2) with respect to the surface.

Assuming elastic collisions and that $\beta_1 = \beta_2$, the expression for λ_m becomes:

$$\lambda_m \simeq d_p^{-5}\, N_p^{-2} \cos^2 (\pi/2 - \beta_1) \tag{33}$$

where N_p is the number of particles per unit volume in the flow. Requiring that an approaching particle should travel a distance λ_m with angle β_1 prior to collision, Eq. (33) provides a relation between particle size and concentration. Of course, this result is specific to the sand-blast type flow configuration idealized by the authors and is subject to the assumptions mentioned.

Relations describing the self-scattering of a dilute ensemble of moving spheres for the sand-blast configuration were also described in [36]. Scattering was modeled by presuming elastic collisions between pairs of spheres the orientation of which, at the instant of impact, was taken to be random. From the results for the relative energy of the scattered spheres as a function of

scatter angle, two especially interesting observations emerge: a) Except for a very small fraction of spheres, one of each pair of spheres which collide returns to strike the surface, the second sphere having a finite probability of doing likewise. b) Because the orientation angle between colliding spheres is presumed to be random, a distribution arises of possible particle speeds and trajectories for both the particles approaching and those leaving the surface.

The first point is significant in that it supports the idea that interparticle collisions at low levels of flux do not necessarily reduce the number of particles striking a surface. This contradicts the notion that a protective barrier can be set up at a surface through interparticle collision, as suggested in [20]. Instead, it can be argued that collisions can reduce the energy content of approaching particles by transmitting some of this energy to particles rebounding from the surface. Thus, while the number of surface impacts will increase with increasing particle concentration in a constant speed jet sandblast, the energy per particle can be reduced, thus resulting in less damaging impacts and reduced wear.

The second point suggests the interesting possibility of non-uniform surface erosion due to the redirection of particles as a consequence of collision. Thus, for example, a stream of particles approaching a ductile surface at about $\beta_1 = 25^\circ$ should produce maximum wear [6]. However, the analysis in [36] shows that, due to particle redirection, erosion must be integrated over jet blast angles ranging from 0° to 50°, approximately. The opposite is also possible, that particles initially directed along non-damaging trajectories can, as a result of collision, be redirected along potentially more erosive routes.

In spite of the relative simplicity of the analysis in [36], which is devoid of fluid mechanic effects, experiments performed by the authors with fairly inertial particles appear to support some of their theoretical predic-

tions. The motions of large glass spheres impacting a target of variable inclination angle were investigated photographically. The spheres had $d_p \simeq 600$ μm and a speed of 13 ± 1 m/s. The incidence angle was varied over the range $20^o < \beta_1 < 50^o$. The average flux of spheres investigated experimentally was 0.03 - 0.3 gr cm^{-2} s^{-1}, and was within the low-flux limit of the analysis. Unfortunately, the majority of the collisions observed in the experiment were between fast arriving spheres and slow stray spheres, which affected the results and their interpretation. Whether the same observations would apply to particles in the range of 1 - 100 μm impacting solid surfaces in the presence of strong turbulence effects remains to be shown. The corresponding problem of indirect particle-particle interactions modulated by the presence of a solid surface has not been investigated extensively.

While idealized approaches to analyzing particle-particle collisions are useful, continued work must emphasize the the simulation of more realistic conditions. Future analyses and experimentation should include the investigation of: interactions among particles of differing sizes, densities and shapes; particle rotation (prior to and as a consequence of, collision); non-elastic collision conditions; three-dimensionality; the influence of the flow field, particularly near-wall turbulence; high particle concentrations; and particle fragmentation.

3.3.5 Surface Topography

The result of erosion by particle impact is the alteration of surface topography. Cracks, grooves and craters with raised edges, scales, etc., are the product of multiple, irregular, particle-surface collisions. Scarring of the material surface at the microscopic level has a random appearance, but large-scale patterns and regularly spaced ripples have been observed [13,193].

A study by Scattergood and Routbort [194], using 37 μm and 270 μm diameter Al_2O_3 particles impacting perpendicularly upon (111) silicon single crystal surfaces at 210 m/s shows that the initial transient in the weight loss curve depends on the condition of the surface prior to erosion. If the surface is pre-eroded by particles larger than those used subsequently, a decelerating transient is observed. An accelerating transient is observed when pre-erosion is conducted with particles smaller than those used subsequently. The authors explained their results by comparing the length scale of the subsurface flaws with that of the impacting particles. If the characteristic scale of the subsurface flaws is smaller than that corresponding to the impacting particle, the transient accelerates and vice versa. Similar observations have been made in [195].

Experiments on the time-dependence of plexiglass erosion by 10 and 30 μm diameter alumina particles at speeds of 84 and 65 m/s respectively, show that $E \alpha t^c$ with $c = -0.1$ [22]. The parameter c is a system constant and was found to be independent of particle speed, incidence angle and particle size. The decrease in erosion with time was attributed, in part, to increasing surface roughness but, as in [194], the explanation offered was entirely within the context of a mechanism for erosion: "It can be seen that after a few seconds of erosion the surface is considerably roughened and that particle impingement is no longer occurring at a normal angle of impingement." In fact, at an exposure time of about 120 s, the effective particle-surface incidence angle was about 55° and it is known that for brittle materials a departure from a normal incidence angle reduces erosion [4].

For both brittle and ductile materials, the evolution of surface topography is important. Observable surface changes due to material removal form the basis for hypothesized mechanisms of erosion as, for example, in the plate-

let mechanism of erosion for ductile metals [196-198]. If erosion is accompanied by corrosion, the formation of corrosion scale may enhance or inhibit erosion depending on the particle depth of cut, the rate and nature of scale growth and the adhesiveness of the scale to the surface.

The above studies focus on the role of surface roughness in mechanisms for explaining erosion. Except for the interesting turbulent flow study of Mason and Smith [165], little attention has been given to the synergistic effects between erosion-induced surface-evolving topographies and the associated fluid motion. The study in [165] centered on large scale changes in the topography of bends. However, the local influence of surface roughness on fluid and particle motions was not investigated and this is briefly discussed below.

The "wall region" of a developed turbulent flow is characterized by a large spectrum of scales of motion and vigorous unsteady dynamics [199]. However, the average velocity component, U_f, of fluid moving parallel to a solid surface can be expressed as:

$$\frac{U_f}{u_\tau} = \frac{1}{\kappa} \ln \left(\frac{y\, u_\tau}{\nu}\right) + f\left(\frac{h\, u_\tau}{\nu}\right) \qquad (34)$$

where: u_τ is the wall friction velocity, defined earlier, y is the normal distance from the surface, h is the "equivalent" roughness height and κ is the von Karman constant. The wall region to which Eq. (34) applies is bounded by $40\nu/u_\tau < y < 0.2\ \delta$) where δ is the boundary layer thickness. For values $h\, u_\tau/\nu > 5$ the roughness has the effect of reducing the mean fluid velocity relative to that which would arise along a smooth wall, and for $h\, u_\tau/\nu > 70$ this effect becomes pronounced. Appropriate forms for the function $f(h\, u_\tau/\nu)$ in Eq. (34) are summarized in [200].

For a pipe flow at room temperature with $Re_D = 10^5$, the value of the friction velocity is $u_\tau = O$ (10 m/s). This means that roughness elements of height $h > 100$ μm in air, or $h > 10$ μm in water, will significantly reduce the mean speed of fluid near a surface (relative to a smooth surface) at this value of the Re_D number. Photographic evidence suggests that typical values of h for surfaces roughened by particle impacts range between 1 and 1000 μm. Because of viscous damping in the sublayer region of the flow, fluids with high kinematic viscosity, ν, are less sensitive than fluids with low ν to the presence of protrusions on a surface. However, in both cases the effect of the roughness is to retard the mean component of fluid motion and, hence, particle motion parallel to the surface.

The ultimate consequences to erosion due to surface roughness are hard to generalize since the particle incidence speeds and angles that determine the amount and spatial distribution of surface wear depend markedly on λ and the local flow turbulence. Nevertheless, relative to a smooth pipe it seems reasonable to expect that, in an initially rough pipe, particles with $\lambda > 1$ approaching the pipe wall at shallow erosive angles on average will be deviated less from their damaging trajectories by the component of fluid motion parallel to the wall.

Even from such a crude picture, based on a mean-flow interpretation of a region of flow that is characterized by intense velocity fluctuations distributed randomly in time and over space, it must be concluded that roughness elements can alter both the magnitude and topography of surface erosion through their effects on the flow. Such a possibility must be considered when planning experiments and interpreting observations or when attempting to calculate the trajectories of particles near a surface.

3.4 Temperature Effects

Several investigators have argued that localized high temperature conditions created by high speed particle impacts can cause softening and even melting of metal surfaces at the impact locations [33,201]. On this point there are two views: a) the fundamental mechanisms governing erosion are mechanical, if thermal phenomena favor erosion the effect is small; b) thermal phenomena, namely melting, can significantly increase erosion. Prior to discussing some of the main studies adopting one of these two points of view, it is important to note that many of them have employed relatively large particles (d_p = O (1mm)) to induce the thermal effects observed. Whether or not the observations also apply to smaller particles (d_p = O (10 μm), more likely to occur in erosive flows, has yet to be established through rigorous similarity considerations and experimentation.

Some authors claim that metal softening and localized shear deformation facilitate the formation of deep craters with extended edges from which metal pieces break off easily during subsequent impacts [20,23,202]. High speed photographs of the impacts of steel spheres projected obliquely onto mild steel targets show that target material is detached along a band of intense subsurface shear [203]. Calculations of the phenomenon, based on an energy balance on the sphere, show that it is associated with the high temperatures induced locally by the impacts. Other authors argue that at high impact speeds a quick melting-resolidification process of the metal can take place at the particle metal interface [47,201,204-206]. In this model, as the particle rebounds it removes solidified metal material which has adhered to its surface. This mechanism is favored when target surfaces are already at high temperatures.

Against the melting-enhanced erosion arguments are the observations that high temperatures can increase metal ductility, facilitate particle embedding

and produce oxide films. A sufficiently ductile metal will allow a grazing particle to plow along its surface, moving material to either side of the grove, without actually removing material from the surface. Oxide films and embedded particles can work to shield a surface from subsequent damaging particle impacts. However, the results for embedding are inconclusive. For example, while it has been found that embedding significantly reduces particle surface deposition [183] much of the erosion data available suggests that embedding does not inhibit wear significantly [33].

The above studies pertain to localized temperature effects produced by particles impacting surfaces at high speed. The response of erosion to controlled variations of target temperature has also been investigated [11,18,31,170,201,207]. Andrews and Field [201] measured the wear of annealed copper targets impacted by 5 mm diameter hardened steel spheres at speeds ranging from 110 to 150 m/s. The experiments were performed in a non-oxidizing (argon gas) environment and showed that erosion increased with increasing target temperature over the range 800-1400°K. However, the authors note that the mass losses may have been affected by additional temperature increases at the positions of particle impact.

Experiments conducted in more realistic corrosive environments yield contrasting results. For example, Ganesan, et al [208] have measured the room temperature erosion by 30 μm sized alumina particles of 304 and 310 stainless steel specimens previously exposed to a gas mixture of 1% H_2S in N_2 at 600°, 700° and 800°C respectively. They attribute the differences observed in the erosion behavior of specimens corroded at different temperatures to differences in the nature of the scales formed. At low temperature the scales were crystalline and weakly adherent, whereas at high temperatures they were more strongly adherent but appeared to be more brittle. Notwithstanding, corroded

specimens always showed greater initial rates of erosion relative to uncorroded specimens.

By contrast, Young and Ruff [170] have observed that the erosion of various types of stainless steel by 5 and 50 μm Al_2O_3 particles suspended in a gas jet is less at 500°C than at 25°C. The authors attributed the reduction in erosion to the better protection afforded by the thicker oxide coating formed at 500°C. The comparatively smaller reduction in erosion for the case of the 50 μm particles was attributed to the particle depth-of-cut being larger than the thickest oxide scale thickness formed which, therefore, offered little protection. However, the authors' interpretation is confounded with particle motion considerations that also work to reduce erosion at high temperatures. A similar configuration was analyzed by Dosanjh and Humphrey [39] who calculated the flows of particle-laden gas jets aimed at flat surfaces. They show that increasing the carrier gas temperature (as Young and Ruffs did, to 300°C for the runs with the specimens at 500°C) decreases the particle incidence speed (V_1) and angle (β_1) as well as the particle flux (F_1) to the surface. The reason for this is readily explained in fluid mechanics terms, by noting that the ratio of momentum equilibration numbers at the same location between two flow configurations I and II that differ only in temperature and particle size is:

$$\frac{\lambda_I}{\lambda_{II}} = \frac{\mu_{II}}{\mu_I} \left(\frac{d_{pI}}{d_{pII}}\right)^2 \tag{35}$$

If $d_{pI} = d_{pII}$, and we assume $\mu \propto T^{1/2}$ (ideal gas) then:

$$\frac{\lambda_I}{\lambda_{II}} \propto \left(\frac{T_{II}}{T_I}\right)^{1/2} \qquad \text{(temperature effect on } \lambda\text{)} \tag{36}$$

If, however, $T_I = T_{II}$ but $d_{pI} \neq d_{pII}$ then:

$$\frac{\lambda_I}{\lambda_{II}} \propto \left(\frac{d_{pI}}{d_{pII}}\right)^2 \quad \text{(particle size effect on } \lambda\text{)} . \tag{37}$$

Therefore, small values of λ, characteristic of particles that closely follow the fluid motion and tend not to impact the surface, are moderately favored by increasing the gas stream temperature and substantially favored by reducing the particle size. In particular, from Eq. (35) one expects very large differences in erosion betweeen 5 μm particles in a gas jet at 300°C and 50 μm particles in a gas jet at 25°C (as observed by Young and Ruff) independently of oxide scale considerations.

There is yet another interesting feature in the observations by Young and Ruff that is explained by them in terms of the oxidation scales formed on the materials investigated but which admits a purely fluid mechanical interpretation. Figure 13, taken from their paper, shows that the erosion by 50 μm particles at 500°C is less than that at 25°C. In addition, relative to the results at 25°C, those at 500°C are displaced towards smaller particle incidence angles[1]; meaning that particles of a fixed size with small incidence angles and in streams at high temperature will erode equivalently to identical particles having large incidence angles in streams at low temperature. That this is the expected result can be shown using the cutting model proposed by Finnie [6] and the numerical fluid mechanics results obtained by Dosanjh and Humphrey [39]. For incidence angles $18.5° < \beta_1 < 90°$ the cutting model yields:

$$E \propto F_1 V_1^2 \cos^2 \beta_1 \tag{38}$$

****

[1]In the absence of experimental values, the particle incidence angle is assumed to be proportional to the acute angle formed by the gas jet and the target surface.

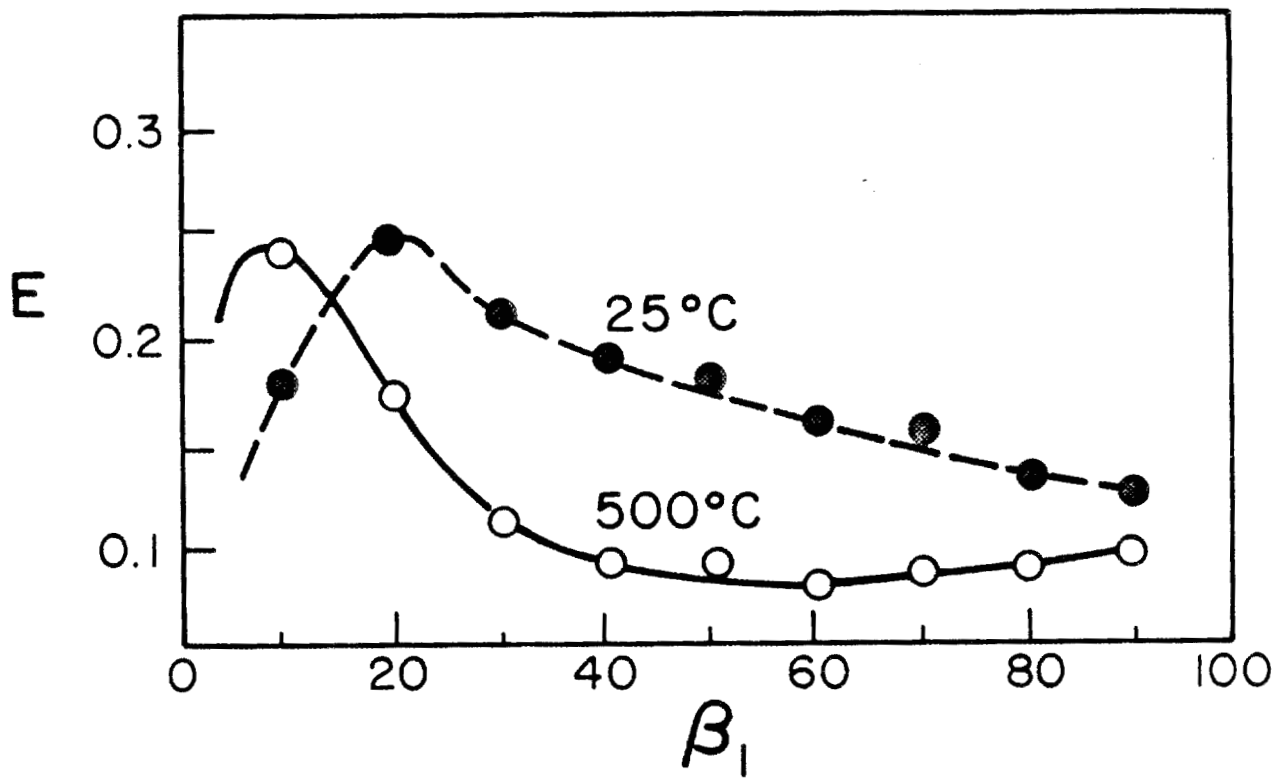

Figure 13. Erosion of an isothermal surface by a particle-laden jet of CO_2 gas as a function of the blast jet incidence angle. Conditions correspond to a stainless steel target at two temperatures impacted by Al_2O_3 particles of diameter 50 μm at a speed of 30 m/s. Based on measurements by Young and Ruff [170].

For two identical flow configurations, I and II, that differ only in temperature, $E_I = E_{II}$ when

$$(F_1 V_1^2 \cos^2 \beta_1)_I = (F_1 V_1^2 \cos^2 \beta_1)_{II} . \qquad (39)$$

The results in [39] show that, generally $(F_1 V_1^2)_{1200K}/(F_1 V_1^2)_{300K} < 1$ for the range of β_1 of interest here. It follows from Eq. (39) that $(\cos \beta_1)_{300K} < (\cos \beta_1)_{1200K}$ and, therefore, that $(\beta_1)_{300K} > (\beta_2)_{1200K}$. The conclusion is that the incidence angles of particles in a cold gas stream must be larger than those of identical particles in a hot stream to attain the same rates of erosion. This interpretation of the data in Fig. 13 does not necessarily imply that the protective oxide film hypothesis of Young and Ruff [170] is incorrect. The only conclusions to be drawn here are that: a) both interpretations are valid, but there is insufficient information available, from this or any other experiment, to rank them in order of importance; and, b) thermally-induced viscous effects can significantly affect particle motion and hence erosion in gas-solid flows.

Unfortunately, in oxidizing and other corrosive environments, clear and generally applicable interpretations of the effects of temperature on erosion are difficult to formulate. The synergistic effects between the two modes of mass loss are complex, insufficiently documented, poorly understood and, as a result, difficult to model. Hogmark et al [209] point out that no material has yet been completely characterized in terms of its corrosion/erosion behavior, which includes knowing: a) the corrosion and erosion properties of the base material; b) the erosion properties of the corroded surface layer; c) the erosion properties of the base material coated with a corroded layer, in particular the dynamics of the particle-corrosion layer interaction especially when the latter takes the form of a flaky material of ill-defined material properties

and mechanical behavior. Suffice it to say that for most systems of practical interest the fluid mechanics (turbulence especially) plays a critical role. This is because many surface corrosion reactions are diffusion-controlled. The rates at which chemical species and particles with $\lambda < 1$ approach or leave a surface ultimately depend on the large-scale convective motions which transport them between regions near the surface and the bulk of the flow, and on the interaction of the flow with the surface which may be smooth or rough. In this regard, corrosion scales can behave like roughness elements and will affect the transport process. There is a considerable body of literature on the subject of corrosion and, increasingly, more studies are appearing on the subject of erosion-corrosion [24,209-221].

4. CONCLUSIONS

Particle-laden fluids are responsible for costly erosion problems of grave concern to many important industries. The reasons for needing to understand and control erosion revolve about major issues of economy, safety and resources conservation. Certainly, with direct and indirect losses sustained by the industry and the military amounting to hundreds of millions of dollars annually, the primary motivation for understanding and controlling erosion is the economic factor.

This review has centered on uncovering and discussing various, previously neglected, fundamental issues having to do with the role played by fluid mechanics in erosion by solid particle impact. Emphasis was placed on understanding physical phenomena which could, in principle, lead to an improved control of particle motion in order to eliminate, or at least minimize, wear. The review reveals several major points.

1. There are numerous instances in the erosion literature, a few of which have been discussed here, of findings that have been attributed to materials-related causes but which admit purely fluid mechanics interpretations.

2. Previous experimental work in erosion has failed to adequately control, let alone measure with any degree of accuracy, the fluid mechanics variables that affect solid particle motion and surface impact. The variables include the instantaneous velocities of the fluid and particle phases, especially near the surfaces undergoing erosion, and temperature in non-isothermal flows.

3. In relation to Point 2, no fundamental experimental study of erosion by particle impact has yet been undertaken where the characteristics of the turbulence are varied in a controlled and systematic manner over a meaningful range of the relevant parameters. The experimental methodologies exist, and it is imperative to conduct such investigations since they will provide the data (and uncertainty bounds) so necessary for guiding and testing mathematical model developments that will render erosion predictable in systems of interest to industry.

4. In his review, Leschziner [79] concludes that computational fluid dynamics has reached the stage where it can be applied almost routinely to many single phase flows in highly complex three-dimensional geometries typical of industrial processes. Even though problems remain, they are of a solvable nature as research advances have shown. However, direct numerical simulations of turbulent flows are unlikely to benefit the industry in the immediate future, and phenomenological modeling approaches will continue to be the workhorse for predictors of turbulent flows in complex configurations. Extensions of single phase phenomenological models to two phase flows have already been undertaken and some have been discussed here. For purposes of modeling erosion by solid particle impact, lagrangian formulations of the particle phase are preferred to eulerian formulations since they are based on a physically intuitive force balance applied to the particle that explicitly allows, for example, the inclu-

sion of lateral forces which can remarkedly alter the trajectory of a particle near a surface. In this regard, significant progress has been made in the modeling of mono-disperse dilute systems where particles collide infrequently among themselves in the bulk of the flow or near the surface undergoing erosion. However, the corresponding behavior of more realistic concentrated polydispersed particle-gas flows has yet to be modeled satisfactorily, especially near surfaces.

5. There are important aspects of the erosion process that are, at present, too complex to model and for which accurate direct measurements are probably impossible. These relate to particle-particle collisions, and particle-surface interactions such as rebounding, fragmentation and spin. Here, innovative experimental and theoretical approaches are sorely needed, but they must be tempered by weighing the benefits of developing procedures aimed at measuring or computing details against the value of establishing simpler but proven approaches that will provide results quickly and with acceptable uncertainties.

6. Ultimately, the prediction of wear by particle impact must rely on the formulae derived by the material scientists for calculating erosion. Much of the early work was experimental in nature consisting, primarily, in establishing empirical correlations describing the erosion (often accelerated) of very specific material pairs for very specific experimental conditions. As a result, little of a universally applicable nature has emerged from this effort. More recently, significant theoretical advances have been made in the materials area (not reviewed here) that show promise for the development of more generally applicable erosion equations. However, it is important to stress that such research cannot be concluded successfully without close scrutiny and control of the fluid mechanics aspects of the erosion problem. In this regard, effective

technical communication between material scientists and fluid mechanicists is indispensable.

ACKNOWLEDGEMENTS

This review was motivated by the pioneering work of J.A. Laitone on the effects of fluid motion in erosion by solid particle impact. Special thanks go to I. Cornet and A. Levy who introduced me to the subject topic. Partial support for the review and related ongoing research in Berkeley has been provided by the Assistant Secretary for Fossil Energy Research, University Coal Research Division, U.S. Department of Energy, under Contract No. DE-AC03-76SF00098, and by Martin Marietta through subcontract No. 19X-55936C, under a prime contract from the Department of Energy. I am grateful for this support and to S. Dapkunas, R. Judkins, and P. Carlson for their interest in the work. Finally, I am indebted to the secretarial staff of the Department of Mechanical Engineering, in particular M.A. Peters and C. Schoon, for the competence and patience displayed in preparing this manuscript.

REFERENCES

1. Zahavi, J. and Schmitt, G.F. [1981] Solid particle erosion of reinforced composite materials, Wear, 71, pp. 179-190.

2. Zahavi, J. and Schmitt, G.F. [1981] Solid particle erosion of polymeric coatings, Wear, 71, pp. 191-210.

3. Zahavi, J. and Schmitt, G.F. [1982] Solid particle erosion of coatings on transparent polycarbonate and reinforced composites, Selection and Use of Wear Tests for Coatings, ASTM STP 769 (R.G. Bayer, Ed.) American Society for Testing and Materials, pp. 28-70.

4. Adler, W.F. [1979] Assessment of the state of knowledge pertaining to solid particle erosion, Final Report, No. CR79-680, to the U.S. Army Research Office for contract DAAG29-77-C-0039.

5. Finnie, I. [1958] The mechanism of erosion of ductile metals, Proceedings, 3rd U.S. National Congress of Applied Mechanics, pp. 527-532. Pergamon Press, London.

6. Finnie, I. [1960] An experimental study of erosion, Proc. Soc. Exptl. Stress Anal., 17:2, pp. 65-70.

7. Finnie, I. [1960] Erosion of surfaces by solid particles, Wear, 3, pp. 87-103.

8. Finnie, I. [1972] Some observations on the erosion of ductile metals, Wear, 19, pp. 81-90.

9. Finnie, I. [1978] On the velocity dependence of the erosion of ductile metals by solid particles at low angles of incidence, Wear, 48, pp. 181-190.

10. Finnie, I. and McFadden, D.H. [1978] On the velocity dependece of the erosion of ductile metals by solid particles at low angles of incidence, Wear, 48, pp 181-190.

11. Finnie, I., Levy, A. and McFadden, D.H. [1979] Fundamental Mechanisms of the Erosive Wear of Ductile Metals by Solid Particles, Erosion: Prevention and Useful Applications, ASTM STP 664, W.F. Adler, Ed., American Society for Testing and Materials, pp. 36-58.

12. Finnie, I. [1980] The mechanisms of erosive wear in ductile metals, Corrosion-Erosion Behavior Materials (ed. K. Natesan), Metallurgical Society of AIME, pp. 118-126.

13. Bitter, J.G.A. [1963] A study of erosion phenomena (Part 1), Wear, 6, pp. 5-21.

14. Bitter, J.G.A. [1963] A study of erosion phenomena (Part 2), Wear, 6, pp. 169-190.

15. Sheldon, G.L. and Finnie, I. [1966] On the ductile behavior of nominally brittle materials during erosive cutting, J. Eng. Ind., Nov. pp. 387-392.

16. Sheldon, G.L. and Finnie, I. [1966] The mechanism of material removal in the erosive cutting of brittle materials, J. Eng. Ind., Nov. pp. 393-400.

17. Neilson, J.H. and Gilchrist, A. [1968] Erosion by a stream of solid particles, Wear, 11, pp. 11-122.

18. Neilson, J.H. and Gilchrist, A. [1968] An experimental investigation into aspects of erosion in rocket motor tail nozzles, Wear, 11, pp. 123-143.

19. Tilly, G.P. and Sage, W. [1970] The interaction of particle and material behavior in erosion processes, Wear, 16, pp. 447-465.

20. Uuemois, H. and Kleis, I. [1975] A critical analysis of erosion problems which have been little studied, Wear, 31, pp. 359-371.

21. Sage, W. and Tilly, P. [1969] The significance of particle size in sand erosion of small gas turbines, The Aeronautical Journal of the Royal Aeronautical Society, 73, pp. 427-428.

22. Sargent, G.A. Mehrota, P.K. and Conrad, H. [1979] A model for the multi-particle erosion of brittle solids by spherical particles, Paper No. 28, Proc. 5th Int. Conf. on Erosion by Liquid and Solid Impact, (Ed. J.E. Field), Cambridge, England.

23. Hutchings, I.M. [1979] Mechanisms of the erosion of metals by solid particles, Erosion: Prevention and Useful Applications, ASTM STP 664, W.F. Adler, Ed., American Society for Testing and Materials, pp. 59-76.

24. Hutchings, I.M. [1980] Recent advances in the understanding of solid particle erosion, Mecanique, Materiaux, Electricite, 365, pp. 185-192.

25. Hutchings, I.M. [1981] A model for the erosion of metals by spherical particles at normal incidence, Wear, 70, pp. 269-281.

26. Andrews, D.R. [1981] An analysis of particle erosion mechanisms, J. Phys. D: Appl. Phys., 14, pp. 1979-1991.

27. Söderberg, S., Hogmark, S., Engman, U., and Swahn, H. [1981] Erosion classification of materials using a centrifugal erosion tester, Tribology International, pp. 333-344.

28. Söderberg, S., Hogmark, S., and Swahn, H. [1982] Mechanisms of material removal during erosion of a stainless steel, Paper No. 82-AM-4A-1, 37th ASLE Annual Meeting, Cincinnati, Ohio, May 10-13.

29. Mills, D. and Mason, J.S. [1975] Learning to Live with Erosion of Bends, Proceedings of the First International Conference on the Internal and External Protection of Pipes, University of Durham, Paper G1, pp. G1-1 to G1-19, September 9-11.

30. Adler, W.F. (editor) [1979] Erosion; prevention and useful applications, STP 664 (Philadelphia: ASTM).

31. Tilly, G.P. [1979] Erosion caused by impact of solid particles, Treatise on Materials Science and Technology, Vol. 13, Academic Press.

32. Schmitt, G.F. [1980] Liquid and solid particle impact erosion, Wear Control Handbook, pp. 231-282, (M.B. Peterson and W.O. Winer, Eds.) American Society of Mechanical Engineers, New York.

33. Shewmon, P.G. and Sundarajan, G. [1983] The erosion of metals, Annual Reviews of Material Science, 13, pp. 301-318.

34. Cousens, A.K. and Hutchings, I.M. [1983] A critical study of the erosion of an aluminum alloy by solid spherical particles at normal impingement, Wear, 88, pp. 335-348.

35. Laitone, J.A. [1979] Aerodynamic effects in the erosion process, Wear, 56, pp. 239-246.

36. Andrews, D.R. and Horsfield, N. [1983] Particle collisions in the vicinity of an eroding surface, J. Phys, D. Appl. Phys., 16, pp. 525-538.

37. Laitone, J.A. [1979] Erosion prediction near a stagnation point resulting from aerodynamically entrained solid particles, J. Aircraft, 16, pp. 809-814.

38. Laitone, J. [1983] Characterization of particle rebound phenomena in the erosion of turbomachinery, J. Aircraft, 20, pp. 275-281.

39. Dosanjh, S. and Humphrey, J.A.C. [1985] The influence of turbulence on erosion by a particle-laden fluid jet, Wear, 102, pp. 309-330.

40. Youngdahl, C.A. and Ellingson, W.A. [1982] Acoustic system for monitoring pressure boundary wear, presented at the Symposium on Instrumentation and Control for Fossil Energy Processes, June 7-9, Houston, Texas.

41. Hutchings, I.M. [1983] Introduction to the microscopy of erosion, Journal of Microscopy, 130, pp. 331-338.

42. Andrews, D.R. [1983] A gravity-insensitive technique for measuring mass changes in hostile environments, including erosion, J. Phys. E: Scientific Instruments, 16, pp. 803-806.

43. Thomas, G.P. [1966] The initial stages of deformation in metals subjected to repeated liquid impact. Phil. Trans. Roy. Soc. A, 260, 140.

44. Ives, L.K. and Ruff, A.W. [1978] Transmission and scanning electron microscopy studies of deformation at erosion impact sites, Wear, 46, pp. 149-162.

45. Ives, L.K. and Ruff, A.W. [1979] Electron microscopy study of erosion damage in copper, Erosion: Prevention and useful applications, ASTM STP664. (W.F. Adler, ed) American Society for Testing and Materials, pp.5-35.

46. Brainard, W.A. and Salik, J. [1980] Scanning-electron-microscope study of normal-impingement erosion of ductile metals, NASA TP 1609, Lewis Research Center, Cleveland, Ohio.

47. Brainard, W.A. and Salik, J. [1980] An investigation into the role of adhesion in the erosion of ductile metals, ASLE Trans., 24, pp 302-306.

48. Ruff, A.W. and Ives, L.K. [1975] Measurement of solid particle velocity in erosive wear, Wear, 35, pp. 195-199.

49. Ponnaganti, V., Stock, D.E., and Sheldon, G.L. [1980] Measurement of particle velocities in erosion processes, in the Proceedings of the Symposium on Polyphase Flow and Transport Technology (edited by R.A. Bajura), pp. 217-222, Century 2- Engineering Technology Confgerences, ASME.

50. Sheldon, G.L., Maji, J., and Crowe, C.T. [1977] Erosion of a tube by gas-particle flow, J. Eng. Mater., 99, pp. 138-142.

51. Chigier, N.A. [1971] Velocity measurements of particles in sprays, Paper No. 1-4-30, in the Proceedings of the Symposium on Flow - Its Measurement and Control in Science and Industry, Pittsburgh, Pennsylvania, May 1971.

52. Hutchings, I.M. [1977] Errosion of metals by solid particles-study using high-speed photography, BK# 01318, pp. 358-361.

53. Van Horn, G.R. [1977] Rotating drum cameras for high speed photography, electro-optical systems design, pp. 26-29.

54. Meynart, R. [1983] Speckle velocimetry study of vortex pairing in a low-Re unexcited jet, Phys. Fluids, 26, pp. 2074-2079.

55. Meynart, R. [1983] Instantaneous velocity field measurements in unsteady gas flow by speckle velocimetry, Applied Optics, 22, pp. 535-540.

56. Durst, F., Melling, A. and Whitelaw, J.H. [1976] Principles and practice of laser-Doppler anemometry, Academic Press, London.

57. Drain, L.E. [1980] The laser-Doppler technique, John Wiley and Sons, New York.

58. Dring, R.P. [1982] Sizing criteria for laser anemometry particles, J. Fluids Eng. 104, pp. 15-17.

59. Einav, S. and Lee, S.L. [1973] Measurement of velocity distributions in two-phase suspension flows by the laser-Dopper technique, Rev. Sci. Instrum., 44, pp. 1478-1480.

60. Durst, F. and Zare, M. [1975] Laser doppler measurements in two-phase flows, Proceedings of the LDA-Symposium, pp. 403-429, University of Denmark, Copenhagen.

61. Yule, A.J. Chigier, N.A., Atakans, S., and Ungut, A. [1977] Particle size and velocity measurement by laser anemometry, Journal of Energy, 1:4, pp. 220-228.

62. Ungut, A., Yule, A.J., Taylor, D.S. and Chigier, N.A. [1978] Particle size measurement by laser anemometry, Journal of Energy, 2:6, pp. 330-336.

63. Lee, S.L. and Srinivasan [1978] Measurement of local size and velocity probability density distributions in two-phase suspension flows by laser-Doppler technique, Int. J. Multiphase Flow, 4, pp. 141-155.

64. Lee, S.L. and Srinivasan [1982] An LDA technique for in situ simultaneous velocity and size measurement of large spherical particles in a two-phase suspension flow, Int. J. Multiphase Flow, 8, pp. 47-57.

65. Durst, F. [1982] Review-combined measurements of particle velocities, size distributions, and concentrations, J. Fluids Eng., Trans. ASME, 104, pp. 284-296.

66. Tsuji, Y., Morikawa, Y., Shiomi, H. [1984] LDV measurements of an air-solid two-phase flow in a vertical pipe, J. Fluid Mech., 139, pp. 417-434.

67. Buchave, P., Delhaye, J.M., Durst, F., George, W.K., Refslund, K. and Whitelaw, J.H. (editors) [1976] The accuracy of flow measurements by laser-Doppler methods, Proceedings of the LDA-Symposium, Copenhagen, 1975.

68. Buchave, P., George, W.K. and Lumley, J.L. [1979] The measurement of turbulence with the laser-Doppler anemometer, A. Rev. Fluid Mech., 11, pp. 443-503.

69. Thompson, H.D. and Stevenson, W.H. (editors) [1979] Laser velocimetry and particle sizing, Proceedings of the Third International Workshop on Laser Velocimetry, Purdue University 1978, Hemisphere Publishing Corporation.

70. Adrian, R.J., Durao, D.F.G., Durst, F., Mishina, H. and Whitelaw, J.H. (editors) [1982] Proceedings of the First International Symposium on Applications of Laser-Doppler Anemometry to Fluid Mechanics, Lisbon, Portugal.

71. Adrian, R.J., Durao, D.F.G., Durst, F., Mishina, H. and Whitelaw, J.H. (editors) [1984] Proceedings of the Second International Symposium on Applications of Laser-Doppler Anemometry to Fluid Mechanics, Lisbon, Portugal.

72. Adrian, R.J., Durao, D.F.G., Durst, F., Mishina, H. and Whitelaw, J.H. (editors) [1986] Proceedings of the Third International Symposium on Applications of Laser-Doppler Anemometry to Fluid Mechanics, Lisbon, Portugal.

73. Tabakoff, W. and Sugiyama, Y. [1980] Experimental method of determining particle restitution coefficients, in the Proceedings of the Symposium on Polyphase Flow and Transport Technology, (edited by R.A. Bajura), pp. 203-210, Century 2-Engineering Technology Conferences, ASME.

74. Tennekes, H. and Lumley, J.L. [1972] A first course in turbulence, The MIT Press, Cambridge, Massachusetts.

75. Reynolds, W. [1976] Computation of turbulent flows, Ann. Rev. of Fluid Mech., 8, p. 183-208.

76. Frost, W. and Moulden, T.H. [1977] (editors) Handbook of turbulence, Vol. 1, fundamentals and applications, Plenum Press, New York.

77. Bradshaw, P., Cebeci, T., Whitelaw, J. [1981] Engineering calculation methods for turbulent flow, Academic Press Inc., London.

78. Bradshaw, P. (editor) [1978] Turbulence, Topics in applied physics, Vol. 12, Second Edition, Springer-Verlag, New York.

79. Leschziner, M.A. [1989] Modeling turbulent recirculating flows by finite-volume methods-current states and future directions, Int. J. Heat and Fluid Flow, 10, pp. 186-202.

80. Launder, B.E. [1989] Second-moment closure: present... and future, Int. J. Heat and Fluid Flow, 10, pp. 282-300.

81. Elgobashi, S.E. and Abou Arab, T.W. [1983] A two-equation turbulence model for two-phase flows, Physics of Fluids, 26, pp. 931-938.

82. Pourahmadi, F. and Humphrey, J.A.C. [1983] Modeling solid-fluid turbulent flows with application to predicting erosive wear, Int. J. PhysicoChemical Hydrodynamics, 4, pp. 191-219.

83. Schuh, M.J., Schuler, C.A. and Humphrey, J.A.C. [1989] Numerical calculation of two phase flow and erosion in particle-laden gas flows past tubes. AIChE Jl., 35, pp.466-480.

84. Torobin, L.B. and Gauvin, W.H. [1959] Fundamental aspects of solid-gas flow, Can. J. Chem. Engrg. 37, p. 129, p. 167, p. 224.

85. Torobin, L.B. and Gauvin, W.H. [1960] Fundamental Aspects of solid-gas flow, Can. J. Chem. Engrg., 38, p. 142, p. 189.

86. Torobin, L.B. and Gauvin, W.H. [1961] Fundamental aspects of solid-gas flow, Can. J. Chem. Engrg., 39, p. 113.

87. Marble, F.E. [1963] Dynamics of a gas containing small solid particles, Combustion and Propulsion, 5th AGARD Colloquium, pp. 175-215, Pergamon Press, Oxford.

88. Marble, F.E. [1964] Mechanism of particle collision in the one-dimensional dynamics of gas-particle mixtures, Physics of Fluids, 7, pp. 1270-1282.

89. Marble, F.E. [1970] Dynamics of dusty gases, Annual Rev. of Fluid Mech., 2, p. 397.

90. Soo, S.L. [1967] Fluid Mechanics of Multiphase Systems, Blaisdell Publishing Company, London.

91. Wallis, G. [1969] One-dimensional two-phase flow, McGraw-Hill, New York.

92. Owen, P.R. [1969] Pneumatic transport, J. Fluid Mech., 39, pp. 407-432.

93. Hinze, J.O. [1972] Turbulent fluid and particle interaction, Vol. 6, Progress in Heat and Mass Transfer, Pergamon Press, New York.

94. Happel, J. and Brenner, H. [1973] Low Reynolds number hydrodynamics, 2nd ed., Noordhoff, Leyden, Netherlands.

95. Batchelor, G.K. [1974] Transport properties of two-phase materials with random structure, Annual Rev. of Fluid Mech., 6, p. 227.

96. Peskin, R.L. [1975] Some fundamental research problems in gas-solid flow, American Institute of Chemical Engineers Symposium Series, 71, No. 147, pp. 52-59.

97. Clift, R., Grace, J.R. and Weber, M.E. [1978] Bubbles, drops and particles, Academic Press, New York.

98. Rudinger, G. [1980] Fundamentals of gas-particle flow, Vol. 2 of Handbook of Powder Technology, (Williams, J.C. and Allen, T.,eds), Elsevier Scientific Publishing Company, Amsterdam.

99. Di Giacinto, M., Sabetta, F. and Piva, R. [1982] Two-way coupling effects in dilute gas-particle flows, J. Fluids Eng., 104, pp. 304-312.

100. Drew, D.A. [1983] Mathematical modeling of two-phase flow, Annual Rev. of Fluid Mech., 15, pp. 261-291.

101. Jurewicz, J.T., Stock, D.E. and Crowe, C.T. [1977] The effect of turbulent diffusion on gas particle flow in an electric field, Thermal Energy Laboratory Report No. 77-6, Mechanical Engineering Department, Washington State University.

102. Shuen, J.S., Chen, L.D. and Faeth, G.M. [1983] Predictions of the structure of turbulent, particle-laden round jets, AIAA Jl, 21, pp. 1483-1484.

103. Shuen, J.S., Solomon, A.S.P., Zhang, Q.F. and Faeth, G.M. [1985] Structure of particle-laden jets: measurements and predictions, AIAA Jl, 23, pp. 396-404.

104. Faeth, G.M. [1983] Recent advances in modeling particle transport properties and dispersion in turbulent flow, Vol. 2, pp. 517-534, of the Proceedings of the ASME-JSME Thermal Engineering Joint Conference, Honolulu, Hawaii, March 20-24.

105. Yeung, W.S. [1978] Fundamentals of the particulate phase in a gas-solid mixture, Report No. LBL-8440, Lawrence Berkeley Laboratory, University of California, Berkeley.

106. Abrahamson, J. [1975] Collision rates of small particles in vigorously turbulent fluid, Chem. Eng. Sc., 30, pp. 1371-1379.

107. Dukowicz, J.K. [1980] A particle-fluid numerical model for liquid sprays, J. Comp. Physics, 35, pp. 229-253.

108. Lee, J.S. and Humphrey, J.A.C. [1986] Radiative-Convective heat transfer in dilute particle-laden channel flows, Int. J. Physicochemical Hydrodynamics, 7, pp. 325-351.

109. Doss, E.D. [1985] Analysis and application of solid-gas flow inside a venturi with particle interaction, Int. J. Multiphase Flow, 11, pp. 445-458.

110. Gouesbet, G. Berlement, A. and Picart, A. [1984] Dispersion of discrete particles by continuous turbulent motions. Extensive discussion of the Tchen theory, using a two-parameter family of Lagrangian correlation functions, Phys. Fluids, pp. 27, pp. 827-837.

111. Goldschmidt, V.W., Householder, M.K. Ahmadi, G. and Chuang, S.C. (1972) Turbulent diffusion of small particles suspended in a turbulent jet, Prog. Heat Mass Trans., 6, pp. 487-508.

112. Lilly, G.P. [1973] Effect of particle size on particle eddy diffusivity, Chem. Fundam. 12, pp. 268-275.

113. Peskin, R.L. and Kau, C.J. [1979] Numerical simulation of particle motion in turbulent gas-solid channel flow, J. Fluids Eng., 101, p. 9.

114. Brown, D.J. and Hutchinson, P. [1979] The interaction of solid or liquid particles and turbulent fluid flow fields - a numerical simulation, J. Fluids Eng., 101, pp. 265-269.

115. Rizk, M.A. and Elgobashi, S.E. [1985] The motion of a spherical particle suspended in a turbulent flow near a plane wall, Phys. Fluids, 28, pp. 806-817.

116. Chao, B.T. [1964] Turbulent transport behavior of small particles in dilute suspension, Osterr. Ing. Arch., 18, pp. 7-21.

117. Kreplin, H.P. and Echelmann, H. [1979] Behavior of the three-fluctuating velocity Components in the wall region of a turbulent channel flow, Phys. Fluids, 22, pg. 1233.

118. Crowder, R.S., Daily, J.W. and Humphrey, J.A.C. [1984] Numerical calculation of particle dispersion in a turbulent mixing layer flow, Journal of Pipelines, 4, pp. 159-169.

119. Abramovich, G.N. [1971] Effect of solid-particle or droplet admixture on the structure of a turbulent gas jet, Int. J. Heat and Mass Transfer, 14, pp. 1039-1045.

120. Boothroyd, R.G. and Walton, P.J. [1973] Fully developed turbulent boundary-layer flow of a fine solid-particle gaseous suspension, Ind. Eng. Chem. Fundam., 12, pp. 75-82.

121. Zisselmar, R. and Molerus, O. [1979] Investigation of solid-liquid pipe flow with regard to turbulence modification, The Chemical Engineer Jl., 18, pp. 233-239.

122. Crowe, C.T. [1982] Review-numerical models for dilute gas-particle flows, J. Fluid Eng., 104, pp. 297-303.

123. Durst, F., Milojevic, D. and Schonung, B. [1984] Eulerian and lagrangian predictions of particulate two-phase flows: a numerical study, Appl. Math. Modeling, 8, pp. 101-116.

124. Kallio, G.A. and Stock, D.E. [1986] Turbulent particle suspension: A comparision between lagrangian and eulerian model approaches, in "Gas-Solid Flows- 1986," FED-Vol. 35, The American Society of Mechanical Engineers, Library of Congress catalog Card Number 83-73579.

125. Hetsroni, G. [1988] Particles-turbulence interaction, in "Third International Symposium on Liquid-Solid Flows," FED-Vol. 75, The American Society of Mechanical Engineers Library of Congress Catalog Card Number 83-73577.

126. Drew, A.D. [1971] Averaged field equations for two-phase media, in Studies in Applied Mathematics, Vol. L, No. 2, pp. 133-166, The Massachusetts Institute of Technology.

127. Drew, A.D. and Segel, L.A. [1971] Averaged equations for two-phase flows, in Studies in Applied Mathematics, Vol. L, No. 3, pp. 205-231, The Massachusetts Institute of Technology.

128. Whitaker, S. [1973] The transport equations for multi-phase systems, Chem. Eng. Sc., 28, pp. 139-147.

129. Sha, W.T. and Soo, S.L. [1978] Multidomain multiphase fluid mechanics, Int. J. Heat Mass Transfer, 21, pp. 1581-1595.

130. Hinze, J.O. [1962] Momentum and mechanical-energy balance equations for a flowing homogeneous suspension with slip between the two phases, Appl. Sci. Res., Section A, 11, pp. 33-46.

131. Murray, J.D. [1965] On the mathematics of fluidization. Part 1. Fundamental equations and wave propagation, J. Fluid Mech., 2, pp. 465-493.

132. Looney, M.K., Issa, R.I., Gosman, A.D. and Politis, S. [1985] Modelling of the turbulent flow of solid/liquid suspensions in stirred vessels, presented at the 5th Int. Conf. "Mathematical Modelling", U.C. Berkeley, July 29-31.

133. Taylor, G.I. [1940] Notes on possible equipment and technique for experiments on icing on aircraft, Aero. Res. Com., Rep. and Mem. No. 2024.

134. Wenglarz, R.A. [1982] Boundary layer effects on impingement and erosion, ASME Fluids Engineering Conference, 17th Annual Cavitation and Poly-Phase Flow Forum Proceedings, St. Louis, MO, June 7-11.

135. Boothroyd, R.G. [1971] Flowing gas-solids suspensions, Chapman and Hall, London.

136. Neilson, J.H. and Gilchrist, A. [1968] An analytical and experimental investigation of the velocities of particles entrained by the gas flow in nozzles, J. Fluid Mech., 33, pp. 131-149.

137. Menguturk, M. and Sverdrup, E.F. [1979] Calculated tolerance of a large electric utility gas turbine to erosion damage by coal gas ash particles, Erosion: Prevention and Useful Applications, ASTM STP 664, W.F. Adler, Ed., American Society for Testing and Materials, pp. 193-224.

138. Rodi, W. [1982] Examples of turbulence models for incompressible flows, AIAA Jl., 20, pp.872-879.

139. Patel, V.C., Rodi, W. and Scheuerer, G. [1985] Turbulence models for near-wall and low Reynolds number flows: A Review, AIAA Jl, 23, pp. 1308-1219.

140. Kratina, P. and McMillian, J. [1982] Fly ash erosion in utility boilers-prediction and protection, Combustion Engineering Power Systems, Report No. TIS-7309. Presented at the Canadian Electrical Association Conference, Regina, Saskatchewan, October 26-28.

141. Reinhard, K.G. [1976] Turbine damage by solid particle erosion, Paper No. 76-JPGC-Pwr-15, IEEE-ASME Joint Power Generation Conference, Buffalo, New York, September 19-22

142. Field, J.E. (editor) [1979] Proc. 5th Int. Conf. on Erosion by liquid and solid impact, Cambridge, England.

143. Field, J.E. and Corney, N.S. (editors) [1983] Proc. 6th Int. Conf. on Erosion by liquid and solid impact, Cambridge, England.

144. Tabakoff, W. and Hussein, M.F. [1971] Effect of suspended solid particles on the properties in cascade flow, AIAA Journal, 9, pp. 1514-1519.

145. Tabakoff, W. and Hussein, M.F. [1971] Pressure distribution on blades in cascade nozzle for particulate flow, Journal of Aircraft, 8, pp. 736-738.

146. Tabakoff, W. Hosny, W. and Hamed, A. [1976] Effect of solid particles on turbine performance, J. Eng. for Power, 98, pp. 47-52.

147. Hussein, M.F. and Tabakoff, W. [1973] Dynamic behavior of solid particles suspended by polluted flow in a turbine stage, Journal of Aircraft, 10, pp. 434-440.

148. Hussein, M.F. and Tabakoff, W. [1974] Computation and plotting of solid particle flw in rotating cascades, Journal of Computers and Fluids, 2, pp. 1-15.

149. Grant, G. and Tabakoff, W. [1975] Erosion prediction in turbomachinery resulting from environmental solid particles, Journal of Aircraft, 12, pp. 471-478.

150. Hamed, A. [1982] Particle dynamics of inlet flow fields with swirling vanes, J. Aircraft, 19, pp. 707-712.

151. Katsanis, T. and McNally, W.D. [1977] Revised fortran program for calculating velocities and streamlines on the hub-shroud midchannel stream surface of an axial, radial or mixed flow turbomachine or annular duct: Vol. 1 and 2, NASA TN D8430, and NASA TN D8431.

152. Beacher, B., Tabakoff, W. and Hamed, A. [1982] Improved particle trajectory calculations through turbomachinery affected by coal ash particles, Journal of Engineering for Power, Trans. ASME, 104, pp. 64-68.

153. Hamed, A. and Fowler, S. [1983] Erosion pattern of twisted blades by particle laden flows, Journal of Engineering for Power, Trans. ASME, 105, pp. 839-843.

154. Wenglarz, R.A. and Menguturk, M. [1982] Use of cascade and small turbine tests to determine erosion of utility turbines, Journal of Engineering for Power, 104, pp. 58-63.

155. Wenglarz, R.A. [1983] Erosion potential resulting from particulate flow in a multi-stage turbomachine, Report No. 83-2E3-FACTA-P1, Westinghouse R+D Center, Pittsburgh, Pennsylvania.

156. Gunes, D. and Menguturk, M. [1983] Improved particle trajectory calculation around blade leading edge, Proc. 6th Int. Conf. on Erosion by Liquid and Solid Impact, Cambridge, England.

157. Humphrey, J.A.C. [1978] Numerical calculation of developing laminar flow in pipes of arbitrary curvature radius, Can. J. Chem. Eng., 56, p. 151.

158. Humphrey, J.A.C., Whitelaw, J.H. and Yee, G. [1981] Turbulent flow in a square duct with strong curvature, J. Fluid Mech., 103, pp. 443-463.

159. Chang, S.M., Humphrey, J.A.C. and Modavi, A. [1983] Turbulent flow in a strongly curved U-bend and downstream tangent of square cross-sections, Int. J. PhysicoChemical Hydrodynamics, 4, pp. 243-269.

160. Iacovides, H. and Launder, B.E. [1984] The computation of momentum and heat transport in turbulent flow around pipe bends, 1st U.K. National Heat Transfer Conference, Leeds, July (Inst. Chem. Engrs. Symposium Series 86).

161. Ghia, F.N., Mueller, T.J. and Patel, B.R. [1981] Computers in flow predictions and fluid dynamics experiments, ASME Winter Annual Meeting, Washington, D.C., November 15-20, Library of Congress Catalog Card Number 81-69010.

162. McNally, W.D. and Sockol, P.M. [1985] Review computational methods for internal flows with emphassis on turbomachinery, J. Fluids Eng., 107, pp. 6-22.

163. Menguturk, M. and Sverdrup, E.F. [1981] A theory for fine particle deposition in 2-D boundary layer flows and application to gas turbines. Paper No. 81-GT-54, Gas Turbine Conference and Products Show, March 9-12, Houston, Texas.

164. Menguturk, M., Gunes, D., Mimaroglu, H.K. and Sverdrup, E.F. [1983] Blade boundary layer effects on turbine erosion and deposition, Journal of Fluids Engineering, 105, pp. 270-276.

165. Mason, J.S. and Smith, B.V. [1972] The erosion of bends by pneumatically conveyed suspensions of abrasive particles, Powder Technology, 6, pp. 323-335.

166. Ulke, A. and Rouleau, W.T. [1976] The effects of secondary flows on turbine blade erosion, Paper No. 76-GT-74, Gas Turbine and Fluids Engineering Conference, New Orleans, LA, March 21-25.

167. Abdel Azim, A.F., Lasser, R. and Rouleau, W.T. [1982] Three-dimensional viscous particulate flow in a typical turboexpander, paper presented at the International Symposium on Modeling, Policy and Economics of Energy and Power Systems - Alternative Energy Sources and Technology (IASTED), Cambridge, Massachusetts, July 7-9.

168. Abdel Azim, A.F. and Rouleau, W.T. [1983] Secondary flow effect on erosion damage of stationary cascade, Proc. 6th Int. Conf. on Erosion by Liquid and Solid Impact, Cambridge, England.

169. El-Sayed, A.F. (Abdel Asim), Lasser, R. and Rouleau, W.T. [1986] Effects of secondary flow on particle motion and erosion in a stationary cascade, 7, pp. 146-154.

170. Young, J.P. and Ruff, A.W. [1977] Particle erosion measurements on metals, Journal of Engineering Materials and Technology, 99, pp. 121-125.

171. Wolak, J., Worm, P., Patterson, I. and Bodoia, J. [1976] Parameters affecting the velocity of particles in an abrasive jet, paper No. 76-WA/Mat-6, pp. 1-6, Jl. Eng. Materials and Tech., Trans. ASME.

172. Benchaita, M.T., Griffith, P. and Rabinowicz, E. [1983] Erosion of metallic plate by solid particles entrained in a liquid jet, Jl. Eng. Ind., 105 pp. 215-227.

173. Hashish, M. [1984] Cutting with abrasive waterjets, Mechanical Engineering Jl., March 1984, pp. 60-69.

174. Raask E. [1969] Tube erosion by ash impaction, Wear, 13., pp. 301-315.

175. Riley, J.J. and Patterson, G.S. [1974] Diffusion experiments with numerically integrated isotropic turbulence, Phys. Fluids, 83, p. 529.

176. McLaughlin, J.B. [1989] Aerosol particle deposition in numerically simulated channel flow, Phys. Fluids, A1, pp. 1211-1224.

177. Brauer, H. [1980] Report on investigations on particle movement in straight horizontal tubes, particle/wall collision and erosion of tubes and tube bends, Journal of Powder and Bulk Solids Technology, 4, pp. 3-12.

178. Hutchings, I.M., Macmillan, N.H. and Richerby, D.G. [1981] Further studies of the oblique impact of a hard sphere against a ductile solid, Int. J. Mech. Sci., 23, pp. 639-646.

179. Armstrong, J.D., Collings, N. and Shayler, P.J. [1984] Trajectory of particles rebounding off plane targets, AIAA JL., 22, pp. 214-218.

180. Tilly, G.P. [1973] A two stage mechanism of ductile erosion, Wear, 23, pp. 87-96.

181. Goodwin, J.E., Sage, W. and Tilly, G.P. [1969] Study of erosion by solid particles, Proc. Inst. Mech. Eng., 184, pt. 1, No. 15, pp. 279-292.

182. Chorin, A.J. [1973] Numerical study of slightly viscous flow, J. Fluid Mech., 57, pp. 785-796.

183. Schweitzer, M. and Humphrey, J.A.C. [1988] Note on the experiemtal measurement of particle flux to one and two in-line tubs, Wear, 126, pp. 211-218.

184. Rubinow, S.I. and Keller, J.B. [1961] The transverse force on a spinning sphere moving in a viscous fluid, J. Fluid Mech., 11, pp. 447-459.

185. Saffman, P.G. [1965] The lift on a small sphere in a slow shear flow, J. Fluid Mech., 22, pp. 385-400. (see also: Saffman, P.G. [1968] Correction, J. Fluid Mech., 31, p. 624.)

186. Lawler, M. and Lu, P.C. [1971] The role of lift in the radial migration of particles in pipe flow, Paper No. 3 in Advances in Solid-Liquid Flow in Pipes and Its Application, edited by I. Zandi, pp. 39-57, Pergamon Press, Oxford.

187. Poe, G.G. and Acrivos, A. [1975] Closed-streamline flows past rotating single cylinders and spheres-inertia effects, J. Fluid Mech., 72, pp. 605-623.

188. Tsuji, Y., Morikawa, Y., and Mizuno, O. [1985] Experimental measurement of the Magnus force on a rotating sphere at low Reynolds numbers, J. Fluids Eng., 107, pp. 484-488.

189. Schlichting, H. [1979] Boundary layer theory, McGraw-Hill Book Company, New York.

190. Reynolds, A.J. [1974] Turbulent flows in engineering, John Wiley and Sons, New York.

191. Dennis, S.C.R., Singh, S.N. and Ingham, D.B. [1980] The steady flow due to a rotating sphere at low and moderate Reynolds numbers, J. Fluid Mech., 101, pp. 257-279.

192. Schneider, P.J. [1983] Multiparticle erosion test facility, Proc. 6th Int. Conf. on Erosion by Liquid and Solid Impact, pp. 66-1 through 66-9, (J.E. Field and N.S. Corney, Eds.) Cambridge, England.

193. Finnie, I. and Kabil, Y.H. [1965] On the formation of surface ripples during erosion, Wear, 8, pp. 60-69.

194. Scattergood,R.O. and Routbort, J.L. [1981] Transient and synergetic effects erosion of silicon, J. Am. Ceram. Soc., 64:8, pp. C-104 to 106.

195. Gulden, M.E. [1980] Effect of number of impacts on erosion of polycrystalline MgF_2 in the elastic-plastic response regime, J. Am. Ceram. Soc., 63, [3-4], pp. 121-126.

196. Rickerby, D.G. and Macmillan, N.H. [1980] The erosion of aluminum by solid particle impingement at normal incidence, Wear, 60, pp. 369-382.

197. Bellman, R. and Levy, A. [1981] Erosion mechanism in ductile metals, Wear, 70, pp. 1-27.

198. Brown, R., Jun, E.J. and Edington, J.W. [1981] Erosion of α-Fe by spherical glass particles, Wear, 70, pp. 347-363.

199. Cantwell [1981] Organized motion in turbulent flow, Ann. Rev. Fluid Mech., 13, pp. 457-515.

200. Fernholz, H.-H. [1976] External flows, in Turbulence, (Ed. P. Bradshaw), Topics in Applied Physics, Vol. 12, pp. 45-107, Springer-Verlag .

201. Andrews, D.R. and Field, J.E. [1982] Temperature dependence of the impact response of copper: erosion by melting, J. Phys. D: Appl. Phys., 15, pp. 2357-2367.

202. Hammartsen, A., Soderberg, S. and Hogmark, S. [1983] Study of erosion mechanisms by recovery and analysis of wear fragments, Wear of Materials (Ed.) K.C. Ludema, Book No. H00254, American Society of Mechanical Engineers, New York.

203. Hutchings, I.M., Winters, R.E. and Fields, J.E. [1976] Solid particle erosion of metals - removal of surface material by spherical projectiles. Proc. Roy. Soc., A348, pp. 379-392.

204. Jennings, W.H., Head, W.J., and Manning, C.R. [1976] A mechanistic model for the prediction of ductile erosion, Wear, 40, pp. 93-112.

205. Smeltzer, C.E., Gulden, M.E. and Compton, W.A. [1970] Mechanisms of metal removal by impacting dust particles, J. of Basic Eng., Trans. ASME D, 92, pp. 639-654.

206. Shewmon, P.G. [1979] Mechanism of erosion of aluminum alloys, Paper No. 37, Proc. 5th Int. Conf. on Erosion by Liquid and Solid Impact, (Ed. J.E. Field), Cambridge, England.

207. Tilly, G.P. [1969] Erosion caused by airborne particles, Wear, 14, pp. 63-79.

208. Ganesan, P., Mehrotra, P.K. and Sargent, G.A. [1982] A microstructural study of the erosion/corrosion behavior of type 304 and 310 stainless steel, in Microstructural Science, (White, Richardson, McCall, Eds.), Vol. 10, pp. 91-102, Elsevier Science Publishing Co., Inc.

209. Hogmark, S., Hammarsten, A. and Soderberg, S. [1983] On the combined effects of corrosion and erosion, Proc. 6th Int. Conf. on Erosion by Liquid and Solid Impact, Cambridge, England.

210. Uhlig, H.H. [1971] Corrosion and corrosion control, John Wiley and Sons, Inc., New York.

211. Scully, J.C. [1975] The fundamentals of corrosion, Pergamon Press, Oxford.

212. Fontana, M.G. and Greene, N.D. [1978] Corrosion engineering, McGraw-Hill, New York.

213. Sedriks, A.J. [1979] Corrosion of stainless steels, John Wiley and Sons, Inc., New York.

214. Pini, G.C., Bachmann, E. and Orkenyl, j G. [1976] Errosion-corrosion tests at high velocity flows, Mater. Perf., 15, pp.37-38.

215. Zambelli, G. and Levy, A.V. [1981] Particulate erosion of NiO scales, Wear, 68, pp. 305-331.

216. Maasberg, J.A. and Levy, A.V. [1981] Erosion of elevated-temperature corrosion scales on metal, Wear, 73, pp. 355-370.

217. Levy, A.V. and Slamovich, E. [1984] Combined corrosion-erosion of steels in oxidizing environments, Report No. LBL-15657, Materials and Molecular Research Division, Lawrence Berkeley Laboratory, University of California, Berkeley.

218. Ives, L.K. [1977] Erosion of 310 stainless steel at 975·C in combustion gas atmospheres, J. Eng. Mater. Tech., April issue, pp. 126-132.

219. Ives, L.K., Yound, J.P. and Ruff, A.W. [1976] Particle erosion measurements on metals at elevated temperatures, 24th Meeting of the Mechanical Failures Prevention Group., April issue, pp. 145-158.

220. Ruff, A.W., Young, J.P. and Ives, L.K. [1976] Erosion measurements on metals at elevated temperatures, 2nd Int. Conf. on Mech. Behavior of Materials, August, pp. 1989-1993.

221. Kang, C.T., Chang, S.L., Birks, N. and Pettit, F.S. [1982] Erosion-corrosion of coatings and super alloys in high velocity hot gases, Proc. 3rd J.I.M. Int. Conf. on High Temp. Corrosion of Metals, Japan.

Numerical Calculation of Particle-Laden Gas Flows Past Tubes

A numerical study has been conducted for the flow of a dilute particle-laden gas moving past one or more tubes undergoing erosion. A nonorthogonal body-fitted coordinate system was used to calculate three tube configurations for laminar and turbulent flow regimes. The assumption of one-way coupling allows the calculation of individual particle velocities from the fluid flow field. The significant effects of turbulent velocity fluctuations are taken into account by means of the stochastic separated flow model. The particle flow field information is then used to predict circumferential distributions of particle flux and erosion. Predictions of trajectories for the case of two in-line tubes show that particles with inertia numbers $\lambda > 1$ will strike many tubes in a tube bank due to particle rebounding from tube surfaces. By contrast, particles with $\lambda < 1$ are entrained in the bulk flow between tubes. In general, the effect of increasing the particle-gas suspension temperature is to couple the particle-fluid motion more closely through viscous drag and, thus, to decrease erosion.

M. J. Schuh
C. A. Schuler
J. A. C. Humphrey
Department of Mechanical Engineering
University of California
Berkeley, CA 94720

Introduction

The problem of interest

The erosion of tubes in tube banks by particles suspended in gas flows is a major problem in the power industry. Such erosion is especially important in the reheaters and economizers of coal-fired boilers utilizing fluidized bed combustors. A survey of the literature on the subject, available in Schuh (1987), has uncovered a considerable amount of work on single-phase flow and heat transfer for single tubes, but less for the case of tube banks. In addition, much of what is available for tube banks tends to be semiempirical or qualitative in nature and often in the vein of correlations for predicting overall values of pressure drop and heat transfer. The level of corresponding information relating to particle-laden gas flows, especially the effects of fluid motion on particle motion and hence on tube erosion, is virtually nil.

The study reported here is part of a research effort aimed at measuring and rendering predictable the flow of dilute concentrations of solid spherical particles suspended in isothermal gas streams moving past one or two in-line tubes, or past a tube in a tube bank. The turbulent flow regime is of special interest for which, computationally, the condition of statistical stationarity is assumed. The three configurations of interest are shown in Figure 1. Experimental measurements of the circumferential distributions of particle flux for the one and two in-line tubes in the figure have been reported by Schweitzer and Humphrey (1988) who argue that particle flux, as opposed to erosion where material properties intervene, is a more fundamental quantity to determine experimentally for guiding and testing numerical models for predicting particle motion and surface erosion.

Related work

A review of work pertinent to this study, concerning flow past tubes and the numerical modeling of dilute particle-laden gas flows, has been given by Schuh (1987). A summary of his main findings is provided here.

Particle Tracking and Erosion. The prediction of erosion requires that individual particle speeds and trajectories be known. For this, a Lagrangian formulation of the particle equation of motion is necessary. In order to be able to neglect particle-particle interactions in such a formulation, the particle volume fraction of a solid-gas suspension must be less than approximately 0.001 (Pourahmadi and Humphrey, 1983). In such dilute suspensions, provided that the average particle size is

C. A. Schuh is presently with Astron Research and Engineering, 130 Kifer Court, Sunnyvale, CA 94086.
Correspondence concerning this paper should be addressed to J. A. C. Humphrey.

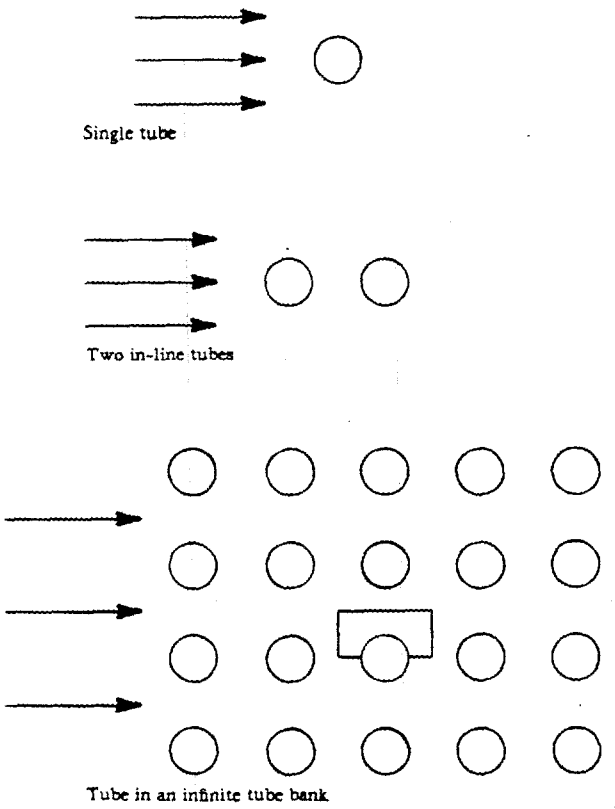

Figure 1. Three flow configurations.

several orders of magnitude smaller than the largest eddies in the flow, one-way (fluid to particle) coupling may be assumed.

Studies using a Lagrangian formulation approach include Laitone (1979a, b, c, 1983; Benchaita et al. 1983; Dosanjh and Humphrey, 1985; Vittal and Tabakoff, 1986; Shuen et al., 1983, 1985; Ormancey and Martinon, 1984). Laitone's work was crucial for demonstrating that fluid mechanic effects alone account for the 2.0–4.6 range in the exponent, m, of the free stream velocity, U, in the expression for erosion, E; $E \propto U^m$. Similarly, the study of Dosanjh and Humphrey established the importance of accounting for the turbulent nature of particle-laden erosive flows. In that study, the authors point to the need for performing erosive wear experiments under carefully controlled fluid mechanic conditions. In contrast to the deterministic approach used by Dosanjh and Humphrey to simulate particle-turbulence interactions, Shuen et al., and Ormancey and Martinon have developed respective approaches that account explicitly for random particle-eddy interactions. The present study builds upon the type of methodology developed by Shuen et al.

Numerical Calculation of Turbulent Flow Past Tubes. While this topic has been the subject of considerable research for the case of a single tube in a free stream, little work exists for the cases of two in-line tubes or a tube in a tube bank. Single tubes have been investigated by, for example, Celik et al. (1985) and Majumdar and Rodi (1985). The latter show that the assumption of a statistically stationary flow leads to inaccurate predictions in the wake region when the approaching flow is irrotational and transition to turbulence must occur in the boundary layer developing along the tube surface. Notwithstanding, highly refined grid predictions of mean flow quantities obtained with a two-equation model of turbulence, using either cylindrical polar coordinates or a streamline/potential grid, are in reasonable agreement with the data available. The laminar flow experiments of Taneda (1956), Grove et al. (1964), Acrivos et al. (1968), and Coutanceau and Bouard (1977), as well as the laminar flow calculations of Majumdar and Rodi, represent important test cases for present validation purposes.

Launder and Massey (1978), Antonopoulos (1979, 1985), Fujii et al. (1984), Chilukuri et al. (1987a, b), and Faghri and Rao (1987) have calculated tube bank flows. Except for Antonopoulos, all of these authors used Cartesian or overlapping Cartesian/cylindrical grids to resolve the flows. By contrast, using a two-equation model of turbulence, Antonopoulos (1979) calculated staggered contravariant velocity components on an orthogonal curvilinear grid. The laminar and turbulent flow calculations in Antonopoulos (1979), the laminar flow calculations in Fujii et al. (1984), the laminar flow measurements in Bergelin et al. (1952), and the turbulent flow measurements in Achenbach (1971) are important test cases for the present work. These are all in-line tube bank configurations.

While Schuh's (1987) review also includes work performed on two in-line tube configurations, all of the studies uncovered were of an experimental nature and none has been of sufficient consequence to this work to be reported here. Two extensive reviews of experimental work on flow and heat transfer for single tubes and tube banks have been written by Zukauskas (1972) and Zukauskas and Ziugzda (1985).

Outline of present approach

Following Thompson et al. (1985), we have chosen in this work to predict the flow past one or more tubes by solving finite difference approximations to the conservation equations on a numerically-generated body-fitted nonorthogonal curvilinear coordinate grid. This avoids the cumbersome use of overlapped orthogonal grids and the attendant interpolation practices required to transfer information between grids, as proposed in some of the references above. By using curvilinear coordinates, the ease of specifying boundary conditions (one of the reasons for employing overlapping grids) is retained. Finally, the use of control functions to specify grid line spacings and shapes allows an arbitrary degree of distributed grid refinement, so that any tube configuration of possible interest can be mapped and computed accurately.

For the turbulent flow calculations at high Reynolds number, a two-equation ($k - \epsilon$) model was used. In this model, a logarithmic wall function for velocity is employed to approximate the wall layer. A generalization of the Boussinesq assumption fixes the dependence of the stress on the rate of strain via an isotropic turbulent viscosity. In contrast to the work of Majumdar and Rodi (1985), here the flow approaching the tube(s) is turbulent. This obviates the need to predict transition to turbulence on the tube surface. Implicit is the assumption of a statistically stationary flow and, while this is incorrect for one or two in-line tubes in a free stream, it is not an unreasonable supposition for the case of a tube in an infinite tube bank. In any event, the assumption is necessary if a practical numerical simulation of the problem is to be achieved.

A Lagrangian-formulated deterministic particle equation of motion is solved via an advanced Runge-Kutta method to pre-

dict particle speeds and trajectories once the fluid flow field is known. The effects of turbulence on particle dispersion are included by superposing a random distribution of turbulent eddies upon the calculated mean flow field, as in Shuen et al. By tracking a statistically significant number of particles, released at different initial locations, overall pictures of particle flow fields, surface fluxes and erosion are obtained. The gas-solid suspensions investigated are assumed to be in thermal equilibrium. Because particle response time to a change in fluid motion depends on viscosity, calculations of the particle flow fields for different values of a prescribed fluid viscosity correspond to fluid flow fields evaluated at *different but uniform* temperatures. Upon striking a tube surface, a particle is forced to rebound according to prescribed restitution relations. Particle fragmentation and/or particle rotation are not considered. The restitution relations employed are the simplest that will provide qualitative pictures of real phenomena.

Fluid-Phase Numerical Procedure

This section summarizes the main features of the numerical procedure developed to calculate the fluid phase flow field. By necessity it is brief. A detailed exposition of this and related material is available in Schuh (1987).

Grid generation

To generate nonorthogonal curvilinear coordinate grids, we have followed closely the work by Thompson et al. (1985, 1986, 1987) and the references therein. Coordinate line generation can be accomplished by a variety of procedures including algebraic, elliptic, graphical and hyperbolic generation methods. The elliptic method was chosen for this work because of its ability to produce grids in a reasonable amount of time with controllable line and point distributions on the geometry of interest. In this method, the following Poisson equations can be solved for the coordinate lines ζ and η in a two-dimensional physical domain

$$\nabla^2\zeta = \frac{g_{22}}{g} P \tag{1}$$

$$\nabla^2\eta = \frac{g_{11}}{g} Q \tag{2}$$

However, it is computationally advantageous to solve for x and y, the cartesian coordinates, for fixed values of ζ and η with the following equation

$$g_{22}(r_{\xi\xi} + Pr_\xi) + g_{11}(r_{\eta\eta} + Qr_\eta) - 2g_{12}r_{\xi\eta} = 0 \tag{3}$$

in the transformed or computational domain. The control functions (source terms P and Q in Eqs. 1–3) are used to control the spacing of the ζ and η coordinate lines, respectively. Two methods were used to control the spacing in this work. The first attracts lines to a point or a line by using equations for P and Q wherein the magnitude of the attraction (or repulsion) and the rate at which it is damped can be separately prescribed. The second method involves derivative line spacing control functions, which are used to maintain the same spacings between coordinate lines in the interior of the calculation domain as the spacings imposed on the boundaries of the domain. Of the two, the derivative line spacing approach was the preferred method in this work. For some of the turbulent flow calculations requiring grid points very near a tube surface, a combination of the two methods was necessary in order to obtain an acceptable distribution of points in front and behind the tube.

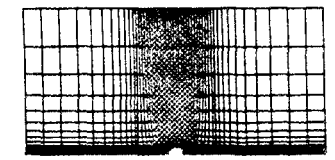

Single tube

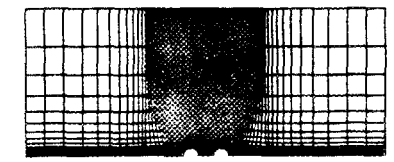

Two in-line tubes

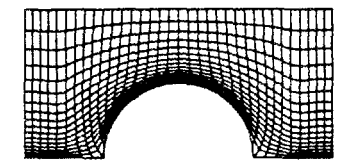

Tube in an infinite tube bank

Figure 2. Examples of curvilinear coordinate grids used for the three flow configurations.

Grids are generated in three steps.

- First, a point distribution is chosen on the boundary.
- Then, the interior of the grid is generated by solving Eq. 3.
- Finally, ends are added with the aid of cubic spline interpolation (Press et al., 1986).

The ends are made up of two rectangular cells and an interpolated region between the three points on the end of the interior grid. This procedure is fast and straightforward, while providing orthogonal boundaries which eases the implementation of the outflow and periodic boundary conditions. Figure 2 shows examples of the grids used in this work.

Transport equations and boundary conditions

For steady, two-dimensional, incompressible, constant property, turbulent flow the modeled transport equations written in a conservative form relative to an arbitrary curvilinear coordinate system are:

Continuity of mass

$$(\sqrt{g}\rho U^i)_{\xi^i} = 0 \tag{4}$$

u momentum

$$[\sqrt{g}(\rho U^i u - \mu_e g^{ij} u_{\xi^j})]_{\xi^i} + (y_{\xi^2}P)_{\xi^1} - (y_{\xi^1}P)_{\xi^2} = 0 \tag{5}$$

v momentum

$$[\sqrt{g}(\rho U^i v - \mu_e g^{ij} v_{\xi^j})]_{\xi^i} - (x_{\xi^2}P)_{\xi^1} + (x_{\xi^1}P)_{\xi^2} = 0 \tag{6}$$

Turbulent kinetic energy, k

$$\left[\sqrt{g}\left(\rho U^i k - \frac{\mu_e}{\sigma_k} g^{ij} k_{\xi^j}\right)\right]_{\xi^i} - \sqrt{g}G + \sqrt{g}C_D\rho\epsilon = 0 \qquad (7)$$

Dissipation of turbulent kinetic energy, ϵ

$$\left[\sqrt{g}\left(\rho U^i \epsilon - \frac{\mu_e}{\sigma_\epsilon} g^{ij} \epsilon_{\xi^j}\right)\right]_{\xi^i} - \sqrt{g}C_1 \frac{\epsilon}{k} G + \sqrt{g}C_2\rho \frac{\epsilon^2}{k} = 0 \qquad (8)$$

Generation of turbulent kinetic energy, G

$$G = \mu_t u^i_{x^j}(u^i_{x^j} + u^j_{x^i})$$
$$u^i_{x^j} = \frac{1}{\sqrt{g}}[(y_{\xi^2} u^i)_{\xi^1} - (y_{\xi^1} u^i)_{\xi^2}]$$
$$u^j_{x^i} = \frac{1}{\sqrt{g}}[-(x_{\xi^2} u^i)_{\xi^1} + (x_{\xi^1} u^i)_{\xi^2}] \qquad (9)$$

where

$$x^1 = x \quad \text{and} \quad x^2 = y$$
$$\xi^1 = \zeta \quad \text{and} \quad \xi^2 = \eta$$
$$U^i = a^i \cdot (u\hat{i} + v\hat{j})$$
$$a^i = \nabla \xi^i$$
$$g^{ij} = a^i \cdot a^j \qquad (10)$$

Here the two-equation ($k - \epsilon$) model of turbulence of Launder and Spalding (1974) has been used; see also Rodi (1982, 1984). In this model:

μ_e is the effective viscosity

$$\mu_e = \mu + \mu_t \qquad (11)$$

μ_t is the turbulent viscosity

$$\mu_t = C_\mu \rho \frac{k^2}{\epsilon} \qquad (12)$$

and the following are empirically determined (or numerically optimized) constants from Rodi (1984):

$$\sigma_k = 1 \quad C_\mu = 0.09 \quad C_1 = 1.44 \quad C_2 = 1.92 \quad C_D = 1$$
$$\sigma_\epsilon = \frac{\kappa^2}{(C_2 - C_1)\sqrt{C_\mu}} \quad \text{and} \quad \kappa = 0.40 \qquad (13)$$

The boundary conditions for the flow fields are shown in Figure 3. For the single tube or the two in-line tubes, u, v, k, and ϵ values are prescribed at the inlet boundary and the flow is assumed to be fully developed at the outlet boundary. The top and bottom boundaries of the solution domain (except for the tube surface) are taken as symmetry planes. On the tube surface, the fluid velocity is zero. For turbulent flow calculations, the equilibrium approximation is used to fix boundary conditions for k and ϵ in the region between the tube surface and the first grid node adjacent to it (Launder and Spalding, 1974).

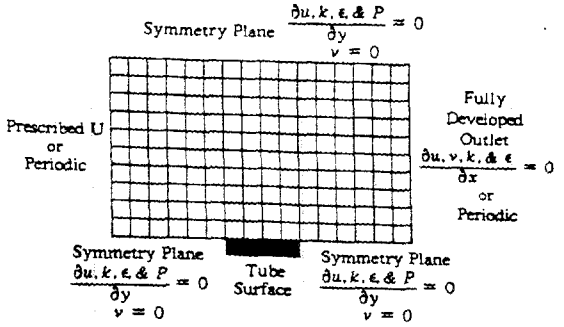

Figure 3. Boundary conditions for the flow field.

In the laminar flow calculations, only the continuity, u momentum, and v momentum equations are solved with the viscosity set to the molecular viscosity, $\mu_e = \mu$. For all cases, the boundary conditions are implemented by using source terms, modification of the convection and diffusion derivatives, or other changes. The velocities, k, and ϵ are prescribed on the inlet plane for the single tube and in-line pair of tubes, so their respective equations are not solved on this plane. However, the pressure is required on the inlet plane (it is used in the pressure derivatives in the momentum equations on the second plane) so the continuity equation is solved to determine the pressure on the inlet plane. (The solution method for the pressure field is discussed in a separate section.) The outlet boundary condition of fully developed flow is implemented by not solving the momentum equations at the exit plane, but by setting the values of the velocities at the exit plane equal to those at the plane directly upstream, and then adjusting these velocities to ensure that continuity of mass is preserved. (In the code, this is implemented by using a grid that is Cartesian for the last three planes and copying the u and v velocities from the plane before the outlet to the outlet plane.) The conservation of mass at the exit plane is assured by correcting the u velocity profile on this plane. For fully developed turbulent flow, the k and ϵ values are also copied from the plane directly upstream of the exit to the exit plane without modification. Like the first plane, the pressure is required on the exit plane so the continuity equation is also solved on the exit plane. The v velocity on the top and bottom symmetry planes and on the tube surface is zero. Therefore the v-momentum equation is not solved on the top and bottom planes. The p, u, k, and ϵ equations are solved on the top and bottom symmetry planes. A very detailed description concerning the practical implementation of these boundary conditions in finite difference form is available in Schuh (1987).

Finite difference approximation

The u, v, k, and ϵ equations can be written in identical form according to

$$[\sqrt{g}(\rho U^i \phi - \Gamma g^{ij} \phi_{\xi^j})]_{\xi^i} - b = 0 \qquad (14)$$

where ϕ is an arbitrary variable, thus admitting a common solution procedure. The equivalent finite difference form of this general equation is readily obtained by a cell or volume integration following the rules and guidelines in Patankar (1980). The

result is

$$A_P\phi_P = A_N\phi_N + A_S\phi_S + A_E\phi_E + A_W\phi_W + S_u \qquad (15)$$

where subscripts N, S, E, and W denote the grid points adjacent to P. The upwind-central differencing scheme discussed by Patankar (1980) was used to derive the convection-diffusion A terms in Eq. 15 for the nonstaggered grid used in this work. (The grid used here will be detailed further later.) Detailed expressions for these terms and for linearized forms of the source terms, S_u, are given in Schuh (1987).

The application of Eq. 15 to each variable at each point on the calculation grid yields a set of equations that are solved iteratively. This is accomplished by repeated applications of the tridiagonal matrix algorithm in its standard form (Patankar, 1980) for single and two in-line tubes, and in its cyclic form (Patankar et al., 1977) for the case of a tube in an infinite tube bank.

Treatment of pressure

The calculation of pressure proceeds along the lines of the SIMPLE algorithm of Patankar (1980) by making pressure corrections from iteration to iteration, until the velocities calculated in conjunction with the corrected pressure field satisfy the momentum and continuity equations simultaneously. There are, however, two important differences:

1) A central difference scheme is used for the pressure derivatives in the momentum equations in both the present work and in Patankar's work. This scheme has a $2\Delta\xi^i$ dependence on the type of nonstaggered grid used here, while it has a $\Delta\xi^i$ dependence on a staggered grid. A $2\Delta\xi^i$ dependence results in a pressure oscillation when velocities are averaged to obtain the flux into the control volume used in the pressure calculation. (It is exactly this problem that the staggered grid was created to solve. The staggered grid does not require averages of the velocities to obtain the fluxes into the control volume used in the pressure calculation.) To obviate velocity averaging at the control volume walls, a localized solution of the momentum equation is calculated at each control volume wall. The localized solution of the momentum equation has a $\Delta\xi^i$ dependence in the direction of the two nodes normal to the control volume wall (this is the wall that the flow passes into or out of the control volume) and a $2\Delta\xi^i$ dependence in the tangential direction. The use of the localized solution of the momentum equation eliminates any pressure oscillations in the solution.

2) Pressure corrections of the velocities, as performed by Patankar (1980), are dispensed with, since they do not improve the convergence rate enough to offset the added cost of computing them.

Solution algorithm

The overall solution algorithm is iterative in nature and performs the following steps:

1) Guess an initial velocity and pressure flow field. For this, use a flow field from a previous solution or set all the variables equal to the inlet values except for the tube surface where u and v are set to zero.

2) Calculate a new u velocity field.

3) Calculate a new v velocity field using the same A_N, A_S, A_E, A_W, S_P, and C_P values from the u velocity iteration. (The use of the same coefficients is allowed by virtue of the uniform nature of the grid in the transformed $\zeta - \eta$ plane.)

4) Calculate the pressure correction and obtain the new pressure field.

5) If the flow is turbulent, calculate new k and ϵ fields and update the viscosity field.

6) If the calculation has not converged, go to step 2.

Convergence is checked by monitoring the sum of the residuals for each variable over the entire calculation grid. The numerical solution is taken as converged when the largest of the residual error sums is less than 5.0×10^{-4}.

Miscellaneous matters

Location of Variables. The use of a curvilinear grid requires that all the dependent variables be calculated and stored at the intersection of grid lines (the nodes) rather than at staggered (between nodes) grid locations as in Patankar (1980). (This requires the special treatment of pressure described earlier.)

Underrelaxation. All variables are underrelaxed by factors ranging between 0.3 and 0.8 to stabilize and accelerate the calculations.

Localized Solution of the Momentum Equations. The localized solution of the momentum equations is calculated for u and v at two locations relative to each grid point. The location between neighboring points on the ξ^i grid lines is referred to as the u location and the location between neighboring points on

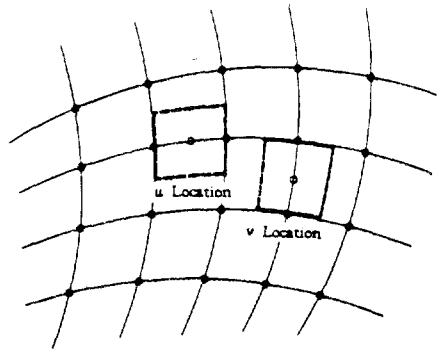

Control volumes for linearized momentum equations

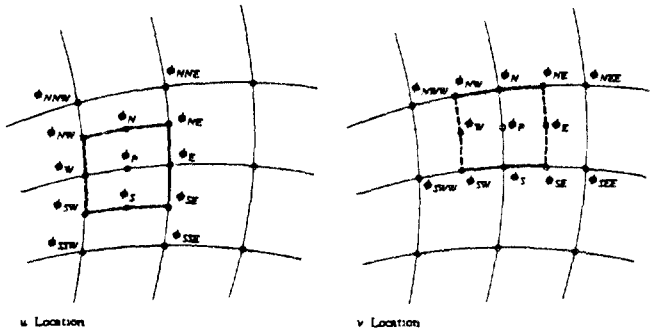

Location of ϕ values on the u location control volume. Location of ϕ values on the v location control volume.

Figure 4. Control volumes used for the localized solution of the momentum equations.

the ξ^2 grid lines is referred to as the v location. These are shown in Figure 4 along with their respective control volumes. This nomenclature of u and v locations is similar to that used in staggered grid configurations. The u and v velocities are calculated at both of these locations by the substitution in Eq. 15 of coefficients derived from flow quantities at the neighboring grid points only. The grid points are indicated for the two control volumes shown in Figures 4b and 4c. The calculated u and v velocities at these locations are referred to as *localized* because they are calculated by using the flow field values from the neighboring points only while the u and v velocities at the intersection of the grid lines are calculated by using an equation solver that includes the global effect of the flow field. Further details are available in Schuh (1987).

Pressure at the Tube Surface. The pressure calculation procedure used in this work results in a slight skewness in the isobars at the tube surface. This is not a serious limitation because as the grid is refined the skewness decreases.

Algorithm Performance. All of the calculations were run on a Digital Equipment Corporation Micro VAX II with 6 Megabytes of memory and a floating point accelerator running Ultrix version 2. The memory requirements for a 119 × 50 grid are 109,568 bytes for the text segment, 18,432 bytes for the initialized data, and 2,885,528 bytes for the uninitialized data. This gives a total memory requirement of 2.87 Megabytes or 506 bytes per grid node. The code uses double precision with 8 bytes per storage location on the Micro VAX II which results in 63 storage locations per grid point. Typical values of convergence time and number of iterations for laminar and turbulent flow are given in Table 1.

Grid Limitations. The grid generation procedure used in this work has difficulty generating grids that change smoothly on the symmetry plane ahead of and behind a tube in the tube bank with spacings less than 1.5 tube diameters. The problem is only serious in a small region for the turbulent flow regime, where jagged mean flow streamlines can result.

Table 1. Characteristics of Algorithm Performance on a Micro Vax II for Maximum Residual Error of 5.0×10^{-4}

Case	CPU Hours	Numerical Iterations	Grid
Laminar Flow*			
Single Tube (Re = 40)	17.8	1,080	119 × 38
Laminar Flow**			
Tube Bank (L/D) = 2, Re = 100)	34.4	3,699	61 × 40
Turbulent Flow†			
Single Tube ($Re = 2.94 \times 10^4$)	28.7	2,026	91 × 28
Turbulent Flow‡			
Tube Bank (L/D) = 2, $Re = 2.56 \times 10^4$)	12.2	1,511	55 × 25

*Calculation initialized by setting the velocity at all grid points to the inlet value and pressure to zero.

**Calculation initialized by setting the velocity at all grid points to one half the average velocity at the minimum cross section and pressure to zero.

†Calculation initialized by setting all variables at all nodes to the inlet values except pressure which was set to zero.

‡As in ** above, but with good estimates of the values for k and ϵ.

Particle-Phase Numerical Procedure

Equation of motion

The following equations are used to describe the motion of an arbitrarily accelerated particle in the fluid flow field

$$\frac{dr_{pt}}{dt} = U_{pt} \tag{16}$$

$$m_{pt}\frac{dU_{pt}}{dt} = m_{pt}g + C_{Dr}\,\tfrac{1}{2}\,\rho|U - U_{pt}|(U - U_{pt})A_{pt} \tag{17}$$

The second equation is the result of a force balance in which, due to the large value of the ratio ρ_{pt}/ρ (2.25×10^3 for glass particles in air), acceleration-dependent drag terms (the added mass and Basset history integral terms) and the lift forces (such as the Magnus and Saffman forces) are negligible. Also small are the pressure gradient forces omitted in the equation. Thus, gravity and drag are the only forces determining the motion of the particle. Equation (17) is taken from Clift et al. [1978], where it is shown that the terms neglected are indeed small compared to those retained. Furthermore, Equation (17) is only valid for non-interacting particles.

It is assumed that the particles are spherical for which, in the creeping flow regime, Stoke's formula for the drag coefficient may be used:

$$C_{Dr} = \frac{24}{Re_{pt}} \tag{18}$$

Since this formula is only valid when the particle Reynolds number, Re_{pt}, is much less than unity, an empirically determined correction factor f is employed when $Re_{pt} \geq 0(1)$. In this work, the following correction factor f given by Boothroyd (1971) was used

$$f = \begin{cases} 1 + 0.15\,Re_{pt}^{0.687} & 0 < Re_{pt} \leq 200 \\ 0.914\,Re_{pt}^{0.282} + 0.0135\,Re_{pt} & 200 < Re_{pt} \leq 2{,}500 \\ 0.0167\,Re_{pt} & 2{,}500 < Re_{pt} \end{cases} \tag{19}$$

Introducing m_{pt} and A_{pt} as defined in the Notation, Eq. 17 is rewritten as

$$\frac{dU_{pt}}{dt} = g + \frac{f}{\tau}(U - U_{pt}) \tag{20}$$

where τ is the particle response time. It is convenient to define a non-dimensional particle response time, or momentum equilibration constant λ, according to:

$$\lambda = \frac{\tau U_{ref}}{L_{ref}} \tag{21}$$

where L_{ref} and U_{ref} are a characteristic length and velocity of the flow field respectively. The quantity λ is the ratio between a time-scale characteristic of the mean particle motion and a time-scale characteristic of the mean fluid flow.

Solution algorithm and boundary conditions

The fourth-order adaptive step size Runge-Kutta scheme in Press et al. (1986) was used to solve Eqs. 16 and 17 subject to the specifications of initial particle location and velocity.

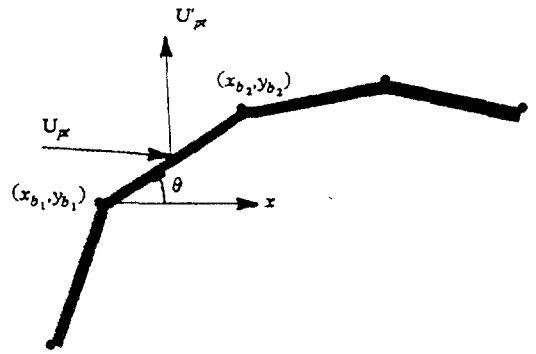

Figure 5. A particle impacting and rebounding from the tube as defined by a series of straight lines.

Special care is required when the particle approaches the tube surface or any other boundary. Figure 5 shows a sketch of a particle impacting and rebounding from the surface of a tube which is defined by a series of straight lines on the curvilinear grid. Because the solution scheme is parabolic in time, a trial and error scheme was implemented to determine the instant and position of impact. For this, a small region around the tube of thickness δ_b is defined. When the particle first approaches the surface, the solution algorithm is unaware of its presence and forces the particle to cross the surface. When this happens, the particle is returned to its previous position, the step size is decreased by a factor of 2, and computation is retried. This procedure is repeated until the particle falls into the δ_b region previously defined. Assuming that the particle velocity remains constant within δ_b, Euler's method is used to determine the position and time of particle impaction (this reduces to finding the intersection of two straight lines). Finally, the velocity of the rebounding particle is calculated assuming constant restitution coefficients for the normal and tangential components of the velocity. Referring to Figure 5, the rebound velocity, U'_{pt}, is calculated by first determining the normal (w_n) and tangential (w_t) velocity components at the boundary from the following equations

$$w_t = u_{pt} \cos\theta + v_{pt} \sin\theta$$
$$w_n = -u_{pt} \sin\theta + v_{pt} \cos\theta \qquad (22)$$

The rebound velocity components normal and tangential to the wall are then calculated using the appropriate restitution coefficients e_t and e_n according to

$$w'_t = e_t w_t$$
$$w'_n = e_n w_n \qquad (23)$$

Finally, the rebound velocity components in the original coordinate system are computed according to

$$u'_{pt} = w'_t \cos\theta - w'_n \sin\theta$$
$$v'_{pt} = w'_t \sin\theta - w'_n \cos\theta \qquad (24)$$

Both restitution coefficients are set to unity at symmetry planes, thus simulating a new particle entering the calculation domain from the opposite direction.

When the particle is very small ($\lambda < 1$), it may rebound from the wall several times. In this case, δ_b must be very small and a very small calculation time step must be used. In this work, δ_b was set to $0.005D$.

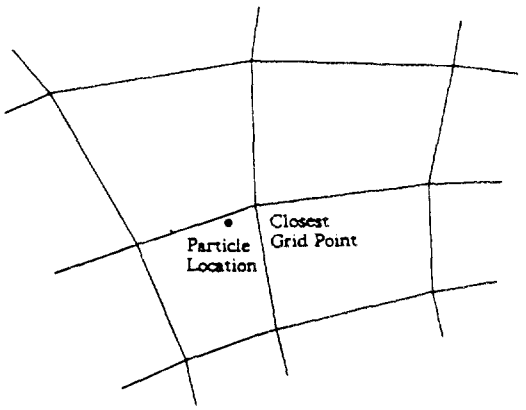

Figure 6a. Particle location and the nearest grid point on a curvilinear grid.

Interpolation of properties on a curvilinear grid

The fluid velocity along the trajectory of a particle must be found by interpolation. Special care is required since the grid used for calculating the velocity field is nonorthogonal. In the present study, an algorithm embodying the following steps was used:

1) Find the grid point closest to the current particle location. (This is called the search step.)

2) Find the cell in which the particle is located, Figure 6a.

3) Divide the cell found in step 2 into four triangles by defining point $c(x_c, y_c)$ in Figure 6b as

$$x_c = \tfrac{1}{4}(x_q + x_r + x_s + x_t) \quad \text{and} \quad y_c = \tfrac{1}{4}(y_q + y_r + y_s + y_t)$$

and then find the triangle in which the particle is located. (Triangle $a - b - c - a$ in Figure 6b.)

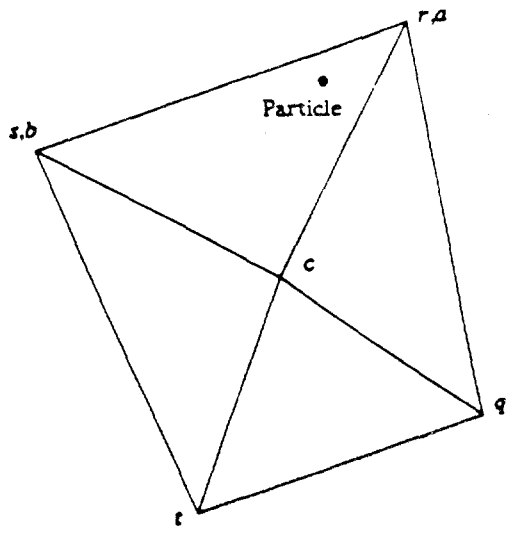

Figure 6b. Division of the grid cell containing the particle into four triangles and the center point $c(x_c, y_c)$.

4) Assume that properties at the center of the grid (point c in Figure 6b) are the mean of the values at the corners of the cell. Linearly interpolate for properties at the particle location using the values at the corners of the triangle $a - b - c - a$ as shown in Figure 6b.)

This procedure ensures continuity of the interpolated properties from cell to cell. It has also proven to be fast to execute numerically. The details of this searching algorithm are given in Schuh (1987).

Influence of turbulent fluctuations

The effect of turbulence on particle dispersion may be neglected when the characteristic particle response time is large compared to the characteristic time of the turbulent fluctuations, i.e., when

$$\tau \gg t_{EDDY} \tag{25}$$

If we assume that the time scale of the turbulent fluctuations is commensurate with the time scale of the mean flow, that is,

$$\frac{L_t}{u'} \approx \frac{L_{ref}}{U_{ref}} \tag{26}$$

we find that Eq. 25 is equivalent to

$$\lambda \gg 1 \tag{27}$$

In order to account for the effects of relative slip velocity fluctuations and turbulent dispersion when the particle response time is comparable to the time scale of the turbulent fluctuations, i.e., when $\lambda \approx 1$, a stochastic separated flow model (SSF) was used. This model requires an estimate of the mean turbulent characteristics of the flow, which can be obtained anywhere in the flow from the field calculations by extending the interpolation procedure described above to include the kinetic energy, k, and its rate of dissipation, ϵ. Particle trajectories are then computed by solving the instantaneous momentum equations (Eqs. 16 and 17), and superposing random velocity fluctuations on the mean flow field to simulate instantaneous properties of the continuous phase.

The influence of turbulent fluid phase fluctuations on particle trajectories is accounted for through random particle-eddy encounters. However, it should be emphasized that the actual particle motion within an eddy is modeled *deterministically*, as described by the instantaneous momentum equation for the particle. For this, the velocity fluctuations are taken as constant during a particle-eddy interaction.

The key element of the SSF model is to specify eddy properties and particle-eddy interaction times in terms of the mean flow field characteristics. The present approach is along the lines of the work by Shuen et al. (1983). The characteristic velocity fluctuations and lifetime associated with each eddy are found at the start of the particle-eddy interaction. The former are obtained by making a random selection from a probability density function for velocity. For simplicity, the velocity fluctuations are assumed to be isotropic, with a Gaussian PDF having a standard deviation equal to $\sqrt{(2/3)k}$. However, at any instant the x and y velocity components are not necessarily equal.

A particle is assumed to interact with an eddy for a time which is the minimum of either the eddy lifetime or the time required for the particle to cross the eddy. These times are estimated by assuming that the characteristic size of an eddy size is equal to the dissipation length scale,

$$L_t = \frac{C_\mu^{3/4} k^{3/2}}{\epsilon} \tag{28}$$

with a lifetime given by

$$t_{EDDY} = \frac{L_t}{u'} = \frac{L_t}{\sqrt{\frac{2}{3}k}} \tag{29}$$

Due to the stochastic nature of the procedure, many particles have to be simulated in order to obtain an acceptable representation of the average particle flux distribution over the tubes. In the present work, 40 particle trajectories were calculated per each of 100 starting locations uniformly distributed over the inlet plane of the calculation domain, for a total of 4,000 particle trajectories.

Results and Discussion

Test cases

Excellent agreement was found between measurements and calculations of the fluid phase for all the laminar flow cases investigated. For a single tube, these include comparisons of: the width and length of the recirculation zone behind a tube as visualized by Taneda (1956) for $Re = 26$ and 40, and computed by Majumdar and Rodi (1985) for $Re = 40$; the centerline velocity downstream of the tube as measured by Coutanceau and Bouard (1977) for $Re = 40$; the pressure distribution on the tube wall as measured by Grove et al. (1964) for $Re = 40$; the shear stress on the tube wall as measured by Acrivos et al. (1968) for $64 \leq Re \leq 150$. For a tube in a tube bank these include comparisons of the flow streamlines for $Re = 10$ and 100 $[(L/D) = 2.0]$; the flow streamlines and pressure profiles for

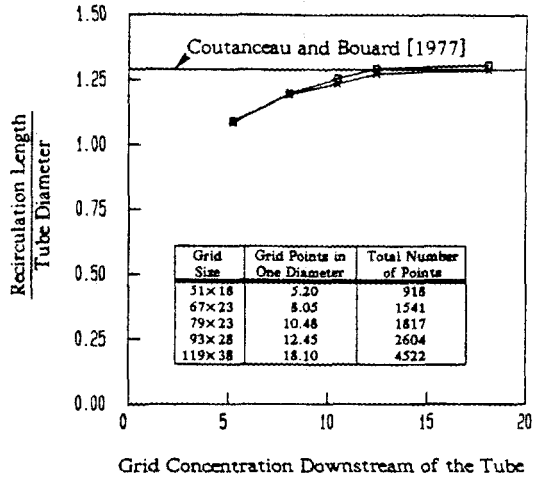

Figure 7. Effect of grid refinement on the recirculation length for $Re = 26$.

Grids used are generated with derivative line spacing with curvature terms only (□) and derivative line spacing with both curvature and spacing terms (×).

Re = 120 [(L/D) = 1.5]; the coefficient of drag as a function of Re for different L/D.

These comparisons, discussed in detail by Schuh (1987), were important for establishing the effects of grid refinement on numerical accuracy for flows free of turbulence model uncertainties. Figure 7 is an example of the type of exercises conducted for single tubes and a tube in a tube bank to generate grid-independent numerical results.

For turbulent fluid motion, comparisons were made with: the channel flow velocity measurements of Laufer (1950) at Re = 61,600; the tube bank calculations of streamlines and turbulent kinetic energy of Antonopoulos (1979) for $Re = 10^6$ [(L/D) = 2] and $Re = 10^5$ [(L_t/D) = 2.06 and (L_t/D) = 1.38]; the surface pressure and shear stress distributions measured for a tube in a tube bank by Achenbach (1971) for $Re = 4 \times 10^5$ (L_t/D) = 2.0 and (L_l/D) = 1.4]; the coefficient of drag as a function of Re for a tube bank with (L/D) = 2.0 as correlated by Zukauskas (1972) and computed by Antonopoulos (1979). For the reasons stated in the Introduction, no attempts were made to predict flows involving transition to turbulence on the tube surface.

The agreement with Laufer's data and that of Antonopoulos at $Re = 10^6$ was quite good. Discrepancies between present calculations and Antonopoulos' results at $Re = 10^5$ were traced to the effects of grid nonorthogonality on numerical diffusion. Thus, we found that by neglecting terms in the turbulence model that account for grid skewness, better agreement could be obtained with Antonopoulos' results. We note that Antonopoulos' method requires an orthogonal grid and provides no means for accounting for nonorthogonality if and when this arises in the *practical implementation* of the code.

The comparisons conducted with respect to Achenbach's pressure data are shown in Figures 8a and 8b. We consider these results to be good indicators of the ability of the code to resolve turbulent flows in tube banks. Grids more refined than 75 x 28 did not yield results better than those shown. The largest discrepancies between measurements and calculations of pressure arise toward the front and rear of the tube, where the assumed law-of-the-wall relation least applies. (This was expected and is a well known failing of the present turbulence model. Notwithstanding, all the qualitative features of the experimental curves are well-represented by the numerical results.) The lack of agreement in pressure suggests that the predicted velocity fields in these regions will also be in error but by a smaller amount proportional to the square root of pressure. This will result in overpredicted velocity magnitudes in the stagnation region and underpredicted values in the wake, which will modify particle trajectories in these regions accordingly.

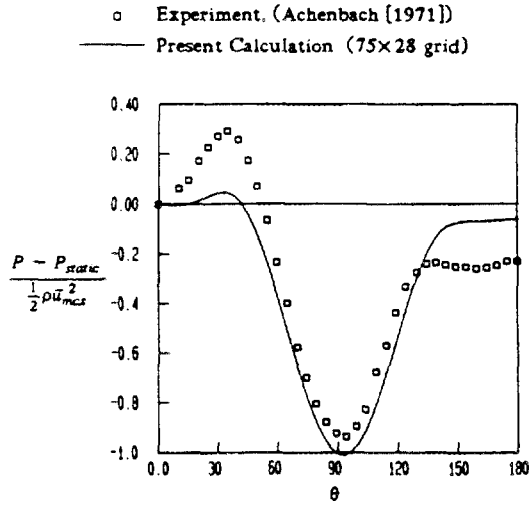

Figure 8a. Pressure distribution on a tube surface for $Re = 4 \times 10^5$, (L_t/D) = 2.0, and (L_l/D) = 1.4 calculation.

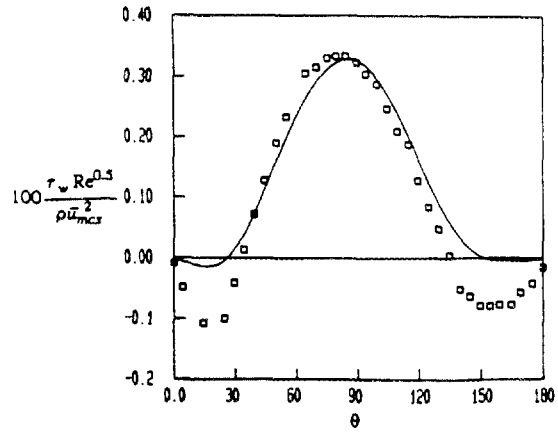

Figure 8b. Shear stress distribution of a tube surface for $Re = 4 \times 10^5$, (L_t/D) = 2.0, and (L_l/D) = 1.4 calculation.

The particle tracking capabilities of the numerical procedure were checked against the analytical results provided by Laitone (1983) for the case of stagnation point flow. Figure 9 shows the very good agreement obtained for three different values of λ. For $\lambda \leq 0.25$ a particle never reaches the surface. For the case λ = 0.5 we have allowed the particle to rebound with values of e_t = 1.0 and e_n = 1.0 set for the restitution coefficients in Eq. 23.

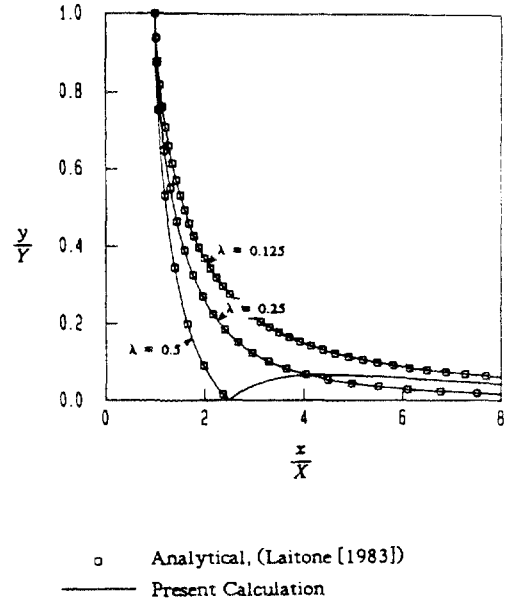

Figure 9. Comparison of calculated particle paths with the analytical solution from Laitone (1983) for stagnation point flow.

Turbulent flow past one and two in-lines tubes

Figure 10 shows the results predicted using the procedure described above, for the flow of air past two in-line tubes. The calculation conditions correspond to those of the particle flux experiments of Schweitzer and Humphrey (1988); $Re = 2.94 \times 10^4$, $(L_t/D) = 4.1$, and $(L_t/D) = 5.0$ with $(k/U_\infty^2) = 0.021$ and $(\epsilon\mu/U_\infty^2) = 7.28 \times 10^{-5}$ at the inlet, $T = 300$ K, $P = 101.3$ kPa. A grid consisting of 117×28 nodes was used. More refined grids did not yield significantly different results. Particle trajectories were simulated using these flow field results for $\lambda = 0.1$, 0.5, 1.0, and 10.0 both neglecting and considering the effect of turbulent velocity fluctuations. These values of λ correspond to glass beads, $\rho_{pt} = 2500$ kg/m^3, of 4.09, 9.15, 12.9, and 40.9 μm in diameter. The results obtained neglecting the effect of the fluctuations are discussed

Figure 11 shows predicted trajectories for particles unaffected by turbulence for different values of λ, corresponding to the flow illustrated in Figure 10. Gravity acts to the right in the figures (in the direction of the flow). The particles were released at the entrance to the calculation domain (not shown in the figure) in increments of $0.1D$ above the bottom symmetry plane with velocities $u_{pt} = u_\infty$. The first particle was released at a slight distance from the symmetry plane so that it would move into the flow field. Fluid flow conditions were the same as discussed for Figure 10. The restitution coefficients were set to $e_n = e_t = 0.3$ in these and all subsequent calculations. These values of e_n and e_t

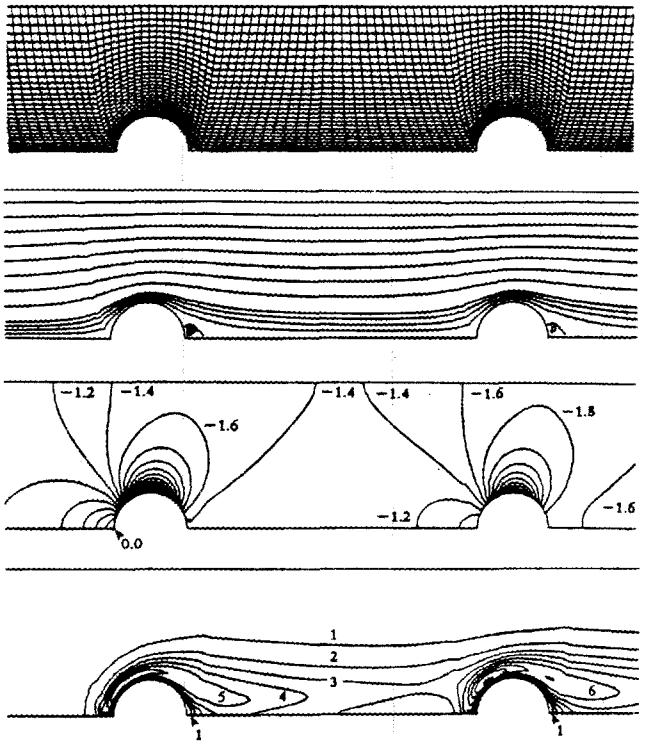

Figure 10. Flow field calculation using: a. 117 × 28 grid; b. streamlines; c. isobars; d. turbulent kinetic energy contours.

Streamline contour intervals are 0.025 and 0.1 for the bulk flow, and 0.001 for the recirculating flow. Isobar contour interval, $(P - P_{static})/(\frac{1}{2}\rho U_\infty^2)$, is 0.2. Turbulent kinetic energy contour interval, $100(k)/(U_\infty^2)$, is 1.0. The left- and righthand planes shown are at $(x/D) = 17.7$ and 26.6, respectively.

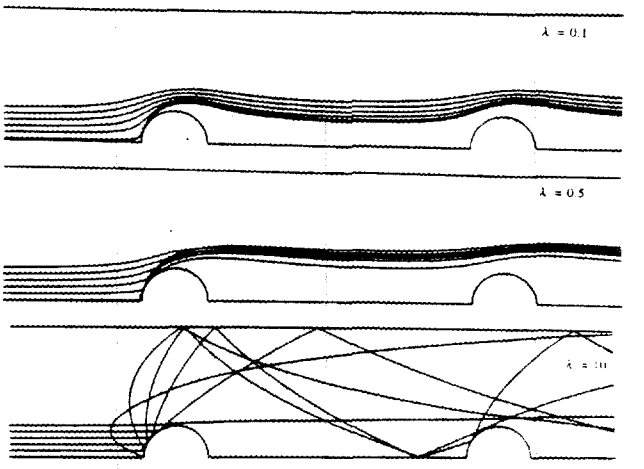

Figure 11. Particle paths for two in-line tubes showing the effect of the particle response time on collisions with the downstream tube.

Left- and righthand planes shown are at $(x/D) = 17.1$ and 26.7, respectively.

were determined by matching calculated rebound heights with corresponding photographic data in Schweitzer and Humphrey (1988). The results show that particles with $\lambda > 1$ are fairly inertial and experience substantial rebounding from a tube surface. The results for $\lambda = 10$ show that rebounding particles can cross the flow symmetry plane. Where this occurs, mirror-image particles are reintroduced in the flow, some of which will impact the second in-line tube.

Particle fluxes to the first of two in-line tube surfaces are shown in Figure 12 for $\lambda = 0.5$ and 10. They are compared to the theoretical maximum particle flux, which occurs when $\lambda = \infty$ for which all the particles released within $\frac{1}{2}$ D of the bottom symmetry plane strike the tube. Due to the curvature of the tube the resulting flux for this case has a cosine dependency on θ. The particle fluxes were calculated by releasing 100 particles at equally spaced intervals from the centerline to $\frac{1}{2}$ D above the

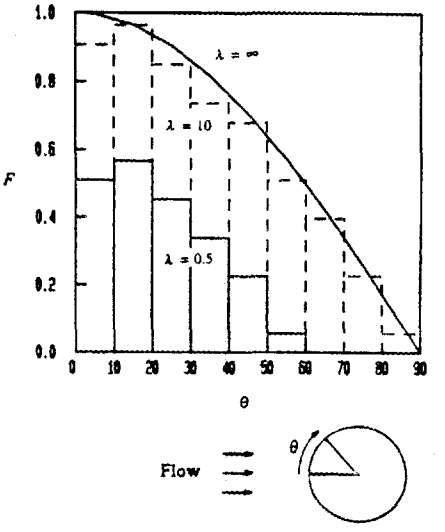

Figure 12. Particle fluxes to the surface of the first tube of two in-line tubes with $(L_t/D) = 5$.

Flow field conditions correspond to those of Figure 10.

bottom symmetry plane and counting the number of impacts occurring over 10° intervals on the tube surface. As expected, the particle flux decreases with decreasing λ since the particles become more responsive to the flow field in passage past the tubes.

A comparison of the particle fluxes to the first of two in-line tubes for two different fluid temperatures is shown in Figure 13a. The particles are 9.15 μm in diameter, which corresponds to $\lambda = 0.5$ at $T = 300$ K, and $\lambda = 0.22$ at $T = 1{,}000$ K, due to the dependence of μ on temperature. The velocity at the inlet plane is the same for both cases. At $T = 1{,}000$ K, the particle flux is larger for $\theta \leq 20°$ and smaller for $\theta > 20°$ compared with the 300 K case. This is explained by the stronger coupling through viscosity at 1,000 K. For $\theta \leq 20°$, particles deviating from the streamlines strike on the front of the tube. As they rebound with a decreased velocity, they interact with the flow field, which forces them to hit the tube again. This process is repeated several times until the particles finally escape, usually by sliding along the tube surface. On the other hand, for $\theta > 20°$ the particles follow the streamlines closely and do not strike the tube.

The particle speeds and impact angles at the instant of impact can be used to determine the relative wear on the tube surface by using Finnie's (1959, 1960) cutting wear model. This model was used by Dosanjh and Humphrey (1985) to predict the erosion of a plate by a particle-laden turbulent air jet. Given the impact information, the volume of material removed per unit time per unit area, Q, is given by

$$Q = \begin{cases} \dfrac{N_{pt} m_{pt} u_{pt}^2}{6\psi} \sin^2 \beta & 0.0° \leq \beta \; 71.5° \\ \dfrac{N_{pt} m_{pt} u_{pt}^2}{2\psi} [\sin (2\beta) - 3 \cos^2 \beta] & 71.5° \leq \beta \leq 90° \end{cases} \tag{30}$$

where ψ is a wear model constant that depends on the material properties. The wear due to particle impact can be normalized by dividing Q by $(N_{pt} m_{pt} u_\infty^2 / 6\psi)$, so that the actual value of ψ is not required. In point of fact, ψ may depend weakly on T for the types of materials from which the tubes in a heat exchanger tube bank are likely to be made. For constant impact velocity, the model predicts maximum wear for impacts at $\beta = 73.2°$ relative to the surface normal.

Figure 13b shows the relative wear of the first of two in-line tubes due to particles in flow fields evaluated at $T = 300$ K and 1,000 K. These results show less erosion for the tube in the high temperature flow due to the stronger coupling, through viscosity, between the particle and the fluid motion. Both the extent and position of maximum wear are predicted to be strongly dependent on temperature.

Attention is now turned to the effect of the turbulent velocity fluctuations on particle motion. Figures 14 a, b and c show the calculations performed for three values of λ using the flow field results presented in Figure 10, this time considering the effects of the fluctuations on the particles. In each case, 20 particles were released at the entrance of the calculation domain (not shown in the figure), at a single location ¼ D above the bottom symmetry plane. These figures show that the importance of the fluctuations diminishes as λ increases, as predicted by the argument leading to Eq. 27. However, examination of Figure 14c reveals that even though a given fluctuation does not affect the motion of the particle significantly when $\lambda = 10$ (as indicated by

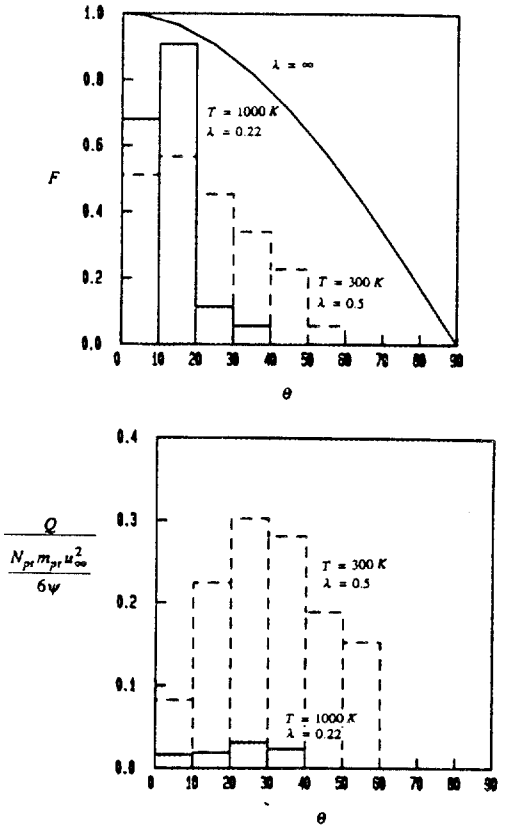

Figure 13. Temperature effects on the particle flux to the surface of the first of two in-line tubes and on its erosion, for the same particle size and inlet velocity: $d_{pt} = 9.15$ μm, $U_\infty = 19.2$ m/s.

a. Angular distribution of flux to the surface.
b. Angular dependence of surface erosion.

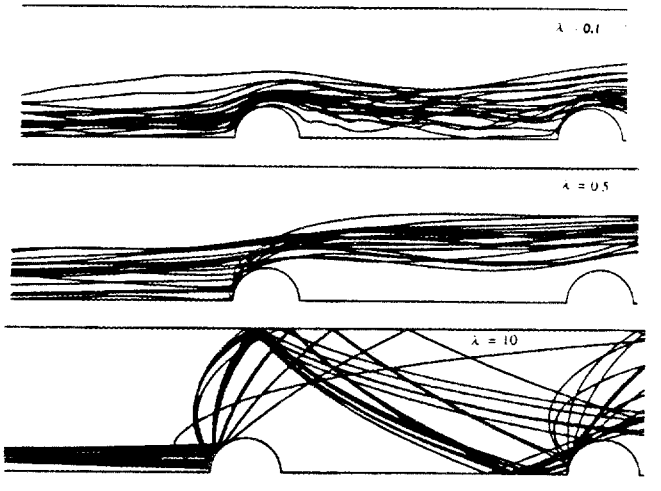

Figure 14. A comparison of particle paths for two in-line tubes showing the effect of different values of λ on the particle response to the turbulent fluctuations.

Fluid flow conditions correspond to those of Figure 10. Left- and righthand planes shown are at $(x/D) = 15.8$ and 25.4, respectively.

the relatively smooth trajectories), the random cumulative effects of the fluctuations result in different trajectories for different particles released at the same starting location. It is also interesting to note that, for $\lambda = 0.1$, some of the particles hit both the first and the second tube, a behavior not predicted when the effects of the fluctuations are ignored (see Figure 11). However, for $\lambda = 0.5$ and 10 the overall patterns of the deterministic and fluctuation trajectories is strikingly similar even though the individual particle trajectories differ.

Figure 15 shows a comparison between particle fluxes over the first of two in-line tubes for the conditions of Figure 10 with $\lambda = 0.5$ and 10. The theoretical maximum for particles with $\lambda = \infty$ is also shown. The effects of the turbulent fluctuations were considered by means of the SSF model with 40 particles being released at each of 100 equally spaced locations between the top and the bottom symmetry planes, for a total of 4,000 particles. Particle impacts were added over 10° increments on the tube surface and, as for the deterministic case, the flux to the tube is observed to decrease with decreasing λ.

The effect of temperature on the particle flux for two in-line tubes corresponding to the conditions of Figure 10 is shown in Figure 16a. Multiple reboundings are not present in this case since, following the first rebound, the fluctuating velocity field carries a particle away from the tube surface. The corresponding erosion comparison is shown in Figure 16b, where higher erosion rates are predicted for the fluctuating case than for the non-fluctuating. This is attributed to the higher particle velocities induced locally by the fluctuations.

Turbulent flow and particle paths in a tube bank

Figure 17a shows the streamlines for the flow past a tube in a rectangular tube bank with $Re = 25{,}600$ and $(L/D) = 2.0$. Particle trajectories for different λ are illustrated in Figures 17b, c and d. The trajectories have been calculated for nonfluctuating flow conditions for $\lambda = 0.1$, 1.0 and 10. (corresponding to particle diameters of 9.26, 29.3 and 92.6 μm, respectively). Three flow field cycles are computed for each λ. In the first cycle, the particles are released at $y = 1/4\ D$ with a velocity equal to the fluid velocity at that point. For each of the two subsequent cycles, the particles reenter the calculation domain at y locations

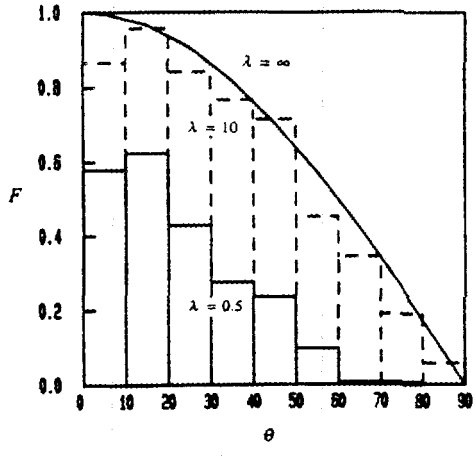

Figure 15. Particle fluxes to the surface of the first of two in-line tubes with $(L_t/D) = 5$.

Flow field conditions correspond to those of Figure 10.

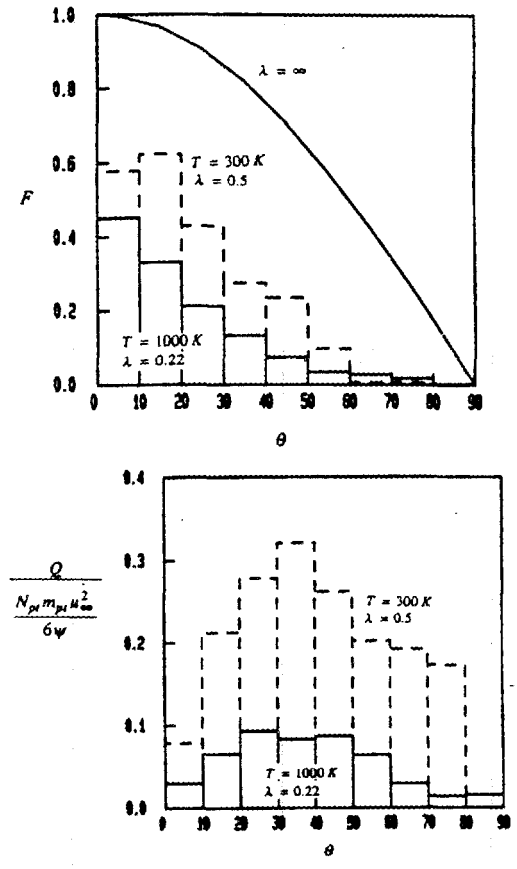

Figure 16. Temperature effects on the particle flux to the surface of the first of two in-line tubes and on its erosion, for the same particle size and inlet velocity: $d_{pt} = 9.15\ \mu$m, $U_\infty = 19.2$ m/s.

a. Angular distribution of flux to the surface.
b. Angular dependence of surface erosion.

corresponding to the previous y locations on the exit plane, and with the corresponding particle velocity at the exit plane. As expected, for low λ a particle is diverted and never hits the tube. However, with increasing λ the particle trajectories become complex due to tube reboundings that induce crossings of the symmetry planes.

Conclusions and Recommendations

A numerical procedure has been developed and tested that calculates 2*D*, steady, constant property flows in nonorthogonal body-fitted curvilinear coordinates. [The entire code is listed and documented in Schuh (1987) and is available on tape or IBM PC diskette from the authors at the University of California, at Berkeley.] It has been applied to predict laminar and turbulent flows past one and two in-line tubes, and past a tube in an infinite tube bank. For the turbulent flow cases, a two-equation $(k - \epsilon)$ model was used that relates the Reynolds stresses to the strain field via an isotropic turbulent viscosity. A logarithmic law-of-the-wall relation was used to connect the shear stress at the tube wall with the velocity in the turbulent part of the flow. Although prone to error in the vicinity of the separation point on the tube, the turbulence model has yielded results in good quali-

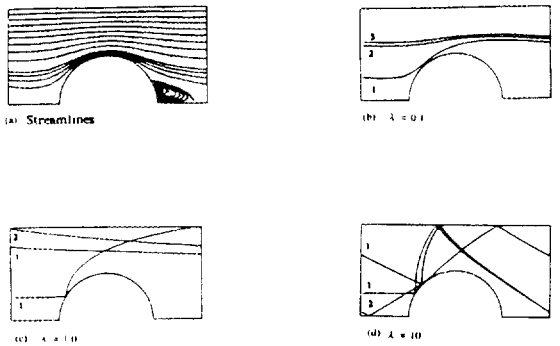

Figure 17. Flow field and particle paths for flow in a tube bank with $Re = 2.56 \times 10^4$ and $(L/D) = 2$.

a. Streamline contour intervals are 0.025 and 0.1 for the bulk flow and 0.001 for the recirculating flow.
b, c, d. Trajectory of a particle released between two tubes with: a. $\lambda = 0.1$; b. $\lambda = 1.0$; and c. $\lambda = 10.0$

tative agreement with the test cases examined. Testing in the laminar flow regime has yielded results in excellent quantitative agreement with the measurements and calculations of others.

The assumption of one-way coupling has allowed the prediction of particle speeds and trajectories for dilute noninteracting particle-laden gas flows for some of the tube configurations examined. For this, a deterministic particle equation of motion formulated in Lagrangian coordinates was used. The calculations yield the necessary impact velocity information from which to evaluate particle flux to, and erosion of, tube surfaces. The predictions show that particles in flows with $\lambda < 1$ follow the streamlines fairly closely, while those with $\lambda > 1$ do not. As a result, the latter induce higher rates of wear than the former and are more likely to rebound from several consecutive tubes in a tube bank. Because the value of λ decreases with increasing gas viscosity, particles in flow fields at high temperatures are expected to follow the streamlines more closely and, as a result, erode less.

The effect of the turbulent velocity fluctuations was explored using a simplified SSF model. Calculations show that the effect of the fluctuations is very important for $\lambda < 1$, since these particles are very responsive to changes in the flow field. Over long times, the history of the fluctuations can also affect the trajectories of inertial particles ($\lambda > 1$).

For fixed Reynolds number, the characteristics of the computed fluid flow fields show a strong dependence on the spacing between tubes, especially in the mean flow direction. Thus, in closely spaced tube configurations the front of a tube is shielded from direct particle impacts by the tube ahead of it. The optimum tube spacing in a tube bank represents a compromise among the wear, pressure drop and heat transfer requirements of the bank. The present numerical procedure provides a valuable design tool for investigating arbitrary tube configurations and flow conditions of practical interest.

Acknowledgements

This research was sponsored by Martin Mariette Energy Systems, Inc. (Subcontract #19X-55936C) under their Principal Contract with the U.S. Department of Energy # DE-AC05-84OR21400. Additional support was received by the second author in the form of a scholarship from MARAVEN S.A., subsidiary of Petroleos de Venezuela S.A. Both sources of support are gratefully acknowledged.

Notation

A = convection-diffusion coefficient, Eq. 15; also used as area
A_{pt} = projected area of the particle
$\boldsymbol{a}^i$ = contravariant base vectors
$\boldsymbol{a}_i$ = covariant base vectors
b = source term in general convection-diffusion equation, Eq. 14
C_D = constant for the dissipation term in the turbulent kinetic energy equation, Eqs. 7 and 13
C_{Dr} = drag coefficient for the particle, Eq. 18
C_p = local cell mass imbalance
C_1 = constant for the generation term in the dissipation of turbulent kinetic energy equation, Eqs. 8 and 13
C_2 = constant for the dissipation term in the dissipation of turbulent kinetic energy equation, Eqs. 8 and 13
C_μ = constant for the turbulent viscosity equation, Eqs. 12 and 13
D = diameter of a tube
d_{pt} = particle diameter
e_n = normal restitution coefficient
e_t = tangential restitution coefficient
F = nondimensional particle Flux over the tube surface, $F = (N_{pt}/N_o \Delta\theta)$
f = correction factor for the Drag Coefficient, Eq. 19
G = generation of turbulent kinetic energy, Eq. 9
g = square of the Jacobian
g^{ij} = component of the contravariant metric tensor
g_{ij} = component of the covariant metric tensor
$\underline{g}$ = acceleration due to gravity
$\sqrt{g}$ = Jacobian
i = index—i = 1, 2, and 3 for three dimensions and i = 1 and 2 for two dimensions
$\hat{i}$ = unit base vector for the cartesian coordinate system
j = index—j = 1, 2, and 3 for three dimensions and j = 1 and 2 for two dimensions
$\hat{j}$ = unit base vector for the cartesian coordinate system
k = turbulent kinetic energy
L = distance between the centers of two tubes in a rectangular infinite tube bank with equal longitudinal and transverse spacing
L_l = longitudinal distance between the centers of two tubes in a rectangular infinite tube bank
L_t = transverse distance between the centers of two tubes in a rectangular infinite tube bank
L_{ref} = characteristic length of the flow field
L_ϵ = integral dissipation scale
m = erosion proportional to the fluid velocity to the power m
m_{pt} = mass of the particle
N_{pt} = number of particles that hit the tube in a given angle interval of the tube surface
N_o = number of particles released at the entrance of the calculation domain between the bottom symmetry plane and $\frac{1}{2} D$
P = pressure
P = source term in the elliptic grid generation equation that controls the verticle lines
Q = volume of material removed per unit time per unit area by N particles each of mass m_{pt}, Eq. 30
Q = source term in the elliptic grid generation equation that controls the horizontal lines
Re = Reynolds number, $(\rho u_\infty D/\mu)$
Re_{pt} = particle Reynolds number, $(\rho |U - U_{pt}| d_{pt}/\mu)$
r = vector location of a point, $r = x\hat{i} + y\hat{j}$
t = time
t_{EDDY} = lifetime of a turbulent eddy
S_u = source term for the convection-diffusion, Eq. 15
S_p = source term for the point of interest in the convection-diffusion equation
U^i = contravariant velocity component
U_{ref} = reference velocity
$\bar{U}$ = vector velocity of the fluid
U_{pt} = vector velocity of the particle
u = x component of the fluid vector velocity
u' = velocity scale of the turbulent fluctuations
u_∞ = free stream velocity for single tubes and two tubes *in tandem;* average velocity at the minimum cross section, $\bar{u}_{mcs}$ for infinite tube banks
u_{pt} = x component of the particle vector velocity

u'_{pt} = x component of the particle vector velocity after rebound
v = y component of the fluid vector velocity
v_{pt} = y component of the particle vector velocity
v'_{pt} = y component of the particle vector velocity after rebound
w_n = particle velocity component normal to the boundary
w'_n = particle velocity component normal to the boundary after rebounding
w_t = particle velocity component tangential to the boundary
w'_t = particle velocity component tangential to the boundary after rebounding
x = Cartesian coordinate location
y = Cartesian coordinate location

Greek letters

β = particle impact angle relative to surface normal
Γ = general diffusion constant, Eq. 14
$\Delta\theta$ = angle interval on the boundary surface
δ = small distance or number
ϵ = dissipation of turbulent kinetic energy
ζ = another name for ξ^1
η = another name for ξ^2
θ = angle on the boundary surface, Figure 5
κ = Von Karman constant
λ = nondimensional particle response time, or momentum equilibrium constant, Eq. 21
μ = dynamic viscosity
μ_e = effective dynamic viscosity, Eq. 11
μ_t = turbulent viscosity, Eq. 12
ξ^i = ith curvilinear coordinate
ρ = density of the fluid
ρ_{pt} = density of the particle
σ_k = constant in turbulent kinetic energy equation, Eqs. 7 and 13
σ_ϵ = constant in the dissipation of turbulent kinetic energy equation, Eqs. 8 and 13
τ = particle response time, $\tau = (\rho_{pt} d_{pt}^2 / 18\mu)$
ϕ = arbitrary variable, u, v, P, k, and ϵ, Eq. 14
ψ = wear model constant, Eq. 30

Subscripts

E = value at the point to the east of the control volume
N = value at the point to the north of the control volume
pt = particle
S = value at the point to the south of the control volume
W = value at the point to the west of the control volume

Literature Cited

Achenbach, E., "On the Cross Flow through In-Line Tube Banks with Regard to the Effect of Surface Roughness," *Wärme und Stoffübertragung*, **4**, 152 (1971).

Acrivos, A., L. G. Leal, D. D. Snowden, and F. Pan, "Further Experiments on Steady Separated Flows Past Bluff Objects," *J. Fluid Mech.*, **34**(1), 1, 25 (1968).

Antonopoulos, K. A. "Prediction of Flow and Heat Transfer in Rod Bundles," Ph.D. Thesis, Imperial College of Science and Technology, London (1979).

———, "Heat Transfer in Tube Banks Under Conditions of Turbulent Inclined Flow," *Int. J. Heat and Mass Transf.*, **28**(9), 1645 (1985).

Benchaita, M. T., P. Griffith, and E. Rabinowicz, "Erosion of Metallic Plate by Solid Particles Entrained in a Liquid Jet," *J. of Eng. for Ind.*, **105**, 215 (1983).

Bergelin, O. P., G. A. Brown, and S. C. Doberstein, "Heat Transfer and Fluid Friction During Viscous Flow Across Banks of Tubes—IV, A Study of the Transition Zone Between Viscous and Turbulent Flow," *Trans. ASME*, **74**, 953 (1952).

Boothroyd, R. G., *Flowing Gas-Solids Suspensions*, Chapman and Hall, London (1971).

Celik, I., V. C. Patel, and L. Landweber, "Calculation of the Mean Flow Past Circular Cylinders by Viscous-Inviscid Interaction," *J. of Fluids Eng.*, **107**, 218 (1985).

Chilukiru, R., and D. A. Steininger, "Large Eddy Simulation of Turbulent Buffeting Forces in Steam Generator Tube Banks," BHRA Int. Conf. on Flow Induced Vibrations, England (1987a).

———, "Numerical Simulation of Turbulence Deep within Heat Exchanger Tube Bundles," ASME PVP Conf., San Diego, CA (1987b).

Clift, R., J. R. Grace, and M. E. Weber, *Bubbles, Drops, and Particles*, Academic Press, New York (1978).

Coutanceau, M., and R. Bouard, "Experimental Determination of the Main Features of the Viscous Flow in the Wake of a Circular Cylinder in Uniform Translation: 1. Steady flow," *J. Fluid Mech.*, **79**(2), 231 (1977).

Dosanjh, S., and J. A. C. Humphrey, "The Influence of Turbulence on Erosion by a Particle-Laden Fluid Jet," *Wear*, **102**, 309 (1985).

Faghri, M., and N. Rao, "Numerical Computation of Flow and Heat Transfer in Finned and Unfinned Tube Banks," *Int. J. Heat and Mass Transf.*, **30**(2), 363 (1987).

Finnie, I., "An Experimental Study of Erosion," *Proc. Soc. Exp. Stress Analy.*, **17**(2), 65 (1959).

———, "Erosion of Surfaces by Solid Particles," *Wear*, **3**, 87 (1960).

Fujii, M., T. Fujii, and T. Nagata, "A Numerical Analysis of Laminar Flow and Heat Transfer of Air in an In-Line Tube Bank," *Num. Heat Transf.*, **7**, 89 (1984).

Grove, A. S., F. H. Shair, E. E. Petersen, and A. Acrivos, "An Experimental Investigation of the Steady Separated Flow Past a Circular Cylinder," *J. of Fluid Mech.*, **19**, 60 (1964).

Laitone, J. A., "Aerodynamic Effects in the Erosion Process," *Wear*, **56**, 239 (1979a).

———, "Erosion Prediction Near a Stagnation Point Resulting From Aerodynamically Entrained Solid Particles," *J. Aircraft*, **16**(12), 809 (1979b).

———, "Separation Effects in Gas-Particle Flows at High Reynolds Numbers," LBL-9996, Ph.D. Thesis (1979c).

———, "Characterization of Particle Rebound Phenomena in the Erosion of Turbomachinery," *J. Aircraft*, **20**(3), 275 (1983).

Laufer, J., "Investigation of Turbulent Flow in a Two-Dimensional Channel," Technical Note 2123, National Advisory Committee for Aeronautics (1950).

Launder, B. E., and T. H. Massey, "The Numerical Prediction of Viscous Flow and Heat Transfer in Tube Banks," *J. of Heat Transf.*, **100**, 565 (1978).

Launder, B. E., and D. B. Spalding, "The Numerical Computation of Turbulent Flows," *Comp. Methods in Appl. Mech. and Eng.*, **3**, 269 (1974).

Majumdar, S., and W. Rodi, "Numerical Calculations of Turbulent Flow Past Circular Cylinders," Symp. on Numerical and Physical Aspects of Aerodynamic Flows, Long Beach, CA (1985).

Ormancey, A., and J. Martinon, "Prediction of Particle Dispersion in Turbulent Flows," *Physico-Chem. Hyrdody.*, **1**(3/4), 229 (1984).

Patankar, S. V., C. H. Liu, and E. M. Sparrow, "Fully Developed Flow and Heat Transfer in Ducts Having Streamwise-Periodic Variations of Cross-Sectional Area," *J. of Heat Transf.*, **99**, 180 (1977).

Patankar, S. V., *Numerical Heat Transfer and Fluid Flow*, Hemisphere Publishing (1980).

Pourahmadi, F., and J. A. C. Humphrey, "Modeling Solid-Fluid Turbulent Flows with Application to Predicting Erosive Wear," *Physico-Chem. Hydrody.*, **4**(3), 191 (1983).

Press, W. H., B. P. Flannery, S. A. Teukolsky, and W. T. Vetterling, *Numerical Recipes*, Cambridge Univ. Press (1986).

Rodi, W., "Examples of Turbulence Model for Incompressible Flows," *AIAA J.*, **20**(7), 872 (1982).

———, *Turbulence Models and Their Application in Hydraulics—A State of the Art Review*, 2nd ed., Int. Assoc. for Hydraulic Research, Delft, Netherlands (1984).

Schuh, M. J., "Numerical Prediction of Fluid and Particle Motions in Flows Past Tubes," Ph.D. Thesis, Univ. of California, Berkeley (1987).

Schweitzer, M. O., and J. A. C. Humphrey, "Note on the Experimental Measurement of Particle Flux to One and Two In-Line Tubes," *Wear*, **126**, 211 (1988).

Shuen, J-S., Chen, L-D., and G. M. Faeth, "Predictions of the Structure of Turbulent, Particle-Laden Round Jets," *Proc. AIAA Aerospace Sci. Meeting*, Reno, NV (1983).

Shuen, J-S., A. S. P. Solomon, Q-F. Zhang, and G. M. Faeth, "Structure of Particle Laden Jets: Measurements and Predictions," *AIAA J.*, **23**(3), 396 (1985).

Taneda, S., "Experimental Investigation of the Wakes behind Cylinders

and Plates at Low Reynolds Numbers," *J. Phys. Soc. of Japan*, **11**(3), 302 (1956).
Thompson, J. F., "A Survey of Dynamically-Adaptive Grids in the Numerical Solution of Partial Differential Equations," *Appl. Num. Math.*, **1**, 3 (1985).
———, "Numerical Grid Generation," A Short Course, Mississippi State Univ. June 9–13 (1986).
———, "A Composite Grid Generation Code For General 3-D Regions," AIAA-87-0275, *AIAA Aerospace Sciences Meeting*, Reno, NV (1987).
Thompson, J. F., Z. A. Warsi, and C. W. Mastin, *Numerical Grid Generation, Foundations and Applications*, North-Holland, New York (1985).
Vittal, B. V. R., and W. Tabakoff, "Effect of Solid Particles in Two Phase Flow Around A Two Dimensional Cylinder," AIAA-86-0349, *AIAA Aerospace Sciences Meeting*, Reno, NV (1986).
Zukauskas, A., "Heat Transfer from Tubes in Crossflow," *Adv. in Heat Trans.*, **8**, 93 (1972).
Zukauskas, A., and J. Ziugzda, *Heat Transfer of a Cylinder in Crossflow*, Hemisphere Publishing (1985).

Manuscript received Mar. 29, 1988 and revision received Nov. 1, 1988.

Fluid Mechanic Effects on Particle Erosion in Non-Isothermal Turbulent Flows Past Tubes

Master of Science Project Report

submitted to

Department of Mechanical Engineering
University of California, Berkeley

in partial fulfillment of the requirements for the degree
Master of Science in Mechanical Engineering

by

Lance L. Smith

February 16, 1990

Nomenclature

Roman symbols

A_i Convection-diffusion coefficient. $i=N, S, E, W, P$ node locations.

A^+ Constant in Van Driest relation for mixing length.

$\vec{a^i}$ Contravariant base vectors: $\vec{a^i}=\nabla\zeta^i$.

a^{1i} x-components of contravariant base vector $\vec{a^1}$: $\vec{a^1}=a^{1i}e_x^{\wedge}+a^{1j}e_y^{\wedge}$.

a^{1j} y-components of contravariant base vector $\vec{a^1}$: $\vec{a^1}=a^{1i}e_x^{\wedge}+a^{1j}e_y^{\wedge}$.

a^{2i} x-components of contravariant base vector $\vec{a^2}$: $\vec{a^2}=a^{2i}e_x^{\wedge}+a^{2j}e_y^{\wedge}$.

a^{2j} y-components of contravariant base vector $\vec{a^2}$: $\vec{a^2}=a^{2i}e_x^{\wedge}+a^{2j}e_y^{\wedge}$.

b Source term in the general convection-diffusion equation.

C_1, C_2, C_D Turbulence model constants.

D Diffusion coefficient in curvilinear form: $D=(\sqrt{g}\,\Gamma g^{ij})$. Also diameter of tube.

$e_x^{\wedge}$ Unit base vector in x-direction for Cartesian coordinate system.

$e_y^{\wedge}$ Unit base vector in y-direction for Cartesian coordinate system.

F Convection coefficient in curvlinear form: $F=(\sqrt{g}\,\rho U^i)$.

G Generation of turbulent kinetic energy (defined in text).

g^{ij} Component of the contravariant metric tensor.

$\sqrt{g}$ The Jacobian of the x–y to ζ–η transformation.

$g\,12term$ Cross terms involving g^{12} and g^{21}. Treated as a source term.

h Heat transfer coefficient.

i Index -- i = 1 and 2 for two dimensions. Equations with indices are written using the Einstein summation convention.

j Index -- j = 1 and 2 for two dimensions. Equations with indices are written using the Einstein summation convention.

k Turbulent kinetic energy.

l Turbulent mixing length.

Nu Local Nusselt number.

$\overline{Nu}$ Mean Nusselt number.

P Non-periodic component of pressure. Also production of turbulent kinetic energy (defined in text). Note that $P=\frac{G}{\rho\nu_t}$.

p Total pressure: $p=P-\beta x$[1].

Pr Prandtl number.

Pr_t Turbulent Prandtl number.

Re Reynolds number ($\mathrm{Re}=\frac{uD}{\nu}$). Periodic boundaries: $u=u_{\max}$. Non-periodic boundaries: $u=u_{inlet}$.

S_μ Source term with no ϕ_P dependence in the convection-diffusion equation.

S_P Source term with linear ϕ_P dependence in the convection-diffusion equation.

T Temperature.

T_x^* Local reference temperature (defined in text).

U x-component of the fluid velocity (a mean quantity for turbulent flow).

U^i Contravariant velocity component: $U^i=\vec{a^i}\cdot(Ue_x^\wedge+Ve_y^\wedge)$.

U_i, U_j Components of Cartesian velocity vector. For turbulent flow U_i or U_j refer to the mean velocity.

u_i, u_j i or j component of fluctuating part of turbulent velocity field.

V y-component of the fluid velocity (a mean quantity for turbulent flow).

x Cartesian coordinate location.

y Cartesian coordinate location.

y^+ Non-dimensional distance from the wall in turbulent flow: $y^+=\frac{y}{\nu}\left[\frac{|\tau_w|}{\rho}\right]^{\frac{1}{2}}$.

Greek symbols

α Thermal diffusivity.

α_e Effective thermal diffusivity: $\alpha_e=\alpha+\alpha_t$.

α_t Turbulent thermal diffusivity.

β Parameter to specify the linear, non-periodic part of the pressure: $\beta=\frac{\partial P}{\partial x}$

Γ General diffusion constant.

ε Dissipation of turbulent kinetic energy.

ζ Curvilinear coordinate location. ($\zeta=\zeta^1$).

η Curvilinear coordinate location. ($\eta=\zeta^2$).

θ Non-dimensional temperature. Also angle around tube from stagnation point.

κ Von Karman constant.

λ Used in solving for θ. (Defined in text).

λ_o λ from last iteration.

ν Kinematic viscosity.

ν_e Effective kinematic viscosity: $\nu_e=\nu+\nu_t$.

ν_t Turbulent kinematic viscosity.

Ω Used in solving for θ. (Defined in text).

ρ Density of the fluid.

Σ Summation.

σ Source term of the non-dimensional energy equation.

σ_k, σ_ε Turbulence model constants.

τ_w Shear stress at the wall.

ϕ General (arbitrary) variable.

Subscripts

E, W, N, S Value at the point to the east, west, north, or south of the control volume.

Eb, Wb, Nb, Sb Value at the control volume boundary to the east, west, north, or south of the control volume.

P Grid point of interest in the control volume.

Other symbols

∞ A large number, set to 10^{30} in this work.

$\max(a,b)$ Maximum value of the values a and b.

$|\ |$ Absolute value

$|_P$ Evaluated at the point P.

Introduction

The aim of this project has been to evaluate computationally, for a variety of flows and tube configurations, erosion by particles of tubes in a cross-flow. This work was begun by Michael Schuh et al. [1,2], who succeeded in calculating laminar and turbulent flow across single tubes, tube pairs, and tubes in in-line banks (these configurations are shown in Figure 1); and from this information calculated isothermal particle trajectories, fluxes, and erosion. The computer codes developed by Schuh et al., called CLEW, consisted of three parts: GRID, a curvilinear grid generator to set up the computational domain; FLOW, a code for calculating both laminar and turbulent flow around tubes; and PARTICLE, a code for calculating particle paths, fluxes, and erosion.

In the present work the calculation procedure has been extended and modified to predict laminar and turbulent flow and heat transfer around tubes, and particle paths in non-isothermal flows. The code in its present form, now called CLEW-T, consists, as before, of three parts: GRID, the curvilinear grid generator; FLOW-T, a code for calculating laminar and turbulent flow and heat transfer; and PARTICLE-T, a code for calculating particle paths, fluxes, and erosion in flows with heat transfer, allowing for variation of viscosity (and therefore drag) with temperature. The majority of the changes and additions were made in FLOW-T. There were two major modifications here: first, the turbulence models were changed for better resolution of the boundary layer region; second, a heat transfer code was implemented which was able to calculate on a curvilinear grid the heat transfer from single tubes, tube pairs, and (most importantly) tubes in banks. The only significant changes to PARTICLE-T were the inclusion of a temperature-varying viscosity, and a temperature interpolation scheme for evaluating temperatures at points not on the grid nodes.

Calculation procedure

Finite difference forms of the steady, two-dimensional, constant property equations for momentum and energy are solved on non-staggered, curvilinear coordinates. Note that the solutions are steady solutions, which in reality do not exist for flow around cylinders at Reynolds numbers in excess of 40 [3]. The results here can be regarded as averaged solutions with respect to the unsteady vortex-shedding phenomenon of cylinders. The curvilinear coordinates allow specification of boundary conditions on complex shapes or on shapes which would otherwise require the simultaneous use of two types of coordinate systems (such as rectangular and cylindrical).

The procedure for calculating particle trajectories in a non-isothermal flow follows this sequence:

1. Set up the calculation domain and generate the curvilinear boundary-fitted coordinates. (Use GRID).

2. Solve the momentum equations (making use of continuity and the turbulence model) to find the distribution of velocity components and pressure. (Use FLOW-T).

3. Solve the energy equation (with the turbulence model) to find the temperature distribution and heat transfer. (Use FLOW-T).

4. Calculate the particle trajectories resulting from the drag force acting on the particle. (Use PARTICLE-T).

Note that each step makes use of the calculations performed in the previous steps. In particular, the energy equation is solved for a given flow field (forced convection). The particle trajectories are then calculated for the same given velocity field, but now assuming a variation of viscosity given by a functional dependence on the calculated temperatures. All calculations reported here are for flows of air.

The fluid phase momentum equation to be solved is the constant-property Navier-Stokes equation:

$$U_j \frac{\partial U_i}{\partial x_j} = \frac{-1}{\rho} \frac{\partial P}{\partial x_i} + \frac{\partial}{\partial x_j} \left(\nu_e \frac{\partial U_i}{\partial x_j} \right) , \tag{1}$$

where ν_e is the effective kinematic viscosity which includes turbulent effects (discussed below). The energy equation employed is the constant-property energy equation for a non-dissipating medium:

$$U_j \frac{\partial T}{\partial x_j} = \frac{\partial}{\partial x_j} \left(\alpha_e \frac{\partial T}{\partial x_j} \right) , \tag{2}$$

where α_e is the effective thermal diffusivity, and includes the effects of turbulence (also discussed below).

These two-dimensional elliptic convection-diffusion equations for momentum and energy require boundary conditions on all four planes of the computational domain: the inlet and outlet planes and the top and bottom symmetry planes (the bottom symmetry plane includes the tube surface). The same boundary regions also apply to the elliptic k and ε convection-diffusion equations, which are solved in conjunction with the momentum equations during the computation of turbulent flows.

There are two general cases considered: a non-periodic case and a periodic case. For the non-periodic case the values of the variables are specified at the entrance plane, while a fully developed situation (in which the derivatives of the variables with respect to x become zero) is specified at the outlet plane. For the periodic case the values of the variables at the entrance plane are set equal to the values of the variables at the exit plane, while a constant (specified) pressure drop across the calculation domain is used to force a forward flow. In both cases, periodic and non-periodic, wall boundary conditions at the tube wall are given, while the remainder of the lower boundary and the entire upper boundary are taken to be planes of symmetry where the transverse velocity and the derivative of all variables with respect to y equal zero. These boundary conditions are shown in Figure 2. The tube boundary condition for the velocity is simply the no-slip condition, $U=V=0$. The temperature calculations assume a constant tube wall temperature, $T=T_w$. The wall boundary conditions for the k and ε variables of turbulent kinetic energy and dissipation of turbulent kinetic energy are not as simple. These will be discussed in connection with the discussion of turbulence models below.

The finite difference forms of the equations are solved using the tri-diagonal matrix algorithm (TDMA) [4]. For the periodic configurations a cyclic tri-diagonal matrix algorithm is used [5]. The flow field solution is found iteratively, following this sequence [1]:

1. Initialize the variables: Set U, k, and ε equal to the specified inlet plane values everywhere in the flow field. Set $P=0$ and $V=0$ everywhere.

2. Calculate new U and V velocity fields sequentially.

3. Update the pressure field to enforce continuity.

4. Calculate new turbulent k and ε fields. Use the new values to re-calculate the turbulent viscosity, ν_t (this is explained below).

5. Check for convergence. If the sum of the residuals is larger than the specified convergence value return to step 2 and repeat the iteration.

The method for solving for the temperature field is similar. Some differences arise due to the more complex form of the source terms for the periodic tube bank case. The solution procedure for the energy equation is discussed below, under the section dealing with the formulation of the periodic energy equation.

Laminar flow calculations are performed using this same sequence, and using the same codes. For laminar calculations the k and ε equations are not solved, and the effective kinematic viscosity is set equal to the molecular kinematic viscosity of the fluid. Laminar heat transfer calculations are performed by the same method as turbulent heat transfer calculations, but without the extra complexities of a turbulent thermal diffusivity. For the laminar calculations the effective thermal diffusivity is simply the molecular thermal diffusivity of the fluid.

Turbulence models

In the earlier work by Schuh [1] a two-equation $k-\varepsilon$ model of turbulence was used to determine the turbulent momentum transfer. Boundary conditions at a tube wall were established through a wall function velocity approach. Essentially, this fixes the values of k and ε adjacent to the physical boundary when the assumption of an equilibrium layer flow is invoked. In the present work this procedure for calculation of the turbulent flow field has been modified, particularly with regard to the tube wall boundary conditions. The two-equation $k-\varepsilon$ model is retained for modelling the turbulent flow, but in the wall boundary layer region a Prandtl-Taylor mixing length model [6] is used instead. The length scale for this mixing length model is determined from the Van Driest relation [7]. The use of a Prandtl-Taylor mixing length model near a tube wall allows for detailed calculation of velocities in the tube wall boundary layer, giving a more accurate picture of the flow conditions near the tube. Since heat transfer is largely determined by the nature of the fluid mechanics in the region very near the tube surface this improved boundary layer resolution

is a necessary preliminary step for establishing a valid procedure for heat transfer and temperature calculations.

The time averaged i-component momentum equation for turbulent, constant property flow in Cartesian coordinates is

$$U_j \frac{\partial U_i}{\partial x_j} = -\frac{1}{\rho}\frac{\partial P}{\partial x_i} + \frac{\partial}{\partial x_j}\left(\nu \frac{\partial U_i}{\partial x_j} - \overline{u_i u_j}\right) . \tag{3}$$

where U and P are the mean values of velocity and pressure, and U is the fluctuating value of velocity. We use the notion of a turbulent kinematic viscosity, ν_t, to relate the turbulent stress, $\overline{u_i u_j}$, to the mean velocity gradient:

$$\overline{u_i u_j} = -\nu_t \left(\frac{\partial U_i}{\partial x_j} + \frac{\partial U_j}{\partial x_i}\right) + \frac{2}{3} k\delta_{ij} . \tag{4}$$

Then, neglecting $\frac{\partial \nu_t}{\partial x}$ and $\frac{\partial \nu_t}{\partial y}$ terms and using continuity, the time averaged momentum equation can be re-written as

$$U_j \frac{\partial U_i}{\partial x_j} = \frac{-1}{\rho}\frac{\partial P}{\partial x_i} + \frac{\partial}{\partial x_j}\left((\nu+\nu_t)\frac{\partial U_i}{\partial x_j}\right) = \frac{-1}{\rho}\frac{\partial P}{\partial x_i} + \frac{\partial}{\partial x_j}\left(\nu_e \frac{\partial U_i}{\partial x_j}\right) , \tag{5}$$

where $\frac{2}{3} k\delta_{ij}$ has been absorbed in the pressure term. In order to use this equation as a basis for calculation it is necessary to know the field variation of the turbulent momentum diffusivity, ν_t. For this we invoke the turbulence models described below.

In the region near the tube wall the Prandtl-Taylor mixing length hypothesis [6, 8] is employed. For a two-dimensional shear flow this states that

$$\nu_t = l^2 \left[\left(\frac{\partial U}{\partial y} + \frac{\partial V}{\partial x}\right)^2 + 2\left(\frac{\partial U}{\partial x}\right)^2 + 2\left(\frac{\partial V}{\partial y}\right)^2\right]^{\frac{1}{2}} , \tag{6}$$

where l is the mixing length evaluated from the Van Driest relation [7]

$$l = \kappa y \left(1 - \exp\left(\frac{-y^+}{A^+}\right)\right) . \tag{7}$$

y is the coordinate perpendicular to the wall, and

$$y^+=\frac{y}{\nu}\left(\frac{|\tau_w|}{\rho}\right)^{\frac{1}{2}},$$

$$A^+=25,$$

$$\kappa=0.41.$$

In the regions where the $k-\varepsilon$ model is used, the turbulent momentum diffusivity is evaluated from

$$\nu_t=C_\mu\frac{k^2}{\varepsilon}, \tag{8}$$

where C_μ is a constant of proportionality (C_μ=0.09) [1, 8]. Values of k and ε are determined from the numerical solution of the k and ε transport equations [8]:

$$U_j\frac{\partial k}{\partial x_j}=\frac{\partial}{\partial x_j}\left[\frac{\nu_e}{\sigma_k}\frac{\partial k}{\partial x_j}\right]+\frac{1}{\rho}G+C_D\varepsilon, \tag{9}$$

$$U_j\frac{\partial \varepsilon}{\partial x_j}=\frac{\partial}{\partial x_j}\left[\frac{\nu_e}{\sigma_\varepsilon}\frac{\partial \varepsilon}{\partial x_j}\right]-C_1\frac{\varepsilon}{k}\frac{1}{\rho}G+C_2\frac{\varepsilon^2}{k}, \tag{10}$$

where σ_k, σ_ε, C_1, C_2, and C_D are empirically determined constants. G is the generation of turbulent kinetic energy, k:

$$G=\rho\nu_t\frac{\partial U_i}{\partial x_j}\left(\frac{\partial U_i}{\partial x_j}+\frac{\partial U_j}{\partial x_i}\right). \tag{11}$$

The near-wall boundary conditions for k and ε are determined by matching the respective expressions for ν_t at the interface of the two calculation regions, where the wall boundary layer meets the core flow. This interface is taken to be at y^+=50. Setting ν_t in the Prandtl-Taylor calculation domain equal to ν_t in the $k-\varepsilon$ calculation domain and assuming that production of turbulent kinetic energy equals dissipation of turbulent kinetic energy, i.e.

$$\nu_t P=\varepsilon \tag{12}$$

where

$$P=\left[\left(\frac{\partial U}{\partial y}+\frac{\partial V}{\partial x}\right)^2+2\left(\frac{\partial U}{\partial x}\right)^2+2\left(\frac{\partial V}{\partial y}\right)^2\right],$$

gives the k and ε values at $y^+=50$ (see Arnal [9]):

$$k=\frac{l^2P}{C_\mu^{\frac{1}{2}}}, \tag{13}$$

$$\varepsilon=l^2P^{\frac{3}{2}}. \tag{14}$$

The $k-\varepsilon$ boundary conditions are shown in Figure 3.

For turbulent heat transfer calculations we use the notion of a turbulent Prandtl number,

$$Pr_t=\frac{\nu_t}{\alpha_t},$$

where α_t is the turbulent thermal diffusivity. Following Arpaci and Larsen [10] we take $Pr_t=0.9$.

The time averaged energy equation for turbulent,two dimensional, constant property, non-dissipating flow is

$$U_j\frac{\partial T}{\partial x_j}=\frac{\partial}{\partial x_j}\left(-\overline{u_jt}+\alpha\frac{\partial T}{\partial x_j}\right), \tag{15}$$

where U and T are the mean values of velocity and temperature, and u and t are fluctuating values. If we define the turbulent thermal diffusivity according to:

$$\overline{u_jt}=-\alpha_t\frac{\partial T}{\partial x_j}, \tag{16}$$

then the time averaged energy equation becomes

$$U_j\frac{\partial T}{\partial x_j}=\frac{\partial}{\partial x_j}\left((\alpha_t+\alpha)\frac{\partial T}{\partial x_j}\right)=\frac{\partial}{\partial x_j}\left(\alpha_e\frac{\partial T}{\partial x_j}\right) \tag{17}$$

with

$$\alpha_t = \frac{\nu_t}{Pr_t} .$$

Values of ν_t are calculated throughout the flow field during the momentum equation solution procedure, using the Prandtl-Taylor mixing length model near the wall, and using the two-equation $k-\varepsilon$ model in the core. Values of α_t are therefore known before the heat transfer calculations are begun.

With the turbulent modelling of the heat transfer thus implemented, the next major difficulty has been to solve, on curvilinear coordinates, for the heat transfer in banks of tubes.

Periodic heat transfer on curvilinear grids

The method employed to calculate heat transfer for the periodic case (tube in a tube bank) is based on the paper by Patankar et al. [5]. Their procedure uses a generalization of the idea of fully developed flow and heat transfer to include configurations with periodically changing boundaries. For a boundary which varies periodically in the x-direction they define

$$\theta(x,y) = \frac{T(x,y) - T_w}{T_x^*(x) - T_w} , \tag{18}$$

$$T_x^*(x) = T_w + \frac{\int_{y_1}^{y_2} (T(x,y) - T_w) \mid U \mid dy}{\int_{y_1}^{y_2} \mid U \mid dy} . \tag{19}$$

$$\lambda(x) = \frac{dT_x^*(x)}{dx} \frac{1}{T_x^*(x) - T_w} , \tag{20}$$

where T_w is the wall temperature, and $T(x,y)$ is the temperature of the fluid. T_x^* is a local reference temperature defined so that it will be a function of x only. The use of the absolute value (of U) in the definition of T_x^* prevents possible division by zero in a recirculating flow. λ is a non-dimensional parameter defined for convenience in working with the non-dimensional energy equation given below. In Cartesian coordinates the non-dimensional energy equation is written as [5]:

$$U \frac{\partial \theta}{\partial x} + V \frac{\partial \theta}{\partial y} - \frac{\partial}{\partial x} \left(\alpha_e \frac{\partial \theta}{\partial x} \right) - \frac{\partial}{\partial y} \left(\alpha_e \frac{\partial \theta}{\partial y} \right) = \sigma , \tag{21}$$

where

$$\sigma=\lambda\left[2\alpha_e\left(\frac{\partial\theta}{\partial x}\right)-U\theta+\theta\frac{\partial\alpha_e}{\partial x}\right]+\alpha_e\theta\left[\lambda^2+\frac{d\lambda}{dx}\right] . \tag{22}$$

In a region of periodically varying boundaries, θ, and therefore also λ, will be periodic quantities, with one period corresponding to the length of the calculation domain [5]. This energy equation has two unknowns: θ and λ. A second equation is therefore needed, this coming from the definition of T_x^*:

$$\int_{y_1}^{y_2}|U|\,dy=\int_{y_1}^{y_2}\theta|U|\,dy . \tag{23}$$

To solve for θ, then, it is necessary to also solve for λ. However, λ does not appear explicitly in equation (23). An equation for $\lambda(x)$ is obtained by integrating the non-dimensional energy equation with respect to y. In finite difference form the equation for $\lambda(x)$ is obtained by summing the columns of grid nodes in the y-direction. The finite difference solution of the non-dimensional energy equation is found by following the iteration sequence given by Patankar et al. [5]:

1. Initialize the variables: set $\theta=1.0$ and $\lambda=0.0$ everywhere.

2. Solve the finite difference equation for θ and let $\theta'=\theta$.

3. Evaluate $\Omega=\dfrac{\int_{y_1}^{y_2}|U|\,dy}{\int_{y_1}^{y_2}\theta|U|\,dy}$ and let $\theta=\Omega\theta'$.

4. Solve the finite difference equation for λ.

5. Check for convergence. If the sum of the residuals is greater than the specified convergence value return to step 2 and continue to iterate.

When the converged solution is found Ω will be equal to one for all x, and equation (23) will be satisfied. The indirect use of the second equation, equation (23), is analogous to the indirect use of the continuity equation to solve for pressure in the momentum equations.

In a curvilinear coordinate system the method is essentially the same. Now, however, the periodicity occurs in the ζ-direction, and the equation for λ is found by integrating with respect to η (which translates in finite difference form to summing the columns of grid nodes in the η-direction). We therefore redefine T_x^* and λ so that they will be functions of ζ only:

$$\theta(x,y)=\theta(\zeta,\eta)=\frac{T(\zeta,\eta)-T_w}{T_x^*(\zeta)-T_w}\ , \tag{24}$$

$$T_x^*(x,y)=T_x^*(\zeta)=T_w+\frac{\int_{\eta_1}^{\eta_2}(T(\zeta,\eta)-T_w)\,|U|\,d\eta}{\int_{\eta_1}^{\eta_2}|U|\,d\eta}\ , \tag{25}$$

$$\lambda(x,y)=\lambda(\zeta)=\frac{dT_x^*(\zeta)}{d\zeta}\frac{1}{T_x^*(\zeta)-T_w}\ . \tag{26}$$

The energy equation in curvilinear coordinates is written [11]

$$\left[\sqrt{g}(\rho U^i T-\rho\alpha_e g^{ij}T_{\zeta^j})\right]_{\zeta^i}=0\ , \tag{27}$$

where $U^i=\vec{a}^i\cdot(U\hat{e}_x+V\hat{e}_y)$ [1], $\vec{a}^i$ are the contravariant base vectors ($\vec{a}^i=\nabla\zeta^i$), and $\sqrt{g}$ and g^{ij} are the metric coefficients of the curvilinear coordinates [12]. Using the above definitions of θ, T_x^*, and λ the curvilinear form of the energy equation can be re-written as [11]

$$\left[\sqrt{g}(\rho U^i\theta-\rho\alpha_e g^{ij}\theta_{\zeta^j})\right]_{\zeta^i}=\sigma\ , \tag{28}$$

where

$$\sigma=\lambda\theta\left[(\rho\alpha_e\sqrt{g}g^{11})_{\zeta^1}+(\rho\alpha_e\sqrt{g}g^{12})_{\zeta^2}-\rho\sqrt{g}U^1\right]+ \tag{29}$$

$$+2\lambda\rho\alpha_e\sqrt{g}(g^{11}\theta_{\zeta^1}+g^{12}\theta_{\zeta^2})+\rho\alpha_e\theta g^{11}\sqrt{g}(\lambda^2+\frac{d\lambda}{d\zeta})\ .$$

This non-dimensional energy equation can be solved using the periodicity of θ as a boundary condition on the inlet and exit planes of the computational domain. The solution procedure follows the sequence given above. Because T_x^* has been redefined here for curvilinear grids, however, the parameter Ω, which is used during the iteration process to guide the variables toward the proper solution, must also be redefined. The definition of Ω is now motivated by the following equality, which comes directly from the definition of T_x^*:

$$\int_{\eta_1}^{\eta_2}|U|\,d\eta=\int_{\eta_1}^{\eta_2}\theta\,|U|\,d\eta\ . \tag{30}$$

This equality must be satisfied when convergence is achieved. To force this condition to hold, then, we define

$$\Omega = \frac{\int_{\eta_1}^{\eta_2} |U| \, d\eta}{\int_{\eta_1}^{\eta_2} \theta |U| \, d\eta} \tag{31}$$

in analogy with the earlier Cartesian definition of Ω, and use the iteration sequence from Patankar:

1. Initialize the variables: set $\theta=1.0$ and $\lambda=0.0$ everywhere. The flow field variables come from the previous solution of the momentum and k and ε equations.

2. Solve the finite difference equation for θ. Let $\theta^l=\theta$.

3. Evaluate $\Omega = \dfrac{\int_{\eta_1}^{\eta_2} |U| \, d\eta}{\int_{\eta_1}^{\eta_2} \theta |U| \, d\eta}$. Let $\theta=\Omega\theta^l$.

4. Solve the finite difference equation for λ.

5. Check for convergence. If the sum of the residuals is greater than the specified convergence value return to step 2 and continue to iterate.

Ω will everywhere equal one when the converged solution is found.

Note that this method assumes periodicity of the non-dimensional temperature for all regions of the flow. In reality there will be a developing region where the assumption of periodicity will not be valid. If we look at tubes far enough downstream, however, this effect will be negligible, especially for configurations which have short thermal entrance lengths (such as heat transfer in banks of tubes).

In the periodic calculations it is necessary, upon finding a converged solution for θ, the non-dimensional temperature, to evaluate the actual (dimensional) temperature distribution at some region within the tube bank. Viscosity can then be taken as a function of temperature in calculating particle trajectories through the flow.

The method used to evaluate actual temperatures is similar to that given by Patankar [5]. In the present work, however, the method is modified to make use of the curvilinear formulation of the energy equation, with the variables defined above. A solution of this equation gives values of θ and λ everywhere in the computational domain. Integrating the definition of λ with respect to ζ gives the expression for $T_x^*(\zeta)$:

$$T_c^*(\zeta)-T_w=(T_c^*(0)-T_w)\exp\left(\int_0^{\zeta}\lambda(\zeta^*)d\zeta^*\right) . \tag{32}$$

$\zeta=0$ is the inlet plane of the periodic domain. We specify the local reference temperature $T_c^*(0)$ at this plane as a parameter of the problem. Now $T_c^*(\zeta)$ and $\theta(\zeta,\eta)$ are known everywhere in the region of interest. The temperature $T(x,y)=T(\zeta,\eta)$ is obtained from the definition of θ:

$$T(x,y)=T(\zeta,\eta)=\theta(\zeta,\eta)(T_c^*(\zeta)-T_w)+T_w . \tag{33}$$

For the non-periodic case the dimensional energy equation is used, with boundary conditions given by a specified inlet temperature at the inlet plane and a fully developed temperature profile at the exit plane. The solution is found by iterating until convergence is achieved. There is no need to calculate λ or Ω.

Discretization of the equations

Computations are performed in the $\zeta-\eta$ domain. The curvilinear coordinates in real (Cartesian $x-y$) space are mapped into $\zeta-\eta$ space where the unit grids have an area equal to one, and sides of length one [12]. The grid nodes, where the values of all variables are specified, are located at the intersections of the grid lines (see Figure 4). The calculations are therefore performed on a non-staggered grid. Boundary values are given at the boundary grid points which, for the non-staggered grid, lie directly on the boundary lines.

The generalized convection diffusion equation in curvilinear coordinates is written [1, 12] for an arbitrary scalar quantity ϕ with the source term b

$$\left[\sqrt{g}(\rho U^i\phi-\Gamma g^{ij}\phi_{\zeta^j})\right]_{\zeta^i}-b=0 . \tag{34}$$

Expanding this gives

$$(\sqrt{g}\rho U^1\phi)_{\zeta^1}-(\sqrt{g}\Gamma g^{11}\phi_{\zeta^1})_{\zeta^1}-(\sqrt{g}\Gamma g^{12}\phi_{\zeta^2})_{\zeta^1}+ \tag{35}$$

$$+(\sqrt{g}\rho U^2\phi)_{\zeta^2}-(\sqrt{g}\Gamma g^{21}\phi_{\zeta^1})_{\zeta^2}-(\sqrt{g}\Gamma g^{22}\phi_{\zeta^2})_{\zeta^2}=b .$$

Here, as before,

$$U^i=\vec{a}^i\cdot(U\hat{e}_x+V\hat{e}_y)$$

and

$$\vec{a}^i = \nabla \zeta^i \ ,$$

and $\sqrt{g}$ and g^{ij} are the metric coefficients. i and j take on the values 1 or 2 for the two-dimensional calculation domain. For convenience the symbols $\zeta = \zeta^1$ and $\eta = \zeta^2$, are also used in the text.

Define

$$g12term = (\sqrt{g}\Gamma g^{12}\phi_{\zeta^2})_{\zeta^1} + (\sqrt{g}\Gamma g^{21}\phi_{\zeta^1})_{\zeta^2} \ , \tag{36}$$

so that

$$(\sqrt{g}\rho U^1\phi)_{\zeta^1} + (\sqrt{g}\rho U^2\phi)_{\zeta^2} - (\sqrt{g}\Gamma g^{11}\phi_{\zeta^1})_{\zeta^1} - (\sqrt{g}\Gamma g^{22}\phi_{\zeta^2})_{\zeta^2} = b + g12term \tag{37}$$

This allows the cross-terms involving g^{12} and g^{21} to be treated as source terms.

To discretize this equation we follow the method given by Patankar [4] and integrate it over a unit control volume (see Figure 4). The discretized form of the equation requires the evaluation of derivatives at the control volume boundaries. If we assume a piecewise-linear profile for the variable and use central differencing to evaluate the derivatives we obtain the desired form of the discretized equation. Values of the various parameters, as well as the variables, at the control volume boundaries are obtained from the piecewise-linear profile assumption. The source term $b + g12term$ is assumed to be constant throughout the control volume. The discretized form of the equation is [1]:

$$A_P\phi_P = A_E\phi_E + A_W\phi_W + A_N\phi_N + A_S\phi_S + S_\mu \ , \tag{38}$$

where

$$S_\mu + S_P\phi_P = b + g12term \ ,$$

$$A_P = \frac{1}{2}(\sqrt{g}\rho U^1)\Big|_{Eb} - \frac{1}{2}(\sqrt{g}\rho U^1)\Big|_{Wb} + \frac{1}{2}(\sqrt{g}\rho U^2)\Big|_{Nb} - \frac{1}{2}(\sqrt{g}\rho U^2)\Big|_{Sb} +$$

$$+ (\sqrt{g}\Gamma g^{11})\Big|_{Eb} + (\sqrt{g}\Gamma g^{11})\Big|_{Wb} + (\sqrt{g}\Gamma g^{22})\Big|_{Nb} + (\sqrt{g}\Gamma g^{22})\Big|_{Sb} - S_P \ ,$$

$$A_E = (\sqrt{g}\Gamma g^{11})\Big|_{Eb} - \frac{1}{2}(\sqrt{g}\rho U^1)\Big|_{Eb} \ ,$$

$$A_W=(\sqrt{g}\Gamma g^{11})\Big|_{Wb}+\frac{1}{2}(\sqrt{g}\rho U^1)\Big|_{Wb},$$

$$A_N=(\sqrt{g}\Gamma g^{22})\Big|_{Nb}-\frac{1}{2}(\sqrt{g}\rho U^2)\Big|_{Nb},$$

$$A_S=(\sqrt{g}\Gamma g^{22})\Big|_{Sb}+\frac{1}{2}(\sqrt{g}\rho U^2)\Big|_{Sb}.$$

By continuity, and using the curvilinear relation from Thompson [12] for the divergence, it can be shown that

$$\sqrt{g}(\nabla\cdot\vec{u})=(\sqrt{g}\rho U^1)_{\zeta^1}+(\sqrt{g}\rho U^2)_{\zeta^2}=0. \tag{39}$$

In finite difference form this expression becomes

$$\frac{1}{2}(\sqrt{g}\rho U^1)\Big|_{Eb}-\frac{1}{2}(\sqrt{g}\rho U^1)\Big|_{Wb}+\frac{1}{2}(\sqrt{g}\rho U^2)\Big|_{Nb}-\frac{1}{2}(\sqrt{g}\rho U^2)\Big|_{Sb}=0. \tag{40}$$

Therefore,

$$A_P=A_E+A_W+A_N+A_S-S_P. \tag{41}$$

Define the convection terms by

$$F=(\sqrt{g}\rho U^i) \tag{42}$$

and define the diffusion terms by

$$D=(\sqrt{g}\Gamma g^{ij}). \tag{43}$$

Then the above can be written

$$A_E=D_e-\frac{1}{2}F_e,$$

$$A_W=D_w+\frac{1}{2}F_w,$$

$$A_N = D_n - \frac{1}{2} F_n \ ,$$

$$A_S = D_s + \frac{1}{2} F_s \ ,$$

where

$$D_e = (\sqrt{g}\Gamma g^{11})\Big|_{Eb} \ , \ F_e = (\sqrt{g}\rho U^1)\Big|_{Eb} \ ,$$

$$D_w = (\sqrt{g}\Gamma g^{11})\Big|_{Wb} \ , \ F_w = (\sqrt{g}\rho U^1)\Big|_{Wb} \ ,$$

$$D_n = (\sqrt{g}\Gamma g^{22})\Big|_{Nb} \ , \ F_n = (\sqrt{g}\rho U^2)\Big|_{Nb} \ ,$$

$$D_s = (\sqrt{g}\Gamma g^{22})\Big|_{Sb} \ , \ F_s = (\sqrt{g}\rho U^2)\Big|_{Sb} \ .$$

Now we redefine the A coefficients using the hybrid scheme. This scheme prevents divergence of the code by modifying the finite differencing method. In the derivation above it is assumed that the value of ϕ at a control volume boundary is given by the weighted average of the values of ϕ at the two grid points adjacent to the control volume boundary. At high Reynolds numbers, however, this assumption is not valid; the values of ϕ at the control volume boundary will be very near to the values of ϕ at the grid point just upwind of this boundary. The upwind scheme uses these upwind grid point values at the control volume boundary and dispenses with the averaging. In the hybrid scheme the finite differencing method is varied according to the relative magnitude of convective and diffusive effects. When the convective terms, F, are larger than twice the diffusive terms, $2D$, the upwind scheme is used. If the diffusive effects are larger, or if convection and diffusion are on the same order of magnitude ($F<2D$), then the finite differencing method is as given above: the value of ϕ at the control volume boundary is taken to be the weighted average of the values of ϕ at the grid nodes adjacent to the control volume boundary. The hybrid scheme is implemented by adjusting the A coefficients as follows:

$$A_E = \max\left(\left|\frac{F_e}{2}\right|, D_e\right) - \frac{F_e}{2} \ , \tag{44}$$

$$A_W = \max\left(\left|\frac{F_w}{2}\right|, D_w\right) + \frac{F_w}{2} \ , \tag{45}$$

$$A_N=\max\left(\left|\frac{F_n}{2}\right|,D_n\right)-\frac{F_n}{2}\ , \tag{46}$$

$$A_S=\max\left(\left|\frac{F_s}{2}\right|,D_s\right)+\frac{F_s}{2}\ , \tag{47}$$

$$A_P=A_E+A_W+A_N+A_S-S_P+\max((F_n-F_s+F_e-F_w),0)\ . \tag{48}$$

The only term which remains to be specified is the source term $b+g12term$. Integrating over the unit control volume (which leaves the source terms unchanged for the case of the assumed stepwise profile) and then using central differencing to evaluate the derivatives gives the result for $g12term$:

$$g12term=\frac{1}{4}\left[(\sqrt{g}\Gamma g^{12})\Big|_E(\phi_{NE}-\phi_{SE})-(\sqrt{g}\Gamma g^{12})\Big|_W(\phi_{NW}-\phi_{SW})\right]+ \tag{49}$$

$$+\frac{1}{4}\left[(\sqrt{g}\Gamma g^{21})\Big|_N(\phi_{NE}-\phi_{NW})-(\sqrt{g}\Gamma g^{21})\Big|_S(\phi_{SE}-\phi_{SW})\right]\ .$$

The discretized form of the source term b depends on the continuous form of b. We are principally concerned with three cases: 1. the momentum equations, in which b is related to the pressure gradient; 2. the k and ε equations for turbulent kinetic energy and dissipation of turbulent kinetic energy, in which b comes from the generation and loss of turbulent energy and dissipation of turbulent energy [10]; and 3. the energy equation, in which b results from the non-dimensionalization of the periodic form of the energy equation.

Consider first the U-momentum equation. In Cartesian coordinates the equation to be solved is

$$(U^1\rho U-\mu_e U_{x^1})_{x^1}+P_{x^1}=\beta\ , \tag{50}$$

where

$$p=-\beta x^1+P\ . \tag{51}$$

$p(x,y)$ is the total pressure, which is equal to the periodic pressure $P(x,y)$ plus a pressure-drop term $-\beta x^1$. The pressure-drop coefficient β is specified as an input to the problem. The flow rate in a periodic calculation is determined by the magnitude of β. For the non-periodic case $\beta=0$. The V-momentum equation is similar, but does not contain the β-term:

$$(U^{i}\rho V-\mu_{e}V_{x^{i}})_{x^{i}}+P_{x^{2}}=0 \ . \tag{52}$$

In curvilinear coordinates these momentum equations become, respectively,

$$[\sqrt{g}(\rho U^{i}U-\mu_{e}g^{ij}U_{\zeta^{j}})]_{\zeta^{i}}+(y_{\zeta^{2}}P)_{\zeta^{1}}-(y_{\zeta^{1}}P)_{\zeta^{2}}=\sqrt{g}\beta \ , \tag{53}$$

and

$$[\sqrt{g}(\rho U^{i}V-\mu_{e}g^{ij}V_{\zeta^{j}})]_{\zeta^{i}}-(x_{\zeta^{2}}P)_{\zeta^{1}}+(x_{\zeta^{1}}P)_{\zeta^{2}}=0 \ . \tag{54}$$

For the U-momentum equation the source term is

$$b=\sqrt{g}\beta-(y_{\zeta^{2}}P)_{\zeta^{1}}+(y_{\zeta^{1}}P)_{\zeta^{2}} \ , \tag{55}$$

and for the V-momentum equation the source term is

$$b=(x_{\zeta^{2}}P)_{\zeta^{1}}-(x_{\zeta^{1}}P)_{\zeta^{2}} \ . \tag{56}$$

The $\frac{\partial P}{\partial x}$ and $\frac{\partial P}{\partial y}$ terms in curvlinear form come from the expressions for derivatives given by Thompson [12]. For a general variable ϕ:

$$\frac{\partial\phi}{\partial x}=\frac{1}{\sqrt{g}}\left[\left(\frac{\partial y}{\partial\eta}\phi\right)_{\zeta}-\left(\frac{\partial y}{\partial\zeta}\phi\right)_{\eta}\right]=\frac{1}{\sqrt{g}}\left[\left(\sqrt{g}a^{1i}\phi\right)_{\zeta}+\left(\sqrt{g}a^{2i}\phi\right)_{\eta}\right] \ , \tag{57}$$

$$\frac{\partial\phi}{\partial y}=\frac{1}{\sqrt{g}}\left[\left(\frac{\partial x}{\partial\zeta}\phi\right)_{\eta}-\left(\frac{\partial x}{\partial\eta}\phi\right)_{\zeta}\right]=\frac{1}{\sqrt{g}}\left[\left(\sqrt{g}a^{2j}\phi\right)_{\eta}+\left(\sqrt{g}a^{1j}\phi\right)_{\zeta}\right] \ . \tag{58}$$

The last equality in both equations comes from the relations

$$\frac{1}{\sqrt{g}}\frac{\partial y}{\partial\eta}=\frac{\partial\zeta}{\partial x}=a^{1i} \ , \ -\frac{1}{\sqrt{g}}\frac{\partial y}{\partial\zeta}=\frac{\partial\eta}{\partial x}=a^{2i} \ ,$$

$$-\frac{1}{\sqrt{g}}\frac{\partial x}{\partial\eta}=\frac{\partial\zeta}{\partial y}=a^{1j} \ , \ \frac{1}{\sqrt{g}}\frac{\partial x}{\partial\zeta}=\frac{\partial\eta}{\partial y}=a^{2j} \ .$$

Applying central differencing in the $\zeta-\eta$ space to the terms of the equations for $\frac{\partial\phi}{\partial x}$ and $\frac{\partial\phi}{\partial y}$ gives

$$\left.\frac{\partial\phi}{\partial x}\right|_P = \left.\frac{1}{2\sqrt{g}}\right|_P \left[a^{11}\sqrt{g}\Big|_E \phi_E - a^{11}\sqrt{g}\Big|_W \phi_W + a^{21}\sqrt{g}\Big|_N \phi_N - a^{21}\sqrt{g}\Big|_S \phi_S \right] , \tag{59}$$

$$\left.\frac{\partial\phi}{\partial y}\right|_P = \left.\frac{1}{2\sqrt{g}}\right|_P \left[a^{22}\sqrt{g}\Big|_N \phi_N - a^{22}\sqrt{g}\Big|_S \phi_S + a^{12}\sqrt{g}\Big|_E \phi_E - a^{12}\sqrt{g}\Big|_W \phi_W \right] . \tag{60}$$

This gives the discretized form of the source term for the U-momentum equation.

$$b = \sqrt{g}\beta - \frac{1}{2}\left\{ (a^{11}\sqrt{g})\Big|_E P_E - (a^{11}\sqrt{g})\Big|_W P_W + (a^{21}\sqrt{g})\Big|_N P_N - (a^{21}\sqrt{g})\Big|_S P_S \right\} . \tag{61}$$

For the V-momentum equation,

$$b = -\frac{1}{2}\left\{ (a^{12}\sqrt{g})\Big|_E P_E - (a^{12}\sqrt{g})\Big|_W P_W + (a^{22}\sqrt{g})\Big|_N P_N - (a^{22}\sqrt{g})\Big|_S P_S \right\} . \tag{62}$$

$S_P=0$ for the momentum equations, so $S_\mu = b + g\,12 term$.

The convection-diffusion equations for turbulent kinetic energy k and dissipation of turbulent kinetic energy ε are given in curvilinear form as [1]

$$\left[\sqrt{g}(\rho U^i k - \rho\alpha_e g^{ij} k_{\zeta^j})\right]_{\zeta^i} - \sqrt{g}G + \sqrt{g}C_D\rho\varepsilon = 0 , \tag{63}$$

and

$$\left[\sqrt{g}(\rho U^i \varepsilon - \rho\alpha_e g^{ij} \varepsilon_{\zeta^j})\right]_{\zeta^i} - \sqrt{g}C_1\frac{\varepsilon}{k}G + \sqrt{g}C_2\rho\frac{\varepsilon^2}{k} = 0 . \tag{64}$$

The source term for the k-equation is then

$$b = \sqrt{g}G - \sqrt{g}C_D\rho\varepsilon . \tag{65}$$

For the ε-equation the source term is

$$b = \sqrt{g}C_1\frac{\varepsilon}{k}G - \sqrt{g}C_2\rho\frac{\varepsilon^2}{k} . \tag{66}$$

From the relation given earlier, $\nu_t = C_\mu\dfrac{k^2}{\varepsilon}$, these become, respectively,

$$b=\sqrt{g}G-\sqrt{g}C_D C_\mu \rho \frac{k^2}{\nu_t} , \tag{67}$$

and

$$b=\sqrt{g}C_1 G\frac{k}{\nu_t}-\sqrt{g}C_2\rho\frac{\varepsilon^2}{k} . \tag{68}$$

Discretizing as before gives, simply,

$$b=\sqrt{g}\,|_P G\,|_P-\sqrt{g}\,|_P C_D C_\mu \rho\frac{k_P^2}{\nu_t\,|_P} , \tag{69}$$

and

$$b=\sqrt{g}\,|_P C_1 G\,|_P\frac{k}{\nu_t}-\sqrt{g}\,|_P C_2\rho\frac{\varepsilon_P^2}{k_P} . \tag{70}$$

G is the generation of turbulent kinetic energy. In cartesian coordinates this is

$$G=\rho\nu_t\frac{\partial U_i}{\partial x_j}\left(\frac{\partial U_i}{\partial x_j}+\frac{\partial U_j}{\partial U_i}\right)=\rho\nu_e\left[2\left(\frac{\partial U}{\partial x}\right)^2+2\left(\frac{\partial V}{\partial y}\right)^2+\left(\frac{\partial U}{\partial y}+\frac{\partial V}{\partial x}\right)^2\right] . \tag{71}$$

G is evaluated at the grid point P, so in discretized form we have to evaluate:

$$G_P=\rho\nu_t\,|_P\left[2\left(\frac{\partial U}{\partial x}\bigg|_P\right)^2+2\left(\frac{\partial V}{\partial y}\bigg|_P\right)^2+\left(\frac{\partial U}{\partial y}\bigg|_P+\frac{\partial V}{\partial x}\bigg|_P\right)^2\right] . \tag{72}$$

To this end, the derivatives of the velocities are evaluated from the derivative expressions from Thompson given above.

From the expressions for the source terms b we see that S_μ and S_P for the k and ε equations, respectively, are

$$S_{\mu_k}=\sqrt{g}\,|_P G_P+g\,12term , \tag{73}$$

$$S_{P_k}=-\sqrt{g}\,|_P C_D C_\mu \rho\frac{k_P}{\nu_t\,|_P} , \tag{74}$$

$$S_{\mu_e}=\sqrt{g}\,|_P C_1 C_\mu G\,|_P \frac{k_P}{\nu_t\,|_P} + g\,12 term \ , \tag{75}$$

$$S_{P_e}=-\sqrt{g}\,|_P C_2 \rho \frac{\varepsilon_P}{k_P} \ . \tag{76}$$

Finally we must consider the energy equation. In Cartesian coordinates the non-dimensional energy equation is

$$(U^i \rho\theta - \rho\alpha_e \theta_{x^i})_{x^i}=\sigma \ . \tag{77}$$

σ is the source term which results from non-dimensionalizing the periodic energy equation.

In curvilinear coordinates,

$$[\sqrt{g}(\rho U^i \theta - \rho\alpha_e g^{ij}\theta_{\zeta^j})]_{\zeta^i}=\sigma=b \ , \tag{78}$$

where

$$b=\sigma=\lambda\theta\left[(\rho\alpha_e\sqrt{g}g^{11})_{\zeta^1}+(\rho\alpha_e\sqrt{g}g^{12})_{\zeta^2}-\rho\sqrt{g}U^1\right]+ \tag{79}$$

$$+2\lambda\rho\alpha_e\sqrt{g}(g^{11}\theta_{\zeta^1}+g^{12}\theta_{\zeta^2})+\rho\alpha_e\theta g^{11}\sqrt{g}(\lambda^2+\frac{d\lambda}{d\zeta}) \ .$$

For the computations we let $\lambda^2=2\lambda\lambda_o-\lambda_o^2$ where λ is the current value of λ (to be solved for) while λ_o is the value of λ from the last iteration. This keeps the finite difference equation for λ linear in λ (no λ^2 term):

$$\sigma=\lambda\left\{\theta\left[(\rho\alpha_e\sqrt{g}g^{11})_{\zeta^1}+(\rho\alpha_e\sqrt{g}g^{12})_{\zeta^2}-\rho\sqrt{g}U^1\right]\right\}+ \tag{80}$$

$$+\lambda\left\{2\rho\alpha_e\sqrt{g}(g^{11}\theta_{\zeta^1}+g^{12}\theta_{\zeta^2})+2\lambda_o\rho\alpha_e\theta g^{11}\sqrt{g}\right\}+$$

$$+\frac{d\lambda}{d\zeta}\rho\alpha_e\theta g^{11}\sqrt{g}-\lambda_o^2\rho\alpha_e\theta g^{11}\sqrt{g} \ .$$

Using the stepwise profile assumption for this source term, with central differencing to evaluate the derivative of λ, gives

$$b=Q\lambda_P+P\lambda_W+R\lambda_E+S \ , \tag{81}$$

where

$$Q=\theta_P\left\{\frac{1}{2}\left[(\rho\alpha_e\sqrt{g}g^{11})\Big|_E-(\rho\alpha_e\sqrt{g}g^{11})\Big|_W\right]+\frac{1}{2}\left[(\rho\alpha_e\sqrt{g}g^{12})\Big|_N-(\rho\alpha_e\sqrt{g}g^{12})\Big|_S\right]-\rho\sqrt{g}\left[(a^{1i}u)\Big|_P+(a^{1j}v)\Big|_P\right]\right\}+$$

$$+2\rho\alpha_e\sqrt{g}\left[g^{11}\frac{1}{2}(\theta_E-\theta_W)+g^{12}\frac{1}{2}(\theta_N-\theta_S)\right]+2\rho\alpha_e\lambda_o\sqrt{g}g^{11}\theta_P \ ,$$

$$R=\frac{1}{2}\rho\alpha_e\sqrt{g}g^{11}\theta_P \ ,$$

$$P=-R=-\frac{1}{2}\rho\alpha_e\sqrt{g}g^{11}\theta_P \ ,$$

$$S=-\rho\alpha_e\lambda_o^2g^{11}\sqrt{g}\theta_P \ .$$

Here we have used the metric factors a^{1i} and a^{1j} defined by Schuh [1] as

$$\vec{a^1}=a^{1i}\hat{e_x}+a^{1j}\hat{e_y} \ ,$$

with the definition of U^1 [1],

$$U^1=\vec{a^1}\cdot(U\hat{e_x}+V\hat{e_y})=a^{1i}U+a^{1j}V \ .$$

For the non-dimensional energy equation, then,

$$S_\mu=Q\lambda_P+P\lambda_W+R\lambda_E+g12term \ , \tag{82}$$

and

$$S_P=\frac{S}{\theta_P} \ . \tag{83}$$

The equation for λ, which is solved together with θ, comes from summing the equation for θ over all j nodes (summing in the η direction). The equation for θ can be

written

$$A_P \theta_P = A_E \theta_E + A_W \theta_W + A_N \theta_N + A_S \theta_S + g\,12 term + Q\lambda_P + P\lambda_W + R\lambda_E \ , \tag{84}$$

or for the entire field of points

$$A_{P_{i,j}} \theta_{P_{i,j}} = A_{E_{i,j}} \theta_{i+1,j} + A_{W_{i,j}} \theta_{i-1,j} + A_{N_{i,j}} \theta_{i,j+1} + A_{S_{i,j}} \theta_{i,j-1} + g\,12 term_{i,j} + Q_{i,j}\lambda_i + P_{i,j}\lambda_{i-1} + R_{i,j}\lambda_{i+1} \ . \tag{85}$$

Now summing over j gives

$$-\left(\sum_j Q_{i,j}\right)\lambda_i = \sum_j \left(-A_{P_{i,j}}\theta_{i,j} + A_{E_{i,j}}\theta_{i+1,j} + A_{W_{i,j}}\theta_{i-1,j} + A_{N_{i,j}}\theta_{i,j+1} + A_{S_{i,j}}\theta_{i,j-1}\right) + \tag{86}$$

$$+\sum_j g\,12 term_{i,j} + \left(\sum_j R_{i,j}\right)\lambda_{i+1} + \left(\sum_j P_{i,j}\right)\lambda_{i-1} \ .$$

Define

$$A_i = -\left(\sum_j Q_{i,j}\right) \ ,$$

$$B_i = \left(\sum_j R_{i,j}\right) \ ,$$

$$C_i = \left(\sum_j P_{i,j}\right) = -B_i \ ,$$

$$D_i = \sum_j g\,12 term_{i,j} +$$

$$+\sum_j \left(-A_{P_{i,j}}\theta_{i,j} + A_{E_{i,j}}\theta_{i+1,j} + A_{W_{i,j}}\theta_{i-1,j} + A_{N_{i,j}}\theta_{i,j+1} + A_{S_{i,j}}\theta_{i,j-1}\right) \ .$$

so that

$$A_i \lambda_i = B_i \lambda_{i+1} + C_i \lambda_{i-1} + D_i \ . \tag{87}$$

This is the finite difference equation for λ, which is solved together with the un-summed energy equation for θ.

For the non-periodic dimensional energy equation in curvlinear coordinates,

$$\left[\sqrt{g}(\rho U' T - \rho\alpha_e g'' T_{\zeta'})\right]_{\zeta'} = 0 \,, \tag{88}$$

the source term b is zero. Then

$$S_\mu = g\,12 term \,, \tag{89}$$

and

$$S_P = 0 \,. \tag{90}$$

Implementation of the boundary conditions.

There are four types of boundary conditions around the calculation domain, as shown in Figure 2. These are:

1. the tube surface, where the variables are held at specified values,
2. the top and bottom symmetry planes where $\frac{\partial \phi}{\partial y} = 0$ and $V = 0$,
3. the fully developed exit plane (for the non-periodic case) where $\frac{\partial^2 \phi}{\partial x^2} = 0$, and
4. the periodic case in which the values of the variables at the inlet planes are matched to (set equal to) the values at the exit plane.

At the inlet plane of the non-periodic flow region the values of the variables are specified as parameters of the problem. The non-periodic inlet plane grid nodes are therefore not part of the solution domain. All boundary values are given at the boundary grid points, which lie directly on the boundary lines for the non-staggered grid.

At boundaries where the variables are fixed at specified values, the A coefficients for the boundary points are modified, and the variables are set to the required values. For a boundary grid node the finite difference equation of a general variable ϕ at the point is

$$A_P \phi_P = A_E \phi_E + A_W \phi_W + A_N \phi_N + A_S \phi_S + S_\mu \,. \tag{91}$$

For a bottom boundary such as the tube surface A_S is zero. Likewise, for a top boundary A_N is zero. This is an equation which will be solved for ϕ_P. We require, however, to fix ϕ_P to a particular specified value $\phi_{P_{boundary}}$. This is done by setting the variable, coefficients, and source terms as follows:

$$\phi_P = \phi_{P_{boundary}} \tag{92}$$

$$S_P = -\infty \tag{93}$$

$$S_\mu = \infty \phi_{P_{boundary}} \tag{94}$$

Here we have used the terms S_P and S_μ, which are components of the total source term:

$$b + g\,12 term = S_\mu + S_P \phi_P \tag{95}$$

S_P is the source term with linear dependence on ϕ_P. S_P can be absorbed into the A_P coefficient to give [4]:

$$A_P = A_E + A_W + A_N + A_S - S_P \tag{96}$$

S_μ is the source term without linear dependence on ϕ_P. In practice, ∞ is a very large number. The CLEW-T codes use $\infty = 10^{30}$.

Symmetry is imposed at the top and bottom boundary planes by modifying the A_N and A_S coefficients. At a symmetry plane the node above a boundary node will have the same values of the variables as the node below the boundary node, i.e. $\phi_N = \phi_S$. Likewise, the convection and diffusion coefficients for the up and down directions will have equal values at a symmetry boundary node, i.e. $A_N = A_S$. For a top symmetry boundary node, then, the finite difference equation reads

$$A_P \phi_P = A_E \phi_E + A_W \phi_W + A_N \phi_N + A_S \phi_S + S_\mu = A_E \phi_E + A_W \phi_W + 2A_S \phi_S + S_\mu \,, \tag{97}$$

while for a bottom symmetry boundary node the finite difference equation is

$$A_P \phi_P = A_E \phi_E + A_W \phi_W + A_N \phi_N + A_S \phi_S + S_\mu = A_E \phi_E + A_W \phi_W + 2A_N \phi_N + S_\mu \,. \tag{98}$$

We therefore modify the A coefficients at the symmetry boundaries as follows: for a top symmetry boundary

$$A_N = 0 \tag{99}$$

$$A_S = 2A_S \,, \tag{100}$$

and for a bottom symmetry boundary,

$$A_S = 0 \tag{101}$$

$$A_N=2A_N \quad . \tag{102}$$

To accomodate the implementation of the inlet and exit boundary conditions the grids are generated so that they will be left-right symmetric about the center of the calculation domain and Cartesian for the last three columns of grid nodes. The grid is $N+1$ columns long, but the finite difference equations are only solved in the region from $i=2$ to $i=N$. The $i=1$ and $i=N+1$ columns of grid nodes are used to set the inlet and exit boundary conditions. Note that although the inlet and exit plane are not solved for by the tri-diagonal matrix algorithm, their values do affect the values of the variables at the adjacent grid columns through the A_E and A_W coefficients at $i=2$ and $i=N$.

For the non-periodic calculations the inlet variables at $i=1$ are imposed as parameters of the problem. The fully developed exit condition is imposed by copying the values of the variables in the $i+N$ column into the $i=N+1$ column. For the periodic calculations the periodic boundary condition is imposed by setting the variable values in the first two columns of nodes equal to the variable values in the last two columns of nodes. This is done by copying the $i=2$ column values into the $i=N+1$ variables, and copying the $i=N$ values into the $i=1$ variables. In addition, the cyclic tri-diagonal matrix algorithm is used to solve the matrix of finite difference equations from $i=2$ to $i=N$ during periodic calculations.

For the matching of the k and ε values at $y^+=50$ the method of modifying the A coefficients is the same as that for setting the boundary values at the tube surface. For the k and ε equations, however, the boundary condition is at $y^+=50$, not at the tube surface. The values to be specified as boundary conditions come from the Prandtl-Taylor mixing length model with the Van Driest relation for mixing length, as discussed earlier. The matching equations are

$$k=\frac{l^2P}{C_\mu^{\frac{1}{2}}} , \tag{103}$$

and

$$\varepsilon=l^2P^{\frac{3}{2}} , \tag{104}$$

where

$$P=\left[\left(\frac{\partial U}{\partial y}+\frac{\partial V}{\partial x}\right)^2+2\left(\frac{\partial U}{\partial x}\right)^2+\left(\frac{\partial V}{\partial y}\right)^2\right] .$$

At grid nodes where $y^+<50$ the k and ε variables are kept at these values. The nodes just below $y^+=50$ become the boundary nodes for the k and ε equations. The nodes further below the $y^+=50$ line are not used. $\left.\frac{\partial U}{\partial y}\right|_P$ and $\left.\frac{\partial V}{\partial x}\right|_P$ are evaluated from the discretized

form of the curvilinear derivative expressions as discussed earlier in connection with the discretization of the source terms for the momentum equations.

Heat transfer results

Most of the turbulent flow calculations have been performed for the case of a tube in a tube bank. Fortunately, for this case the difficult problem of predicting the point of transition to turbulence ceases to exist. At Reynolds numbers of 40, vortex shedding in the wake of a cylinder begins. At about $Re=150$ the shed vortices begin a transition to a turbulent state, and for Reynolds numbers greater than 300 the shed vortices are fully turbulent [3]. At still higher Reynolds numbers (on the order of 1000) the wake region is fully turbulent immediately behind the cylinder [13]. At Reynolds numbers above 10^5 the boundary layer on the cylinder becomes turbulent before separation [14]. The flow in a bank of tubes will therefore be in a turbulent state for Reyolds numbers greater than about 1000. Tubes away from the entrance to the bank will see a state of fully developed turbulence, so that it is not necessary to attempt to calculate a point of turbulent transition on such downstream tubes. The calculations performed here assume fully developed turbulent flow at the inlet to the calculation domain. It is worth noting that most practical applications involve banks of tubes rather than single tubes or pairs of tubes, so that the conditions simulated here have very practical applications and implications.

Notwithstanding, one turbulent calculation was performed for a tube not in a bank. This calculation was for an approaching turbulent flow at a Reynolds number based on tube diameter of 100,000. The single tube $Re=100000$ case was run as part of the code verification procedure, for comparison to experimental values of Nusselt number obtained for this configuration.

Plots of the flow fields for a single tube, in-line pairs of tubes and a tube in a bank have been given in Schuh [1]. Heat transfer results for single tubes are presented here on plots of Nusselt number (Nu) versus increasing angle from the stagnation point on the tube (θ). For tubes in banks the results are given as $\frac{Nu}{\overline{Nu}}$, where $\overline{Nu}$ is the mean Nusselt number over the tube. This is the way the experimental results for tubes in banks are presented in the literature [15]. This method of presenting the results also overcomes any ambiguities in the definition of Nusselt number. Specifically, the Nusselt number is defined as $Nu=\frac{hD}{k}$, where h is the heat transfer coefficient which satisfies the relation $q=h\Delta T$. In a tube bank it is not clear what temperature difference the ΔT should refer to. If it is defined as $\Delta T=T_{bulk}-T_{wall}$ then the appropriate definition of a bulk temperature in this complex, recirculating flow is unclear. If, on the other hand, it is defined as $\Delta T=T_{inlet}-T_{wall}$ then (for the constant tube wall temperature case) the heat transfer coefficient h will not be the same for tubes nearer the front of the bank as it will be for tubes further from the front. To overcome this difficulty all experimental and numerical results for tubes in banks are presented as $\frac{Nu}{\overline{Nu}}$. For single tubes the absolute Nusselt number is given, where the Nusselt number is defined as $Nu=\frac{hD}{k}$, with D representing the diameter of the tube. Isotherms are also shown for both the single tube and the tube bank configurations.

Laminar calculations were performed during the development of the calculation procedures and codes for comparison to the experimental results of others. These checks were performed to assure that the method of solving for temperatures and heat transfer is valid and accurate. Turbulence models were then introduced for higher Reynolds number flows. Schweitzer [12] gives a more detailed discussion of the laminar results.

The laminar heat transfer from a single tube at Re=120 was calculated for a flow of air entering with a free stream temperature of 320 K. The tube wall temperature was fixed at 300 K. The streamlines and isotherms from this calculation are shown in Figure 5. Figure 6 shows a comparison of Nusselt numbers from the calculated results with the experimental results of Eckert [16]. The plots show Nusselt number as a function of angle from the stagnation point at the front of the tube. The calculations compare extremely well for all points on the tube except for the very front and rear. The deviation from a smooth curve (and from the experimental results) at these points is due to the extreme distortion of the curvilinear grid at these corners. The distorted grid introduces convergence difficulties and errors in interpolating values and evaluating derivatives. Errors in the Nusselt number plots can be seen on all of the calculated results at the front and rear of the tubes, although the relative magnitude of this error varies considerabley. Sometimes the result is over-prediction of heat transfer at the stagnation points (as in the Re=120 case), while at other times the result is under-prediction of heat transfer at these points (as in the $Re=10^5$ case).

The case of a tube bank in a laminar flow of air at Re=450 was calculated also. In this tube bank the ratio of distance between tube centers to tube radius is given by $\frac{L}{D}=1.5$. The normalized Nusselt numbers ($\frac{Nu}{\overline{Nu}}$) for this flow are shown in Figure 7, together with the experimental results from Zhukauskus [15], and the calculated results from Wung and Chen [17, 18]. The figures compare well qualitatively, but the curves do show some differences. The largest discrepancies occur near the front and rear of the tube, where the oscillating vortex shedding of a real flow would be expected to give higher heat transfer rates. This may account for the under-prediction of heat transfer by calculation. The resulting lower mean Nusselt number raises the peaks of the curve of $\frac{Nu}{\overline{Nu}}$, so that the curve maintains the correct shape, but becomes higher and lower in magnitude at its extremes. The calculation by Wung and Chen, which is also based on a steady-flow model, suffers from the same problem. It is interesting then to note that the magnitudes of the present calculations are very close to those of the calculation by Wung and Chen.

Figure 8 shows a plot of the Nusselt numbers for a single tube in a turbulent free stream of air at a Reynolds number of 100,000. The calculations can be compared with the empirical data from Achenbach [14]. The data from Achenbach is for an approaching laminar flow, while the calculated results are for an approaching turbulent flow. Taking the minimum Nusselt number point as the point at which separation occurs, the calculation shows separation at about 100 degrees from the stagnation point, while the data from Achenbach shows separation at about 85 degrees. The greater momentum of the turbulent boundary layer in the calculations delays the separation point 15 degrees. In addition, the levels of turbulence in the calculations and the experiments are not the same, and the values of the Nusselt numbers are therefore different. This difficulty is compounded by the fact that Achenbach fails to define the heat transfer coeffiecient used in the definition of the Nusselt number. It is therefore not possible to compare the experimental and calculated results exactly. The significance is that the shapes of the curves compare well, although the

distortion of the curvilinear grid at the front and rear of the tube affects the calculated Nusselt numbers, causing under-prediction of heat transfer at the front and rear stagnation points. Given these shortcomings, however, it is worth noting that the calculations do give qualitatively reasonable results in terms of the general shapes of the plots. Perfect quantitative comparison cannot be expected in such a high Reynolds number regime, where levels of turbulence in experiments are not well controlled, and are not reported with the experimental results.

Figure 9 shows the calculated isotherms for a Re=140,000 flow in a tube bank with an aspect ratio of $\frac{L}{D}$=2.0. Figure 10 gives particle trajectories for this flow.

Particle trajectories

Particle trajectories are calculated with the procedure developed by Schuh and Schuler [2]. Their method was modified by the addition of a temperature-varying viscosity for the carrier fluid, air, and an interpolation procedure for evaluating the temperatures of points not on the grid nodes. For isothermal calculations the viscosity is fixed at the value it would have for some intermediate temperature. If, for example, the highest temperature in a calculation were 515 K, with the lowest temperature being, say, 400 K, then the viscosity would be held at the value of viscosity for air at, say, 500 K. Flux and erosion calculations were not performed for tubes in banks because of the arbitrary nature of the imposed particle release points.

Particle trajectories for the Re=140,000 tube bank flow of Figure 9 are shown in Figure 10. Here, the dashed trajectory shows the calculated particle path for a particle in the non-isothermal flow, to be compared with the solid trajectory which shows the particle path for the same particle in an isothermal flow. The configuration is an in-line tube bank, with a tube spacing to tube diameter ratio of two. The effect of temperature-varying viscosity in the non-isothermal flow is small but apparent. The cooler air near the tube surface, with its lower viscosity, is not quite as effective as the isothermal flow at deflecting the particle from its path. The result is that the particles in a non-isothermal flow are not entrained in the bulk flow between the cylinders as quickly as are the particles in the non-isothermal flow.

Acknowledgements

This research was sponsored by Martin Marietta Energy Systems, Inc. (Subcontract # 19X-55936C) under their Principal Contract with the U.S. Department of Energy # DE-AC05-84OR21400.

The authors would also like to acknowledge and thank Marc Schweitzer, whose work at the University of Liverpool, England, contributed substantially to this research effort.

References

[1] Schuh, Michael J., (1987) "Numerical Prediction of Fluid and Particle Motions in Flows Past Tubes," Ph.D. Thesis, The University of California at Berkeley, 365 pages.

[2] Schuh, M.J., Schuler, C.A., and Humphrey, J.A.C., (1989) "Numerical Calculation of Particle-Laden Gas Flow Past Tubes," A.I.Ch.E. Jl., **35**, pp. 466-480.

[3] Zhukauskus, A., and Zhiugzhda, J., (1985) *Heat Transfer of a Cylinder in Crossflow*, Hemisphere Publishing Corp., New York.

[4] Patankar, S.V., (1980) *Numerical Heat Transfer and Fluid Flow*, Hemisphere Publishing Corp., New York.

[5] Patankar, S.V., Liu,C.J., and Sparrow, E.M., (1976) "Fully Developed Flow and Heat Transfer in Ducts Having Stream-Wise-Periodic Variation of Cross-Sectional Area," J. Heat Transfer, **99**, pp.180-186.

[6] Prandtl, L., (1925) "Bericht ueber Untersuchungen zur ausgebildeten Turbulenz," Zeit. Angew. Math. Mech., **5**, p. 136.

[7] Van Driest, E.R., (1956) "On Turbulent Flow Near A Wall," J. Aerosp. Sci., **23**, p. 1007.

[8] Rodi, W., (1984) *Turbulence Models and Their Applications in Hydraulics -- A State of the Art Review*, International Association for Hydraulic Research, Delft, the Netherlands.

[9] Arnal, M.P., (1988) "Investigation of Developing Laminar and Turbulent Flow in Curved Ducts," Ph.D. Thesis, The University of California at Berkeley.

[10] Arpaci, V., and Larsen, P.S., (1984) *Convection Heat Transfer*, Prentice-Hall, Inc., Englewood Cliffs, NJ.

[11] Schweitzer, Marc O., (1990) " Numerical Calculation of Heat Transfer and Particle Flow in a Tube Bank," M.S. Thesis, The University of Liverpool, 107 pages.

[12] Thompson, Joe F., Warsi, Z.U.A., and Mastin, C. Wayne, (1985) *Numerical Grid Generation*, Elsevier Science Publishing Co., Inc., New York.

[13] Majumdar, S., and Rodi, W., (1985) "Numerical Calculation of Turbulent Flow Past Circular Cylinders," paper presented at Third Symposium onn Numerical and Physical Aspects of Aerodynamic Flows, Long Beach, CA, Jan. 1985.

[14] Achenbach, Elmar, (1975) "Total and Local Heat Transfer From a Smooth Circular Cylinder in Cross-Flow at High Reynolds Number," Int. Journal of Heat and Mass Transfer, **18**, p. 1387.

[15] Zhukauskus, A., and Ulinskas, R., (1988) *Heat Transfer in Tube Banks in Crossflow*, Hemisphere Publishing Corp., New York.

[16] Eckert, E.R.G., and Soehgen, E., (1953) "Distribution of Heat Transfer Coefficients around Circular Cylinders in Crossflow at Reynolds Number from 20 to 500," Trans. ASME, **75,** p. 343.

[17] Wung, Tzung-Shyan, and Chen, Ching Jen, (1989) "Finite Analytic Solution of Convective Heat Transfer for Tube Arrays in Crossflow: Part II -- Heat Transfer Analysis," Journal of Heat Transfer, **111,** pp. 641-648.

[18] Wung, Tzung-Shyan, and Chen, Ching Jen, (1989) "Finite Analytic Solution of Convective Heat Transfer for Tube Arrays in Crossflow: Part I -- Flow Field Analysis," Journal of Heat Transfer, **111,** pp. 633-640.

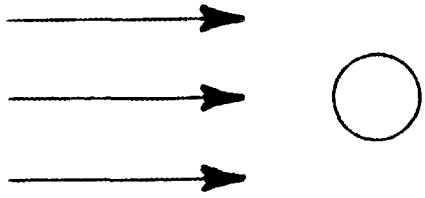

Single tube

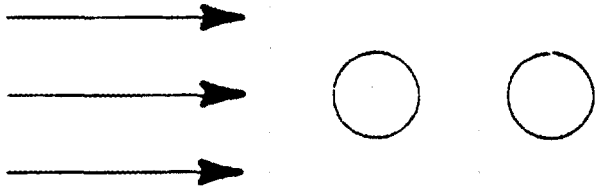

Two tubes in tandem

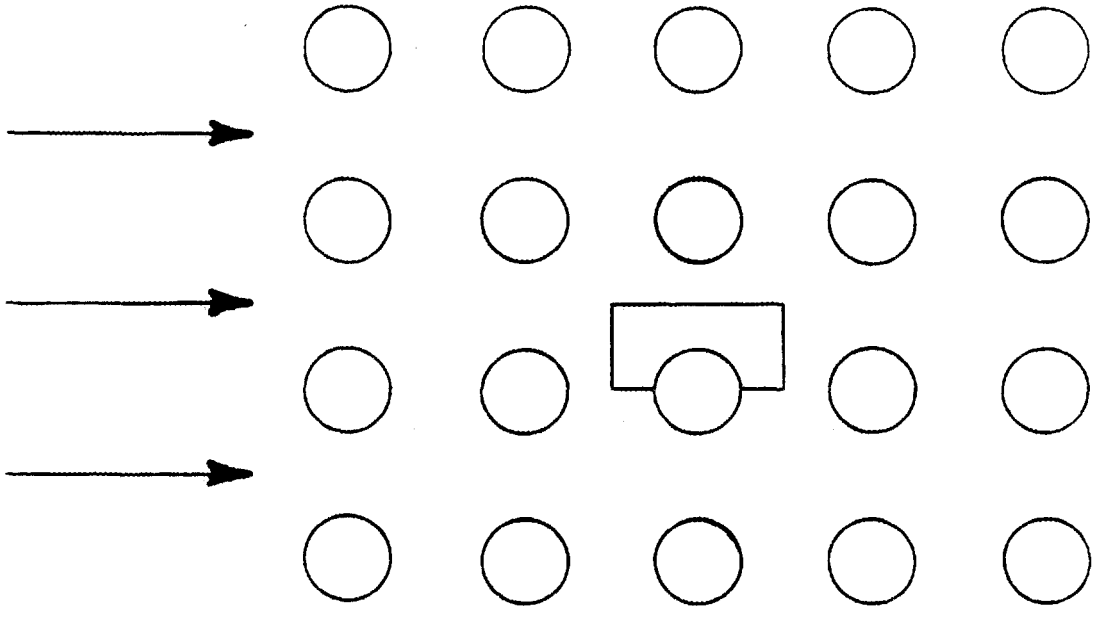

Tube in an infinite tube bank

Figure 1. The three flow fields of interest.

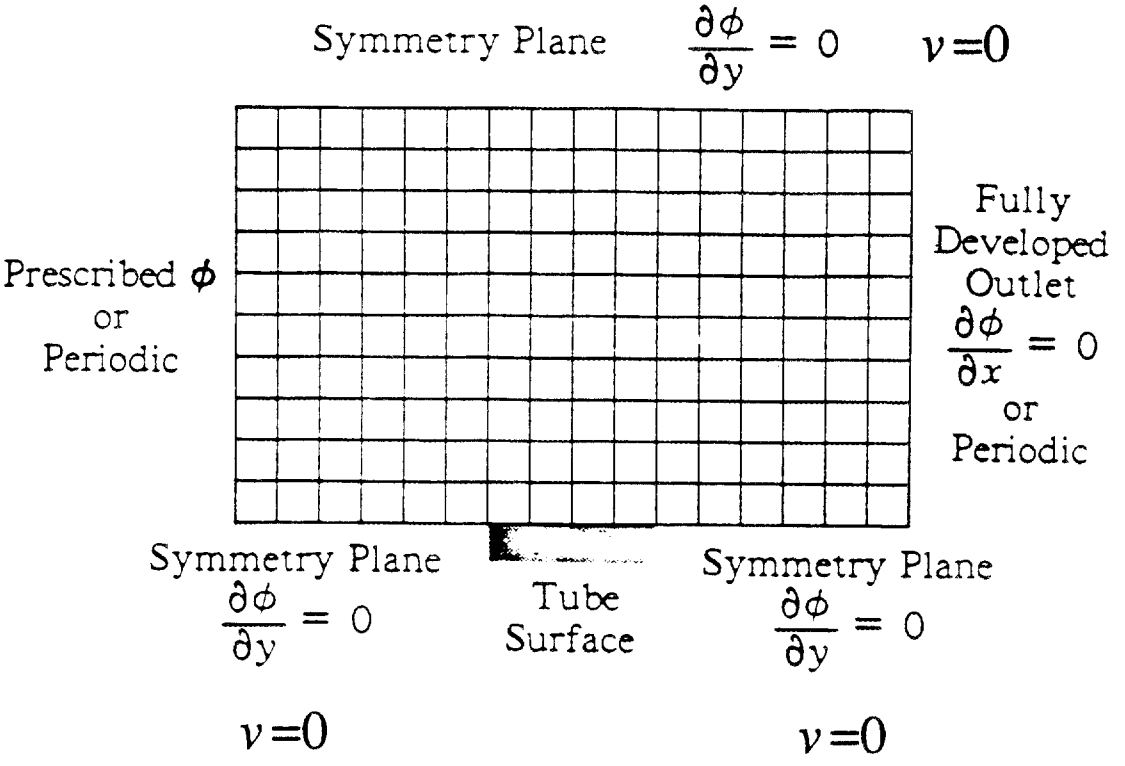

Figure 2. Boundary conditions for the general variable ϕ. Also $v=0$ at the symmetry planes.

$\phi = U, V, k, \varepsilon, T, or\ \theta$

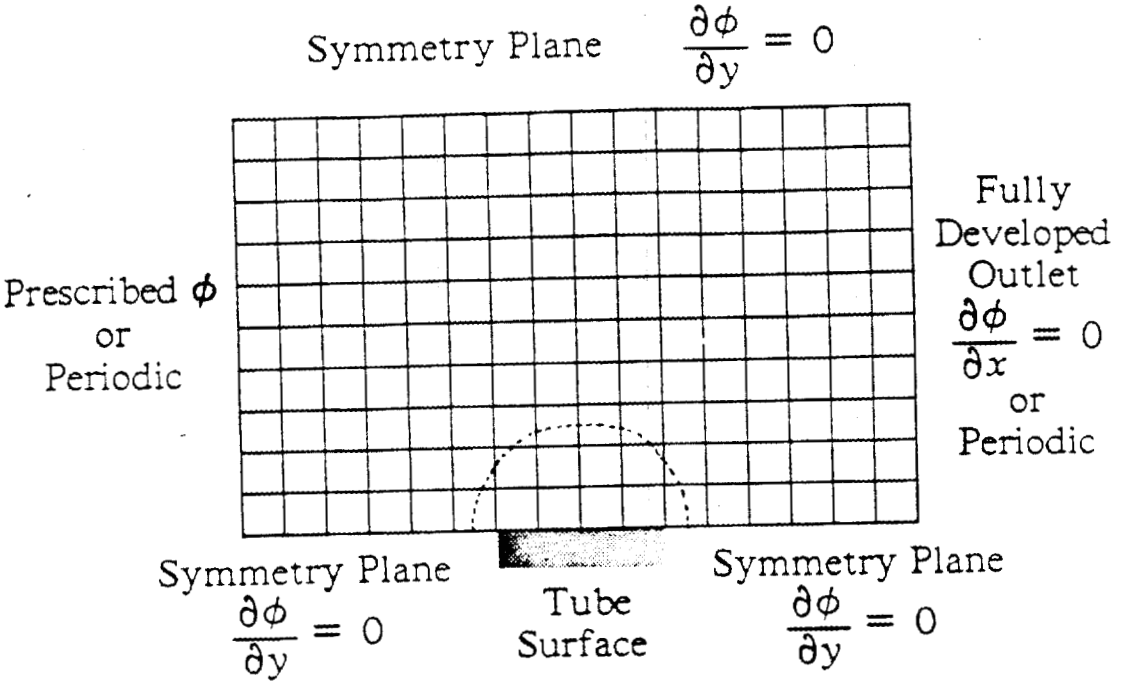

$$\text{At } y^+=50:\ k=\frac{l^2\left[\frac{\partial U}{\partial y}+\frac{\partial V}{\partial x}\right]^2}{C_\mu^{\frac{1}{2}}},\ \varepsilon=l^2\left[\left[\frac{\partial U}{\partial y}+\frac{\partial V}{\partial x}\right]^2\right]^{\frac{3}{2}}.$$

Figure 3. k and ε boundary conditions at tube surface.

$\phi = k$ *or* ε

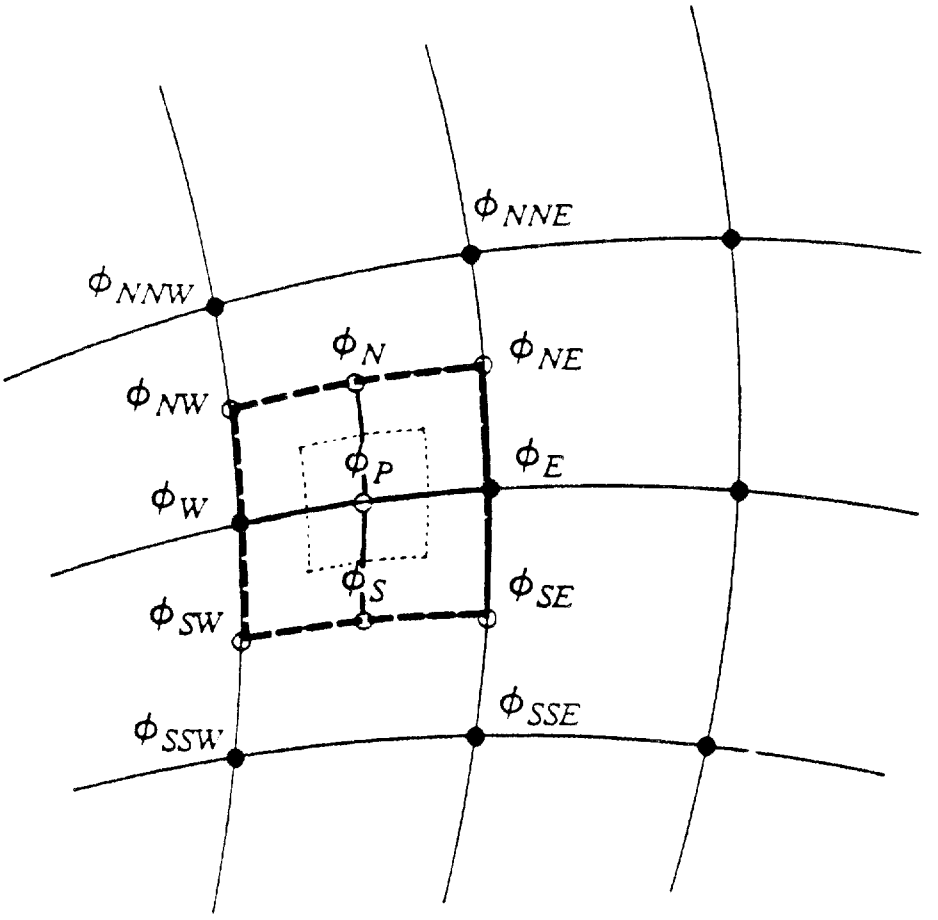

Figure 4. ····· Unit control volume on curvilinear grid.

▬ ▬ ▬ The region encompassing the points ϕ_N, ϕ_S, ϕ_E, ϕ_W.

Note that all variables (U, V, P, k, ε, T, θ) are assigned or solved for at the grid node locations (at the intersection of the grid nodes).

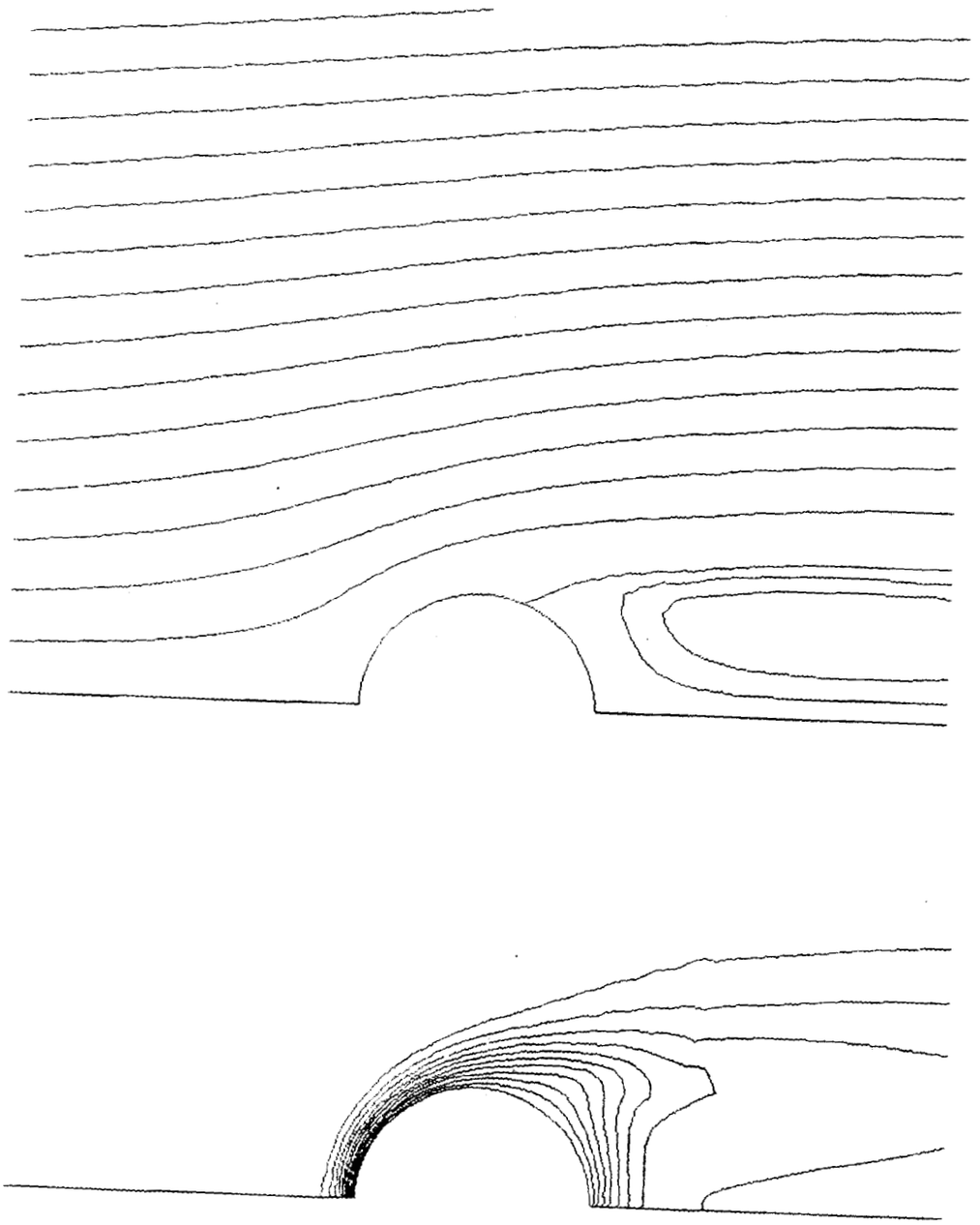

Figure 5. Streamlines and isotherms for single tube, Re=120.

Above: Streamlines

Below: Isotherms [T_{inlet}=320 and T_w=300.]

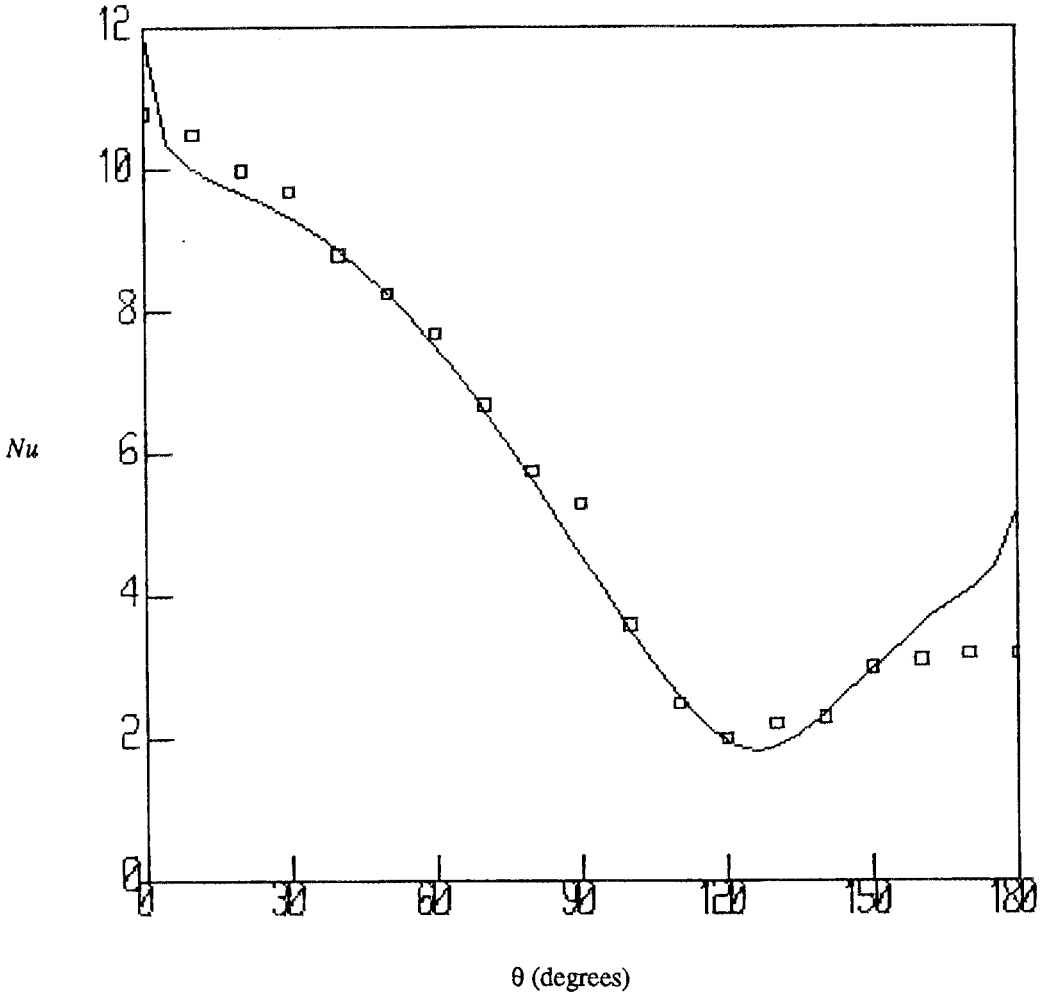

Figure 6. Nusselt numbers for single tube, Re=120 flow of air.

□ - Experimental results from Eckert [16].

— - Calculated results.

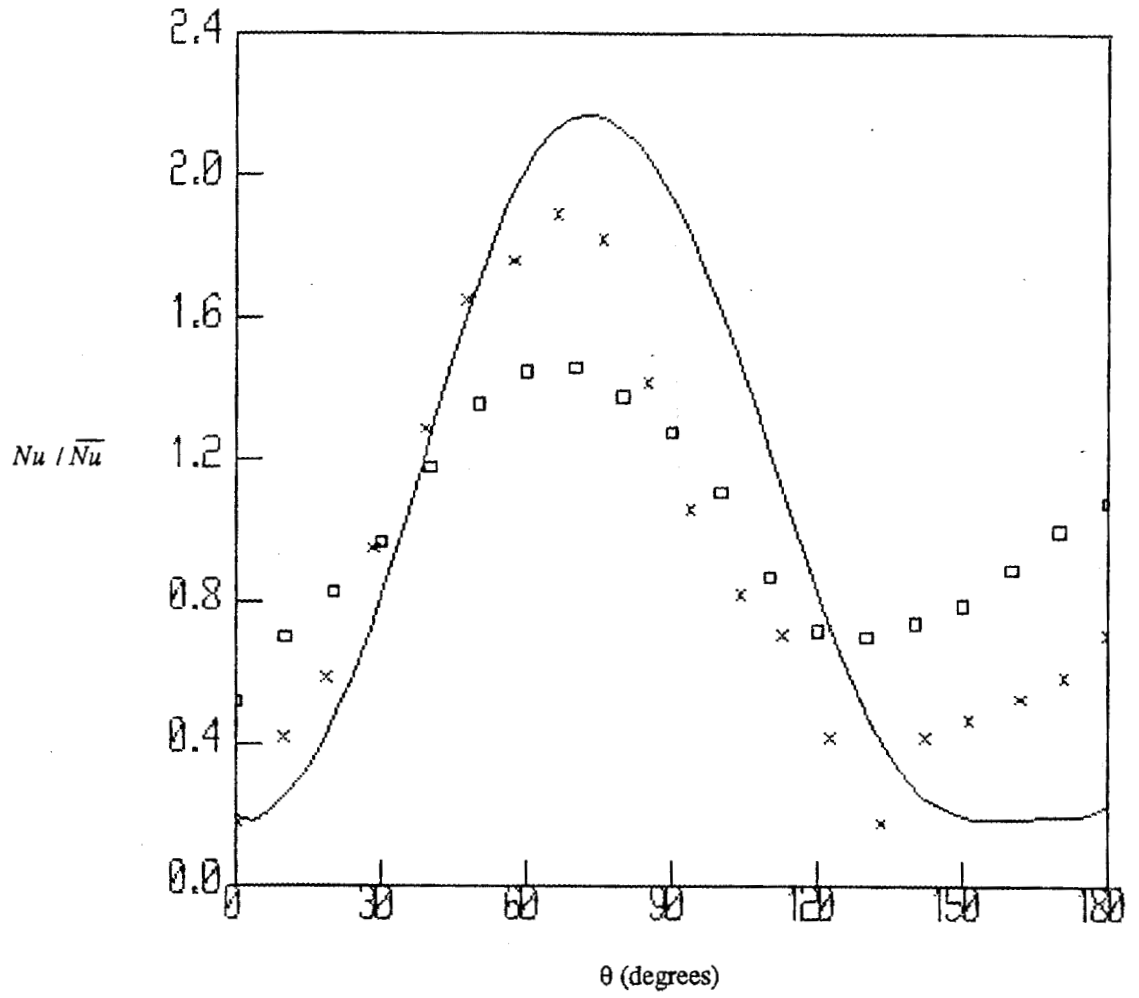

Figure 7. Nusselt numbers for tube in a bank ($\frac{L}{D}$=1.5), Re=450 flow of air.

□ – Experimental results from Zhukauskus [15]

× – Calculated results from Wung and Chen [17, 18].

—— – Calculated results.

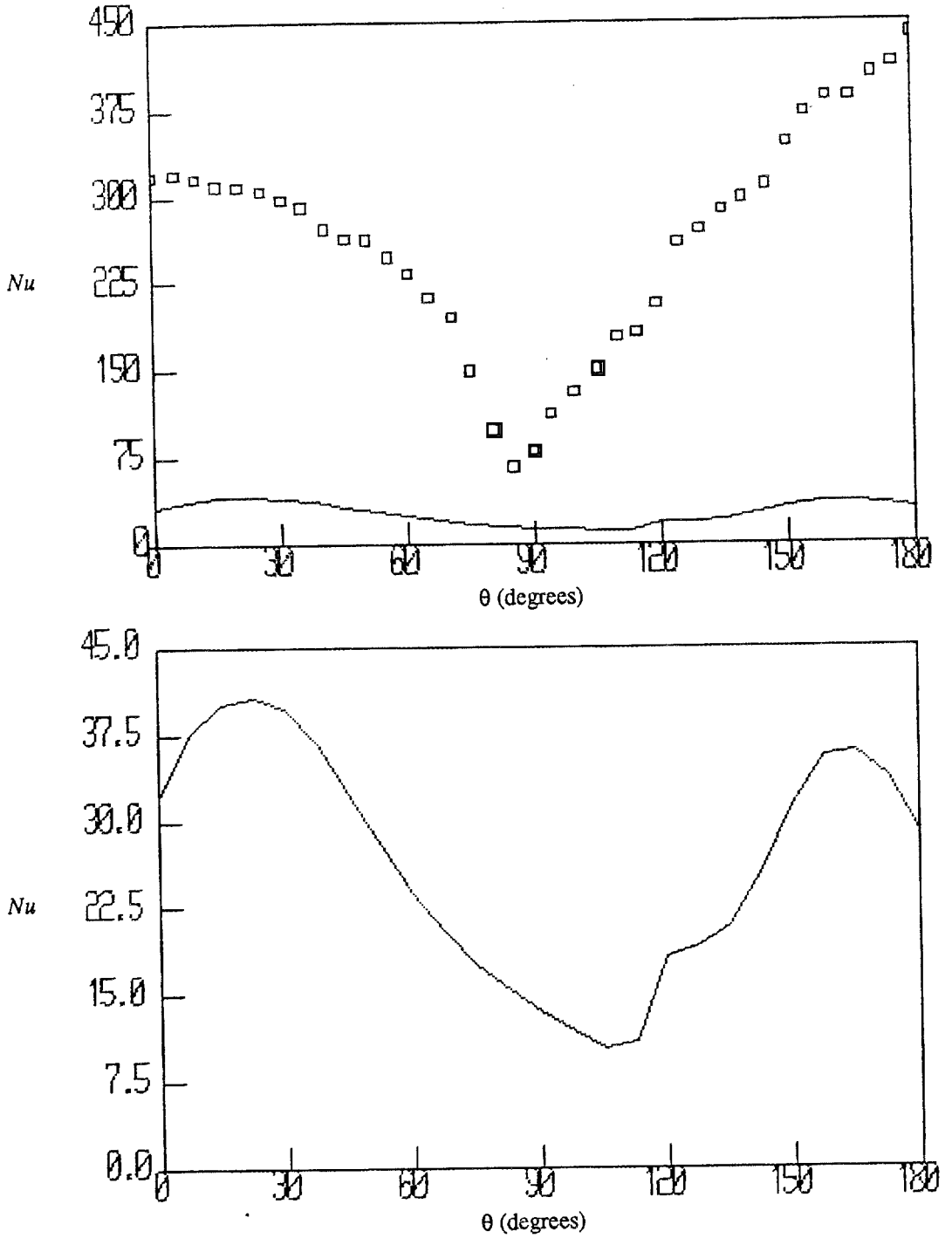

Figure 8. Nusselt numbers for single tube, Re=10^5.

Above:

□ - Experimental results from Achenbach [14].

—— - Calculated results.

Below:

—— - Calculated results on larger vertical scale.

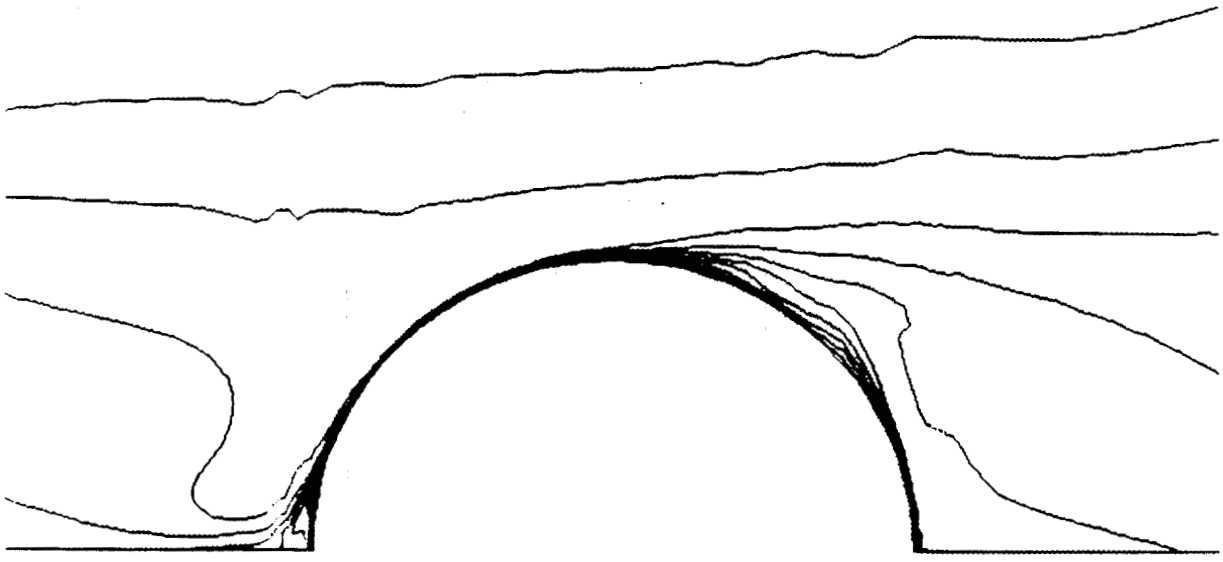

Figure 9. Isotherms for tube bank ($\frac{L}{D}$=2.0), Re=140000.

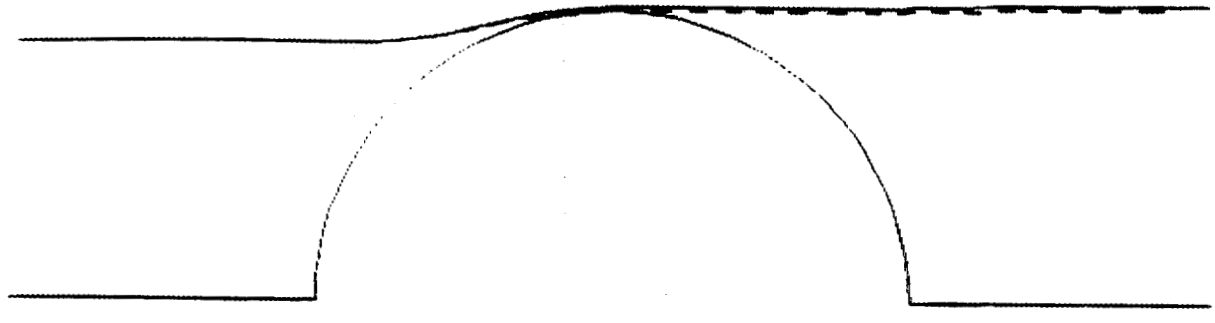

Figure 10. Particle trajectories for tube bank ($\frac{L}{D}$=2.0), Re=140000

Dashed line -- non-isothermal trajectory.

Solid line -- isothermal trajectory.

Wear, *126* (1988) 211 - 218

NOTE ON THE EXPERIMENTAL MEASUREMENT OF PARTICLES EMBEDDED IN ONE AND TWO IN-LINE TUBES IN A HIGH SPEED GAS STREAM

M. O. SCHWEITZER and J. A. C. HUMPHREY*

Department of Mechanical Engineering, University of California at Berkeley, Berkeley, CA 94720 (U.S.A.)

(Received October 22, 1987; revised May 9, 1988; accepted May 11, 1988)

Summary

Solid particle deposition on one and two in-line tubes has been measured. Experiments were conducted in a vertical duct containing the tube(s) oriented perpendicular to the mean flow. Dilute particle concentrations corresponding to 40 or 97 μm glass beads, at mass loading ratios less than 0.007, were investigated. Air approaching the tube(s) at 18.5 m s^{-1} and 1.4% turbulence intensity was used as the carrier fluid. Various differences observed in the circumferential depositions for the two bead sizes are attributed to the fivefold difference between their respective inertia numbers. In the case of two in-line tubes, the wake of the first substantially alters the deposition characteristics of the second. Some photographic evidence of this effect was obtained.

1. Introduction

The erosion of material by solid particle impact is a serious problem in chemical plants, coal combustion equipment and heat exchangers when operated in contaminated environments. Of special interest here is the study of dilute particle suspensions flowing normal to a tube bank. Such flows exist in the convective zone (or free-board) of a fluidized bed combustor and in primary superheaters, reheaters and economizers of coal-fired boilers. These systems present complex erosion problems of great practical consequence and considerable fundamental interest.

In contrast to the relatively large number of experimental and computational investigations conducted to clarify the single-phase flow and heat transfer characteristics of tube bank configurations, little work of compar-

*On leave of absence as Harrison Professor of Mechanical Engineering, University of Liverpool, U.K.

0043-1648/88/$3.50

able extent has been done to improve the understanding of the corresponding particle impact erosion problems. While interesting in their own right, numerical studies of particles impacting single tubes, such as have been performed by Tilley [1], Healy [2], Laitone [3], and Vittal and Tabakoff [4], are of limited value for rendering predictable the erosion of tubes in tube banks. Similarly, the experimental data available, particularly those pertaining to particle motion in turbulent flow, are of limited use for advancing fundamental insight of important basic mechanisms. This is because in attempting to simulate systems of practical (industrial) interest, various factors such as temperature, particle size and concentration, material properties and fluid flow conditions (especially turbulence, unknowingly) are frequently varied simultaneously. Thus often the experimental task is reduced to simply obtaining a correlation for erosion, in terms of the independent variables, that is highly specific to the system under investigation. See, for example, Tsai *et al.* [5], Bauver *et al.* [6], Gilmour *et al.* [7] and the various references therein.

The measurement of erosion, particularly as a quantity for guiding and testing numerical model developments for predicting particle trajectories in two-phase flows, is not as fundamental a measurement as particle deposition. In the erosion process, the properties of the materials involved, the topography of the surface being eroded and the particle shape, and interactions between approaching and rebounding particles affect the erosion measurand (mass or volume of material removed, depth of penetration etc.). To deduce from erosion measurements the characteristics of particle flow is extremely difficult.

By constrast, regardless of how erosion takes place or the particle–surface mechanisms that control it, the particles must first arrive at the surface. Therefore particle deposition on the surface, a quantity considerably easier to predict (and to measure), is the preferred measurand in this study.

To our knowledge, an in-depth study of particle-laden erosive flows in tube banks has not yet been performed. This is not surprising given the complexity of the problem. It is the purpose of this work to overcome partly the knowledge gap by performing an experimental investigation of a simpler flow configuration using a very simple measurement technique.

In the experiment, attention is focused on the flow of air at high speeds through a vertical duct with two in-line tubes of discretely variable spacing aligned normal to the flow. (The single-tube configuration is also documented as a reference standard.) The air carries a dilute concentration of glass beads of mass loading $\Gamma < 7 \times 10^{-3}$ and of mean (gaussian distributed) diameter of either $d_p = 97\ \mu m$ or $d_p = 40\ \mu m$. (Here Γ equals mass particles/mass air.) The speed and turbulence intensity of the air approaching the tubes have been held constant at 18.5 m s^{-1} and 1.4% respectively, for the data provided here. (The turbulence intensity is defined in Section 4.) Experiments at 5% turbulence level were also performed but the results obtained were not considered reliable enough to be included in this work. In addition to the particle deposition measurements, flow visualization experi-

ments were also performed using an argon ion laser light sheet to illuminate the glass beads.

2. Experimental apparatus

A schematic of the experimental apparatus is provided in Fig. 1. Air at high speed is drawn from a stagnation chamber into a vertical duct of square cross-section (hydraulic diameter $D = 10$ cm) by a continuously variable speed, axial flow, Lansom blower. Measurements of the air velocity through the duct are obtained with a static pressure pitot tube connected to an oil manometer. The air speed used in the experiments was 18.5 m s^{-1}, although higher speeds could be achieved. The blower was sound proofed for ease of operation.

A four-to-one contraction at the duct inlet is followed by two fixed screens of discretely variable spacing used to generate the turbulent air flow condition. The screen characteristics are as follows: width of grid element, b = 3.175 mm; distance between grid element centres, M = 6.845 mm. Two in-line tubes of diameter d = 2.42 cm are located downstream of the screens in the vertical duct. The spacing between the tubes is discretely variable and the first, upstream tube, is placed at $x = 8.8D$ duct diameters downstream from the last screen. The axes of the tubes are aligned normal to the main flow (as well as to two facing side walls) and contained in the duct centre.

Particles of either diameter d_p = 97 μm or d_p = 40 μm (approximately) are introduced into the duct flow by gravity feed from a hopper whose mass flow *vs.* time has been previously calibrated. The flow of particles is controlled by the size of the orifice through which they pass. The particles fall onto two successive orbitally vibrating screens (isolated from the vertical test

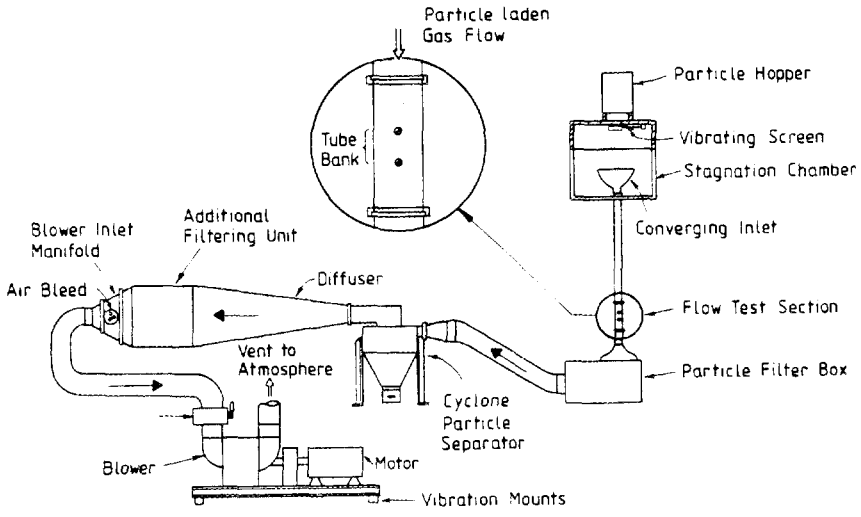

Fig. 1. Schematic of experimental apparatus and flow test section.

section) which distribute them evenly over the duct cross-section. A filter box downstream of the duct test section removes most of the particles from the flow. A cyclone separator removes those particles that have been comminuted and have escaped the screens in the filter box. Additional filters at the end of the diffuser connected to the blower ensure that very small particles that might damage the blower are removed. The filtered air from the blower is exhausted to the atmosphere.

3. Measurement procedure

Of the two tubes placed in the test section, one is constructed from steel and is perfectly circular while the other is machined from aluminium. The cross-section of the latter is shown in Fig. 2 where it is seen that 36 shallow grooves of triangular cross-section are evenly distributed around the periphery of the tube. Crisco shortening (hydrogenated palm and soya oil) is carefully packed into the grooves and serves to trap any particles that strike a groove cross-section. After an experimental run, the Crisco–particle mixture is carefully removed from a groove and placed on a pre-weighed screen. The Crisco is then melted using a heat lamp and removed by carefully washing with a warm mixture of isomer hexanes (C_6H_{14}). The mass of particles remaining after washing is dried and then weighed on a Mettler balance to within $\pm 4 \times 10^{-5}$ g. In this way, the circumferential distribution of particles deposited in the grooves around the aluminium tube during an experiment can be determined. Although laborious, the procedure is simple, accurate and inexpensive.

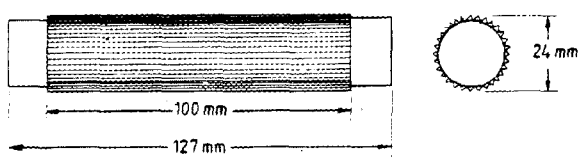

Fig. 2. Side and end views of machined aluminium tube with triangular grooves for capturing particles.

The tubes are positioned at their respective locations by insertion through snug-fitting holes in two facing walls of the test section. By aligning two marks, one on a tube and one on a wall, the relative orientation is maintained between a tube and the flow. For experiments involving a single tube, the aluminium tube was always used. For experiments involving two tubes, the aluminium tube was always the second (downstream) tube. The walls of the vertical duct are constructed from thick transparent Plexiglass, 9.5 mm thick, for ease of optical access.

4. Experimental results

The measured results are shown in Figs. 3 - 6. The experimental conditions are given in the figure captions. The quantity

$$\tilde{u} \left\{ \equiv \left(\overline{u^2} \right)^{1/2} \times \frac{100}{U_B} \right\} \tag{1}$$

is the per cent streamwise turbulence intensity based on the bulk average velocity U_B through the duct; Re_d ($\equiv dU_B/\nu$) is the Reynolds number of the flow based on the tube diameter d and Re_D ($\equiv DU_b/\nu$) is the Reynolds number of the flow based on the duct diameter D. The quantity ν is the fluid (air) kinematic viscosity taken at 25 °C.

In eqn. (1), $(\overline{u^2})^{1/2}$ is the r.m.s. of the air flow velocity fluctuations. This can be determined from a knowledge of the grid characteristics and the bulk average velocity as explained in Nandascher *et al.* [8].

The curves in Fig. 3 represent the total particle mass captured by a single tube as a function of the particle mass injected into the duct. This shows that by the time 10 g of particles (97 μm in diameter) have been injected into the duct, for the experimental conditions investigated, a "surface saturation" condition has occurred with the tube having captured about 0.57 g of particles at this time. These data suggest that after one or two layers of particles are embedded in the grooves, further embedding is inhibited, presumably by rebounding of the particles from encrusted portions of the tube surface. The figure also suggests that particles, 40 μm in diameter, saturate the surface of the tube faster than the larger particles, 97 μm in

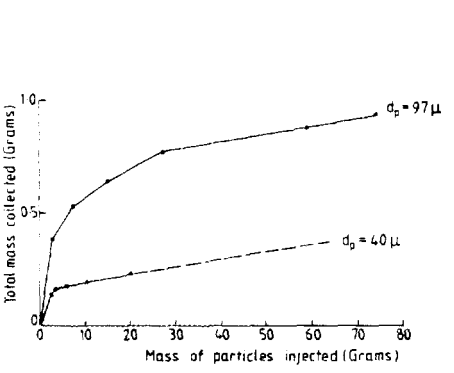

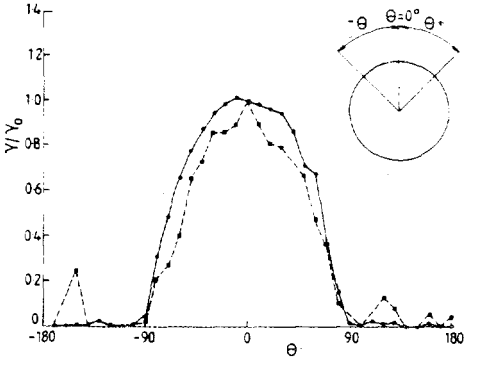

Fig. 3. Total particle mass collected on a single tube as a function of the mass of particles injected into duct. Relevant conditions are: x/D = 8.8; Re_d = 28 500; Re_D = 117 000; $\tilde{u}$ = 1.4%; U_B = 18.49 m s^{-1}; Γ = 6.81 x 10^{-3}.

Fig. 4. Circumferential distribution of normalized particle deposition on the surface of a single tube. Conditions are as specified in Fig. 3. Total mass collected: ●, 0.5318 g (97 μm); ■, 0.1464 g (40 μm).

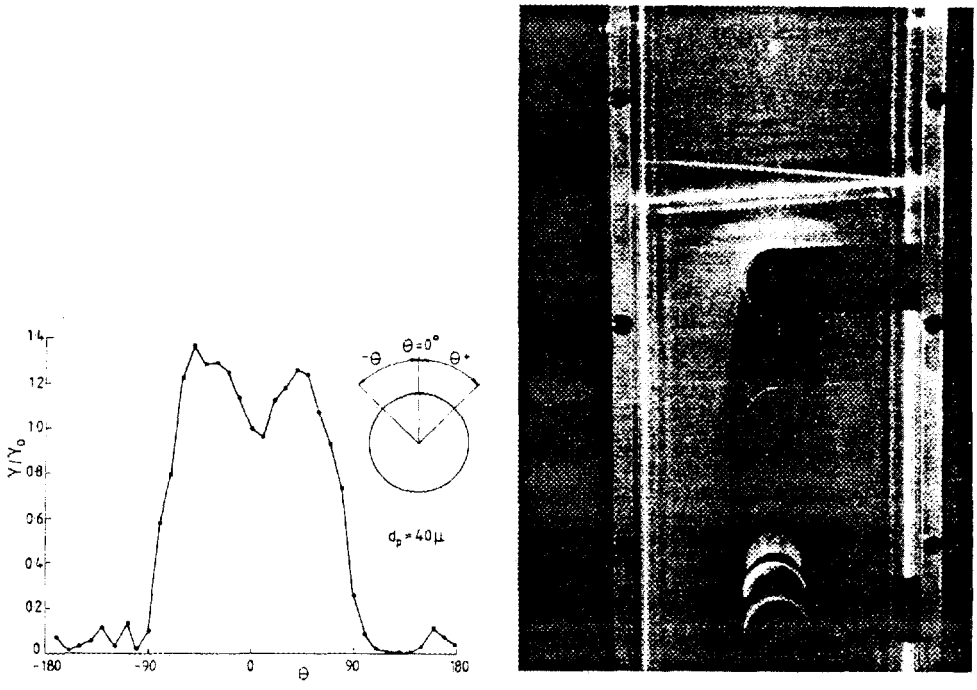

Fig. 5. Circumferential distribution of normalized particle deposition on the surface of the second of two in-line tubes spaced 5*d* apart. Conditions are as specified in Fig. 3. Total mass collected, 0.1125 g.

Fig. 6. View of particle flow past two solid smooth cylinders (black disks) spaced 5*d* apart. Flow is from top to bottom. The centre black disk is a plug. d_p = 97 μm. Conditions are as specified in Fig. 3.

diameter. This is to be expected because it can be shown that the smaller particles (40 μm in diameter) have more than twice the coverage area of the larger particles (97 μm diameter) for equal mass fluxes. The conclusion is that particle deposition measurements using this technique must be limited to low values of the total particle phase mass to avoid a bias in the peripheral distribution of the deposition measurement. The maximum run time that avoids the surface saturation condition must be determined experimentally as a function of the flow and configuration conditions. The total injected particle phase mass is a function of the size of the particles used.

Figure 4 shows the circumferential distribution of particle deposition, γ, to a single tube normalized by the particle deposition measured at $\theta = 0°$, γ_0, on the tube. These data are especially interesting for three reasons: (1) for both particle sizes they show a maximum deposition at 0° (corresponding to the stagnation point on the tube); however, a projected area (or cosine) fall-off between 0° and 90° is only shown by the larger, more inertial, particles; (2) they show a small, but measurable number of particles impacting the tube past the ±90° locations; (3) they show that the larger

particles (97 μm diameter) are more likely to impact the tube than the smaller particles (40 μm diameter). The third result is to be expected because of the large particle inertia number, λ, for the 97 μm particles; $\lambda_{97}/\lambda_{40} = 5.88$. The particle inertia number is defined as

$$\lambda = \frac{\rho_p d_p^2}{18\mu} \frac{U_B}{D} \tag{2}$$

where ρ_p is the particle density, μ the air viscosity and the remaining variables are as defined above.

The first of the above three points illustrates the fact that the small particles deviate from the trajectories of the larger, more inertial, particles and should not be expected to display the same cosine dependence. This is important because the ductile metal erosion of tubes is dependent on particle impact angle; see Bauver *et al.* [6]. The second point illustrates the possibility of particle re-entrainment in the wake region of the tube, where some particles are redirected towards, and embedded in, the tube's rear surface.

Results for the deposition of particles on the second of two in-line tubes are shown in Fig. 5. The conditions stipulate particles 40 μm in diameter and tubes spaced 5*d* apart from their centres. The protective influence of the upstream tube was noted in two ways: (a) by a reduction in the total particle deposition on the second tube relative to the first (not evident from the plots because of the choice of normalization); (b) by the reduction in relative deposition to the second tube around the 0° location as a result of the protective influence of the wake from the first (upstream) tube. The mass of particles, 40 μm in diameter, deposited on the second of two in-line tubes spaced 2*d* apart from their centres was too small to be measured by the present technique.

A typical flow visualization result is shown in Fig. 6. The conditions stipulate particles 97 μm in diameter and solid smooth surface tubes spaced 5*d* apart from their centres. Three black disks are visible in the photograph. The centre disk is a plug. The top and bottom disks are the ends of tubes. The dark bars emanating to the right of the tubes are shadows created by the laser light sheet. The halo above the upstream tube is formed by particles rebounding from the tube surface. The extent to which the upstream tube shields the downstream tube from impacting particles is clear from this long-term exposure.

The photograph also illustrates why we consider the deposition measurements with the 97 μm particles, to the second tube in an in-line tube arrangement, to be inaccurate. Some of the particles striking the upstream tube rebound from the test section wall and are redirected towards the second downstream tube. The particles, 40 μm in diameter, did not exhibit this behaviour. Therefore the results given in Fig. 7 for the deposition of particles on the second of two in-line tubes spaced 2*d* and 5*d* apart using particles, 97 μm in diameter, should be considered with caution.

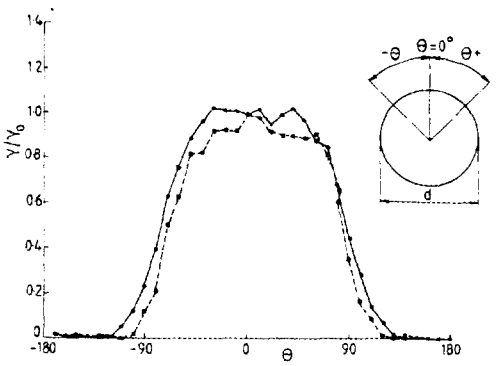

Fig. 7. Circumferential distribution of normalized particle deposition (d_p = 97 μm) on the surface of the second of two in-line tubes spaced as indicated. Conditions are as specified in Fig. 3. Total mass collected: 0.3555 g ($2d$); 0.3422 g ($5d$). Cylinder spacing: ●, $2d$; ■, $5d$.

Acknowledgments

We are pleased to acknowledge the financial support of this work by the Department of Energy through subcontract 19X-55936C under the technical monitoring of the Oakridge National Laboratory, Fossil Energy Research Program. Thanks go to Messieurs M. Schuh and C. Schuler for their assistance in interpreting some of the results of this study using numerical simulation techniques.

References

1 G. P. Tilly, Erosion caused by airborne particles, *Wear, 14* (1969) 63 - 79.
2 J. V. Healy, Perturbed two-phase cylindrical type flows, *Phys. Fluids, 13* (1970) 551 - 557.
3 J. A. Laitone, Characterisation of particle rebound phenomena in the erosion of turbomachinery, *J. Aircr., 20* (1983) 275 - 281.
4 B. V. R. Vittal and W. Tabakoff, Effect of solid particles in two phase flow around a two dimensional cylinder, *AIAA Aerospace Sciences Meet., Reno, NV, 6 - 9 January, 1986*, Paper AIAA-86-0349.
5 W. Tsai, J. A. C. Humphrey, I. Cornet and A. V. Levy, Experimental investigation of accelerated erosion in a slurry pot tester, *Wear, 68* (1981) 289 - 303.
6 W. P. Bauver, T. C. McGough and G. T. McGowan, A facility for the characterisation of erosion of heat transfer tubing. In J. J. Jurewicz (ed.), *Gas Solid Flows*, FED — Vol. 10, American Society of Mechanical Engineers, New York, 1984, pp. 115 - 122.
7 J. B. Gilmour, H. Hindam, A. W. Liu and D. C. Briggs, The EMR/NSPC/AFBC materials program: evaluation of probes removed at the end of run 5, *Physical Metallurgy Research Laboratories Rep. ERPR/PMRL 85-12 (TR)*, 1985, (Canada Centre for Mineral and Energy Technology, Energy Mines and Resources, Canada).
8 E. Nandascher, M. Asce and C. Farell, Unified analysis of grid turbulence, *J. Eng. Mech. Div. ASCE, EM2* (1970) 121 - 141.

DISTRIBUTION

AIR PRODUCTS AND CHEMICALS
P.O. Box 538
Allentown, PA 18105
S. W. Dean
S. C. Weiner

ARGONNE NATIONAL LABORATORY
9700 S. Cass Avenue
Argonne, IL 60439
W. A. Ellingson
K. Natesan

AVCO RESEARCH LABORATORY
2385 Revere Beach Parkway
Everett, MA 02149
R. J. Pollina

BABCOCK & WILCOX
1562 Beeson St.
Alliance, OH 44601
T. I. Johnson
T. Modrak

BABCOCK & WILCOX
Domestic Fossil Operations
20 South Van Buren Avenue,
Barberton, OH 44023
M. Gold

BABCOCK & WILCOX
Lynchburg Research Center
P.O. Box 11165
Lynchburg, VA 24506
H. Moeller

BATTELLE-COLUMBUS LABORATORIES
505 King Avenue
Columbus, OH 43201
V. K. Sethi
I. G. Wright

BRITISH COAL CORPORATION
Coal Research Establishment
Stoke Orchard, Cheltenham
Glochester, England GL52 4RZ
M. Arnold
C. Bower
A. Twigg

BRITISH GAS CORPORATION
Westfield Development Centre
Cardenden, Fife,
Scotland KY5OHP
J. E. Scott

BROOKHAVEN NATIONAL LABORATORY
Department of Applied Science,
Upton, Long Island, NY 11973
T. E. O'Hare

CANADA CENTER FOR MINERAL & ENERGY TECHNOLOGY
568 Booth Street
Ottawa, Ontario
Canada K1A OG1
R. Winston Revie
Mahi Sahoo

COMBUSTION ENGINEERING
911 W. Main Street
Chattanooga, TN 37402
D. A. Canonico

CONSOLIDATION COAL COMPANY
4000 Brownsville Road
Library, PA 15129
S. Harding

ELECTRIC POWER RESEARCH INSTITUTE
P.O. Box 10412
3412 Hillview Avenue
Palo Alto, CA 94303
W. T. Bakker
R. L. S. Chang
J. T. Stringer

EUROPEAN COMMUNITIES JOINT RESEARCH CENTRE
Petten Establishment
P.O. Box 2
1755 ZG Petten
The Netherlands
M. Van de Voorde

FOSTER WHEELER DEVELOPMENT CORPORATION
Materials Technology Department
John Blizard Research Center
12 Peach Tree Hill Road
Livingston, NJ 07039
J. L. Blough

GAS RESEARCH INSTITUTE
8600 West Bryn Mawr Avenue
Chicago, IL 60631
H. S. Meyer

GENERAL ELECTRIC COMPANY
1 River Road,Bldg. 55, Room 115
Schenectady, NY 12345
R. W. Haskell

GEORGIA INSTITUTE OF TECHNOLOGY
Georgia Tech Research Institute
Atlanta, GA 30332
T. L. Starr

LANXIDE CORPORATION
1 Tralee Industrial Park
Newark, DE 19711
E. M. Anderson

LAWRENCE BERKELEY LABORATORY
University of California
Berkeley, CA 94720
A. V. Levy

LAWRENCE LIVERMORE LABORATORY
P.O. Box 808, L-325
Livermore, CA 94550
W. A. Steele

MOBIL RESEARCH & DEVELOPMENT CORPORATION
P. O. Box 1026
Princeton, NJ 08540
R. C. Searles

NATIONAL INSTITUTE OF STANDARDS AND TECHNOLOGY
Materials Building
Gaithersburg, MD 20899
S. J. Dapkunas
L. K. Ives

NATIONAL MATERIALS ADVISORY BOARD
National Research Council
2101 Constitution Avenue
Washington, DC 20418
K. M. Zwilsky

NEW ENERGY DEVELOPMENT ORGANIZATION
Sunshine 60 Bldg.
P.O. Box 1151
1-1, Higashi-Ikebukuro 3-chrome
Toshima-Ku
Tokyo, 170
Japan
S. Ueda

OAK RIDGE NATIONAL LABORATORY
P.O. Box 2008
Oak Ridge, TN 37831
P. J. Blau
D. N. Braski
P. T. Carlson
W. N. Drewery, Jr. (8 copies)
R. R. Judkins
J. R. Keiser

RISOE NATIONAL LABORATORY
P.O. Box 49
DK-4000, Roskilde
Denmark
Aksel Olsen

SHELL DEVELOPMENT COMPANY
P. O. Box 1380
Houston, TX 77251-1380
L. W. R. Dicks

TENNESSEE VALLEY AUTHORITY
Energy Demonstration & Technology
MR 2N58A
Chattanooga, TN 37402-2801
C. M. Huang

TENNESSEE VALLEY AUTHORITY
1101 Market Street
MR 3N57A
Chattanooga, TN 37402
R. Q. Vincent

UNITED ENGINEERS & CONSTRUCTORS
30 South 17th Street
P.O.Box 8223
Philadelphia, PA 19101
A. J. Karalis

UNIVERSAL ENERGY SYSTEMS. INC.
4401 Dayton-Zenia Road
Dayton, OH 45432
V. Srinivasan

UNIVERSITY OF NOTRE DAME
Department of Materials Science and Engineering
P.O. Box E
Notre Dame. IN 46556
T. H. Kosel

WESTINGHOUSE ELECTRIC CORPORATION
Research and Development Center
1310 Beulah Road
Pittsburgh. PA 15235
S. C. Singhal

WESTINGHOUSE HANFORD COMPANY
P.O. Box 1970
W/A-65
Richland. WA 99352
R. N. Johnson

DOE
OAK RIDGE OPERATIONS OFFICE
P. O. Box 2001
Oak Ridge, TN 37831
Assistant Manager for Energy Research and Development

DOE
OAK RIDGE OPERATIONS OFFICE
Oak Ridge National Laboratory
P. O. Box 2008
Building 4500N, MS 6269
Oak Ridge, TN 37831
E. E. Hoffman

DOE
OFFICE OF BASIC ENERGY SCIENCES
Materials Sciences Division
ER-131, GTN
Washington, DC 20545
J. B. Darby

DOE
OFFICE OF FOSSIL ENERGY
Washington, DC 20545
D. J. Beecy (FE-14) GTN
J. P. Carr (FE-14) GTN
F. M. Glaser (FE-14) GTN
T. B. Simpson (FE-25) GTN

DOE
MORGANTOWN ENERGY TECHNOLOGY CENTER
P.O. Box 880
Morgantown, WV 26505
R. A. Bajura
R. C. Bedick
F. W. Crouse, Jr.
N. T. Holcombe
W. J. Huber
M. J. Mayfield
J. E. Notestein
J. S. Wilson

DOE
PITTSBURGH ENERGY TECHNOLOGY CENTER
P.O. Box 10940
Pittsburgh, PA 15236
S. Akhtar
T. C. Rupel
R. Santore
T. M. Torkos